VIBRATION-BASED CONDITION MONITORING OF WIND TURBINE BLADES

By

OZAK-OBAZI OLUWASEYI ESU

A Doctoral Thesis

Submitted in partial fulfilment of the requirements for the award of

Doctor of Philosophy (PhD.) in Electronic and Electrical Engineering

Loughborough University, Leicestershire, UK

April, 2016

ABSTRACT

Significant advances in wind turbine technology have increased the need for maintenance through condition monitoring. Indeed condition monitoring techniques exist and are deployed on wind turbines across Europe and America but are limited in scope. The sensors and monitoring devices used can be very expensive to deploy, further increasing costs within the wind industry. The work outlined in this thesis primarily investigates potential low-cost alternatives in the laboratory environment using vibration-based and modal testing techniques that could be used to monitor the condition of wind turbine blades. The main contributions of this thesis are: (1) the review of vibration-based condition monitoring for changing natural frequency identification; (2) the application of low-cost piezoelectric sounders with proof mass for sensing and measuring vibrations which provide information on structural health; (3) the application of low-cost miniature Micro-Electro-Mechanical Systems (MEMS) accelerometers for detecting and measuring defects in micro wind turbine blades in laboratory experiments; (4) development of an in-service calibration technique for arbitrarily positioned MEMS accelerometers on a medium-sized wind turbine blade. This allowed for easier aligning of coordinate systems and setting the accelerometer calibration values using samples taken over a period of time; (5) laboratory validation of low-cost modal analysis techniques on a medium-sized wind turbine blade; (6) mimicked ice-loading and laboratory measurement of vibration characteristics using MEMS accelerometers on a real wind turbine blade and (7) conceptualisation and systems design of a novel embedded monitoring system that can be installed at manufacture, is self-powered, has signal processing capability and can operate remotely.

By applying the conclusions of this work, which demonstrates that low-cost consumer electronics specifically MEMS accelerometers can measure the vibration characteristics of wind turbine blades, the implementation and deployment of these devices can contribute towards reducing the rising costs of condition monitoring within the wind industry.

ACKNOWLEDGEMENTS

LIST OF PUBLICATIONS

List of published contributions from the author occurring during the course of the PhD:

[1]   O. O. Esu, J. A. Flint, and S. J. Watson, "Integration of Low-Cost Accelerometers for Condition Monitoring of Wind Turbine Blades," in *European Wind Energy Association (EWEA) Conference, 2013*.

[2]   O. O. Esu, J. A. Flint, and S. J. Watson, "Condition Monitoring of Wind Turbine Blades with Low-Cost Accelerometers" in *Renewable Energy World Europe (REWE) Conference, 2013*.

[3]   O. O. Esu, J. A. Flint, and S. J. Watson, "Vibration Monitoring of Wind Turbine Blades with Low-Cost Accelerometers" in *School of Electronic, Electrical and Systems Engineering (SEESE) Conference, 2014*.

[4]   O. O. Esu, S. D. Lloyd, J. A. Flint, and S. J. Watson, "Integration of Low-Cost Consumer Electronics for In-situ Condition Monitoring of Wind Turbine Blades" in *3rd Renewable Power Generation (RPG) Conference, 2014*, IET, 2014, pp. 1-6.

[5]   O. O. Esu, J. A. Flint, and S. J. Watson, "Static Calibration of Microelectromechanical Systems (MEMS) Accelerometers for In-Situ Wind Turbine Blade Condition Monitoring," in *Special Topics in Structural Dynamics, Volume 6: Proceedings of the 33rd IMAC, A Conference and Exposition on Structural Dynamics, 2015*, R. Allemang, Ed. Springer International Publishing, 2015, pp. 91–98.

[6]   O. O. Esu, S. D. Lloyd, J. A. Flint, and S. J. Watson, "Feasibility of a Fully Autonomous Wireless Monitoring System for a Wind Turbine Blade" in *Elsevier Renewable Energy, Volume 97, November 2016*, pp. 89-96. http://dx.doi.org/10.1016/j.renene.2016.05.021

Presentations and invited talks:

[7]   "Acoustic Signature Monitoring of Wind Turbine Blade," Loughborough University Research Conference 2012, Loughborough, UK (Poster Presentation – Runner Up).

[8]   "Acoustic Signature Monitoring of Wind Turbine Blade," Loughborough University Research Conference 2012, Loughborough, UK (Invited Short Talk).

[9]   "Signature Monitoring of Wind Turbine Blades," Vice Chancellor's Award for Building Environmental Sustainability Together (BEST) Research and Enterprise Poster Competition, 2012, Loughborough, UK (Winner).

[10]   "Good Blade; Bad Blade: A Cost Effective Vibration-Based Condition Monitoring Technique," School of Electronic, Electrical and Systems Engineering (SEESE) Research Conference 2013, Loughborough University, Loughborough, UK (Poster Presentation).

[11]   "Condition Monitoring of Wind Turbine Blades Using Low-Cost Consumer Electronics," Harnessing the Energy, Institution of Mechanical Engineers (IMechE), London, UK (Invited Presentation).

TABLE OF SYMBOLS

SYMBOL	MEANING
U	Wind Speed [in Metres per Second - (ms^{-1})]
P	Theoretical Wind Power [in Watts – (W)]
M	Total Mass of Air per Second [in Kilogram per Second – (kgs^{-1})]
v	Velocity of Air [in Metres per Second – (ms^{-1})]
A	Area [in Square Metres – (m^2)]
ρ	Density [in Kilogram per Cubic Metre – (kgm^{-3})]
P_{Betz}	Betz Limit Power [in Watts – (W)]
C_{PBetz}	Betz Limit [Constant - 0.59 or 59%]
$2D$	Two Dimensions
$3D$	Three dimensions
m	Mass [in Kilograms – (kg)]
d^2x/dt^2, $a(t)$	Acceleration in Time Domain [in Metres per Second Square – (ms^{-2})]
dx/dt, $v(t)$	Velocity in Time Domain [in Metres per Second – (ms^{-1})]
$x(t)$	Displacement in Time Domain [in Metres – (m)]
k	Spring Constant
c	Damping Constant
$s= jw$	Laplace Transform
$F(s)$	Exciting External Force in 's' Laplace Domain
$f(t)$	Exciting External Force in Time Domain [in Newton – (N)]
$F(f)$	Exciting External Force in Frequency Domain
$X(f)$	Displacement in Frequency Domain
$H(f)$	Frequency Response Function
$F_o e^{j2\pi ft}$	Fourier Transform of the Excitation Force
$Y(f)$	Velocity in Frequency Domain
$A(f)$	Acceleration in Frequency Domain
E	Young's Modulus of Rigidity [in Giga Pascals – (GPa)]
I	Moment of Inertia [in Metres to the Fourth Power – (m^4)]
b	Breadth [in Metres – (m)]
h	Height [in Metres – (m)]
n	Mode of Vibration
ω_n	Circular Natural Frequency [in Radian per Second – (rad/s)]
μ	Mass per Unit Length [in Kilograms per Metre – (kgm^{-1})]
x	Distance [in Metres – (m)]
$Y_n(x)$	Displacement in y direction at distance x
B_n	Constant
L	Length [in Metres – (m)]
$T1$	Transducer 1
$T2$	Transducer 2
$T3$	Transducer 3
$\underline{\hat{a}}_x$, X_{OUT}	Accelerometer Output and Axis of Acceleration Sensitivity along x-axis
$\underline{\hat{a}}_y$, Y_{OUT}	Accelerometer Output and Axis of Acceleration Sensitivity along y-axis
$\underline{\hat{a}}_z$, Z_{OUT}	Accelerometer Output and Axis of Acceleration Sensitivity along z-axis
$\boldsymbol{R}$	Resultant acceleration
R_x	Resultant Acceleration along the x-axis
R_y	Resultant Acceleration along the y-axis
R_z	Resultant Acceleration along the z-axis
$X_{measured}$	Acceleration measured along the x-axis
$Y_{measured}$	Acceleration measured along the y-axis
$Z_{measured}$	Acceleration measured along the z-axis

O_x	Offset or Zero-g Bias Level for Static Acceleration along *x-axis* [in Volts – (*V*)]
O_y	Offset or Zero-g Bias Level for Static Acceleration along *y-axis* [in Volts – (*V*)]
O_z	Offset or Zero-g Bias Level for Static Acceleration along *z-axis* [in Volts – (*V*)]
Δ	Change/Increment
g	Acceleration Due to Gravity (*g = 9.81 ms^{-1}*)
A_{xr}	Angle between the Resultant ***R*** and the *x-axis* of the Accelerometers
A_{yr}	Angle between the Resultant ***R*** and the *y-axis* of the Accelerometers
A_{zr}	Angle between the Resultant ***R*** and the *z-axis* of the Accelerometers
$S1$	Old (Damaged In-Service) Blade – 178.6 grams
$S2$	Fair Blade (Previously In-Service) – 179.5 grams
$S3$	New Blade (Obtained from Manufacturer) – 184.7 grams
$S4$	New Blade (Obtained from Manufacturer) – 167.1 grams
$A1$	Accelerometer 1 – Trailing Edge and Root End
$A2$	Accelerometer 2 – Trailing Edge and Tip End
$A3$	Accelerometer 3 – Leading Edge and Root End
$A4$	Accelerometer 4 – Leading Edge and Tip End
θ	Angle between Accelerometer Axis and Gravity [in Degrees – (°)]
A_x	Normalised Acceleration Values along the *x-axis* of an accelerometer [in *g*]
A_y	Normalised Acceleration Values along the *y-axis* of an accelerometer [in *g*]
A_z	Normalised Acceleration Values along the *z-axis* of an accelerometer [in *g*]
X_G	Global Coordinate *x-axis* for Static Acceleration
Y_G	Global Coordinate *y-axis* for Static Acceleration
Z_G	Global Coordinate *z-axis* for Static Acceleration
θ_G	Global Coordinate Angle of Orientation of Wind Turbine Blade [in Degrees– (°)]
θ_{G1}	0° Global Stationary Position Corresponding with Z_{G_down}
θ_{G2}	180° Global Stationary Position Corresponding with Z_{G_up}
θ_{G3}	90° Global Stationary Position Corresponding with Y_{G_down}
θ_{G4}	270° Global Stationary Position Corresponding with Y_{G_up}
Z_{G_down}	Global Static Position where Z_G is along Gravity
Z_{G_up}	Global Static Position where Z_G is opposing Gravity
Y_{G_down}	Global Static Position where Y_G is along Gravity
Y_{G_up}	Global Static Position where Y_G is opposing Gravity
S_x	Sensitivity along the *x-axis* [in Volts per g of Acceleration – (*V/g*)]
S_y	Sensitivity along the *y-axis* [in Volts per g of Acceleration – (*V/g*)]
S_z	Sensitivity along the *z-axis* [in Volts per g of Acceleration – (*V/g*)]
V_x	Raw Accelerometer Measurements along *x-axis* [in Volts – (*V*)]
V_y	Raw Accelerometer Measurements along *y-axis* [in Volts – (*V*)]
V_z	Raw Accelerometer Measurements along *z-axis* [in Volts – (*V*)]
A_{GX}	Global Normalised Accelerometer Measurements along *X-axis* [in *g*]
A_{GY}	Global Normalised Accelerometer Measurements along *Y-axis* [in *g*]
A_{GZ}	Global Normalised Accelerometer Measurements along *Z-axis* [in *g*]
$B_{10 \dots} B_{33}$	Unknown Calibration Parameters
X	Matrix Representing 12 Calibration Parameters to be Determined
w	Matrix Representing Raw Data Collected at Stationary Points
Y	Global Normalised Earth Gravity Vector
P_R	Received Power in *dBm*
P_T	Transmitter Power in *dBm*
G_T	Antenna Gain at the Transmitter in *dBi*
L_T	Loss Factor at Transmitter in *dB*
L_{FS}	Free Space Loss in *dB*
L_M	Loss Factor for Miscellaneous Mechanisms in *dB*
G_R	Antenna Gain at the Receiver in *dBi*
L_R	Loss Factor at Receiver in *dB*

TABLE OF ACRONYMS

ACRONYM	MEANING
AC	Alternating Current
AD	Anno Domini
ADC	Analogue-to-Digital Converter
AI	Analogue Input
AI FIFO	Analogue Input First-In-First-Out
CFRP	Carbon Fibre Reinforced Plastic
CM	Condition Monitoring
DAQ	Data Acquisition
DC	Direct Current
DNA	Deoxyribonucleic Acid
DOF	Degrees of Freedom
DTU	Technical University of Denmark
EFPI	Extrinsic Fabry-Perot Interferometer
FBG	Fibre Bragg Grating
FDD	Fault Detection and Diagnosis
FEM	Finite Element Method
FFT	Fast Fourier Transform
FRF	Frequency Response Function
GFRP	Glass Fibre Reinforced Plastic
GRE	Glass Reinforced Epoxy
GRP	Glass Reinforced Plastic
GND	Ground
HAWTs	Horizontal Axis Wind Turbines
ICP	Integrated Circuit Piezoelectric
IEEE	Institute of Electrical and Electronics Engineers
IO	Input-Output
ISO	International Organisation for Standardization
MEMS	Micro-Electro-Mechanical Systems
Mux	Multiplexer
NI	National Instruments
O&M	Operations and Maintenance
PCB	Printed Circuit Board
PGA	Programmable Gain Amplifier
RAMS	Reliability Availability Maintainability and Safety
RTC	Real-Time Clock
RSE	Reference Single-Ended
SCADA	Supervisory Control and Data Acquisition
SESS	Smart Embedded Sensor System
SNR	Signal-to-Noise-Ratio
USA	United States of America
USB	Universal Serial Bus
VAWTs	Vertical Axis Wind Turbines
w.r.t.	With Respect To
WT	Wind Turbine

LIST OF FIGURES

LIST OF TABLES

TABLE OF CONTENTS

1 INTRODUCTION

Wind energy is the second fastest growing form of renewable energy worldwide (after photovoltaic energy) and the fastest growing in the European Union [1]. Wind turbines are mechanical systems which harness the kinetic energy of the wind into electrical. Wind flows through the rotor of a wind turbine, causing a turning force. The resulting shaft power can be used for mechanical work, like pumping water, or to turn a generator to produce electrical power [2]. The rotor features blades, which capture energy by producing torque from the wind and transferring their power to the hub. These blades inevitably undergo considerable forces. Wind turbine blades are made of different materials which contribute to a high-level of uncertainty in predicting their health [3], [4]. The turbine rotors are subject to fatigue, which leads to deformation of the blades over the course of operation. Common deformations that occur include cracks, surface damage, structural discontinuity and delamination in composite blades [5], [6]. Non-uniform accumulation of ice, dirt and moisture, manufacturing defects such as imbalance and aerodynamic asymmetry are factors that induce deformations causing the degradation of blades [7]–[11]. Monitoring the structural health and condition of wind turbine blades therefore becomes a necessity, to help improve reliability.

In this chapter, Section 1.1 describes the problem the work outlined in this thesis attempts to address. Section 1.2 details the aim and objectives of the work set out in this thesis. In Section 1.3, the novel contributions of this thesis are stated. Section 1.4 provides an overview of the thesis, briefly describing the content of each chapter and the general thesis layout.

1.1 ADDRESSING THE CHALLENGE

Condition monitoring which triggers subsequent maintenance actions is an important strategy for minimizing breakdown, whilst saving costs by avoiding periodic assessment and associated downtime. Operations and maintenance costs of wind turbines are significantly high and make up 15 – 20% of the overall cost of a wind farm project. These costs are higher for offshore wind projects (£80/kW/pa) and double the onshore cost (£40/kW/pa) due to high costs of accessing turbines offshore [12]. Over half of these operations and maintenance cost are associated with replacement of wind turbine parts.

Several condition monitoring methods currently exist such as vibration analysis, strain measurement, acoustic measurements and visual inspection to list a few [5], [13]–[15]. These techniques are applied widely in many industries (aviation, conventional power generation, heavy industry (e.g. steel and aluminium production), oil and gas, paper and wood products production etc.) and are now being adapted to wind turbines. Prices of these condition monitoring systems range from a few thousands of pounds through to tens of thousands of pounds [12].

Vibration analysis condition monitoring technique is the method applied in the research outlined in this thesis. It is also referred to as *modal analysis* and is the study of the dynamic properties of structures under vibrational excitation. Resonant properties of mechanical structures e.g. wind turbine blades, such as their mass, stiffness and damping properties are directly influenced by their physical properties. Therefore, any change in the physical properties of the turbine blades such as erosion or cracks *etc.*, will cause a change in their modal parameters (natural or resonant frequency, modal damping and modal shape) [16], [17]. Measuring these modes can be accomplished with instrumentation such as piezoelectric accelerometers and indeed systems are already on the market that can measure modal properties [18] in situ. Generally, such systems are retrofitted and can be bulky. However, there is an opportunity to install an integrated monitoring system on blades at manufacture, which has the benefit of avoiding changes to blade aerodynamics. Therefore, this thesis details modal monitoring techniques that were applied to turbine blades in situ, considering off-the shelf low-cost consumer electronics such as piezoelectric sounders used in audio Christmas cards and inexpensive MEMS (Micro Electro-Mechanical Systems) accelerometers [19]–[22].

As a result of the widespread use of MEMS accelerometers in consumer electronics and automotive industries, the costs of these accelerometers have generally been pushed down dramatically, costing as little as £5 each. Low-cost MEMS accelerometers are now available and this thesis aims to contribute knowledge in this area so that the merits of these devices in condition monitoring are investigated, as these accelerometers are potentially amenable to integration into turbine blades during manufacture at a marginal cost.

1.2   AIMS AND OBJECTIVES

The main aim of the work set out in this thesis, was to investigate and explore the viability of low-cost sensing devices for detecting wind turbine blade vibrations that could potentially provide useful information on its structural health. The direct cost-reduction benefits low-cost sensing devices could potentially offer in wind turbine condition monitoring applications was a main motivation for the research. A secondary aim of the research was to demonstrate that accuracy in measurements could be achieved when using the low-cost sensing devices to measure wind turbine blade vibrations.

The objectives of conducting the research work outlined in this thesis were: (a) To investigate and collate information from published literature on wind turbine blade failure, faults and defects; to further contribute towards explaining the relevance and motivation of the research. The presented information explains why and how different factors contribute to the failure of the blades and how they affect increasing costs and reliability in the wind industry. (b) To explore condition monitoring techniques from published literature, with a focus on theoretically and experimentally reviewing vibration analysis methods using natural frequency measurements for wind turbine blades. (c) To demonstrate the application and capability of low-cost sensing devices such as piezoelectric sounders (typically used in audio Christmas cards) and Micro-Electro-Mechanical-Systems (MEMS) accelerometers in laboratory experiments for modal analysis of wind turbine blades. (d) To validate and demonstrate that high-accuracy in measured output data using the low-cost sensing devices is achievable through effective calibration and post-processing of measured data. (e) To provide system design suggestions on the potential implementation and integration of the devices for in-service condition monitoring.

MEMS accelerometers mentioned above are relatively new technologies that are still being improved and advanced to suit desired applications. For this reason, it is necessary to investigate the instrumentation of MEMS accelerometers for wind turbine blade condition monitoring. In the long term, this will contribute to a better understanding of the interpretation of condition monitoring data measured by MEMS accelerometers from wind turbine blades. By applying the results from this work, it may be possible to diagnose problematic turbines or installations and offer detailed mitigation advice.

1.3 CONTRIBUTIONS OF THIS THESIS

The following is a summary of the original contributions to knowledge made by the author; further details can be found in Chapters 3 to 7.

(a) A theoretical and experimental review of vibration-based condition monitoring.

(b) Application of low-cost piezoelectric sounders with attached brass discs to mimic piezoelectric accelerometers for vibration measurements.

(c) The identification, instrumentation and application of Micro Electro-Mechanical Systems (MEMS) accelerometers for laboratory vibration measurements of micro wind turbine blades.

(d) The novel contribution in terms of the development of an in-service calibration technique for arbitrarily positioned MEMS accelerometers on a medium-sized wind real wind turbine blade.

(e) Laboratory validation of low-cost modal analysis techniques on a medium-sized wind turbine blade (4.5 m long).

(f) Laboratory measurement of simulated ice-loading characteristics on a medium-sized wind turbine blade, using MEMS accelerometers.

(g) The identification of electromagnetic exciters for active wind turbine blade excitation as part of a potential condition monitoring system or device.

(h) The conceptualisation and systems design of a novel autonomous condition monitoring device that can potentially be installed at blade manufacture, with a collection of intelligent embedded functions such as;

    a. Being self-powered
    b. Signal processing capability and
    c. Remote operation

1.4 THESIS OVERVIEW

This thesis is divided into chapter sections in the following order:

Chapter 2 provides an introduction to wind energy, covering the subjects of the history and present use of wind energy, wind turbine types and classifications, reliability and maintenance, common blade defects and condition monitoring techniques researched from published literature.

The following three chapters detail experimental work conducted.

Chapter 3 describes vibration-based condition monitoring and modal testing in detail. Theoretical and experimental modal analysis and the methods used with each approach are also introduced. Preliminary tests conducted on coupons, simulating micro wind turbine blades, using piezoelectric sounders and attached brass discs are described in this chapter. The relationship between structural damage such as cracks and natural/modal frequencies is also investigated.

Chapter 4 introduces MEMS accelerometers and their different subtypes. Experimental work conducted, including the methodology and results obtained from using the MEMS accelerometers on micro wind turbine blades to detect variations in dynamic characteristics are discussed. Calibration of the MEMS accelerometers for wind turbine blade condition monitoring application are also discussed in this chapter.

Chapter 5 introduces and describes a novel calibration procedure for MEMS accelerometers installed in arbitrary positions on a medium-sized 4.5 m long wind turbine blade. Experimental work conducted on the wind turbine blade to identify and characterise natural frequencies using these MEMS accelerometers are also detailed.

Chapter 6 expands on the issues of ice-loading and icing measurement on wind turbine blades from published literature. Ice loading is simulated on the medium-sized wind turbine blade by applying mechanical weights and the capability of the MEMS accelerometers to detect changing blade resonance frequencies was investigated.

Chapter 7 explores the conceptualisation and systems engineering approach to designing a novel autonomous in situ condition monitoring device that could potentially be implemented on wind turbine blades. The device will comprise of low-cost consumer electronics such as; MEMS accelerometers, microcontrollers, a wireless transmission module and energy harvesters. The different components that comprise the conceptualised system are investigated in detail in this chapter.

Finally, **Chapter 8** concludes the research work in this thesis and highlights some suggestions for future study in this area.

2 INTRODUCTION TO WIND ENERGY

2.1 WIND ENERGY: HISTORY AND THE PRESENT

Wind energy is one of the oldest sources of energy harnessed by humans, comparable only to the use of animal force and biomass. Historically, wind power has been used for powering sailing vessels for thousands of years. On land, there are references to windmills relating to a Persian millwright in 644 AD and to windmills in Persia in 915 AD [23].

Today's interest in wind as a possible source of energy for producing electricity dates from the oil crisis that occurred in the mid-seventies [24]. This interest has been continuing even in more recent years, in spite of the current availability of plentiful and cheap resources of fossil fuels and nuclear energy. The basic reason for that can be found in the widespread concern about global warming caused by fossil fuel and its effect on the environment, coupled with the fear of possible shortage of fuels due to increasing exploitation of their finite reserves in the coming decades. Indeed, industrialised countries at present produce about 65% of their electricity from fossil fuels. According to current estimates, if developing countries should have a substantial economic growth in the next few decades, as is hoped for, they would produce 50% of the world's electrical energy by 2030. In this case, if the whole world went on having the same 65% recourse to fossil fuels as is done now in industrialised countries, a dramatic rise in greenhouse and polluting emissions could certainly be expected, along with a most probable, significant rise in prices of fossil fuels. Hence the interest in exploring any new, renewable energy sources that can somehow replace, even in a supplementary role, the fuels so far in use [25], [26].

2.2 WIND POWER

Winds are large-scale movements of air masses in the atmosphere. These movements of air are created on a global scale primarily by differential solar heating of the Earth's atmosphere. Therefore, wind power can be thought of as an indirect form of solar energy [1].

Winds are due to the balance between temperature gradients and the Coriolis force. Air in the equatorial regions is heated more strongly than at other latitudes because the earth is wider at the equator and rotates faster at the equator than it does at the poles. This heating causes the air to become lighter and less dense. The warm air rises to high altitudes and then flows northward and southward towards the poles where the air near the surface is cooler. This movement ceases at about 30 °N and 30 °S where the air begins to cool and sink and a return flow of this cooler air takes place in the lowest layers of the atmosphere. The areas of the globe where air is descending are zones of high pressure and where the air is ascending, low-pressure zones are formed. This horizontal pressure gradient drives the flow of air from high to low pressure, which determines the speed and initial direction of the wind motion. Coriolis force deflects the wind in the Northern hemisphere counter-clockwise towards the right and clockwise towards the left in the Southern hemisphere, defining the paths of wind in the atmosphere.

The strongest, steadiest and most persistent winds known as the *Jetstream* occur in bands about 10 km above the earth's surface. Wind turbines, however, are presently limited to the lowest 150 m of the atmosphere (although, Vestas [27] launched a 220 m high V164 - 8.0MW wind turbine prototype at time of writing this thesis). At these heights, where the wind is strongly affected by friction with the earth's surface, the wind speeds tend to be significantly lower. Due to the roughness of the ground, the wind stream near the ground is turbulent. The region below about 1 km, where frictional forces of the Earth's surface influence the wind speed, known as the *planetary boundary layer* is illustrated in Figure 2.1. Wind speed increases with height, tending to a limit which is approximately reached at the *gradient height* which is about 2000 m above ground level [28], [29].
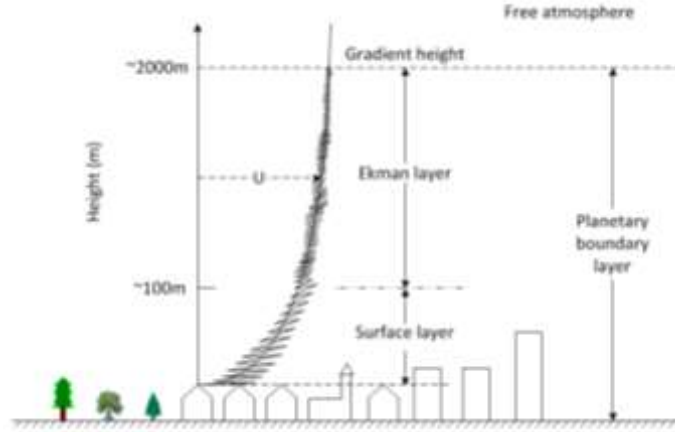
Figure 2.1 Diagram showing the planetary boundary layer adapted from [1] where *U* represents wind speed.

The theoretical wind power, *P*, can be calculated using the formula:

$$P = \frac{1}{2}Mv^2 \qquad\qquad \text{Eqn 2.1}$$

Where *M* is the total mass of air per second passing through a particular area in *kg s⁻¹* and *v* is the velocity of the air in *ms⁻¹*.

The mass per second can be calculated by considering the area swept out by the blade, *A*, the density of air, ρ, and the velocity:

$$M = \rho Av \qquad\qquad \text{Eqn 2.2}$$

This equation can be substituted in the power equation

$$P = \frac{1}{2}(\rho Av)v^2 = \frac{1}{2}\rho Av^3 \qquad\qquad \text{Eqn 2.3}$$

The available wind power therefore increases with the cube of the velocity [1], [29].

The power in the wind is converted into mechanical-rotational-energy of the wind turbine rotor, which results in a reduced speed of the air mass. Like all energy conversion devices, there is a limit on the efficiency with which wind turbines can transform one form of energy into another. For a wind turbine, limited efficiency is caused by the braking of the wind from its upstream speed (wind speed before wind passes through the rotor), to its downstream speed (wind speed after it passes through the rotor), while allowing a continuation of the flow regime. Additional losses for a wind turbine are caused by the viscous and pressure drag on the rotor blades, the swirl imparted to the air flow by the rotor, and the power losses in the transmission and electrical system [30].

Therefore, in reality, wind turbines are capable of converting only a fraction of the kinetic energy contained in the wind into mechanical energy. According to the *Betz limit*, which uses the Bernoulli equation and considers changes in energy along a stream tube passing through the turbine rotor imagined as an actuator disc (upstream and downstream wind speed), the theoretical maximum power that can be extracted from the wind is [1], [28]:

$$P_{Betz} = \frac{1}{2}\rho Av^3 C_{P_{Betz}} \equiv \frac{1}{2}\rho Av^3 \times 0.59 \qquad\qquad \text{Eqn 2.4}$$

Where 0.59 refers to the Betz Criterion or the Betz Limit and is the theoretical ratio of the power produced by the wind turbine to the total power available in the wind.

2.3   WIND TURBINES

A typical wind turbine will contain up to 8,000 different components. The main parts for electricity generation are; the rotor, yaw system, gearbox, bearings, brakes and drivetrain, generator, power electronics converter and the power transmission (interface to supply grid) as shown in Figure 2.2 [31], [32].

(a)

Pitching system

Rotor hub and bearings

Main shaft

Bed plate

Yaw system

Gearbox

Brake system

Generator

Transformer

Power converter

Rotor blades

Nacelle housing

(b)
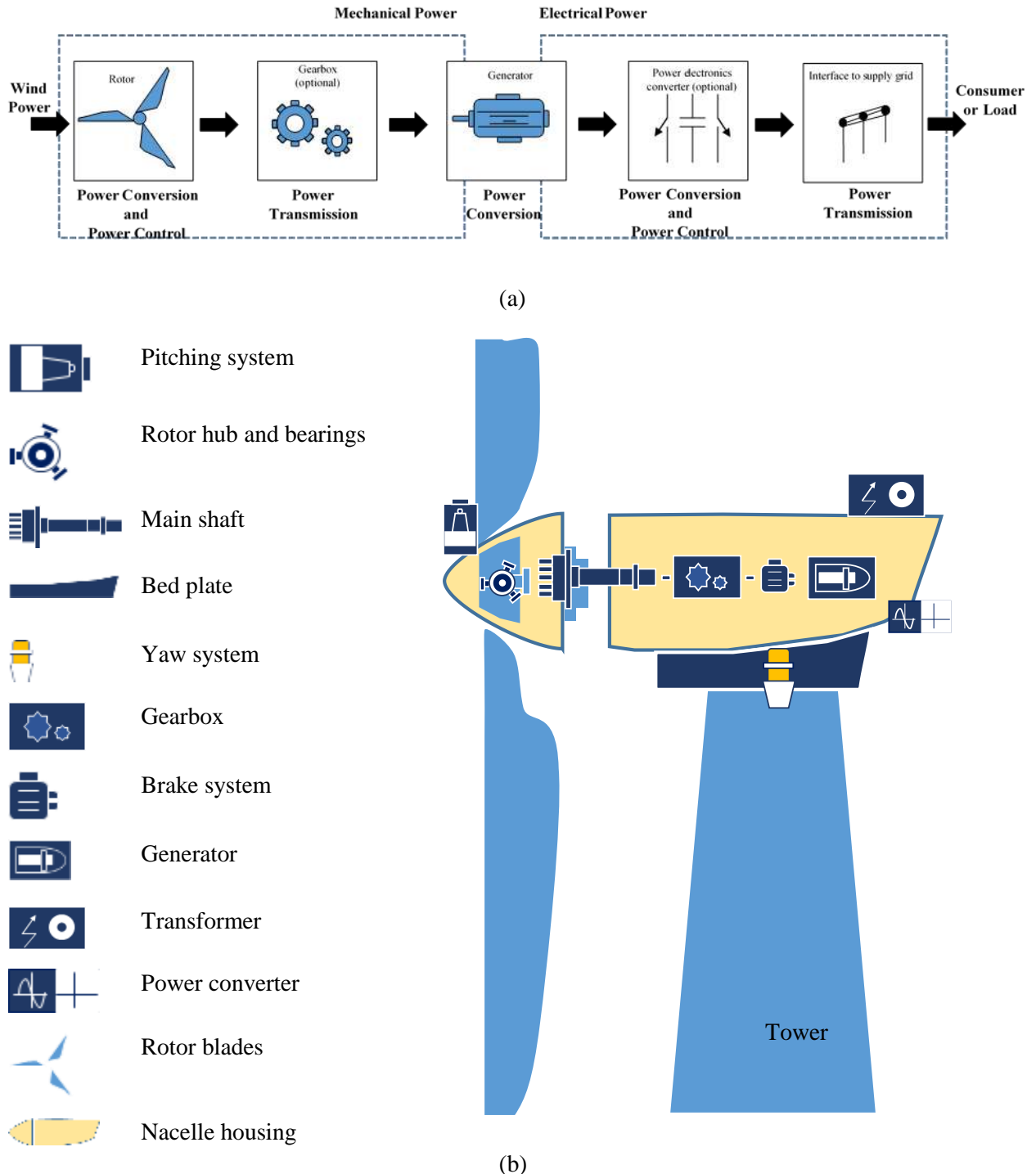
Figure 2.2 Wind turbine: (a) Block diagram showing the operation of a wind turbine for generating electricity (b) Diagram showing all the components of a wind turbine adapted from [31], [32] .

The *tower* of wind turbines usually manufactured in sections from rolled steel, range in height from 40 m up to more than 100 m. Generally, it is an advantage to have a higher tower, as wind speeds increase farther away from ground. The tower carries the nacelle and rotor. The *nacelle housing* is a lightweight glass fibre box that covers the turbine drive train. The *bed plate* made from steel must be strong enough to support the entire turbine drive train, but not too heavy to crush the tower.

The *rotor hub* holds the blades in position, as they turn and are usually made from cast iron. The *rotor blades* are manufactured in specially designed moulds from composite materials, usually a combination of glass fibre and epoxy resin. They vary in length up to more than 60 m and capture energy by producing torque from the wind, transferring their power to the rotor hub. The *rotor bearings* are designed to withstand the varying forces and loads generated by the wind. The *pitch system* adjusts the angle of the blades to make best use of the prevailing wind. The *yaw system* rotates the nacelle to face the changing wind direction.

The *main shaft* transfers the rotational force of the rotor to the gearbox. The *gearbox* houses the gears, which increase the low rotational speed of the rotor shaft in several stages to the high speed needed to drive the generator. The disc *brake system* brings the turbine to a halt when required. The *generator* converts the mechanical energy of the rotating shaft to electrical energy. Most fixed speed commercial grid-connected turbines use induction/asynchronous generators. Variable speed wind turbines use synchronous or asynchronous generators in conjunction with a power electronic interface. The *power converter* converts alternating current from the generator into direct current exported to the grid network. The *transformer* converts the electricity from the turbine to higher voltage required by the grid. Screws designed for extreme loads, hold the main components in place and cables link individual turbines in a wind farm to an electricity sub-station [32].

Wind turbines are classified into two general types based on the orientation of the axis of rotation: *Vertical Axis Wind Turbines (VAWTs)* and *Horizontal Axis Wind Turbines (HAWTs)*. Both of these categories of wind turbines are comprised of different parts designed to perform similar functions. [1], [28], [33]–[38].

1. **Vertical Axis Wind Turbines (VAWTs):** A VAWT has its blades rotating on an axis perpendicular to the ground. The main advantage of a vertical-axis wind turbine over a horizontal-axis wind turbine is its insensitivity to wind direction and turbulence. A VAWT can therefore be mounted closer to the ground, making it safer and cheaper to build and maintain. However, closeness to the ground where wind speeds are influenced by frictional forces reduces and limits output power generated by the turbine as described in section 2.2.

   Although vertical axis wind turbines have existed for centuries, they are not as common as their horizontal counterparts are. The main reason for this is that they do not take advantage of the higher wind speeds at higher elevations above the ground as well as horizontal axis turbines [2], [28], [33], [35], [36], [39].

   There are several types of vertical axis wind turbine blades, some of which are:
   a. **Darrieus turbine:** George Darrieus was the French inventor of the Darrieus vertical-axis wind turbine or 'eggbeater windmill' in 1931 – manufactured by FloWind [33]. The Darrieus turbine shown in Figure 2.3 is the most famous vertical axis wind turbine characterised by its high speed and low torque, suitable for generating alternating current (AC) electricity. The device develops lift from two or three C-shaped blades and is unable to self-start, which necessitates either a manual push or a more elaborate starter mechanism [33], [35], [36], [39].
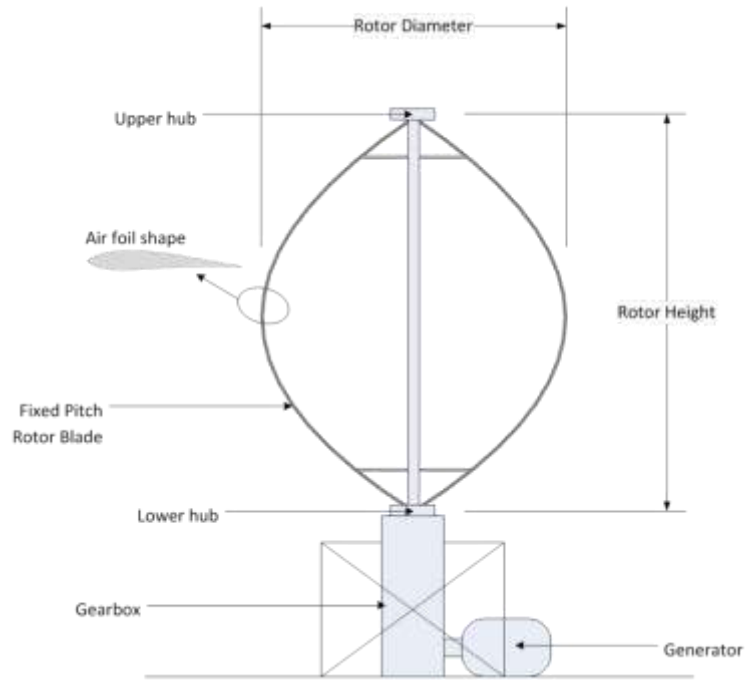
Figure 2.3 Darrieus vertical-axis wind turbine adapted from [33], [35], [36], [39].

b. **Giromill turbine:** A Giromill uses the same principle as a Darrieus turbine to capture wind energy. However, it is powered by two or three vertical aerofoils attached to the central mast by horizontal supports. Giromill turbines shown in Figure 2.4, work relatively well in turbulent wind conditions and are an affordable option where a standard horizontal axis windmill type turbine is unsuitable [33], [35].
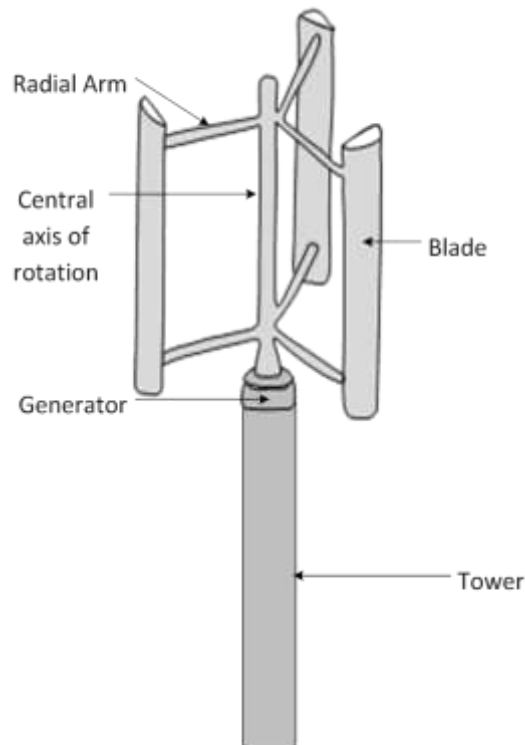
Figure 2.4 Giromill vertical-axis wind turbine adapted from [33], [35].

c. **Helical blades:** Replacing the blades of a Giromill with helical blades wrapped around a vertical axis (in a DNA-like structure), it is possible to minimize the pulsating torque that can cause the main bearings to fail on Darrieus-derived designs. The original idea for the helical wind turbine shown in Figure 2.5, was inspired by the Gorlov Helical Water Turbine, which in turn was originally inspired by the Darrieus wind turbine [33].

Figure 2.5 Helical vertical-axis wind turbine blades adapted from [33].

d. **Savonius turbine:** The Savonius turbine shown in Figure 2.6 is S-shaped if viewed from above. It is a slow rotating, high torque machine that is ideal for driving water pumps and grain grinders but unsuitable for generating electricity on a large-scale. Most wind turbines use lift generated by aerofoil-shaped blades to drive a rotor, the Savonius uses drag and therefore cannot rotate faster than the approaching wind speed. To feed the electricity grid, the relatively slow speed of a Savonius needs to be geared up to produce AC frequencies - increasing cost and reducing overall efficiency [33], [35], [36], [39].
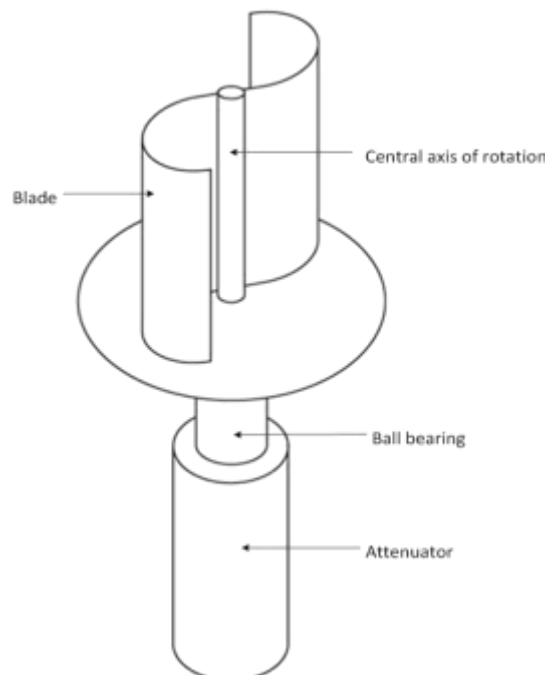
Figure 2.6 Savonius vertical-axis turbine adapted from [33], [35], [36], [39].

2. **Horizontal Axis Wind Turbines (HAWTs):** A HAWT has blades rotating on an axis parallel to the ground and the axis of blade rotation is parallel to the wind flow. It is usually comprised of a rotor that resembles an aircraft propeller, which operates on similar aerodynamic principles, but instead of developing a forward thrust force for propulsion, the blades develop a torque due to the movement of the wind, i.e. the airflow over the aerofoil shaped blades creates a lifting force that turns the rotor. There is also a thrust force developed but this acts to push the rotor back and must be resisted by the structural design of the rotor, tower and foundations.

    HAWTs are the most common, commercially available type and design of modern wind turbines. However, in comparison to VAWTS, they require a massive tower construction to support the heavy blades, gearbox and generator. They also require an additional yaw control mechanism to turn the blades towards the wind and a braking or yawing device in high winds to stop the rotor from over speeding and destroying or damaging itself especially in an upwind design. Nevertheless, they are the most efficient and cost effective design for electricity generation [1], [2], [28], [35]–[37], [40].

    There are primarily two designs of horizontal axis wind turbines. They are:

    a. **Downwind turbine:** Downwind turbines operate in a mode such that the wind passes the tower before striking the blades. Without a tail vane, the machine rotor naturally tracks the wind in a downwind mode. However, there is the problem of mechanically induced turbulence caused by the tower obstructing and deflecting the wind flow. Additionally, in high winds, the blades can be allowed to bend which reduces their swept area and thus their wind resistance. Since turbulence leads to fatigue failures, and reliability is of significance, most HAWTS are of the second type, namely: upwind machines [35], [36].
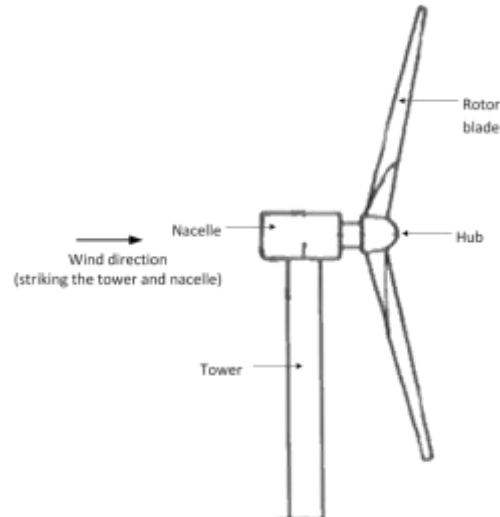
Figure 2.7 Downwind horizontal-axis wind turbine adapted from [35], [36], [41].

    b. **Upwind turbine:** Upwind horizontal axis wind turbines are designed to operate with the blades upwind of the tower. This allows the wind to hit the rotor undisturbed by the tower, and they have a higher efficiency than downwind machines as there is a significant reduction in aerodynamic interference with the tower. On the other hand, the drawback is that they are not self-aligning in the direction of the wind and therefore need a tail vane that keeps the blades facing into the wind in the case of small turbines or a motor-driven yaw mechanism in the case of large turbines that moves the turbine nacelle in response to a change in wind direction [1], [35], [42].

11
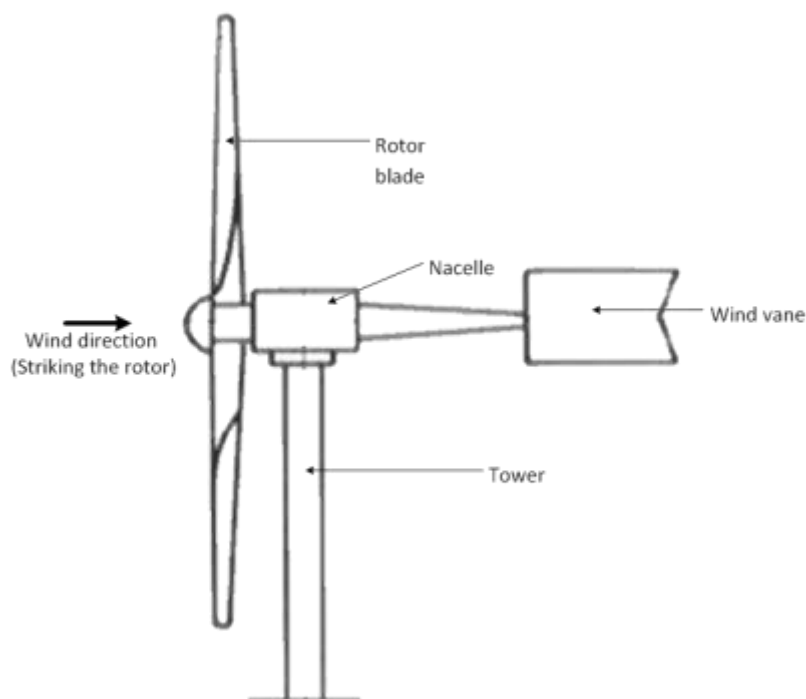
Figure 2.8 Upwind horizontal-axis wind turbine adapted from [35], [41], [42].

The present thesis focuses on upwind horizontal axis wind turbines. However, concepts outlined in this thesis may be adapted to other constructions of wind turbines, which rely on blades to develop torque.

2.4 WIND TURBINE BLADES

Large wind turbines are commonly of the upwind type with two or three blades and a tip speed of 50 - 70 ms^{-1}. Three-bladed machines are now most popular worldwide and are slightly more efficient (2 - 3%) than two-bladed but the main reason for the rise in popularity of the three-bladed machines is one of aesthetics. Two bladed machines give rise to a substantial visual 'flicker' when the blades are in line with the tower and this is reported as being unpleasant on the eye [1].

2.4.1 BLADE CONCEPTS, LOADS AND MATERIALS

Rotor blades resemble aircraft wings in that they consist of two faces, the suction side and the pressure side, which together form an optimized aerodynamic shape shown in Figure 2.9. The faces meet at the leading and trailing edges; the *leading edge* is rounded, but the *trailing edge* is sharp. The straight line between the leading and trailing edge at a given cross section is referred to as the chord line, and its length as the chord. Unlike aircraft wings, wind turbine rotor blades have a built-in twist, which ensures that the effective angle of attack between the blade and the airflow is kept roughly constant along the blade. In many turbine designs, a mechanism is also provided to rotate each blade as a whole (change the pitch angle) to maintain the desired angle of attack under varying wind speed. Such a mechanism can also be used as a braking system. Braking of the rotor can also be achieved by mechanical or electrical means or by rotating just the tip of the blades (so-called tip brakes) [43]–[45]. The *spar or box beam* is the main structural component of wind turbine blades on which the upwind side and downwind side are constructed and joined together at the leading and trailing edge, with adhesive to form the adhesive layer. The *flanges* and *webs* of the box beam perform the function of carrying longitudinal stresses caused by the bending loads.

When the loadings on blades are described, the term *edgewise* is used to indicate loading and bending deformation in the direction of the chord line (the stiff direction), whereas *flapwise* indicates the direction normal to this (the more flexible direction). The main loads on the blades are the wind loads,

which include both flapwise and edgewise bending, and gravity, which induces edgewise bending when the blade is horizontal and some axial tension or compression when the blade is vertical [43]. The loads change with time because of the disturbance of the airflow by the tower and wind shear. Providing effective resistance to flapwise bending is a major consideration in blade design, and the outer shell cannot usually perform this function without the assistance of some internal stiffening, as shown schematically in Figure 2.9 [45].

(a)

(b)
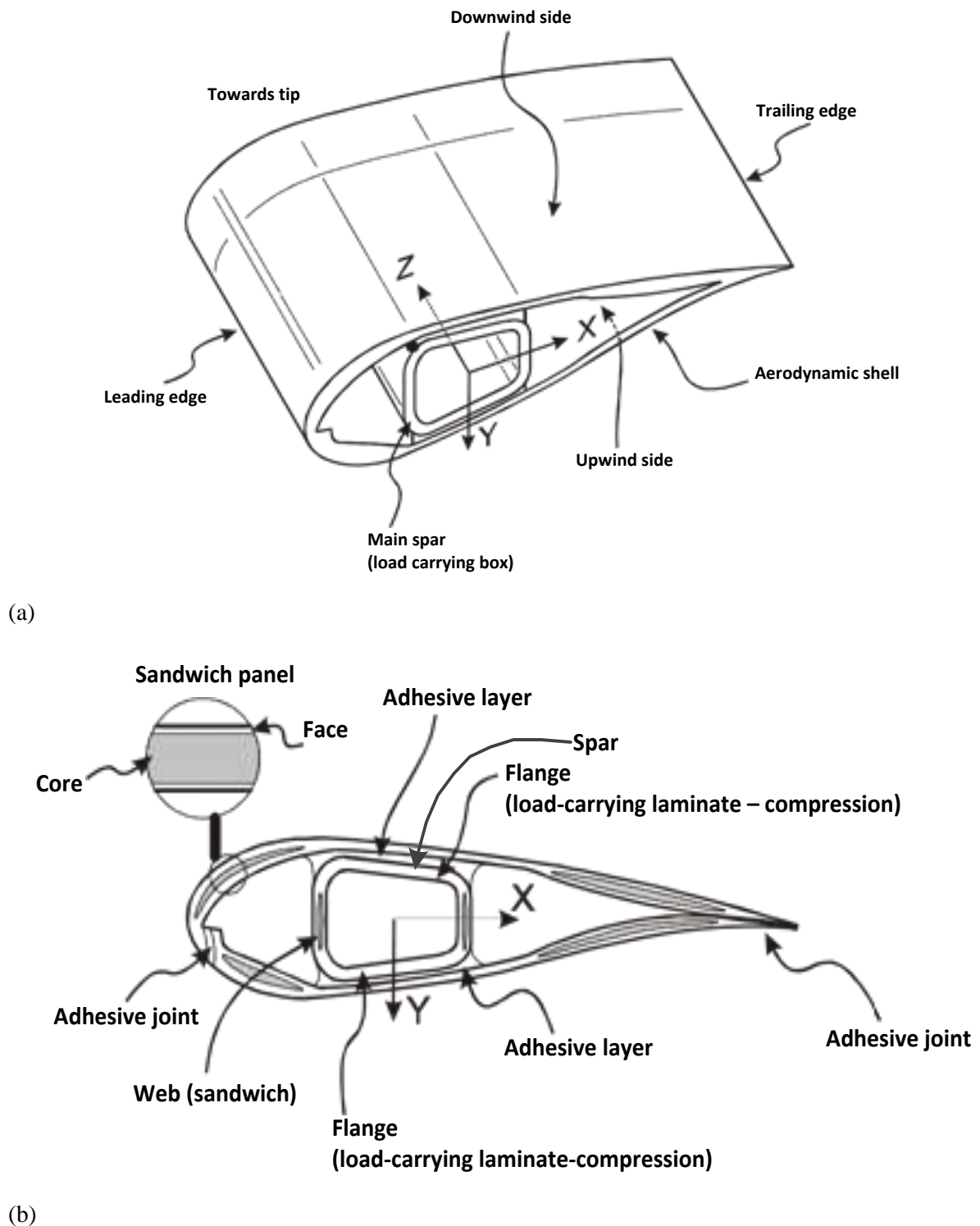
Figure 2.9 Section of blade with load-carrying box and attached shells: (a) perspective view, (b) cross-sectional view adapted from [9]–[11], [43], [46]–[48].

13

Wind turbine blades must be strong enough to withstand the applied loads without fracturing. Thus, the structure must be sufficient to withstand the extreme loads, and the fatigue strength must be sufficient to withstand the time-varying loads throughout the intended lifetime of the blade. The blades must also be stiff enough to prevent collision with the tower under extreme conditions. Stiffness, at a more local level, is also important for preventing buckling of those parts of the blade that experience compressive stresses. To minimize the cost of the power generated, the blade construction needs to be as light as possible. This has to be achieved through optimization of the structural arrangement and dimensions in parallel with the material selection. The production processes used for manufacturing the blades must be sufficiently consistent and reliable to ensure that the end product is always compatible with the design assumptions and calculations [9], [43], [49].

To meet these demands, the blades are usually made from light, strong and stiff material based on fibre-reinforced polymers, wood and combinations thereof. Wind turbine blades are constructed from glass-reinforced plastic (GRP) and glass-reinforced epoxy (GRE), wood and wood laminate, carbon-fibre-reinforced plastic (CFRP), steel or aluminium. For small wind turbines, of less than 5 m in diameter, the issue of the material is usually driven by production efficiency rather than the weight, stiffness or other characteristics of the blades. In addition, the forces are very much less for small machines, making design and construction easier. For large machines, GRP has proven to be the most cost effective material [1]. The blade parts are generally assembled using adhesive bonding. The strength and durability of the adhesive bonds are major design considerations and can become the main limiting performance factor together with the performance of the laminates themselves [43], [47], [48], [50].

2.4.2 BLADE DEFECTS AND FAILURE

Due to the complex structure of wind turbine blades, defects can occur during manufacture, which manifest themselves as cracks and delamination. Also, during operation, wind turbine blades are subject to fatigue originating from surface contaminants such as icing and insects [7]. These are known to increase the blade surface roughness resulting in loss in energy capture efficiency [5]. The wide spread of materials used in the production of wind turbine blades contributes to the high-level of uncertainty in predicting their health [3], [4], decreasing reliability and increasing the need for maintenance and condition monitoring. Defects can also reduce the stiffness, but generally, the effect on stiffness is less than that on strength, as changing the stiffness of a part requires a change in the properties of a significant volume of material whereas the strength can be reduced by very localised changes [43]. Research [51] has shown that the weak point of current wind turbine blades is the structural strength. The safety factor with respect to material strength is unnecessarily higher than the structural strength. The goal is therefore to find a better balance between structural strength collapse and material failure in terms of blade design and manufacturing.

No detailed classification system exists for describing wind turbine blade failures and information on failures are not provided by owners and operators. Turbine manufacturers and operators are not required to provide a detailed root-cause assessment in a publicly available forum therefore this information may be available but only shared between manufacturer and certification agency. However, in this thesis, wind turbine blade defects have been categorised into two groups (*production defects* and *operational defects*) based on how they have been identified from various research conducted [6], [44], [52]–[59].

1. **Production defects:** Production defects are defects that occur during the manufacture and design stage of wind turbines [59], [60]. This also includes faults and failures which have been identified during experimental load testing [6], [44], [52], [53], conducted on turbine blades in laboratory controlled-environments. At present, the defects and imperfections that appear to be of most concern in wind turbine blade production are delaminations, bond defects, wrinkles, and other geometric imperfections that give rise to local stress

concentrations (and thus to reduction of strength and shortening of fatigue life). Larger geometric imperfections that influence the buckling resistance are also of concern [43], [59].

a. **Delaminations:** Delamination is the separation of adjacent laminate piles because of absence or failure of bonding between layers of reinforcement, either locally or covering a wider area. It can occur during either the manufacturing process or the subsequent service life of the laminated part. Contaminated reinforcing fibres, insufficient wetting of fibres and shrinkage, which occur during the curing of the resin, also contribute to delaminations during manufacture. Delaminations generally reduce the compressive strength of wind turbine blades by lowering the resistance to out-of-plane buckling of the groups of piles to either side of the delamination. If the delamination is located near the outer or inner surfaces of the laminate, the delamination may induce local buckling of a group of plies; see Figure 2.10. If the delamination is located near the centre of the laminate, the strength reduction will be caused by global buckling of the laminate; see Figure 2.10 [54], [61].
Delaminations also grow under repeated loading with failure occurring when the delamination reaches a critical size [43], [61]–[63]. The influence of delaminations on the ultimate compression strength has been studied in [61] and [64] for glass-fibre reinforced plastic (GFRP) and in [65] and [66] for sandwich structures exposed to different load cases. The main parameters that influence the strength reduction are the size of the delamination and the through-thickness position. But also other parameters such as the stacking sequence can influence the strength reduction [67].

Local Buckling Mode

Global Buckling Mode
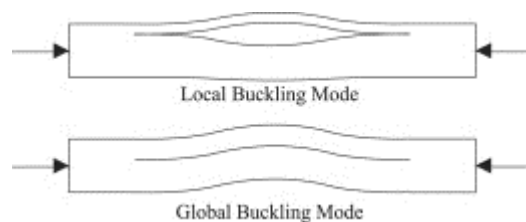
Figure 2.10 Local and global buckling modes for delamination [61], [67].

b. **Debonds:** Debond or disbond is an absence of adhesive layer forming the interface or connection between the face and the core in parts of the blade or if the adhesion is deficient because of inadequate surface preparation or incomplete curing during production. Debonds can also occur as a result of in-service damage [43], [65].

c. **Wrinkles:** A wrinkle is caused by an excess of reinforcement in one or more of the piles (sheets of polymer) in relation to the surface area available when the reinforcement is being placed. These piles are unable to lie completely flat and therefore form a small, outward buckle or wrinkle. The wrinkle can involve only the outermost piles of the laminate, but it can also start deeper down in the lay-up even involving the entire thickness in extreme cases. Wrinkles can significantly reduce the compressive strength of a laminate for in-plane loading applied perpendicularly to the line of the wrinkle [43].

d. **Brazier effect:** This is a nonlinear geometric deformation 'ovalisation' caused by bending of a section of a wind turbine blade. When a wind turbine blade bends in the flapwise (chord-wise) direction, the compressed panel produces a downward crushing

load normal to the surfaces (e.g. the upwind side) while the opposite occurs on the lower panel (e.g. the downwind side). This flattening of the cross section is known as the *Brazier effect*.

The flattening effect is caused by transversal internal forces, which are denoted by the arrows in Figure 2.11 below. This flattening effect manifests itself as an ovalisation in circular sections (as crushing pressure rises quadratically with the longitudinal curvature) and a "sucking in" for the square sections like the flange [6].
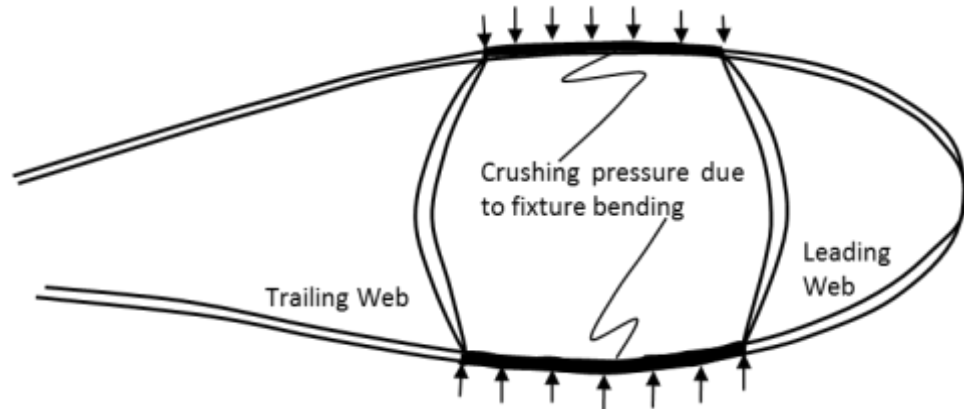
Figure 2.11 Crushing pressure on a wind turbine blade section adapted from [6].

e. **Web failure:** Web failures have been observed as the main reason for collapse in full scale-tests conducted at the Risø Laboratory (now part of the Danish Technical University or DTU) [6]. The web is sandwiched in the main spar wall of some blades as is shown in Figure 2.9. Other blades, which do not have a box spar, have a stand-alone web and spar cap that provide local stiffness for the blade. During the full-scale test [6], the web towards the trailing edge collapsed just before ultimate failure of the entire blade. Figure 2.12 shows the shear webs which collapsed at the first full-scale test which had no additional reinforcement where the two half parts were connected.
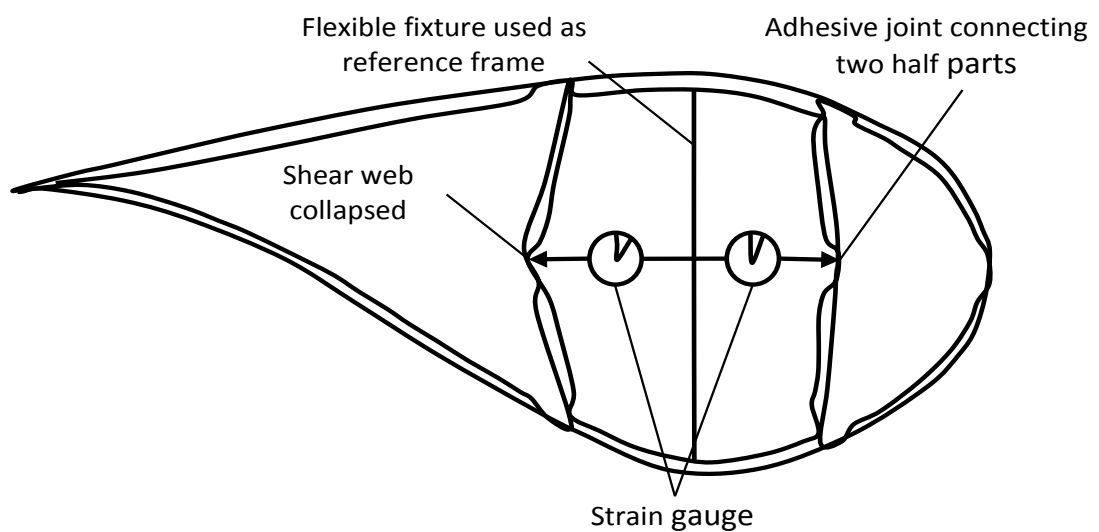
Figure 2.12 A sketch showing the shear web adapted from [6].

f. **Interlaminar shear failure:** Interlaminar shear failure is a mechanism that occurs between the layers in the load-carrying cap (main spar) laminate as shown in Figure 2.13 below. The failure is caused by interlaminar shear force, which is the stress component in parallel with the cross-section of the main spar cap. The interlaminar shear failure develop by crushing pressure causing biaxial stress distributions, interlaminar and peeling stresses due to the curved structure being flattened out. Delamination, which occurs due to high out-of-plane loads where no fibres are present to resist the loading, is the major contributor to this structural failure. The lack of fibres in the transverse direction causes the cap to be relatively flexible in the lateral direction below [6], [9].

Zoomed - in top section showing interlaminar deformation of the load carrying cap

Spar
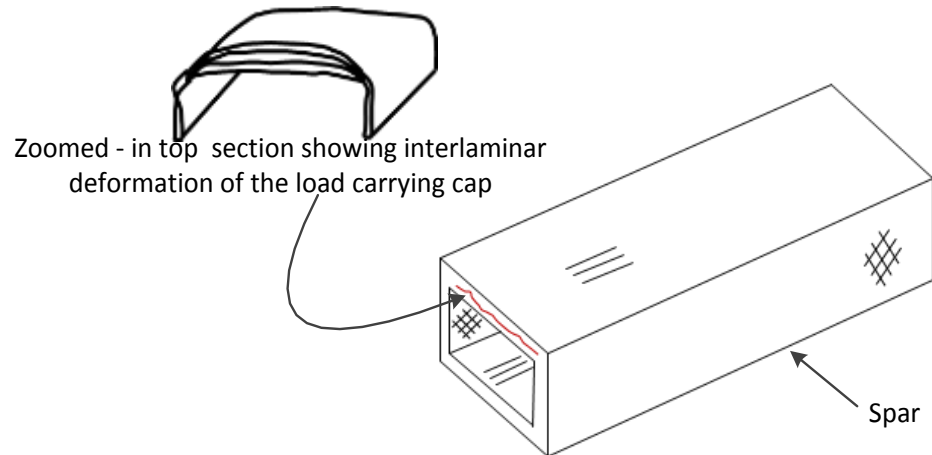
Figure 2.13 Sketch of cap deformation and failure between layers adapted from [6], [9].

g. **Buckling:** Buckling is a structural instability phenomenon of structures that are loaded in compression. It occurs due to the elastic instability of the wind turbine blade when it is subjected to high compressive stress. Skin debonding from box girder, local buckling of the panels in the trailing edge and global buckling of the trailing edge are other buckling failure modes which have been considered by Risø DTU [6].

h. **Panel deformations:** Minimising deformation of the aerofoil is needed for several reasons, e.g. trailing edge fatigue problems and aerodynamic efficiency. Nowadays, forces are carried by double curved airfoils, which leads to out of plane deformation. Out of plane deformations cause peeling stresses in the trailing edge, and failures in the trailing edge often occurs [6].

i. **Transverse shear distortion:** Transverse shear distortion is an important failure mechanism of the wind turbine blade cross-section due to non-linear behaviour. A thin walled structure without any internal reinforcement will always try to distort in the transverse direction. This is even more prominent when the blade is non-symmetric from manufacture in geometry, as the blade will try to twist [6]. Figure 2.14 below shows the distorted and undistorted profile of a wind turbine blade cross-section when transverse shear failure occurs.
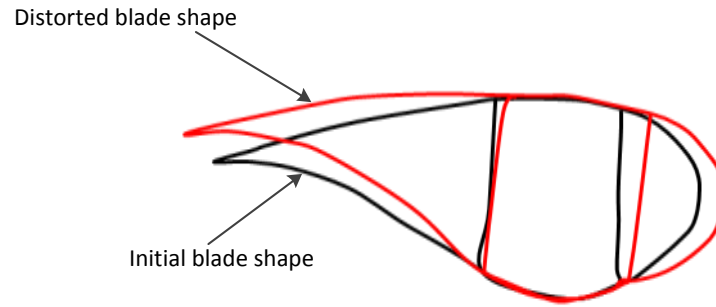
Figure 2.14 Sketch showing the blade undistorted and distorted shape adapted from [6].

Compressive loads were induced experimentally [9]–[11], [46] on a wind turbine blade and Table 2.1 and Figure 2.15 illustrate the common damage types found.

Table 2.1 Typical damage of Carbon Fibre Reinforced Plastic(CFRP) and Glass Reinforced Plastic (GRP) wind turbine blades [9]–[11], [46].

Type	Description
Type 1	Damage formation and growth in the adhesive layer joining skin and main spar flanges (skin/adhesive debonding and/or main spar/adhesive layer debonding).
Type 2	Damage formation and growth in the adhesive layer joining the upwind and downwind skins along leading and/or trailing edges (adhesive joint failure between skins).
Type 3	Damage formation and growth at the interface between face and core in sandwich panels in skins and main spar web (sandwich panel face/core debonding).
Type 4	Internal damage formation and growth in laminates in skin and/or main spar flanges, under a tensile or compression load (delamination driven by a tensional or a buckling load).
Type 5	Splitting and fracture of separate fibres in laminates of the skin and main spar (fibre failure in tension; laminate failure in compression).
Type 6	Buckling of the skin due to damage formation and growth in the bond between skin and main spar under compressive load (skin/adhesive debonding induced by buckling, a specific type 1 case).
Type 7	Formation and growth of cracks in the gel-coat; debonding of the gel-coat from the skin (gel-coat cracking and gel-coat/skin debonding).
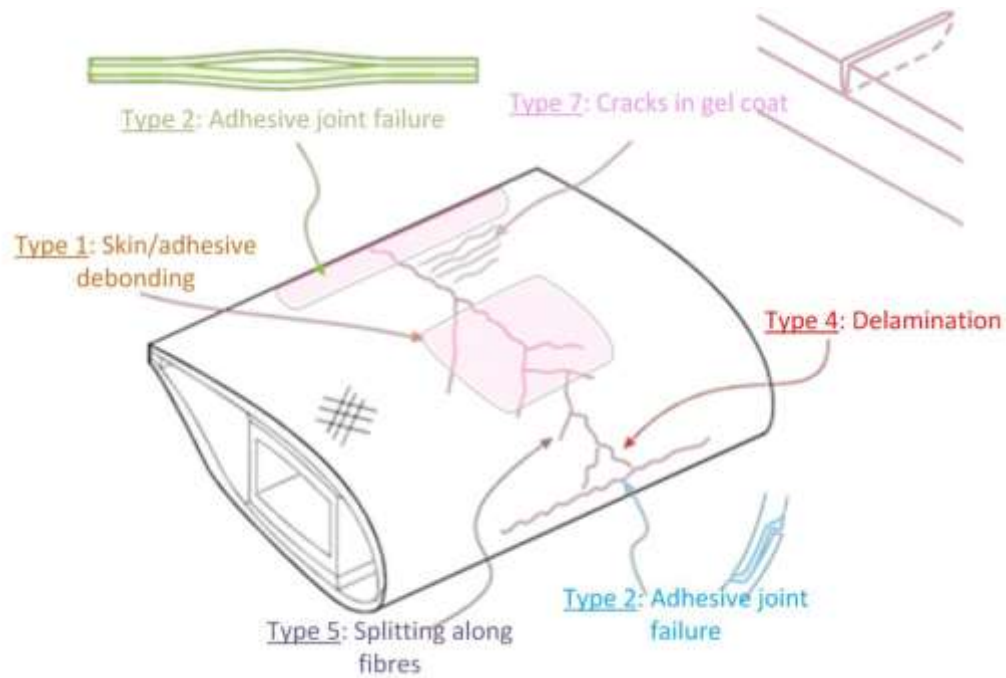
Figure 2.15 Sketch illustrating some of the common damage types found on a wind turbine blade when subjected to a compressive load adapted from [9], [46].

2. **Operational defects:** Operational defects are blade defects that occur during the lifetime of the turbine, due to factors such as dust, ice and insect contaminations. Dust, ice and insects are the contaminates known to increase the roughness of turbine blades the most [54]–[56]. Dirt and contamination accumulate on the wind turbine blade when it operates in the field. The main sources of contamination have a big influence on rotor performance. When insects, smog and dirt accumulate along the leading edge of the blade, the power output may drop up to 40% of its clean value [57], [58].

   a. **Dust accumulation:** Small particles of dust, dirt, and sand can be transported by the wind to the height of the wind turbine rotor. As these particles hit the rotor blade, the smoothness of the surface is perturbed, especially at the leading edge, near the stagnation point. While dust contamination has not been extensively examined, a few studies have resulted in some key findings which explain the effects of dust roughness on wind turbine blades, and the relationship between power output, the duration of dust exposure, and grain size.
   In the study by Khalfallah and Koliub [68], the effects of dust accumulation on a 300 kW pitch regulated wind turbine, over various operational periods, are examined. As expected, the dust accumulation pattern follows the blade profile, with the highest concentration of particles on the leading edge and the tip of the blade.

   b. **Insect contamination:** Insects are the main source of wind turbine blade contamination [58]. Wind turbine blades are contaminated by insect accretion typically at low wind speeds, in which insects can fly [55], [69]–[71]. At these low wind speeds, power production is not influenced significantly by roughness. However, at high wind speeds, there is a remarkable decrease in power output [72]–[76] due to surface roughness generated by insects. The contamination level also depends on the atmospheric conditions in which insects fly, i.e. above 10 °C, and

19

when it is not raining. Very low temperature and low humidity also contribute to an insect-free environment [77]. In addition to atmospheric conditions, insect presence also depends on altitude, with a rapidly decreasing density from ground level to 152 m [78]. The conditions for insect contamination are shown schematically in Figure 2.16. The increase shown in the power curve is the result of the blades having been cleaned by rain.
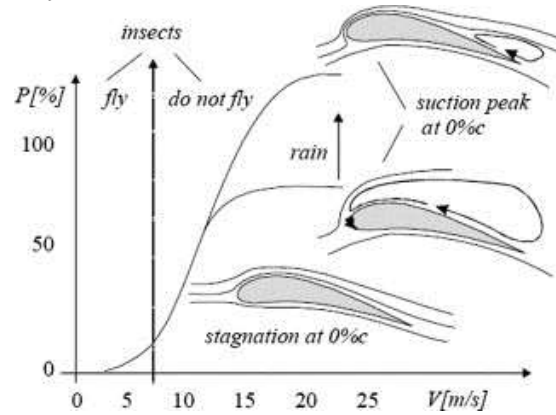
Figure 2.16 Conditions for insect contamination from [54], [69], [70], [76].

c. **Ice accumulation:** The influence of accreted ice has been extensively studied, both for airplanes and wind turbines, as the consequences and risks are considerable for the operation of these machines. Ice accumulates as super-cooled water droplets present in clouds strike the solid surfaces and freeze on contact. The ice shapes that form on these machines and their effect on performance are shown for different types of ice accretion in Figure 2.17 [79], [80]. The ice build-up on these structures is classified as glaze (horn) ice, rime (streamwise) ice, ridge ice, and ice roughness. Glaze ice is horn-shaped, and forms where a thin water layer covers a thicker ice layer. This horn shape originates from the runback water that does not freeze on impact, but after moving towards the trailing edge. Rime, or streamwise ice, contains ice layers that form at the intersection of water droplet streamlines and solid surfaces. As indicated in Figure 2.17, rime ice has a less negative effect on the flow field, whereas glaze ice, because of its shape, has more. These two ice formations are the types most often studied in the literature as they occur most frequently. Ridge ice forms as a single large obstacle on the suction side of the blade, and causes a large separation bubble, deforming the flow field more significantly than the other types of ice, as shown in Figure 2.17. Finally, ice roughness refers to any type of icing at early stage in its formation, where water droplets are not able to form an ice layer, but can perturb the profile of the blade. Although ice roughness exists at the initial stage of any type of icing process, it can influence performance substantially, the extent of its effect, depending on its height, concentration, and location. Ice roughness modifies the thickness of the boundary layer and the extent of its transitional characteristics, depend on its height, location, and Reynolds number. Consequently, the corresponding aerodynamic characteristics, like lift and drag coefficients, are influenced as well [54], [58][80]–[88].
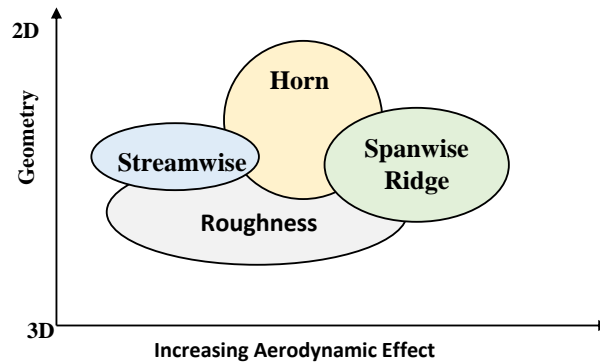
Figure 2.17 Classification of ice accumulation types adapted from [79], [83].

d. **Leading edge erosion:** The leading edge of a blade is the foremost edge of the aerofoil or part of the blade that first contacts air. Areas with high levels of dust, insects, rain, sleet, snow or any other abrasive air particulate is more susceptible to erosion. The tip of the blade is more susceptible to wear due to the operating speed of the blade at the tip. When leading edge erosion is not repaired, vibrations occur which create undesirable loads on the turbine. Overtime, the laminate under the coating cracks and water enters the core material of the blade. As freeze-thaw cycles occur, the blade core expands and contracts separating the laminate from the core. A waterlogged core is also cause for an unbalanced rotor which leads to more unwanted vibrations throughout the drivetrain. When a blade sustains this level of damage, repair options are limited. Generally, leading edge erosion decreases the aerodynamic performance of wind turbine blades.

To mitigate leading edge erosion, most manufacturers offer leading edge protection in the form of a tape or paintable coating. This will aid in the prevention of erosion provided the protection is not damaged during shipping and mounting [89]–[92].

e. **Lightning:** Lightning can be a significant source of blade damage, depending on the geographical location of the particular wind turbine. All megawatt scale blades are equipped with lightning protection systems. These systems employ receptor pucks on the surface of the blade at the tip, with either copper or aluminium conductors, connecting the pucks to a grounding source. However, informal surveys have indicated that several large wind farms in the Midwest region of the USA, an area which is prone to frequent lightning strikes, have seen a large number of their turbine blades, and in some cases all blades, being struck by lightning [28], [52], [93]–[98].

f. **Over-Speed:** Over-speed failures are typically considered a secondary failure mode with respect to blade damage and failure, as a component failure or control system failure is often necessary for this condition to occur. Damage to a blade will not, in almost all cases, directly lead to the system over-speeding. When significant damage to a blade does occur, it will typically lead to out-of-balance conditions that can be detected by basic sensing system sensors, including accelerometers. When these out-of-balance conditions are observed, the turbine *S*upervisory Control and Data Acquisition (SCADA) system would normally place the wind turbine in a shutdown mode [1], [93].

2.5 WIND TURBINE RELIABILITY AND MAINTENANCE

As wind turbines get larger, operating and maintenance costs can be expected to rise unless reliability is improved through condition monitoring [99]. Component failure has a cost associated with the replacement of the component itself as well as lost energy costs. The costs of components in different types and sizes of wind turbines vary depending on turbine type and configuration. For example, the costs of both converters and generators will differ depending on the configuration and some wind turbines do not have a gearbox at all. Figure 2.18 shows the component cost distribution for a typical 2 MW wind turbine based on a Repower MM92 with 45.3 m length blade and a 100 m tower [32], [100].
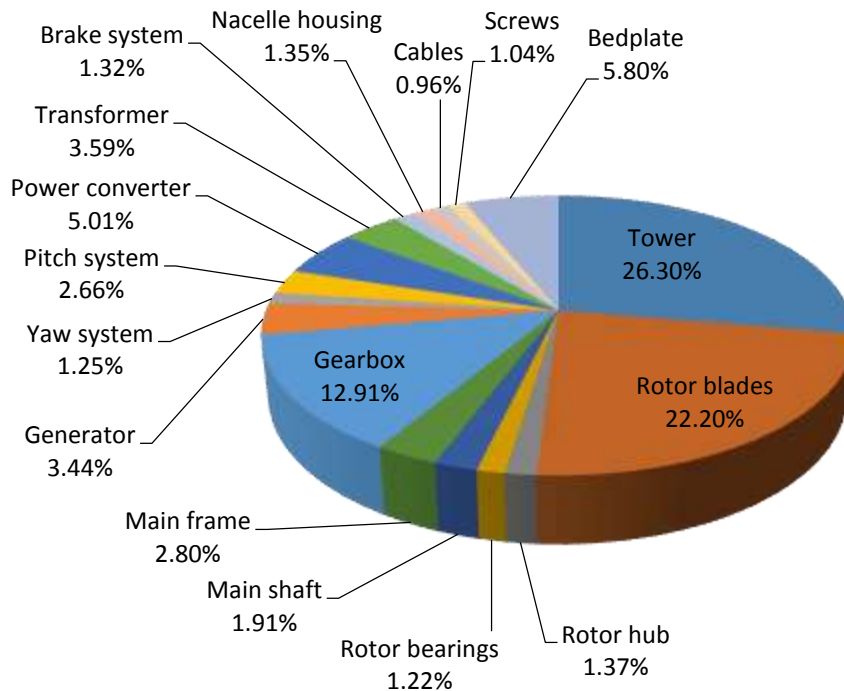
Figure 2.18 Distribution of the component costs for a typical 2 MW wind turbine adapted from [32], [100].

The high cost of the machinery and infrastructure of wind turbines combined with the difficulty of access to them by maintenance personnel, demands complex maintenance systems if high reliability, availability, maintainability and safety (RAMS) [101]–[103] are to be achieved. Wind turbine reliability is a significant factor in ensuring the success of a wind power project [104]. Reliability and condition monitoring benefit the maintenance management of wind power systems [105]–[108] by giving advance warning of failures, reducing the operations and maintenance (O&M) costs.

The wind power industry has thus developed significant improvements in the field of wind turbine maintenance and repair strategies, employing condition monitoring (CM), integrated within supervisory control and data acquisition (SCADA) systems. Fault detection and diagnosis (FDD), CM and fault detection algorithms are used to provide early warning of structural, mechanical and electrical defects, enabling wind farm operators to carry out predictive maintenance and hence reducing failure rates [99]. Predictive maintenance is also used in tandem with preventive maintenance, both being very important for offshore wind turbines where the maintenance personnel operate at the mercy of the weather [5].

Figure 2.19 shows the failure rates per year for components of wind turbines located in Finland, Germany and Sweden. The data was extracted by Ribrant from WindStats gathered over a 10 year

period for over 35,000 reports of failures [5], [93], [107], [109]–[115]. No detailed information was given on the type of failure because the focus of the studies was on establishing the mean time between failures, and defining methods for reducing downtime via condition monitoring. Note that these failure rates data are dependent on factors such as weather conditions, the type and age of the wind turbines.

Considering the cumulative failure rate of each component, the electrical system has the highest failure rates, followed by the hydraulics, control system and blades/pitch respectively. Gears, the yaw system, brake, generator, sensor and others form a group with intermediate failure rate. Hubs, drive trains and structures all have low rates [93], [100], [107], [113], [115]. Note that no failure rate data was recorded for drive trains in Finland.
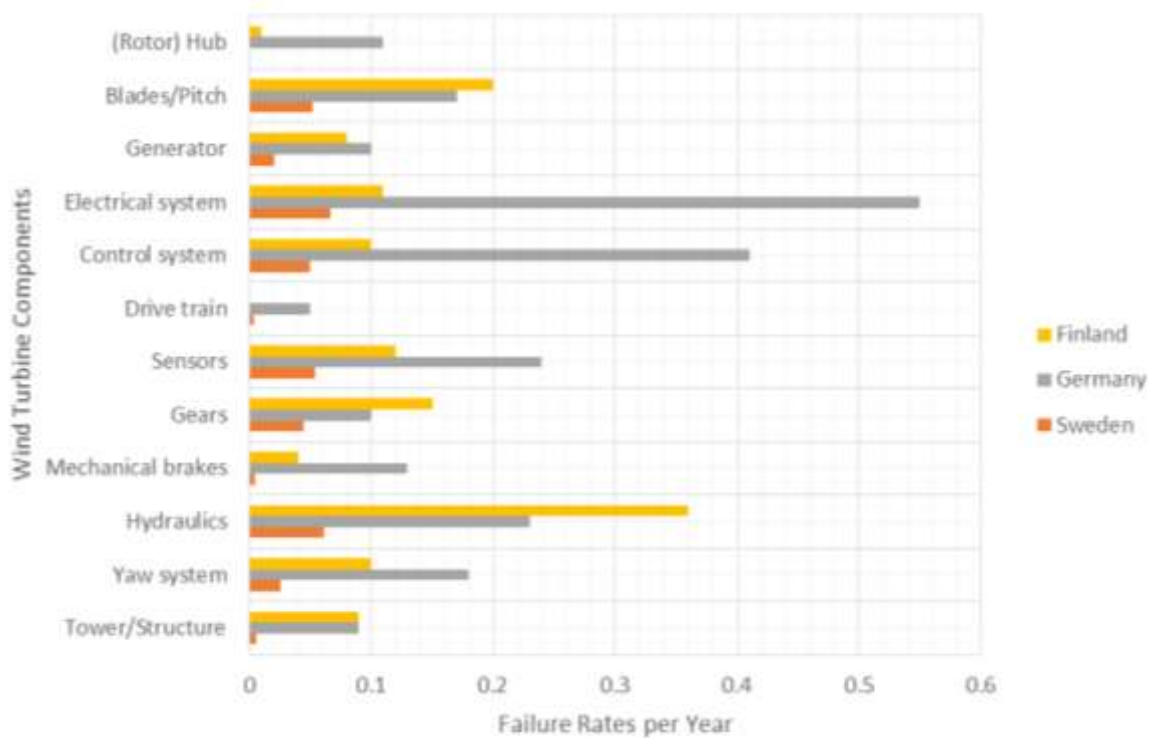
Figure 2.19 Failure rates per year for wind turbine components adapted from [93], [107], [110]–[112].

A study by Bussel and Zaaijer [109] and [110] shows that the blades/pitch present the highest failure rate of 0.72 [100]. This thesis therefore focuses and proposes contributions in the area of condition monitoring of wind turbine blades.

2.6 CONDITION MONITORING

Condition based maintenance is a preventive type of maintenance based on the actual health of the system. At a general level, maintenance can be subdivided into preventive and corrective maintenance. Corrective maintenance is performed after a breakdown or if an obvious fault has occurred. Preventive maintenance is intended to prevent equipment breakdown and consists of repair, service, or component exchange [13]. Condition Monitoring (CM) can also be described as a management tool that provides information about the likely future performance-or lack of it-of an item of equipment or even a complete unit. Its use allows an operational strategy, based on it, to be employed [14]. Figure 2.20 below shows the maintenance sub-categories appropriate for wind turbine technology.
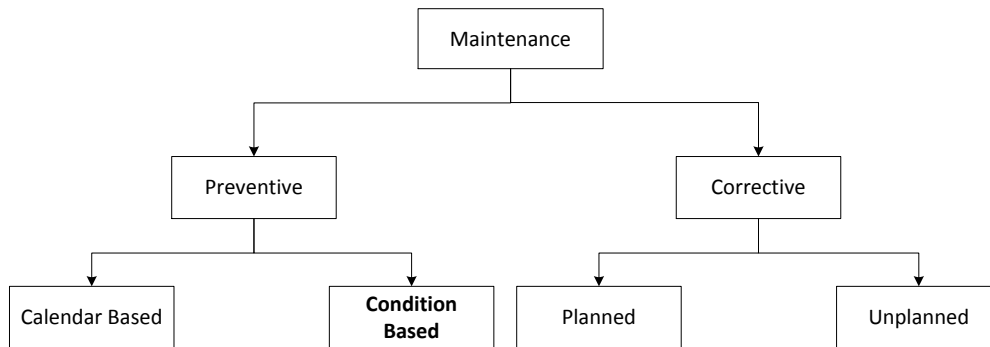
Figure 2.20 Schematic overview of different maintenance types adapted from [13].

In recent times, there has been a significant and rapid growth in the deployment of wind turbines for electricity generation as the world moves towards reducing carbon emissions while tackling current climate change attributed to the effects of global warming. There have been significant advances in wind turbine technology such as improved aerodynamics and improved structural dynamics with the primary purpose of increasing energy yield. A well-known example is the new trend in turbine blade designs with larger and more flexible structures that has been shown to increase energy capture efficiency. These enhancements have associated increased manufacturing costs. Hence the greater emphasis on condition monitoring to manage maintenance of wind turbines as wind farm operators and insurers attempt to protect the capital invested in wind energy projects [15], [116], [117].

2.6.1 CONDITION MONITORING TECHNIQUES

Condition monitoring is well understood for large, high speed rotating machines but has not been widely investigated for wind turbines because they have low speed shafts and highly dynamic variations in torque and speed [118]. Conventional condition monitoring techniques used for wind turbine blades are described below. Most of these techniques are still being researched and require the deployment of a variety of sensors and computationally intensive analysis techniques.

1. **Acoustic emission:** Acoustic emission is considered more robust for the low-speed operation of wind turbines compared to the classical vibration-based methods. This approach is also good for identifying early faults in gearbox bearings. Although the acoustic emission technique is expensive and requires very high sampling rates, it has a few advantages such as; its ability to detect early-stage faults, its high signal-to-noise ratio and the frequency range is far from the load perturbation [5].

   Acoustic emission sensors based on strain measurements, have also been investigated as possible methods useful for fault detection in wind turbine blades. The Risø DTU National Laboratory for Sustainable Energy [119] assessed acoustic emission as being best able to detect and locate small laminate flaws in wind turbine blades.

2. **Fibre optics/ optical strain measurement:** Optical strain measurement is an advanced technique that has been developed for monitoring wind turbine blade integrity. However, it is expensive, and recent surveys conducted by Spinato *et al.* [112] have shown that wind turbine electrical systems have a higher failure rate than mechanical systems [120]. Optical strain measurement can only be applied to the mechanical systems and if their failure rate is lower than the electrical systems in a wind turbine, it may be better to use cheaper alternatives.

   The Risø DTU National Laboratory for Sustainable Energy [119] assessed fibre-optic displacement transducers as being especially effective in detecting adhesion failures in blades. Optical fibre devices can be used to measure other parameters, such as temperature and vibration, as well as load/strain. Blade loads are measured using strategically placed fibre optical strain gauges. A simple way to detect incipient cracking or buckling is to embed optical fibres in strategic areas within the composite laminate and check that light paths down the fibres do not become interrupted, i.e. that the fibres remain continuous. Loads that occur at certain frequencies, such as those due to tower shadow and the cyclic reversal of gravitation load experienced at each blade revolution, are amenable to statistical analysis tools developed for use with rotating machinery, such as fast Fourier transform (FFT) analysis. The two types of fibre optic sensors commonly used to detect and quantify the amount of bending that result from blade loading and hence strain are; the fibre-Bragg gratings (FBGs) and extrinsic Fabry-Perot interferometric (EFPI) sensors [119].

3. **Integrated smart sensor:** Fibre-optics, piezoelectric materials and strain gauges can be used for monitoring different types of damage that may occur in wind turbine blades.

   Moog [121] developed a fibre-optic modular blade load measurement system. Moog claims that the blade sensing system allows adjustment of the pitch of each blade in real time. In principle, this enables turbine designers and builders to balance the loading across the rotor disc, eliminate asymmetric loading and reduce the peak loads.

   Risø DTU in Denmark has reported a sensor system in development for offshore wind turbines to monitor the health of each wind turbine [122], sending the information to the operators on shore. Models describing the reaction of composite materials to various load conditions are tested in the laboratory, and classified by various defects and damage modes that may occur. The idea is to develop a model that follows the principle that many small changes in the blade material should be monitored one at a time in order to assess the overall impact. The sensors will be incorporated into wind turbine blades to detect changes and damage in the blade structure at an early stage before the blade breaks. The project is called *SESS* and stands for Smart Embedded Sensor Systems.

4. **Physical conditions of materials:** This type of monitoring is mainly focused on crack detection and growth. Methods are normally off line and not suitable for on-line condition monitoring of wind turbines. An exception might be the usage of optical fuses in the blades and acoustic monitoring of structures [15].

5. **Stress-wave analysis:** The National Renewable Energy and Sandia Laboratories [119] in the USA have experimented with stress wave analysis, in which low-frequency stress waves are injected into the blade via bonded piezoceramic patches, which also receive the returns. Tests have shown that changes in stress wave parameters, resulting from small initial changes occurring in the structure, can be a useful predictor of failure. However, the technique's cost remains an issue and more affordable options are currently preferred for in-service use.

6. **Vibration-based techniques**: Commercial wind turbine condition monitoring systems mostly employ vibration-based techniques, which are sophisticated, and the sensors and cabling are costly. The technique is also not ideally suited to all wind turbine types and faults [120]. This technique monitors the gearbox, bearing and shaft components of the wind turbine. It is

reliable and standardised (ISO10816). It is however intrusive, subject to sensor failures and has limited performance for low speed rotation [5].

Vibration-based techniques have also been researched for blade fault diagnostics. Piezoelectric impact sensors, which use the piezoelectric effect to measure strain by converting it to an electrical charge, are being investigated as possible blade monitoring devices. However, the major drawback is cabling. Accelerometers have also been examined for sensing and tracking resonant vibrations which reveal changes resulting from material fatigue or other degradation in the wind turbine blade [119].

2.7 CONCLUSIONS

Wind energy is one of the oldest sources of energy used by humankind, comparable only to the use of animal force, water and biomass. A clean source of energy with zero carbon emissions, which does not pollute the air like power plants that rely on combustion of fossil fuels, such as coal or natural gas. Wind turbines are very effective systems for harnessing the power in the wind and horizontal-axis wind turbines are the most efficient and cost effective design for electricity generation. Advances in wind turbine technology such as improved aerodynamics and improved structural dynamics are on the increase with the primary purpose of increasing energy yield. A well-known example is the new trend in turbine blade designs with larger and more flexible structures, which has shown to increase energy capture efficiency. These enhancements have associated increased manufacturing costs unless reliability is improved through condition monitoring to manage maintenance of wind turbines as wind farm operators and insurers attempt to protect the capital invested in wind energy projects. The costs of all components in different types and sizes of wind turbines will vary, but in most cases aside from the tower, the blades are the most expensive.

Wind turbine blades are structurally composed of different types of materials. These include; wood and/or steel used for constructing the main-spar and glass reinforced plastic (GRP) for building the downwind and upwind sides of the blade. During manufacture and over the operational lifetime of wind turbine blades, they are subject to defects and degradation that can result in deformation/fault occurrence (such as cracks) and subsequent failure. The widespread of materials used in their construction makes it difficult for predictions on lifetime health to be made, highlighting the importance of condition monitoring.

Condition monitoring of wind turbine blades is an important strategy for minimising breakdown whilst avoiding periodic assessment and associated downtime, as it will provide information about the likely future performance-or lack of it of the turbine blade. Vibration-based condition monitoring was the selected technique for conditioning monitoring of wind turbine blades in this thesis. This is because it is a promising method for detecting and diagnosing any deviation from normal conditions in large mechanical structures.

The literature explored in this chapter gives some background into the functioning of wind turbines and explains the need for condition monitoring of the blades. Information in this chapter builds understanding of the work outlined in the following chapters of this thesis. In the next chapter, broader investigations into the various methods of conducting vibration–based condition monitoring are examined with theoretical and experimental results.

3 VIBRATION-BASED CONDITION MONITORING

Vibration-based condition monitoring is the in situ non-destructive sensing and analysis of system characteristics – in the time, frequency or modal domains – for the purpose of detecting changes, which may indicate damage or degradation. Monitoring systems have the potential to facilitate the more economical management and maintenance of modern structures and infrastructure [123]. Vibration-based condition monitoring involves an understanding of the theory of vibration and modal analysis in order to achieve success in the methodology.

Measuring vibrations is useful for detecting and diagnosing any deviation from normal conditions in large mechanical structures and rotating machines. The resonant or modal properties of mechanical structures are directly influenced by their physical properties. Therefore, any change in the physical properties of a structure should cause a change in its modal parameters. The elastic modes of a structure are strongly affected by its physical properties and boundary conditions. Its physical properties are summarised by its mass, stiffness and damping properties, and its boundary conditions are influenced by its geometric shape and physical support. Comparing changes between operating and baseline modal parameters with warning levels will indicate for instance, when the blades of a wind turbine have undergone physical damage [16], [19].

Resonant vibration is caused by an interaction between the inertial and elastic properties of the materials within a structure. All vibration is a combination of both forced and resonant vibration. Note that structural *damping* determines how quickly the structure dissipates vibrational energy and returns to rest when the excitation force is removed [17], [124].

Modes are used as a simple and efficient means of characterising resonant vibration, determined by the material properties (mass, stiffness and damping properties) and boundary conditions of the structure. A natural (modal or resonant) frequency, modal damping and a mode shape define each mode. If either the material properties or the boundary conditions of a structure change, its modes will change. The *resonant/natural frequency* is the frequency at which any excitation produces an exaggerated response. This is important to know since an excitation close to a structure's resonant frequency will often produce adverse effects. Deformation patterns at these resonant frequencies take on a variety of different shapes depending on the excitation force frequency on the system. These deformation patterns are the structure's *mode shape*. Mode shapes are the motions or vibration patterns of one point relative to all others on a structure.

Motion is a vector quantity that has both a location and a direction associated with it. A *Degree of freedom* (*DOF*) describes the motion at a point in a direction. The degrees of freedom of a system are the minimum number of independent co-ordinates required to describe its motion completely. There is a one to one relationship between the number of degrees of freedom and the natural frequencies (and modes of vibration) of a system – a system with *n* degrees of freedom will have *n* natural frequencies and *n* modes of vibration.

The time response of vibrating systems can be obtained by solving linear differential equations based upon mathematical models of various equivalent systems. When a finite-number-of-degrees-of-freedom is used, the system is a lumped-parameter system. Here, the real system is approximated by a series of rigid masses, springs and dampers. When an infinite-number-of-degrees-of freedom model is used, the system is a continuous or distributed-parameter system. The differential equation governing the motion of the structure is still the same as for the lumped-parameter system except that the mass, damping and stiffness distributions are now continuous and a wave-type solution to the equations can therefore be obtained theoretically and/or experimentally [124]–[129].

In this chapter, these theoretical and experimental methods are explored.

3.1 THEORETICAL MODAL ANALYSIS

Theoretical modal analysis involves the construction of a somewhat simplified mechanical model referred to as the *spatial model*, and based on the model, to formulate the equations of motion for the system. This model can then be used as a basis for further analysis [130]. The theoretical route to vibration analysis is summarised in Figure 3.1 below.
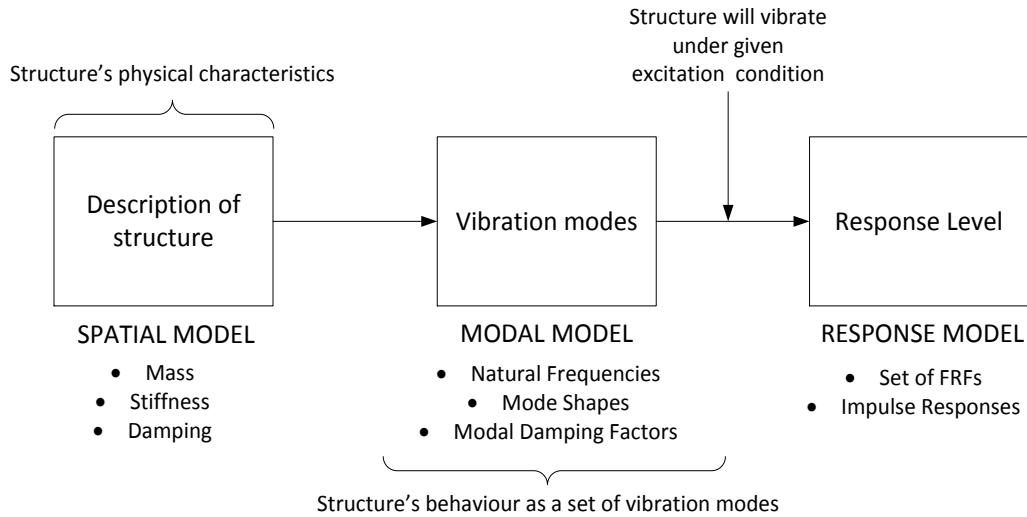
Figure 3.1 Theoretical modal analysis explained, adapted from [126], [130] where FRF means frequency response function and is the transfer function describing the input-output frequency characteristics of the system.
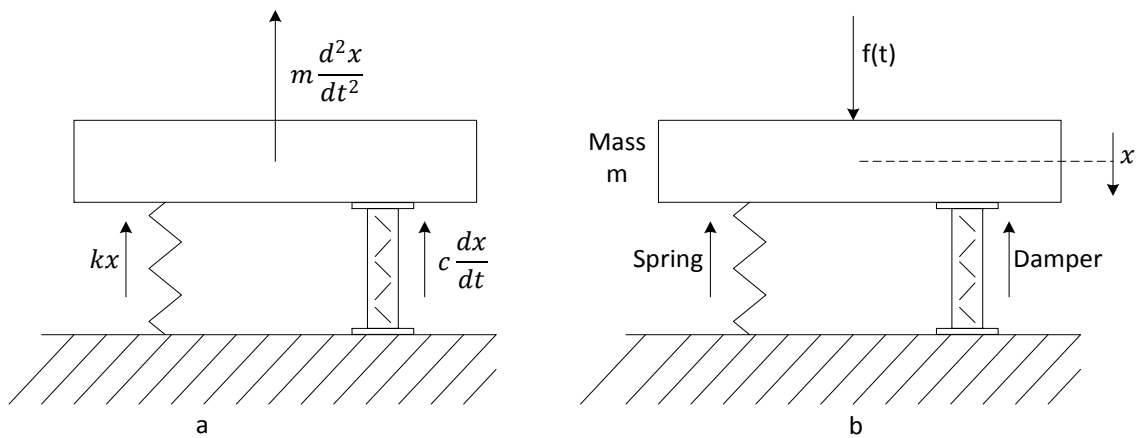
Figure 3.2 Models of a single degree-of-freedom system.
a   System in free vibration
b   System in forced vibration

One of the simplest generic spatial models of a vibrating mechanical system is shown in Figure 3.2a. It consists of a mass m, a spring having spring constant k and a damper having damping constant c. The variable $x(t)$ stands for the position of the mass m at its equilibrium point, i.e. the position of the mass when $f(t) \equiv 0$. If the system behaves linearly (and time-invariant) the equation of free motion of the mass is:

$$m\frac{d^2x}{dt^2} + c\frac{dx}{dt} + kx(t) = 0 \qquad \text{Eqn 3.1}$$

Eqn 3.1 states that the sum of all forces acting on the mass m should be equal to zero. $m\frac{d^2x}{dt^2}$ is the inertial force, $c\frac{dx}{dt}$ the (viscous) damping force, and $kx(t)$ the restoring force. This system is called a *single degree-of-freedom system* in that it consists of one mass only, which moves along one axis only and its motion can thus be described by a single second order differential equation [130]. It is also an example of a lumped-parameter system.

The motion of a mechanical system subjected to external forces is commonly termed the *response of the system* to the particular forces in question. Similarly, the external forces acting upon the system are termed the *exciting forces*, or simply the *excitation* [126].

Applying an external force or excitation to the system as indicated in Figure 3.2b, the equation of motion becomes [130]:

$$m\frac{d^2x}{dt^2} + c\frac{dx}{dt} + kx(t) = f(t) \qquad\qquad \text{Eqn 3.2}$$

Eqn 3.2 states that the sum of all forces acting on the mass should be equal in magnitude and opposite in direction to the externally applied force, $f(t)$.

Therefore, the solution of the above equations gives directly, the *displacement response*, $x(t)$, of the mass, produced by the excitation, $f(t)$. Other response quantities such as the *velocity response* or the *acceleration response* can be found from well-known relationships between displacement, velocity and acceleration:

$$v(t) = \frac{dx}{dt}, \qquad a(t) = \frac{d^2x}{dt^2} \qquad\qquad \text{Eqn 3.3}$$

Where $v(t)$ = velocity and $a(t)$ = acceleration of the mass, m in Figure 3.2b above.

The above equations are linear (and time-invariant) system equations and can be solved to obtain their frequency response using the Laplace transform ($F(s)$ of $f(t) -$ $where$ $s = j\omega$) and/or the Fourier transform ($F(f)$ of $f(t)$).

The Laplace transform is an integral transform that resolves a function into its moments whereas a Fourier transform expresses a function as a series of sinusoidal functions also called modes of vibrations (frequencies). The response of the system to each Fourier component is therefore, studied separately to produce the modal model shown in Figure 3.1. The modal model leads to a description of the mechanical structure's behaviour as a set of vibration modes [125], [126], [128], [130].

The Fourier transforms of the output response is the product of the Fourier transform of the excitation and the frequency response function of the structure.

$$X(f) = H(f) \cdot F_o e^{j2\pi ft} \qquad\qquad \text{Eqn 3.4}$$

Where $X(f)$ is the displacement of the output response in the frequency domain, $H(f)$ = frequency response function and $F_o e^{j2\pi ft}$ is the Fourier Transform of the input excitation with frequency, f and time, t.

From Eqn 3.4, sets of FRFs can be determined for the structure under analysis.

Generally, there are various ways of presenting or displaying frequency response function (FRF) data to obtain descriptions of a mechanical system. Table 3.1 below summarises the main formats of FRF [126], [129]–[132]:

Table 3.1 Definitions of frequency response functions where $F(f)$ denotes the input excitation in the frequency domain.

Response Parameter (R)	Frequency Response Function (R/F)	Inverse Frequency Response Function (F/R)
Displacement $X(f)$	Receptance $\frac{X(f)}{F(f)}$	Dynamic stiffness $\frac{F(f)}{X(f)}$
Velocity $Y(f)$	Mobility $\frac{Y(f)}{F(f)}$	Mechanical impedance $\frac{F(f)}{Y(f)}$
Acceleration $A(f)$	Inertance/Accelerance $\frac{A(f)}{F(f)}$	Apparent mass $\frac{F(f)}{A(f)}$

Systems in which a single mass moves in more than one direction or systems which consist of several, elastically interconnected masses are commonly termed *multi-degree-of-freedom systems*. A linear multi-degree-of-freedom system can be described mathematically, by a set of coupled second-order linear differential equations. When the frequency response curve of the system is plotted, it will normally show one resonance peak per degree-of-freedom. Thus a two degree-of-freedom system shows two resonance peaks, a three degree-of-freedom system shows three resonance peaks etc. [126], [129], [130]. Note that for non-linear systems, the principle of superposition cannot apply and the equation derivations above are therefore no longer valid.

In reality, the mechanical systems encountered are not of the idealized lumped-parameter type, i.e. having their masses assumed as rigid bodies where all points within the body move in phase, and elastic elements assumed to have no mass. In practise, all masses have certain elasticity and all spring elements have masses. For instance, a beam is a continuous combination of masses and springs. This means that such structures have an infinite number of degrees-of-freedom and hence an infinite number of resonances; defining and solving motion equations become almost impossible. Therefore, *Finite Element Method (FEM)* techniques are employed. They enable the reduction of continuous systems to discrete forms using numerical methods to find approximate solutions to the differential equations. A mechanical structure is divided into a finite number of elements connected only at the node points. Each discrete element is idealised. The displacements of these node points are assumed, and the complete solution is obtained by combining displacements so that it satisfies force equilibrium and displacement compatibility at the joints of the elements [128], [130], [133]–[135]. Several finite element software packages are currently available from various sources such as: ANSYS [136], Autodesk Multiphysics [137] and MATLAB [133]. FEM using ANSYS, is a popular method for conducting analysis in research studies on the structural health monitoring of wind turbine blades [138]–[141].

In the next section, an alternative modal analysis method is introduced known as the experimental modal analysis.

3.2 EXPERIMENTAL MODAL ANALYSIS

Experimental modal analysis is performed to obtain frequency response functions (FRF) of mechanical structures and subsequent modal and spatial models of a structure. This method is very useful for relatively large structures such as wind turbine blades for which the structural properties such as stiffness and damping may be unknown. Figure 3.3 illustrates the experimental route to vibration analysis.
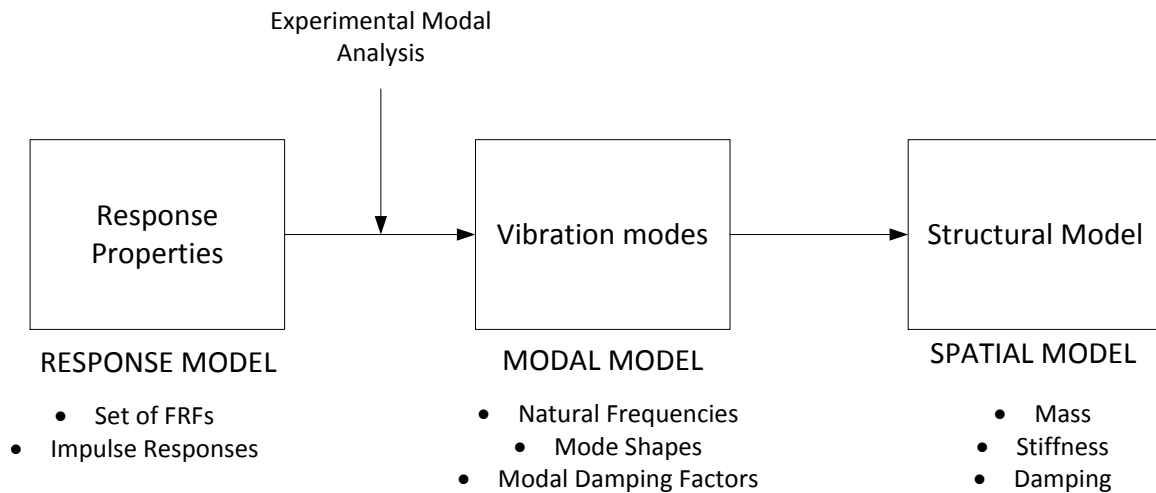
Figure 3.3 Experimental modal analysis explained, adapted from [126], [130].

Generally, FRF measurements are made under controlled conditions, where the test structure is artificially excited using either continuous excitation (forced vibration) from shakers, or transient excitation (free-vibration) from impact hammers [16], [17].

Accelerometers, which measure acceleration of test structures and output the signal in the form of a voltage, are positioned on the mechanical structure under investigation to measure the structure's response to the excitation. It is impossible to measure the motion of all material points of a mechanical structure, thus the motion is discretised. A finite number of degrees-of-freedom (DOF) are used to describe the motion of the mechanical structure and accelerometers are placed at these points for measurement. The characteristics of accelerometers and their configuration along the DOFs, influence the accuracy of the measurements [116], [117], [126], [129], [130].

Recordings of the excitation force and the structural response are measured and information on natural frequencies, deflection, system parameters such as stiffness and mass properties are extracted. The analysis method used to extract these from the measured data in experimental modal testing can be performed either in the time domain or in the frequency domain. The time domain method is based on a least square optimisation of modal amplitudes, modal damping and modal phases, given a selected but arbitrary number of resonances. The frequency domain analysis is based on the spectral energy contained in the resonance peaks [116].

A multi-channel Fast Fourier Transform (FFT) analyser is used, to measure the input from the impact device and the relevant output degrees of freedom [17]. However, data-acquisition (DAQ) systems are increasingly being used for collecting data, for analysis using computer software packages. They offer the most flexibility in the choice of post processing techniques.

Figure 3.4 illustrates the entire process involved in experimental modal analysis and each feature is discussed in detail in the following sections.
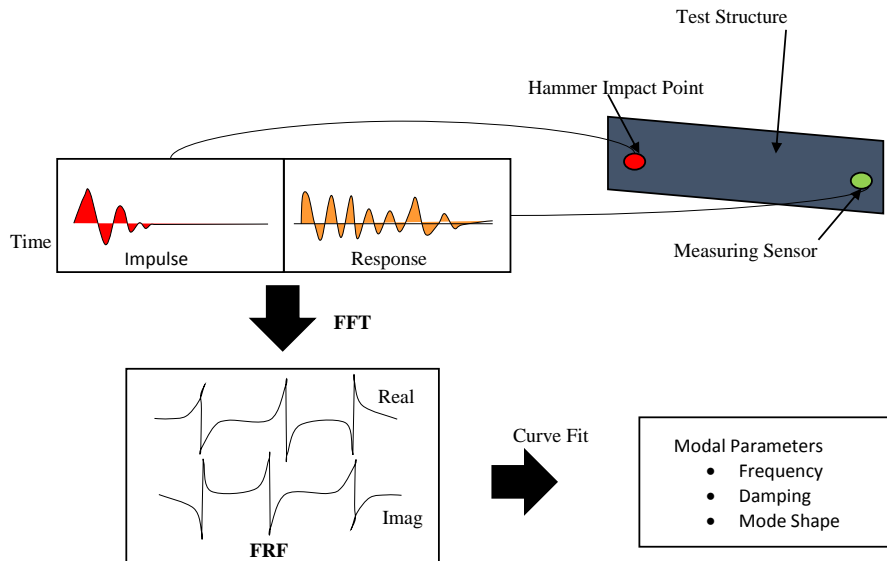
Figure 3.4 Experimental modal analysis often referred to as impact testing adapted from [17].

3.2.1 EXCITATION METHODS

A mechanical structure is generally excited by and responds to ambient forces within its service environment. In wind turbine blades, the variable wind loading is an example. In experimental modal analysis, these excitations are artificially induced using a force hammer for *transient excitation* or a shaker for *continuous excitation* [116], [126].

1. **Transient excitation**: Transient excitation is associated with a burst of short-lived energy such as an impulse force loading or an instantaneous release from an initial deflection of the structure [116]. In transient excitation, a discrete Fourier series description can be obtained, of both the input force signal and the response signal of the structure, and the frequency response function can be computed easily. Transient excitations include:
   a. **Snap-back principle**: Also referred to as a step relaxation. This involves releasing a structure under investigation from a deflected position.
   b. **Force hammer**: Hammers with force transducers attached at the tip/head are used to excite structures on impact. The magnitude of the impact is determined by the mass of the hammer head and the velocity with which it is moving when it hits the structure. The frequency range typically excited by a force hammer is controlled by the stiffness of the structure and the mass of the hammer head. The stiffer the structure, the shorter the duration of the pulse on impact and the higher will be the frequency range covered by the impact.

2. **Continuous excitation**: Continuous excitation is typically performed with electromagnetic or hydraulic based exciters able to produce periodic and random excitation signals (white noise excitation, pseudo-random excitation or periodic-random excitation) [116].
   a. **Chirp**: This involves exciting the structure using a short period (rapid) swept-sinusoidal wave signal. The frequency of the signal is varied through the range of interest and the signal is output through a shaker. This method provides greater control of both the amplitude and frequency contents of the input signal to the structure. It also permits the input of a greater amount of vibration energy.
   b. **Periodic excitation**: This involves a systematic signal in which all the components are mixed with ordered amplitude and phase relationships (e.g. a square wave). The

discrete Fourier transform is computed for both the force and response signals and the ratio of these transforms gives the FRF.

    c. Random excitation: This involves the use of random signals modelled in probabilistic terms to excite a structure. Cross-correlation analysis between the input excitation and the output response of the structure in the frequency domain is used to derive the FRF. Random signals include:

      i. White noise - a random signal with constant power spectral density.

      ii. Pseudo-random - a random mixture of amplitudes and phases for various frequency components.

      iii. Periodic-random - a combination of pseudo-random and periodic excitation signals.

3.2.2 SENSORS

Sensors (predominately accelerometers) also referred to as transducers, are used to measure the output response, i.e. the vibration response of the structure under observation to ambient forces in its service environment or artificially induced excitation described in the section above.

Accelerometers are designed to track the motion at the mounting surface of structures and ideally, not only should their output exactly correspond to the surface motion of the structure under observation, but also the presence of the transducers should not modify the motion to be measured. Balancing these trade-offs in reality is difficult but very vital for accuracy in measurements. Piezoelectric transducers are widely used, although strain gauges are often found to be convenient because of their minimal interference with the test structure. The accuracy of measurements also depends on:

i. **Sensor sensitivity**: In general, high sensitivity is required. However, the higher the sensitivity, the heavier and larger the accelerometer (thus interfering more with the structure) and further, the lower is the transducer's resonant frequency (and thus the maximum working frequency) [126]. Balancing these trade-offs during the selection of accelerometers is necessary to optimise the accuracy of measurements.

ii. **Sensor calibration**: Optimum signal-to-noise ratio is provided by accurately calibrating the accelerometers and this helps to improve the quality of the response measured. Calibration improves the repeatability of measurements. It also improves the quality of the signal above the noise.

iii. **Mounting of the sensor on the structure**: This could employ the use of studs or adhesives depending on the design of the accelerometer. The accelerometer must be positioned such that it is not close to a node of one or more of the structure's modes, as it is very difficult to make an effective measurement of that particular mode. An understanding of the degrees-of-freedom of the structure under observation is therefore necessary prior to mounting the sensors.

In reality, it is impossible and inefficient cost wise to measure the motion of all material points of a wind turbine blade, thus the motion is discretized. This enables decisions on the positioning of accelerometers or measuring sensors in general, to be made. A finite number of degrees of freedom are used to describe the blade motion in this thesis. The mode shapes of the blade are assumed to be described by deflection in the *flapwise* and *edgewise* directions. *Torsion* is assumed to be described by the rotation of the chord about the pitch axis. Hence, the turbine blade is described by three degrees of freedom – two flapwise DOFs describing the flapwise and torsion, and one edgewise DOF describing the edgewise deflection [116], [117], [142] as illustrated along the cross-section of a wind turbine blade in Figure 3.5 below.

Figure 3.5 Cross-section of blade showing the three degrees of freedom.

The work presented in this thesis specifically focuses on the sensor aspect of vibration-based condition monitoring. It introduces the deployment and instrumentation of Micro Electro-Mechanical Systems (MEMS) accelerometers for the condition monitoring of wind turbine blades, discussed in more detail in the following chapters.

3.2.3   DATA ACQUISITION

Simultaneous recordings of the excitation force and the structural response measured from the sensors are obtained using analysers. Types of analysers are frequency response analysers and spectrum analysers. These devices may be either analogue or digital but most often digital. Data acquisition systems (DAQs) which interface between signals and a computer are used most often because of advancements in microelectronic technology.

In all cases, the main purpose of the above devices is to send output signals to the exciter device, sample input signals measured from the sensors and convert the resulting samples into digital values that can be manipulated by a computer. These instruments have an analogue-to-digital converter (ADC) which controls the conversion process. Setting the number of samples to read and the sampling rates of the ADC are very important in the conversion of the signals.

3.2.4   POST-PROCESSING

Post-processing involves the digital signal processing steps and procedures used to analyse the measured data and to digitally improve/enhance the data quality.

The signals (input excitation and sensor output) are typically measured in the time domain and the desired spectral properties are in the frequency domain. Therefore, Fast Fourier Transform (FFT) algorithms are used to provide estimations of the spectrum or power spectral density of the signals. Software such as National Instrument LabVIEW [143] and MATLAB [144] are useful tools for calculating the Fourier Transform of the signals and further analysis of the frequency domain data is often undertaken to extract modal parameters. The FFT approach to spectrum analysis is computationally efficient and produces reasonable results for a large class of signal processes.

In spite of these advantages, there are several inherent performance limitations of the FFT approach. The most prominent limitation is that of frequency resolution, i.e. the ability to distinguish the spectral responses of two or more signals. The frequency resolution in Hertz is the reciprocal of the time intervals in seconds over which sampled data are available. A second limitation is due to aliasing, which is a false translation of signals caused by under sampling (below the Nyquist frequency) is another common problem encountered. The Nyquist frequency is half of the sampling rate of a discrete signal processing system. A solution to the problem of aliasing is to use an anti-aliasing filter, which restricts the bandwidth of a signal to approximately satisfy the sampling theorem. The theorem states that unambiguous interpretation of a signal from its samples is possible when the power of the frequencies above Nyquist frequency is zero. Another option is to increase the underlying sampling rate of the signal to suppress high-frequency components.

Spectral leakage, a phenomenon that causes the fine spectral lines of a frequency spectrum to spread into wider signals is another limitation of FFT. It causes signals to appear as if energy at one frequency leaks into other frequencies.

When the number of periods in the acquisition is not an integer, the endpoints of the signal are discontinuous i.e. sharp transitions. These artificial discontinuities show up in the FFT as high-frequency components not present in the original signals. These frequencies can be much higher than the Nyquist frequency and are aliased between zero and half of the sampling rate. Windowing is a technique applied to address the effects of performing FFT over a non-integer number of cycles and for improving signal clarity. However, windowing manifests itself as "leakage" in the spectral domain, i.e., energy in the main lobe of a spectral response "leaks" into the side lobes, obscuring and distorting other spectral responses that are present [145].

Windowing consists of multiplying the time record by a finite-length window with an amplitude that varies smoothly and gradually towards zero at the edges. This makes the endpoints of the waveform meet and, therefore, results in a continuous waveform without sharp transitions [146].

3.2.4.1 *WINDOWING FUNCTIONS*
An actual plot of a window shows that the frequency characteristics of a window are a continuous spectrum with a main lobe and several side lobes.

i.   The main lobe is centred at each frequency component of the time-domain signal, and the side lobes approach zero.
ii.   The height of the side lobes indicates the effect the windowing function has on frequencies around the main lobes.
iii. The side lobe response of a strong sinusoidal signal can overpower the main lobe response of a nearby weak sinusoidal signal.

Lower side lobes reduce leakage in the measured FFT but increase the bandwidth of the major lobe. The side lobe roll-off rate is the asymptotic decay rate of the side lobe peaks. By increasing the side lobe roll-off rate, you can reduce spectral leakage.

In this thesis, Hann window was used based on trial and error selection method. Hann window is satisfactory in 95% of cases because it has good frequency resolution and reduced spectral leakage [146]. Also, Hann window is the recommended windows to use when the nature of the signal to be measured is unknown and smoothing needs to be applied. Below, shows the statements considered, to estimate the frequency content of the signals to be measured, which guided the window selection.

For vibrations;

i.   The signal could contain strong interfering frequency components distant from the frequency of interest, - *smoothing window with a high side lobe roll-off rate required*.
ii.   The signal could contain strong interfering signals near the frequency of interest, - *window function with a low maximum side lobe required*.
iii. The signal could contain two or more signals very near to each other. Therefore, spectral resolution is important. – *smoothing window with a very narrow main lobe required*.
iv.   Amplitude accuracy of the single mode frequency component is important in the frequency lobe. – *Window with a wide main lobe required*.
v.   The signal spectrum is broadband in frequency content – *uniform window or no window required*.

Hann window is sinusoidal shaped and in the frequency domain, it causes wide peaks but low side lobes with the signal touching zero at both ends of a peak, eliminating all discontinuity.

3.3 VIBRATION-BASED CONDITION MONITORING METHODS

Utilising vibration-based damage detection began during the later 1970s and early 1980s, with particular use in the aerospace and offshore oil industries. The most successful application was in the monitoring of rotating machinery [147]. The early approaches used, were based on correlating numerical models with measured modal properties from undamaged components. Pattern recognition was applied to time histories or spectra, and databases of vibration signatures allowed specific types of damage to be identified. However, these benefits are not shared for large structures like wind turbine blades, as their vibration signatures are more complex [7], [148].

As discussed in the section above, measurements are typically made in the time domain and the condition-monitoring analyst can choose to analyse the data in the time, frequency or modal domains. The modal domain involves a further reduction in data volume compared to the frequency domain and techniques exist to convert data directly from the time domain to the modal domain [128]. The further compression of data into the modal domain has raised disagreements among researchers about the suitability of modal parameters for condition monitoring. One body of opinion suggests that modal domain parameters are sufficiently sensitive enough to detect damage whereas the other disagrees arguing that modal information is a reflection of the global system properties while damage is a local phenomenon on the structure [147]–[152].

Nevertheless, the majority of the literature to date [153] has focused on methods based in the modal domain. This is because natural frequencies and mode shapes are easily interpreted and so are initially more attractive than rather more abstract features extracted in the frequency domains (e.g. the distortion identification function [154], [155]) and time domains (e.g. residuals of autoregressive models [156]) [148].

With the emergence of a broad range of condition monitoring techniques, algorithms and methods, the various methods can be classified based on the level of identification attempted as [147], [148], [157]:

Level 1: Determination that damage is present in the structure

Level 2: Determination of the geometric location of the damage

Level 3: Quantification of the severity of the damage

Level 4: Prediction of the remaining service life of the structure

Identification of Level 4 is undoubtedly the ultimate aim of any condition monitoring system. However, more success has been found with and attention paid to Levels one to three. There are several approaches to identify, locate and quantify damage in vibration-based condition monitoring. Some of these approaches are [147], [148], [156], [157]:

1. Natural Frequency Based Methods
2. Mode shape Based Methods
3. Mode Shape Curvature/Strain Mode Shape
4. Dynamically Measured Flexibility Matrix Based Methods
5. Matrix Update Based Methods
6. Non-linear Methods
7. Neural Network Based Methods.

The work presented in this thesis focuses on Level 1(to determine that damage is present in the wind turbine blade). The natural frequency and mode shape based vibration-based condition monitoring methods were adopted, by measuring changes in modal properties (i.e. natural frequencies and mode shapes). More emphasis was placed on changes in natural frequencies because one of the consequences of the development of a crack is a decrease in local stiffness, which in turn results in a

decrease in some of the natural frequencies. Natural frequencies can be obtained easily from measurements at a single point on the structure. If measurements at several points are carried out, the mode shapes in discrete points of the structure corresponding to the different natural frequencies can be subsequently obtained. It is also commonly acknowledged that natural frequencies can be measured more accurately than mode shapes. Typical resolutions for the natural frequencies of lightly damped mechanical structures are 0.1% whereas typical mode shape errors are 10% or more. The situation is further complicated because mode shapes are relatively insensitive to damage. For example, if a cantilever beam contains a crack, the first bending mode will look very much like the first mode of the undamaged beam, until the damage is very severe. Thus, natural frequencies should be weighted very heavily compared to mode shapes in any identification exercise. Mode shapes are still valuable to pair the analytical and experimental modes, and also for 'symmetrical' structures which often have areas which produce similar changes to the natural frequencies [148], [151], [156]–[158].

3.4 PILOT STUDY

Wind turbine blades are often tapered in shape from root to tip, to generate the maximum power from the wind at minimum cost. Primarily, the design is driven by the aerodynamic requirements, as this tapered shape minimises solidity but also enables strengthening of the root where the blade attaches to the rotor hub; but economics means that the blade shape is a compromise to keep the cost of construction reasonable [159], [160]. It is therefore reasonable to assume that a stationary wind turbine blade attached to the rotor hub is like a tapered cantilever beam [161] as it is fixed at one end (the root) and the other end (the tip) is free (the boundary conditions).

In this section, theoretical modal analysis is explored for several rectangular shaped fibreglass coupons, simulating a non-tapered cantilever blade. This study was conducted to build knowledge in modal analysis, obtain predictions of natural frequencies and correlate with measured experimental values.

3.4.1 METHODOLOGY

3.4.1.1 *THEORETICAL ANALYSIS - MATLAB*

FR-4 material (a grade designation assigned to glass reinforced epoxy laminate sheet used for making printed circuit boards (PCBs)) was used to mimic a micro wind turbine blade (the Marlec Rutland 913 Windcharger [162]). The dimension of the FR-4 coupon was $385 \times 76 \times 1.5$ mm and it was cantilevered i.e. fixed at the root end and free on the tip end. The mounting point of the coupon accounted for 50 mm of the coupon's total length.

Studies [161], [163]–[169] on the free vibration of a cantilever beam were used to deduce equations of motion and simulate the expected natural frequencies of the coupon in MATLAB [144].
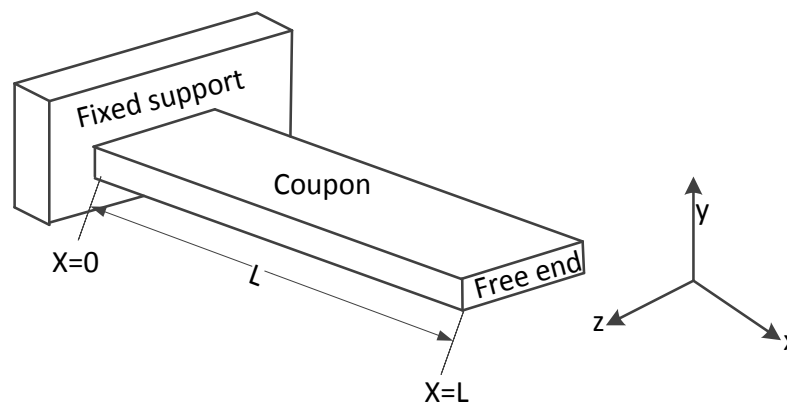
Figure 3.6 A cantilever coupon.

The cantilever coupon (illustrated in Figure 3.6) was assumed to be a continuous system in which the coupon mass was considered to be distributed along with the stiffness. Using Euler-Bernoulli beam theory [170], the equation of the coupon can be written as follows;

$$\frac{d^2}{dx^2}\left\{EI(x)\frac{d^2Y_n(x)}{dx^2}\right\} = \omega_n{}^2\mu(x)Y_n(x) \qquad \text{Eqn 3.5}$$

Where,

E -Young's modulus of rigidity of the coupon material ($E \cong 21\ GPa$). This is a measure of stiffness of a material.

I - Moment of inertia of the coupon, defined as $I = \dfrac{bh^3}{12}$ for a rectangular beam b-breadth and h-height. ($b = 76\ mm\ and\ h = 1.5\ mm$)

$Y_n(x)$ - Displacement in y direction at distance x from fixed end

ω_n- Circular natural frequency of the coupon in rad/s ($\omega_n = 2\pi f_n$ where $f_n -$ frequency (in Hz))

$n = 1,2,3 \cdots \infty$ (mode of vibration)

μ - Mass per unit length ($\mu = \rho A(x)$), ρ is the coupon material density ($\rho = 1{,}850$ kg/m^3) and A is the area ($A = b \times h$)

x - Distance measured from the fixed end.

Euler-Bernoulli is the same as simple beam theory, named after the pair who discovered it in 1750. The simple beam theory assumptions are;

i. A beam is long relative to its depth and width. Thus stresses developed perpendicular to the beam length are much smaller than those parallel, and can be ignored.
ii. The beam cross-section is constant along its length.
iii. The beam is symmetrical about the YY axis, resulting in no twisting or torsion occurring.
iv. Deflections/deformations are small.
v. The material is isotropic and obeys Hooke's law i.e. is linear elastic.
vi. Plane sections remain plane. This is true when a beam is subject to pure bending, and experiences zero shear deformation.

Real life structures never meet these assumptions exactly but usually approximate them well enough for the theory to be fairly accurate. In summary, simple beam theory involves consideration of:

- The type of material (e.g. Young's Modulus E)
- The way the beam deforms (e.g. curves)
- The geometry of the beam (e.g. beam cross-sectional area)
- The internal equilibrium.

As the coupon is cantilevered, boundary conditions therefore apply and are defined as follows:

At $x = 0$,

$$Y_n(x) = 0, \frac{dY_n(x)}{dx} = 0 \qquad \text{Eqn 3.6}$$

At $x = L$,

$$\frac{d^2 Y_n(x)}{dx^2} = 0, \frac{d^3 Y_n(x)}{dx^3} = 0 \qquad \text{Eqn 3.7}$$

For a uniform coupon under free vibration, Eqn 3.5 can be expanded and written as follows:

$$\frac{d^4 Y_n(x)}{dx^4} EI(x) = \omega_n{}^2 \mu(x) Y_n(x)$$

$$\frac{d^4 Y_n(x)}{dx^4} = \frac{\omega_n{}^2 \mu(x) Y_n(x)}{EI(x)}$$

`

$$\frac{d^4 Y_n(x)}{dx^4} - \beta_n{}^4 Y_n(x) = 0 \qquad \text{Eqn 3.8}$$

Where $\beta_n{}^4$ is a constant defined as:

$$\beta_n{}^4 = \frac{\omega_n{}^2 \mu}{EI} \qquad \text{Eqn 3.9}$$

The general solution of the Eqn 3.8 from numerical techniques like Rayleigh-Ritz is given as:

$$Y_n(x) = A_1 \cosh(\beta_n x) + A_2 \sinh(\beta_n x) + A_3 \cos(\beta_n x) + A_4 \sin(\beta_n x) \qquad \text{Eqn 3.10}$$

Where, A_1, A_2, A_3 and A_4 are constants. These constants are unique for a set of boundary conditions. However, the solution for the displacement is not unique and depends on the frequency of the beam.

Note that a displacement solution is called a *mode* and the shape of the displacement curve is the *mode shape*.

Applying the boundary conditions from Eqn 3.6 and Eqn 3.7, in Eqn 3.10, non-trivial solutions are found to exist only if the frequency equation for the cantilever coupon is given as:

$$\cos(\beta_n L) \cosh(\beta_n L) = -1 \qquad \text{Eqn 3.11}$$

When solved numerically, Eqn 3.11 yields an infinite number of solutions for $\beta_n L$. The first few roots are: $\beta_1 L = 1.875$, $\beta_2 L = 4.694$, $\beta_3 L = 7.856$, $\beta_4 L = 10.996$, $\beta_5 L = 14.137, \cdots$

From Eqn 3.9 and the roots of Eqn 3.11, a closed form of the corresponding circular natural frequency of vibration of the coupon can be calculated as:

$$\omega_n = \beta_n{}^2 \sqrt{\frac{EI}{\mu}} \qquad \text{Eqn 3.12}$$

Therefore when $n = 1$:

$$\omega_1 \ (in\ rad/s) = \beta_1{}^2 \sqrt{\frac{EI}{\mu}} \equiv \left(\frac{1.875}{L}\right)^2 \sqrt{\frac{EI}{\mu}} \qquad \text{Eqn 3.13}$$

$$f_1(in\ Hz) \equiv \frac{1}{2\pi}\left(\frac{1.875}{L}\right)^2 \sqrt{\frac{EI}{\mu}} \qquad\qquad \text{Eqn 3.14}$$

Using Eqn 3.12, the roots of Eqn 3.11 and the physical properties of the coupon material, the corresponding natural frequencies of vibration of the coupon were calculated in MATLAB and are discussed in the section 3.4.2.

The boundary conditions corresponding to the eigenvalues of β_n, from the solution for the displacement $Y_n(x)$ were also used to determine the mode shapes for the continuous cantilevered coupon in MATLAB as:

$$Y_n(x) = A_n \{(sin\,\beta_n L - sin\,h\,\beta_n L)(sin\,\beta_n x - sin\,h\,\beta_n x) + (cos\,\beta_n L + cosh\,\beta_n L)(cos\,\beta_n x - cosh\,\beta_n x)\} \qquad \text{Eqn 3.15}$$

Where $n = 1,2,3 \cdots \infty$ (mode of vibration) , $A_1 = 1$ and $\beta_n L = n\pi$

3.4.1.2 *EXPERIMENTAL ANALYSIS*

The copper layer was etched away from a sheet of glass reinforced epoxy laminate. The sheet was split into four coupons, measuring 385 mm long, 76 mm wide and 1.5 mm thick. Each of the coupons was mounted on a wooden block as illustrated in Figure 3.7. 50 mm of the coupon length accounts for mounting to the wooden block. Therefore, 335 mm of each of the coupon's length was suspended.

Three ceramic low-cost piezoelectric sounders/transducers [171] 27 mm in diameter and 1.8 kHz resonant frequency (when unconstrained), labelled T1, T2 and T3 in Figure 3.7 were glued on each of the four coupons. These sounders can typically be found in audio Christmas cards. T1 was the sounder closest to the mounting block and T3 was the furthest, towards the coupon tip/free end. The distance of separation between T1 and T2 was 45 mm and the distance between T2 and T3 was 80 mm.
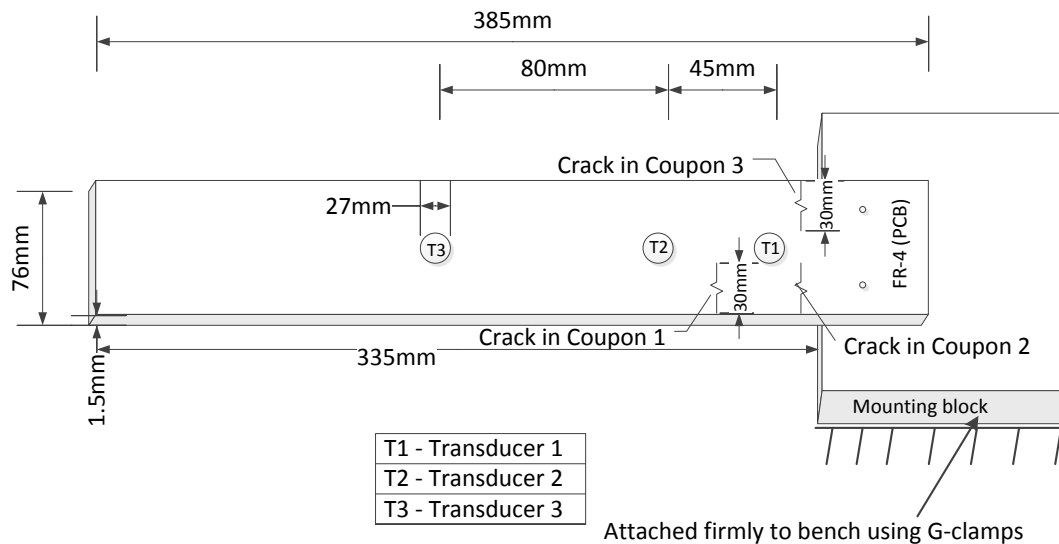
Figure 3.7 Diagram illustrating the experiment set-up, showing the dimensions, transducer and crack locations.

A piezoelectric transducer is a device that transforms mechanical loading to an electric charge. Certain natural and manufactured materials like quartz, tourmaline, lithium sulphate and Rochelle salt, generate electric charge when subjected to a deformation or mechanical stress. These materials are called piezoelectric materials and the electric charge disappears when the mechanical loading is

removed [172]. The piezoelectric transducer takes advantage of this piezoelectric effect. Brass weights of 8 grams were glued on top of each piezoelectric transducer to serve as a proof-mass mimicking a piezoelectric accelerometer. The proof mass improves the mechanical vibrations of the coupons on impact and the sensitivity of the piezoelectric sounder.

Three of the coupons were deliberately damaged by sawing the material at different positions illustrated in Figure 3.7 and shown in Figure 3.8. Coupon 1 had a transverse crack induced immediately after T1 in the direction away from the mounting block. Coupon 2 had a crack induced just before T1, on the left hand side close to the mounting block and Coupon 3 had a similar crack on the opposite side. The cracks were all of equal length of 30 mm. The existence of a crack at a section of the coupon is equivalent to a reduction (proportional to the crack's severity) in the second moment of area. This typically leads to a reduction in the local bending stiffness at that cross-section and is reflected in natural frequency measurements [123], [128], [147], [149], [151], [152], [156].

Transducers on Coupon 0, which had no crack (baseline test piece), were connected to three channels of an oscilloscope. T3 was used as the reference for oscilloscope triggering. The test coupon was clamped to the work bench and wires from the piezoelectric transducer were twisted and glued down to the coupon surface to decrease the measurement of foreign resonant modes that were not of the coupon's vibration. The coupon was struck firmly at the free end with a 20 grams metallic rod with just enough force to vibrate the coupon without destroying it and the natural frequency of the test coupon was measured to be 6.4 Hz. Other resonance frequencies were not measurable using the oscilloscope. This was assumed to be due to quantisation errors. A National Instruments Data Acquisition (DAQ) card, NI USB-6008 [173] was consequently used as a replacement for further measurements.
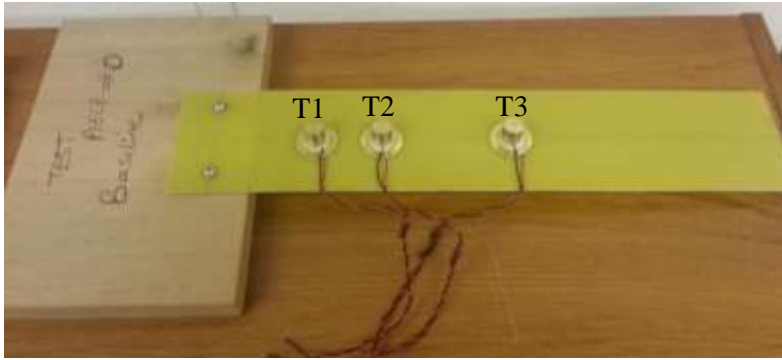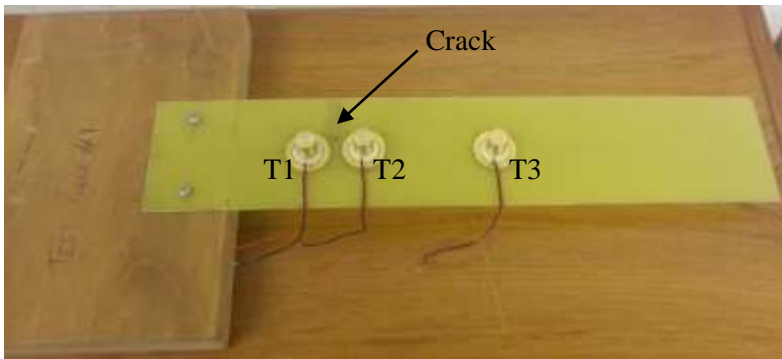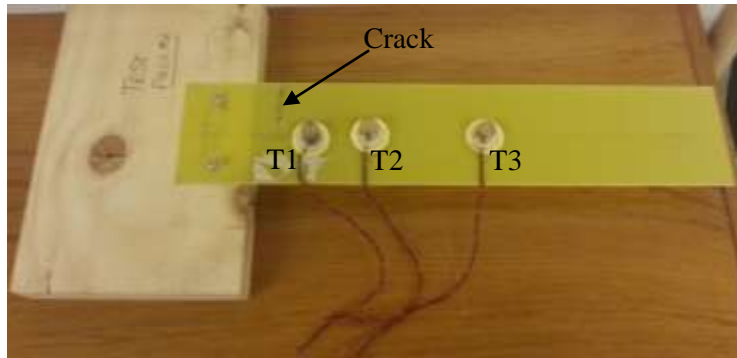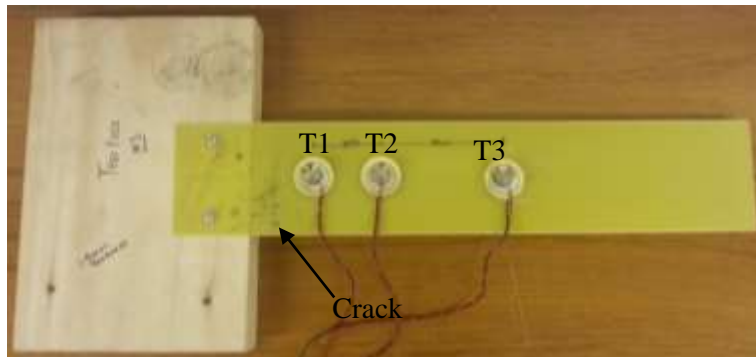
Figure 3.8 Picture showing the four Coupons: (a) Coupon 0 with no crack. (b) Coupon 1 with crack after T1. (c) Coupon 2 with crack before T1 on the left hand side. (d) Coupon 3 with crack located before T1 on the right hand side.
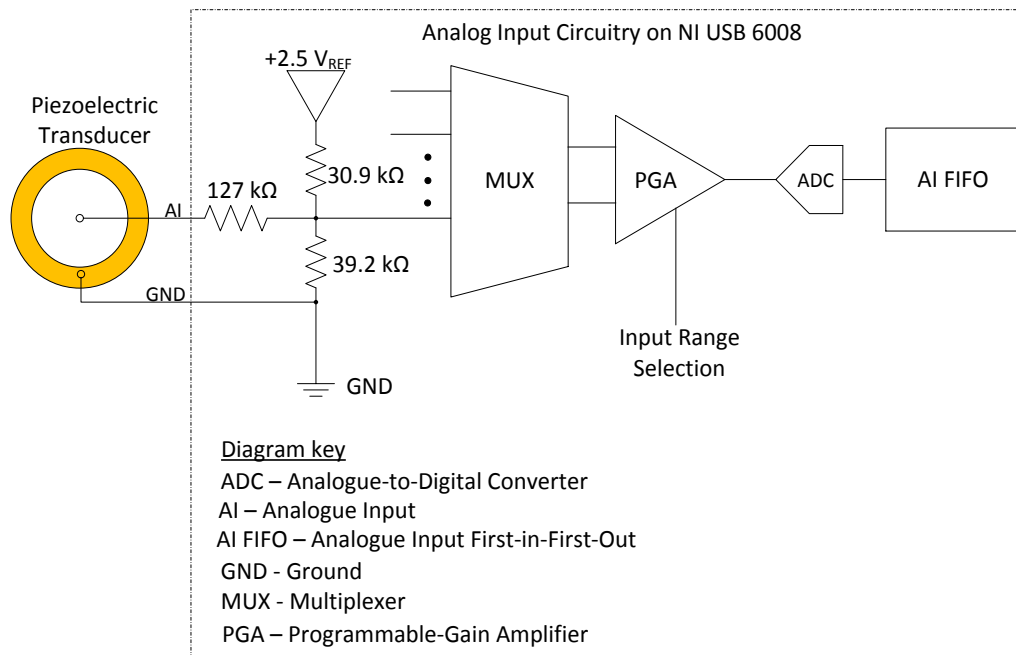
Figure 3.9 Diagram illustrating a Piezoelectric transducer and its connection to an analogue input pin on the National Instruments USB-6008 DAQ adapted from [173].

The piezoelectric transducers [171] were unhoused and had two wires attached to each of them. The transfer characteristics of piezoelectric transducers [171] and their self-generating power properties were of benefit to this experiment as no external voltage source was required. The transducers were powered up by connecting them to the AI pins of the NI USB-6008 DAQ [173] as shown in Figure 3.9 which supplies a 5V, 200 mA output when connected to a computer via USB interface.

The NI USB-6008 DAQ [173] provides connection for four differential AI measurements or eight single-ended AI measurements with a maximum sample rate of one kilo Samples/second (kS/s) per channel. Using National Instruments LabVIEW SignalExpress [174], three AI channels on the DAQ were configured to take referenced single-ended (RSE) measurements for each coupon and to acquire 500 samples at a rate of 1 kSamples/second for 10 seconds.

Measurements were recorded from the transducers, for the coupon responses when stationary and when they were vibrating after impact at the free end. Two methods of excitation (snapback and impulse excitations) were used to impact the free end of the coupons. In the snapback method, the coupons were released from a rest position, simply by holding down the tip of the coupon with one finger and releasing it, allowing the coupons to oscillate. For the impulse excitation, a hammer was manually used to strike the coupons at its free end. The hammerhead had a weight of 340 grams and was held from a distance of 2 cm away, above the coupon at the free end.

In post-processing the measured response from the transducers, the mean value of the direct current (DC) measurement (i.e. when the coupon was stationary) was calculated and subtracted from the measured signal due to impact. This was done in MATLAB and the purpose was to eliminate the DC offset in the measured signal prior to any further analysis. These measurements were then analysed further in MATLAB using the Digital Signal Processing Tool Kit. Fast Fourier Transformation (FFT) was conducted on each signal measured at each transducer on each coupon. Results obtained are compared and discussed in the next section.

3.4.1.3 THEORETICAL ANALYSIS – ANSYS WORKBENCH

All four test coupons were theoretically modelled using ANSYS Workbench [136]. Three 8 grams point masses were added on each coupon to represent the transducers and brass weights (T1, T2 and T3) used in the experiments. The fixed supports were applied to the face of the root end of the coupons and the tip ends were left to oscillate freely. Coupons 1, 2 and 3 had 30 mm cracks. The coupons were assumed to exhibit isotropic elasticity, and were meshed into 968 elements and 7259 nodes. Table 3.2 summarises the material properties assumed for the coupons. Results obtained from this analysis are discussed in the following sections.

Table 3.2 Assumed FR-4 material properties in ANSYS Workbench.

Density (kgm^{-3})	Young's Modulus (GPa)	Poisson's Ratio	Bulk Modulus (GPa)	Shear Modulus (GPa)
1850	21	0.118	9.1623	9.3918

3.4.2 RESULTS AND DISCUSSIONS

This section describes and discusses measured results from all theoretical analysis and experiments conducted.

3.4.2.1 THEORETICAL ANALYSIS - MATLAB

The first five natural frequency modes of the coupon were calculated and the mode shapes plotted using equations Eqn 3.14 and Eqn 3.15. Assumptions on physical properties of the coupon material such as its Young's modulus rigidity and density were made. FR-4 is a composite material, therefore variations in the fibre proportions and orientation, vary the value of these physical properties. The Young's modulus rigidity was assumed to be of cross-wise fibre orientation in the plane of the coupon, 21 GPa and a density of 1850 kg/m^3 [175]. These values were selected to closely match the first modal frequency measured for the coupon by the oscilloscope in the experimental modal analysis. Once the first mode matched, this modulus value of 21 GPa was used to predict and calculate the remaining mode frequencies of the coupon using MATLAB. Table 3.3 summarises the calculated values.

Table 3.3 Calculated natural frequencies of vibration for the FR-4 Coupon for 21 GPa Young's modulus and density of 1850 kg/m^3.

Mode (n)	β_n	Natural Frequencies f_n (Hz)
1	1.875	6.4772
2	4.694	40.5951
3	7.856	113.7079
4	10.996	222.7703
5	14.137	368.2157

Using CES EduPack Software [175], a comprehensive database of information on materials and their structural properties, the Young's modulus of FR-4 was given to be within the range of 35 – 45 GPa. However, solving the theoretical equations for the natural frequency of the coupon in MATLAB gave

very high first mode frequency results. The effect of varying the Young's modulus value on the theoretical frequency modes of the coupon was therefore explored and Figure 3.10 shows the measured plot. As the Young's modulus increases, the mode frequencies increase. Without the initial experimental measurements using the oscilloscope it's almost impossible to determine the natural frequency of the coupon theoretically.
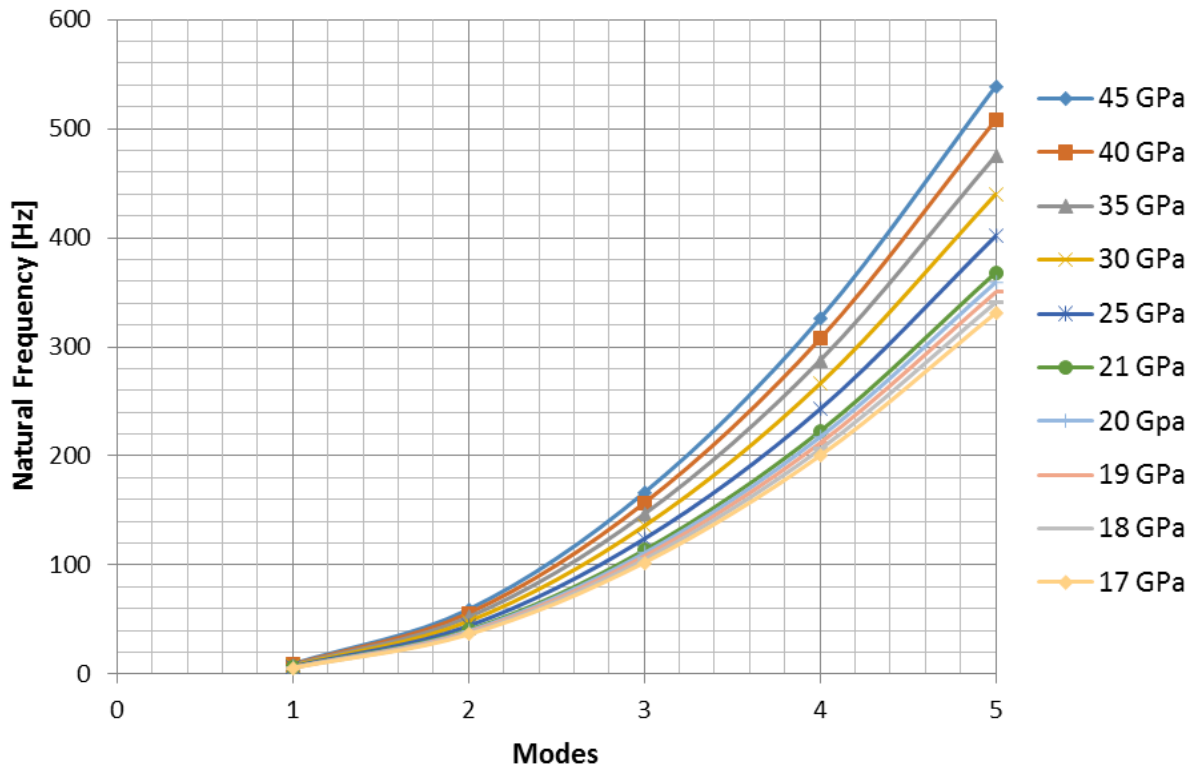
Figure 3.10 Plot showing the effects of changing Young's modulus on the theoretical mode frequencies of the FR-4 coupon.

Note that modes are inherent properties of a structure and do not depend on the forces or loads acting on the structure. A mode of a structure is typically defined by a modal frequency, modal damping and a mode shape. The mode will only change if the coupon properties (mass, stiffness, damping) or boundary conditions (mounting) change. The modes therefore enable the resonances of structures to be characterised and the characterisation of these resonances is useful for understanding structural vibration problems.

Figure 3.11 – Figure 3.15 show the plots of the theoretical mode shapes for the coupon based on the calculated natural frequencies in Table 3.3. The mode shapes generally show the sinusoidal pattern of motion in which all parts of the coupon move at a particular mode. Each mode shape is an independent and normalised displacement pattern, which may be amplified and superimposed to create a resultant displacement pattern. In the graphs, the amplitude of the mode shapes was set arbitrarily and chosen as a normalised unity value (i.e. $A_1 = 1$ in Eqn 3.11). The *x-axis* illustrates the coupon span/length with $x = 0$ m being the fixed end of the coupon and $x = 0.355$ m being the free end of the coupon.
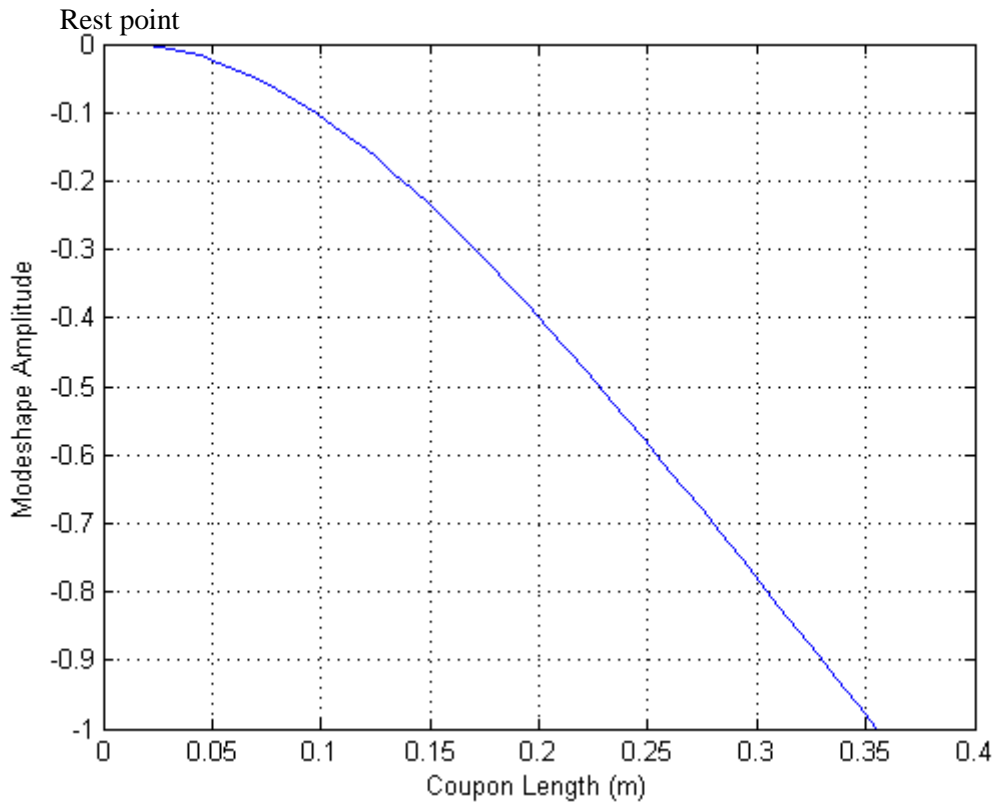
Figure 3.11 First mode shape of the FR-4 coupon with mode frequency of 6.4772 Hz. The coupon dips downwards from rest point.
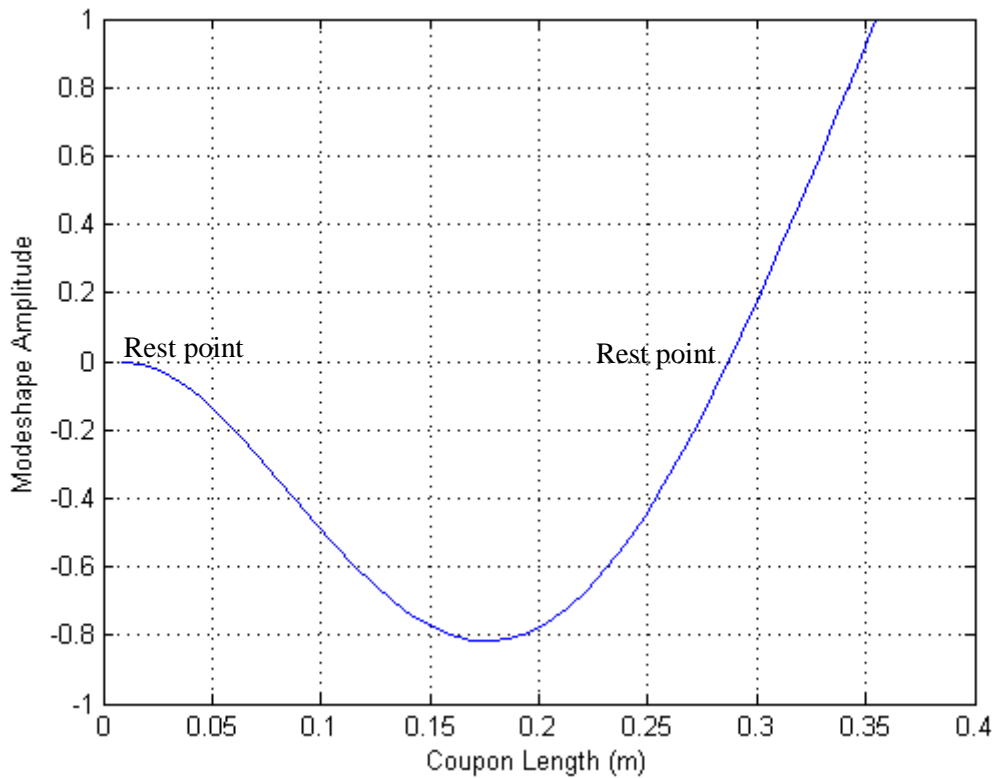
Figure 3.12 Second mode shape of the FR-4 coupon with mode frequency of 40.5951 Hz. The coupon comes back up to rest point and even oscillates further to a maximum point above 0.
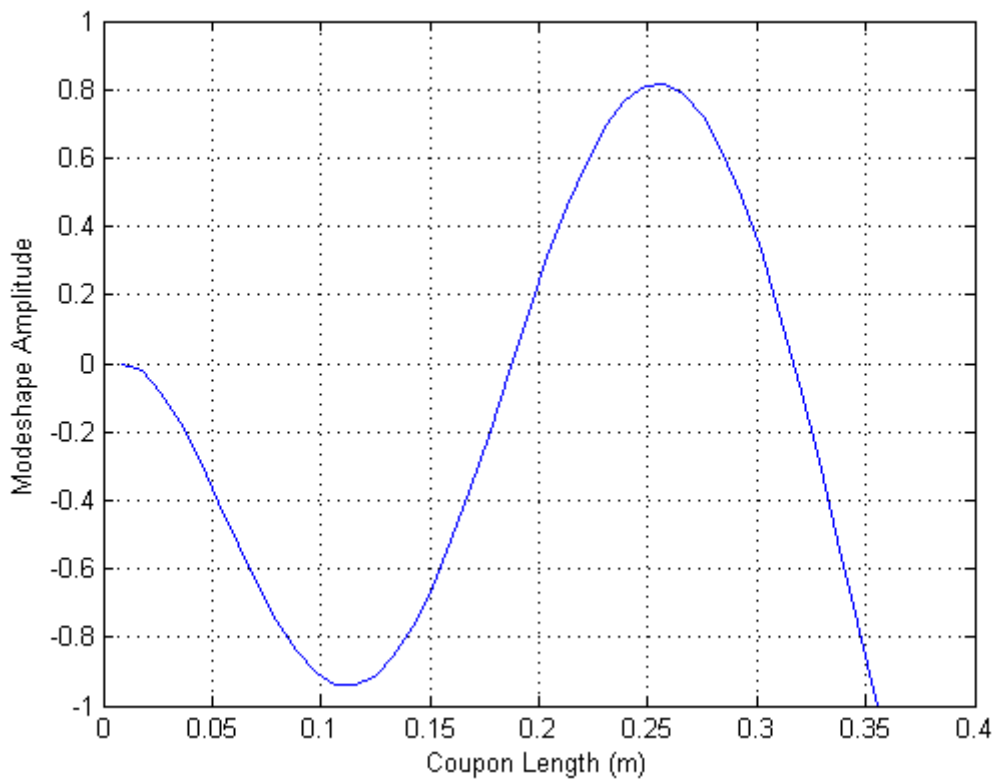
Figure 3.13 Third mode shape of the FR-4 coupon with mode frequency of 113.7079 Hz.
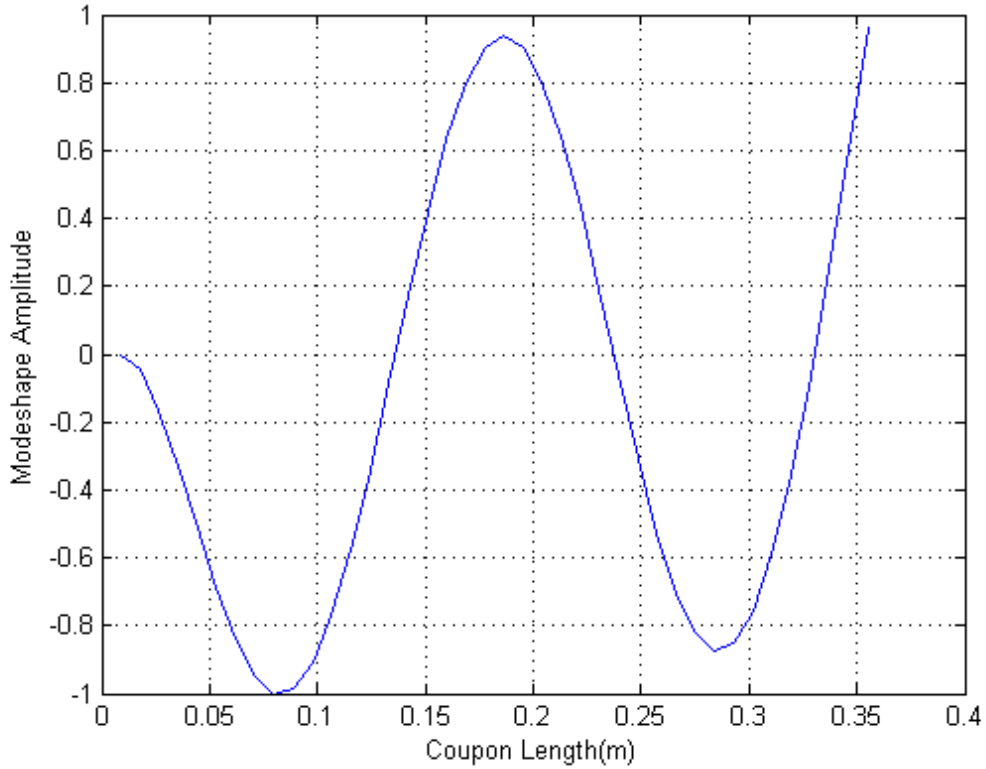
Figure 3.14 Fourth mode shape of the FR-4 coupon with mode frequency of 222.7703 Hz.
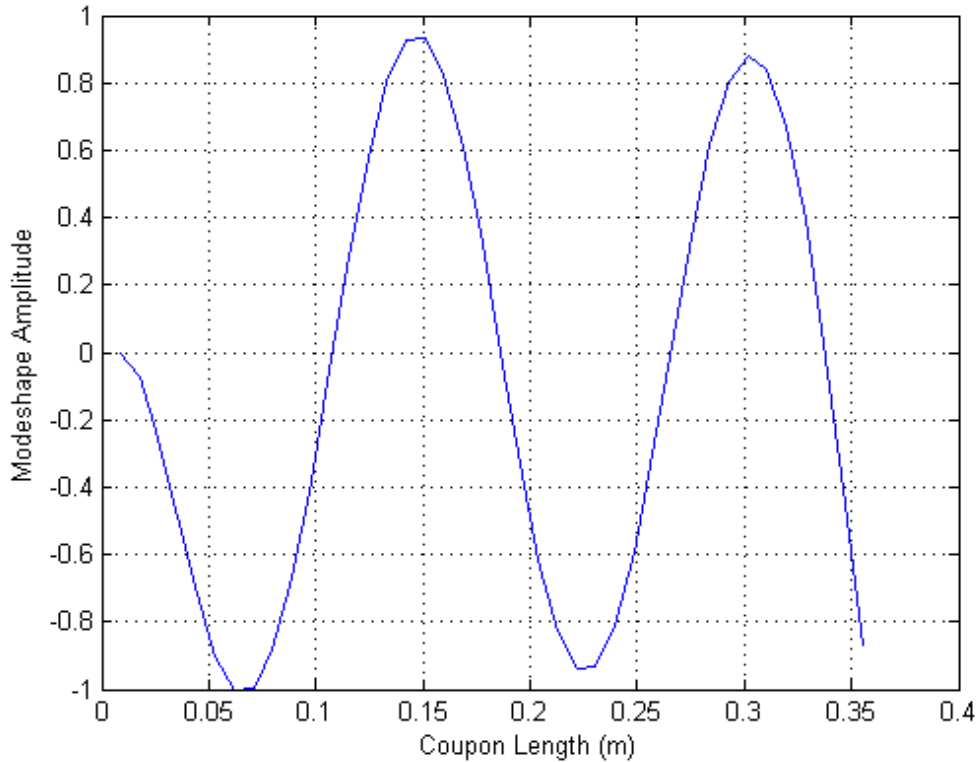
Figure 3.15 Fifth mode shape of the FR-4 coupon with mode frequency of 368.2157 Hz.

These theoretically obtained results above were compared with experimentally obtained results and are described and analysed in the next section.

3.4.2.2 *EXPERIMENTAL ANALYSIS*

Figure 3.16 shows the time domain output responses of the benchmark coupon, (Coupon 0) at T1, T2 and T3, to a snapback excitation. The release point can be seen in the graph at 0.65 seconds. The coupon was allowed to oscillate continuously and freely as shown in the time domain response below for 9.35 seconds. T1, the transducer furthest away from the free end and closest to the fixed end, measured the highest amplitudes, followed by T2 and T3 with the lowest amplitude as shown in the time domain plot.

Figure 3.17 shows the plot of the power spectral density deduced in MATLAB at T1 on Coupon 0 in response to the snapback excitation. The spectra for all the transducers were similar and generally noisy. The first peak observed was at 6.775 Hz and was identified as the first modal frequency of the coupon. Harmonics of this first modal frequency were identified at 13.49 Hz, 20.20 Hz, 26.79 Hz, 33.81 Hz, 40.59 Hz and 47.24 Hz respectively.

Further resonance peaks were observed at 35.58 Hz, 98.21 Hz and 190.10 Hz respectively. These were identified as the second, third and fourth modal frequencies of the coupon. On closer inspection of the power spectrum density of T1, a resonance was observed at 318.80 Hz, which was identified as the fifth modal frequency of the coupon.

A peak was observed at 50.30 Hz for all three transducers, T1, T2 and T3. This was attributed to mains coupling, common in multifunction input/output DAQs [176] such as the one used in these measurements.
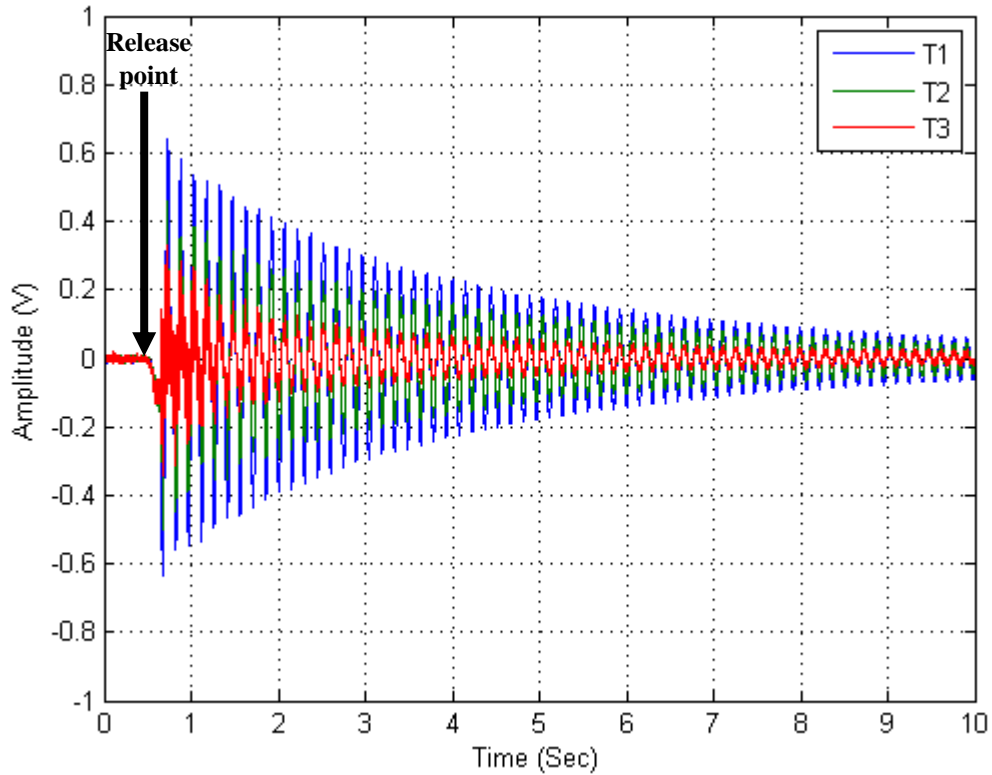
Figure 3.16 Time domain plot for 500 samples read at a rate of 1k samples per second at the three transducers on Coupon 0 in response to a snapback excitation.
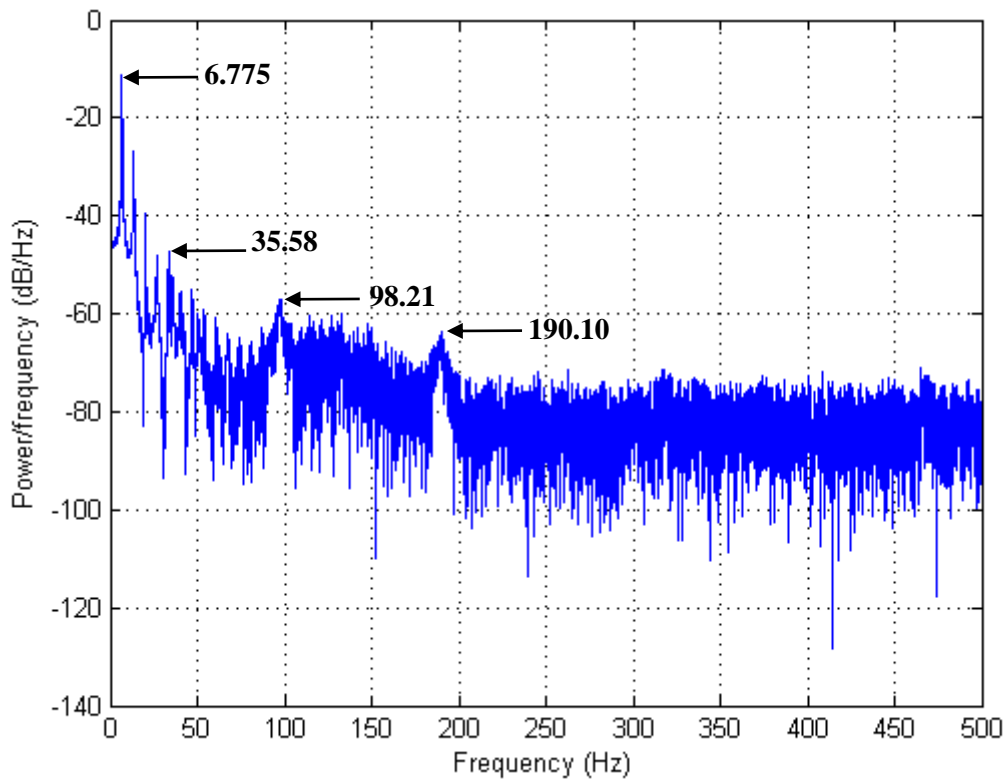
Figure 3.17 Power spectral density in response to a snapback excitation on Coupon 0, for 500 samples read at a rate of 1k samples per second measured at T1 (Near the fixed end)
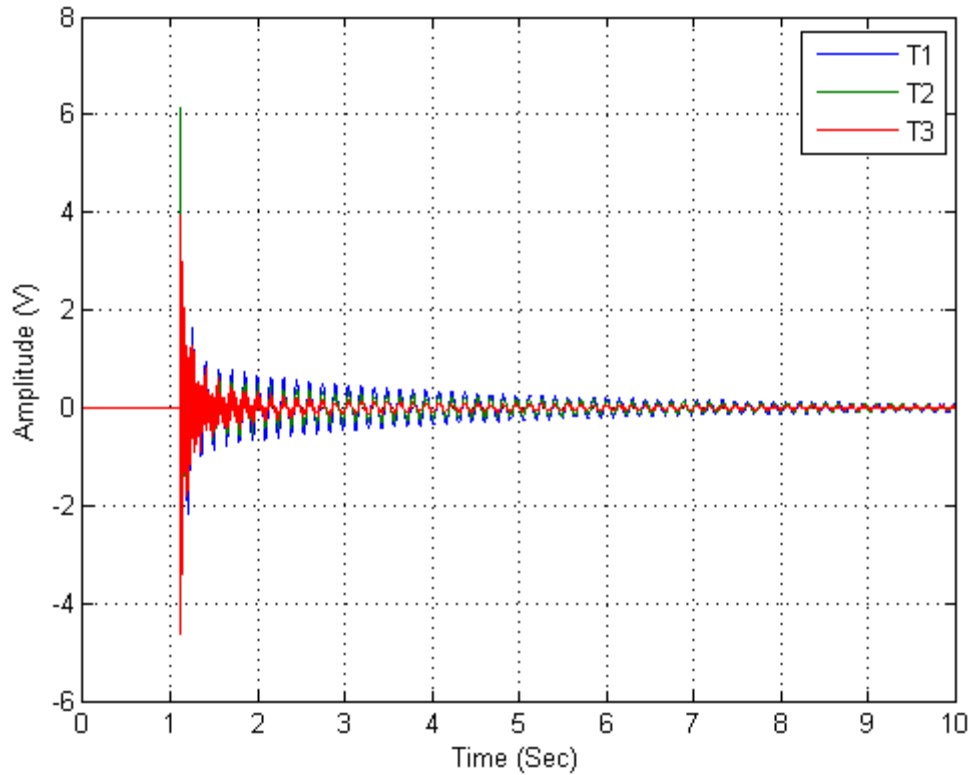
Figure 3.18 Time domain response plots for 500 samples read at a rate of 1k samples per second at the three transducers on Coupon 0 in response to a hammer excitation.
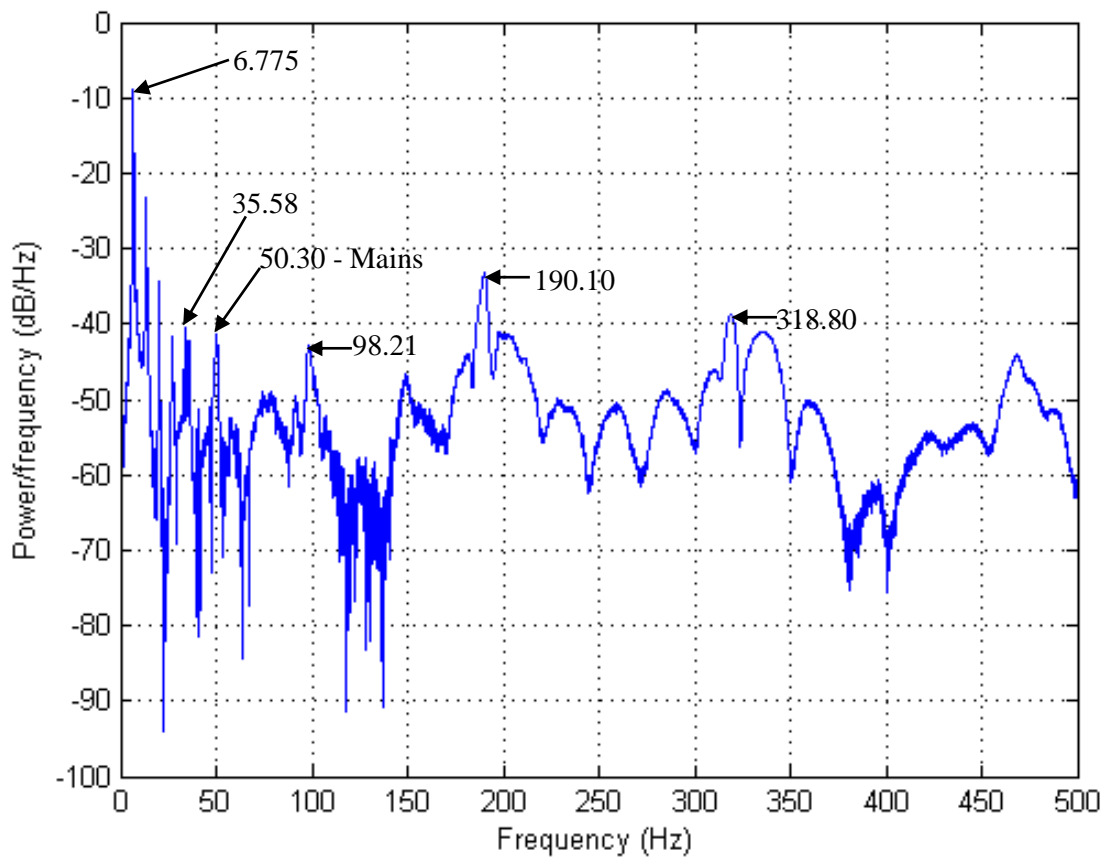
Figure 3.19 Power spectral density in response to a hammer excitation on Coupon 0, for 500 samples read at a rate of 1k samples per second measured at T1 − Near the fixed end.
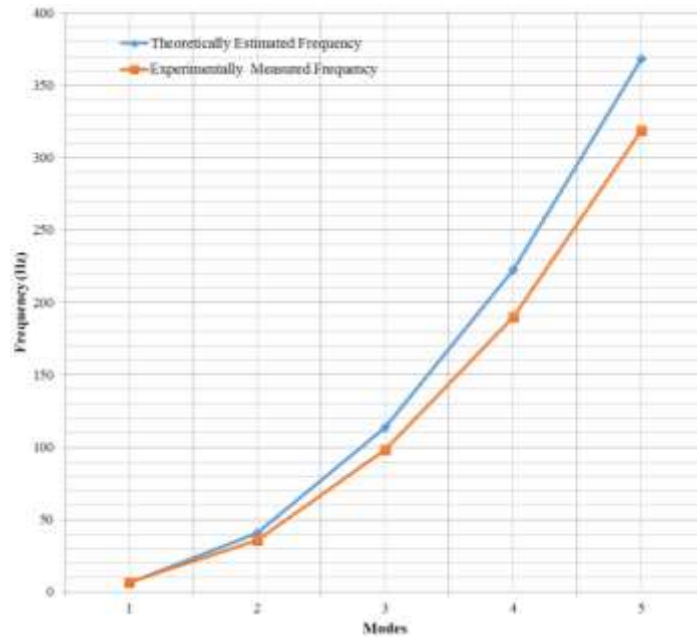
Figure 3.20 Graph showing the theoretically calculated and experimentally measured modal frequencies for the first five modes of Coupon 0.

Figure 3.18 shows the time domain plot of Coupon 0 when an impulse excitation is induced using a hammer. The oscillations of the coupon were allowed to slowly die out after one impact of the hammer. Figure 3.19 shows the plot of the power spectral density of transducer T1 due to the hammer excitation. The power spectral density deduced for the hammer excitation was less noisy in comparison to the snapback excitation and a similar frequency spectrum was observed. This is because both methods of excitation induce a transient response on the coupon as illustrated in the time domain responses in Figure 3.16 and Figure 3.18.

Figure 3.20 shows the theoretically estimated modal frequencies for the first five modes of the coupon with the experimentally obtained values for easier comparison. The deviation between the theoretically calculated frequencies and the experimentally measured frequencies increased linearly as the modal frequency increased. The theoretical frequencies were generally higher than the experimental values.

The theoretically calculated natural frequencies of the coupon, gave predictions on the range of where the actual natural frequencies of the coupon occur in the experimental measurements. However, as assumptions were made to mathematically solve for the theoretical natural frequencies, unmeasurable variations, such as variations in the structural composition and temperature of the coupon, the combination of vibration types (transverse, compressional and torsional) acting on the coupon and even human error which could occur during experiments are unaccounted for, hence, disparity between theoretical and experimental natural frequencies. Nevertheless, the theoretically calculated natural frequencies were useful in distinguishing between the natural frequencies, noise peaks and harmonics in the experimentally measured responses in Figure 3.17 and Figure 3.19.

Figure 3.21 – Figure 3.23 shows the frequency spectra measured at each transducer on each coupon for a hammer excitation. Signals measured at T3 were the noisiest generally. This is because T3 was the transducer closest to the excitation point on the coupons and also at the free end where oscillation is unconstrained. It therefore measures majority of the signal on impact, which is noisy. Distinguishing resonance peaks was more difficult for T3 in comparison to T1 and T2. T1 and T2 measured clearer responses on all coupons up to the fifth mode for Coupons 0, 1 and 2 and up to the third mode for Coupon 3 on zoomed in graphs of Figure 3.21 – Figure 3.23.
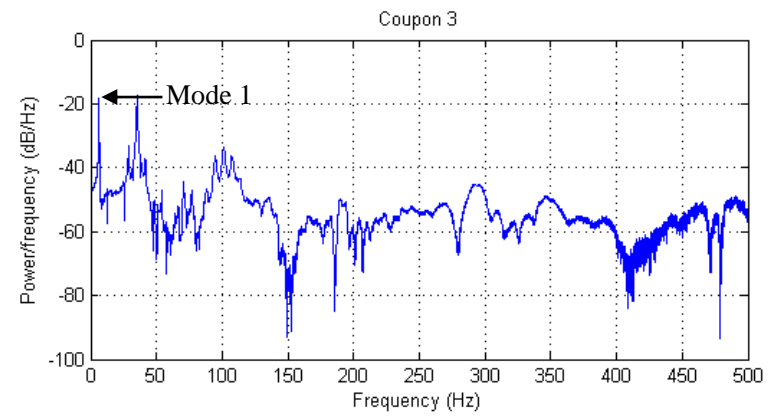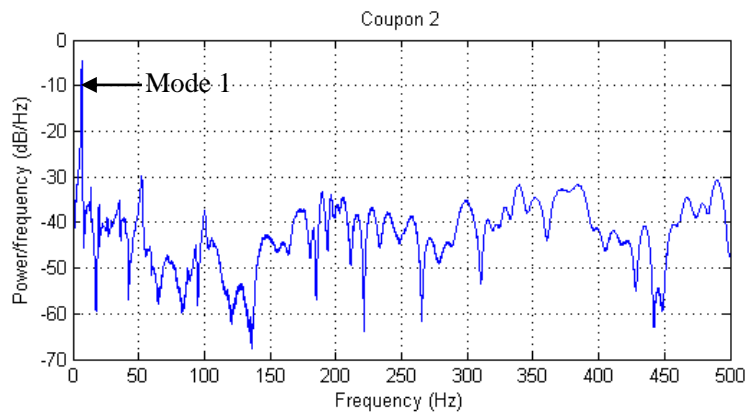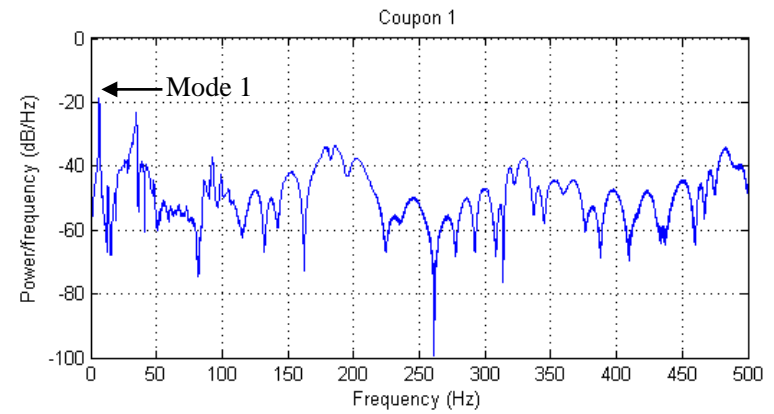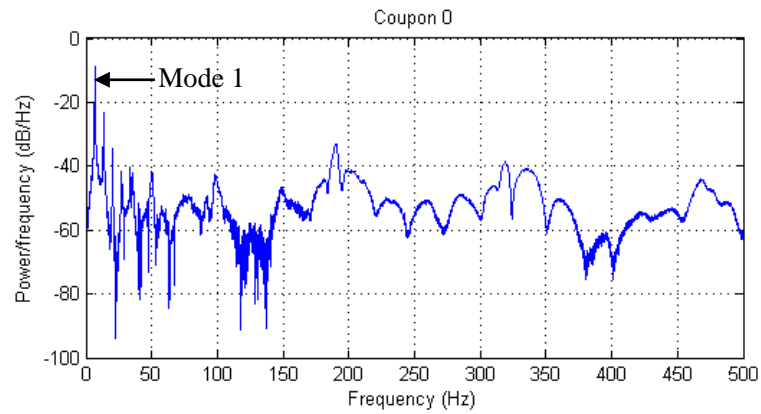
Figure 3.21 Power spectral density measured at the first transducer location (T1) on the four coupons, in response to a hammer excitation for 500 samples of data read at a rate of 1k samples/second.
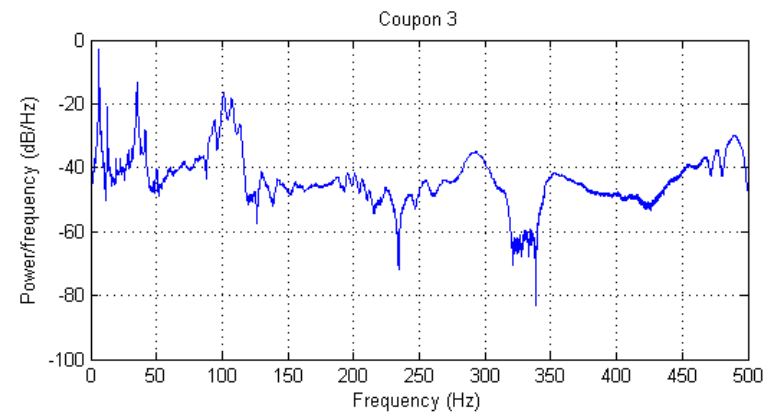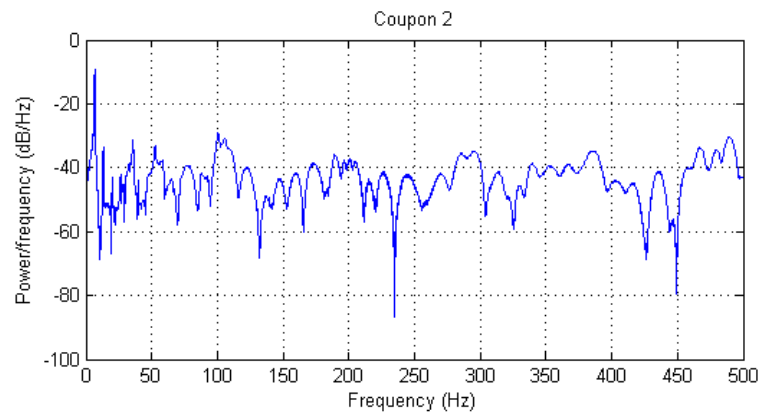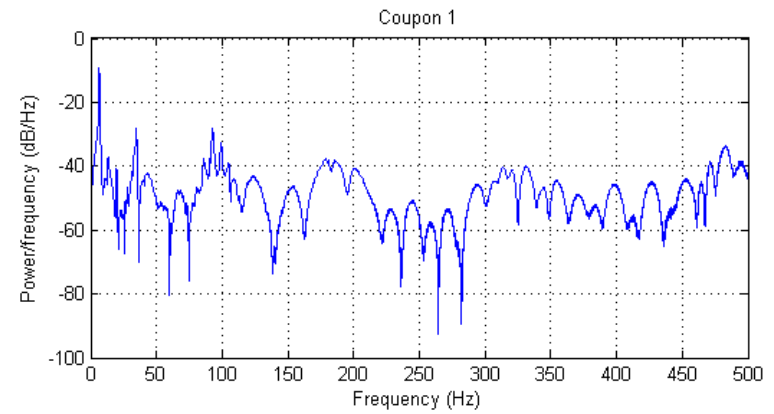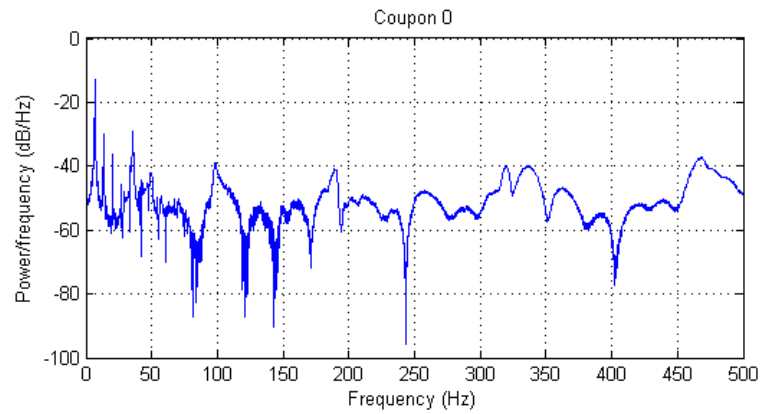
Figure 3.22 Power spectral density measured at the second transducer location (T2) on the four coupons, in response to a hammer excitation for 500 samples of data read at a rate of 1k samples/second.
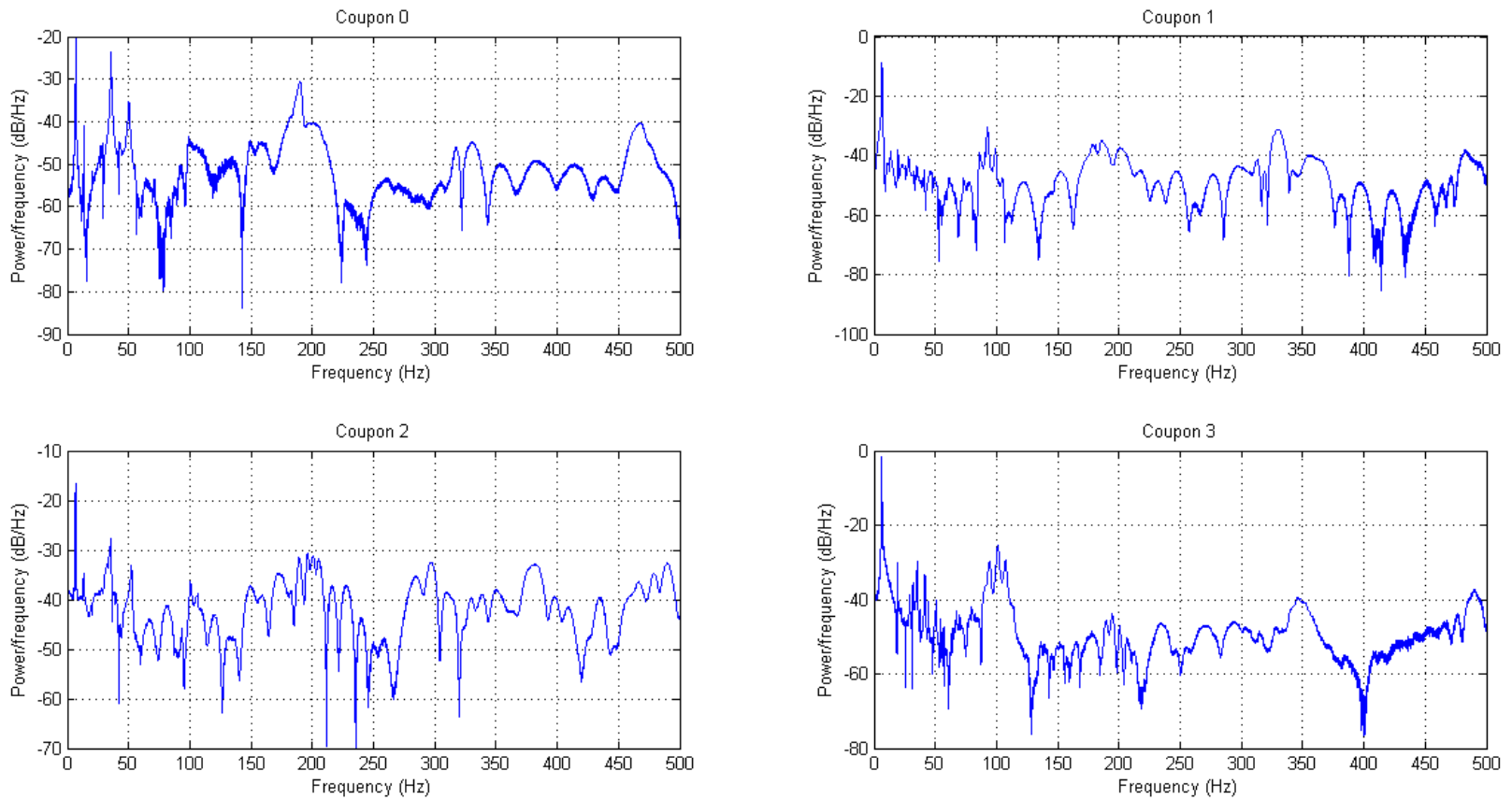
Figure 3.23 Power spectral density measured at the third transducer location (T3) on the four coupons, in response to a hammer excitation for 500 samples of data read at a rate of 1k samples/second.
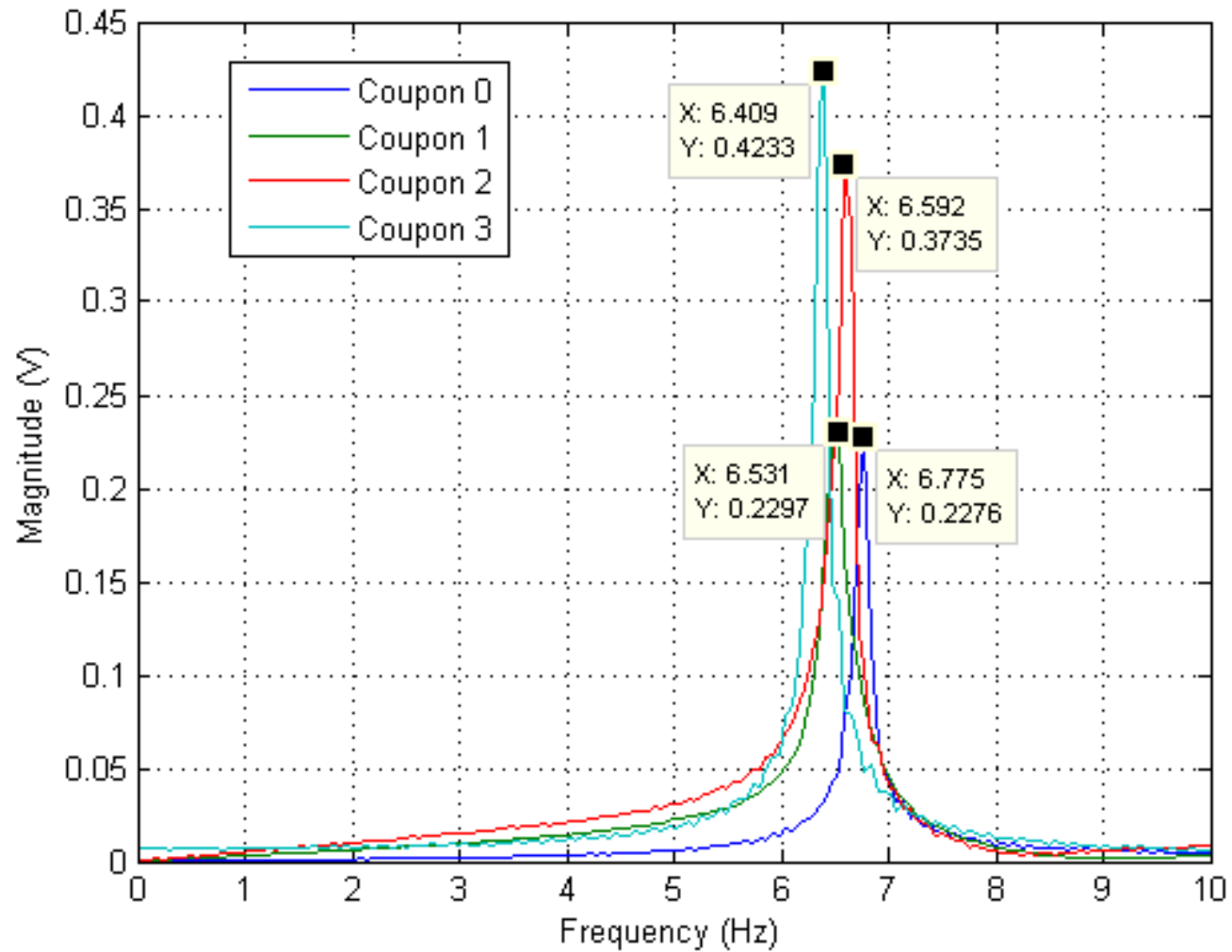
Figure 3.24 Zoomed in Frequency spectrum at the first experimentally measured mode for 500 samples of data read at a rate of 1k samples/second measured for the four coupons at the first transducer location (T1) in response to a hammer excitation.

Figure 3.24 shows a zoomed in section of the frequency response plot on a linear scale, at the first measured mode of all the coupons at T1 (the transducer closest to the fixed end and furthest away from the excitation point). These first mode changes, as well as the other four mode frequencies for the different coupons tested. Table 3.4 summaries the experimentally measured natural frequencies for each coupon at each transducer location. Small changes in the measured natural frequencies were observed for each of the coupons depending on the crack location. In general, all the coupons (Coupons 1, 2 and 3) measured a decrease in the natural frequency values from the benchmark, Coupon 0 at each transducer location.

Table 3.4 Natural frequencies extracted from the frequency spectrum graphs at each transducer location and a diagram of each of the coupons showing the crack location from Coupon 0 (with no crack) to Coupon 3.

Coupon	Transducer	Mode (Hz)				
		1st Mode	2nd Mode	3rd Mode	4th Mode	5th Mode
① ② ③	T1	6.775	35.58	98.21	190.10	318.80
	T2	6.775	35.58	98.21	190.00	319.80
	T3	6.775	35.58	98.82	190.00	317.40
① | ② ③	T1	6.531	34.85	99.00	186.60	312.70
	T2	6.531	34.55	99.06	186.20	313.70
	T3	6.531	34.55	99.06	186.10	311.20
| ① ② ③	T1	6.592	35.71	100.40	189.40	314.90
	T2	6.592	35.83	100.30	189.60	314.10
	T3	6.592	35.64	100.50	189.40	309.90
| ① ② ③	T1	6.409	35.16	98.88	-	-
	T2	6.409	35.22	101.80	-	-
	T3	6.409	35.16	101.80	-	-

3.4.2.3   *THEORETICAL ANALYSIS – ANSYS WORKBENCH*

Figure 3.25 shows the models of the four coupons generated in ANSYS Workbench. Coupon 0 - benchmark which had no cracks, Coupon 1 – with crack on the left side of fixed end between T1 and T2, Coupon 2 - crack on the left side of fixed end before T1 and Coupon 3 – with crack on the right side of fixed end before T1.

Figures 3.26 – Figure 3.29 show the theoretically obtained mode shapes, and natural frequencies estimated for the first six modes (four flapwise and two edgewise modes) of the four coupons. Coupon 0 had the highest natural frequency measurements for all modes when compared to the results for all the other coupons. This means that the occurrence of a crack on the coupon causes a decrease in the natural frequency. However, there are variations in the measured natural frequencies for different crack locations on the coupons.

Theoretical modelling of the coupons in ANSYS provided additional information such as the edgewise – twisting modes, when compared to the results estimated in MATLAB. However, the natural frequency values calculated in ANSYS were generally lower for all coupons than MATLAB and experimental values discussed in the sections above. This may be due to estimations made in the structural characteristics of coupon.

Table 3.5 summaries the natural frequencies measured in ANSYS and these are compared with the average of the experimentally obtained natural frequency measurements for all the coupons measured

at each transducer location in Table 3.4. To ensure coordinated analysis, the edgewise modes were excluded from comparisons. Trend graphs shown in Figure 3.30 – Figure 3.33 were plotted to infer better interpretations of the all the theoretical and experimental measurements.
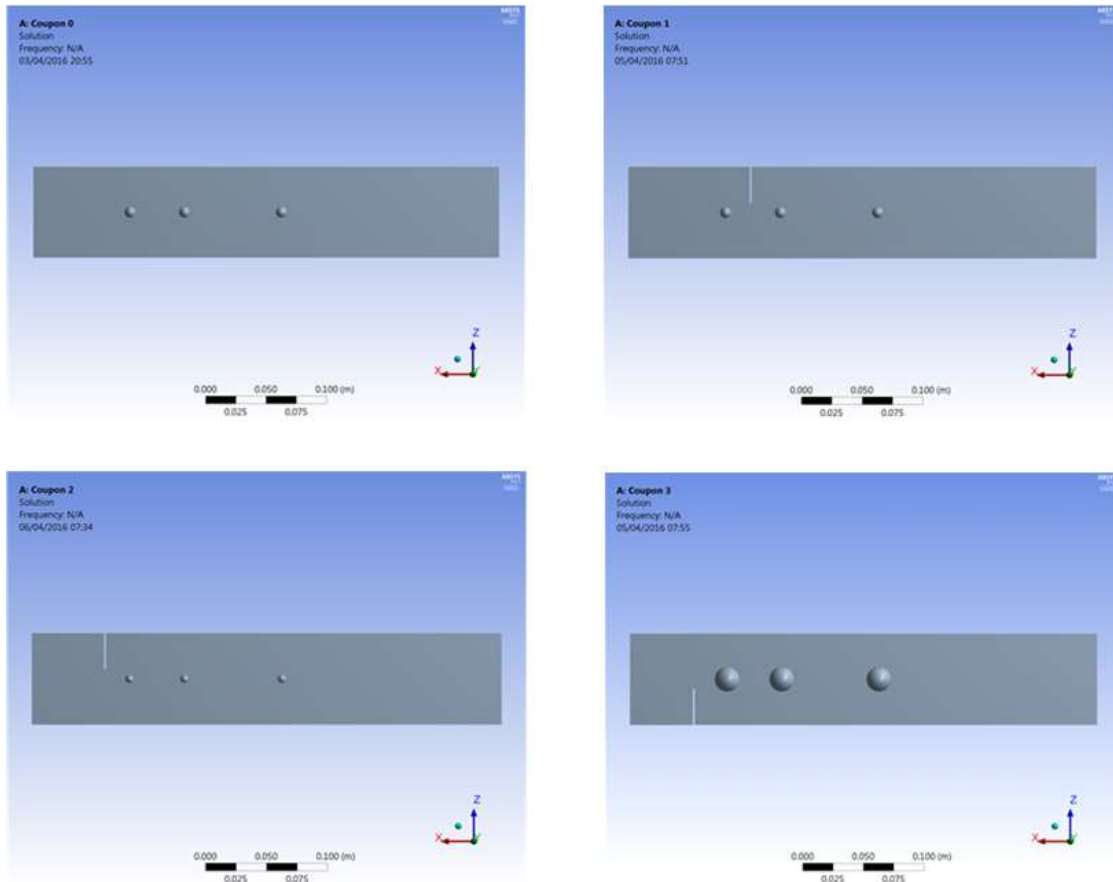
Figure 3.25 ANSYS models of Coupon 0 (top left), Coupon 1 (top right), Coupon 2 (bottom left) and Coupon 3 (bottom right).

Table 3.5 Theoretically (ANSYS) and average experimentally measured natural frequencies of the coupons. Note that the symbol "-" means that no measurement was recorded.

Mode	Coupon	Frequency (Hz)		Difference (%)	Mode type
		Theoretical	Experimental		
1	Coupon 0	5.2849	6.775	22	
	Coupon 1	5.1084	6.531	22	
	Coupon 2	5.0244	6.592	24	Flapwise – Bend around y-axis
	Coupon 3	5.0077	6.409	22	
2	Coupon 0	32.47	35.58	9	
	Coupon 1	32.296	34.65	7	
	Coupon 2	32.224	35.72	10	Flapwise – Bend around y-axis
	Coupon 3	32.099	35.18	9	
3	Coupon 0	94.52	99.06	5	
	Coupon 1	91.826	99.04	7	
	Coupon 2	93.807	100.4	7	Flapwise – Bend around y-axis
	Coupon 3	93.938	100.8	7	
4	Coupon 0	187.4	190.0	1	
	Coupon 1	182.71	186.3	2	
	Coupon 2	183.76	189.46	3	Flapwise – Bend around y-axis
	Coupon 3	184.83	-	-	
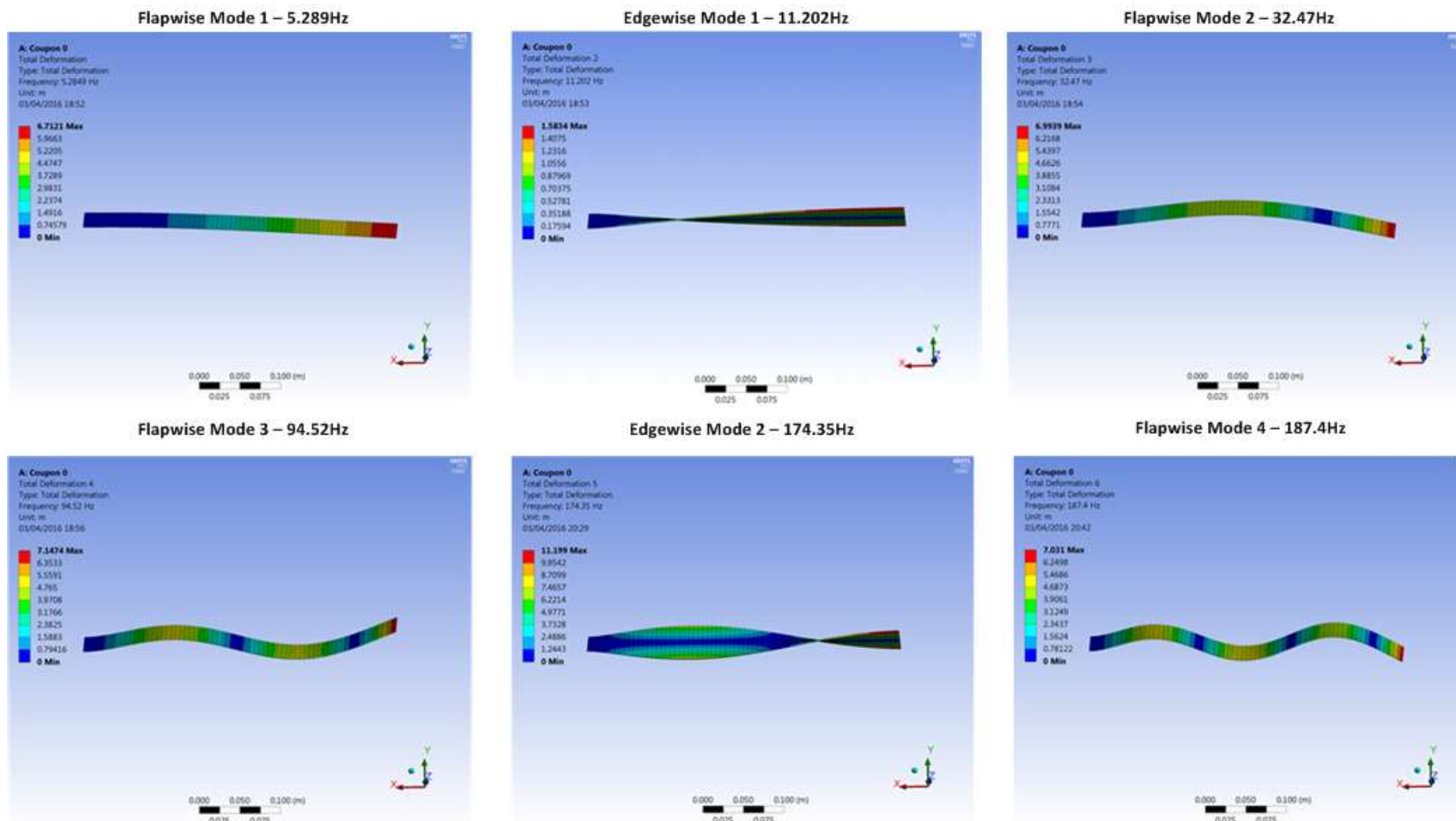
Figure 3.26 Theoretically estimated mode shapes and natural frequencies of Coupon 0 using ANSYS.
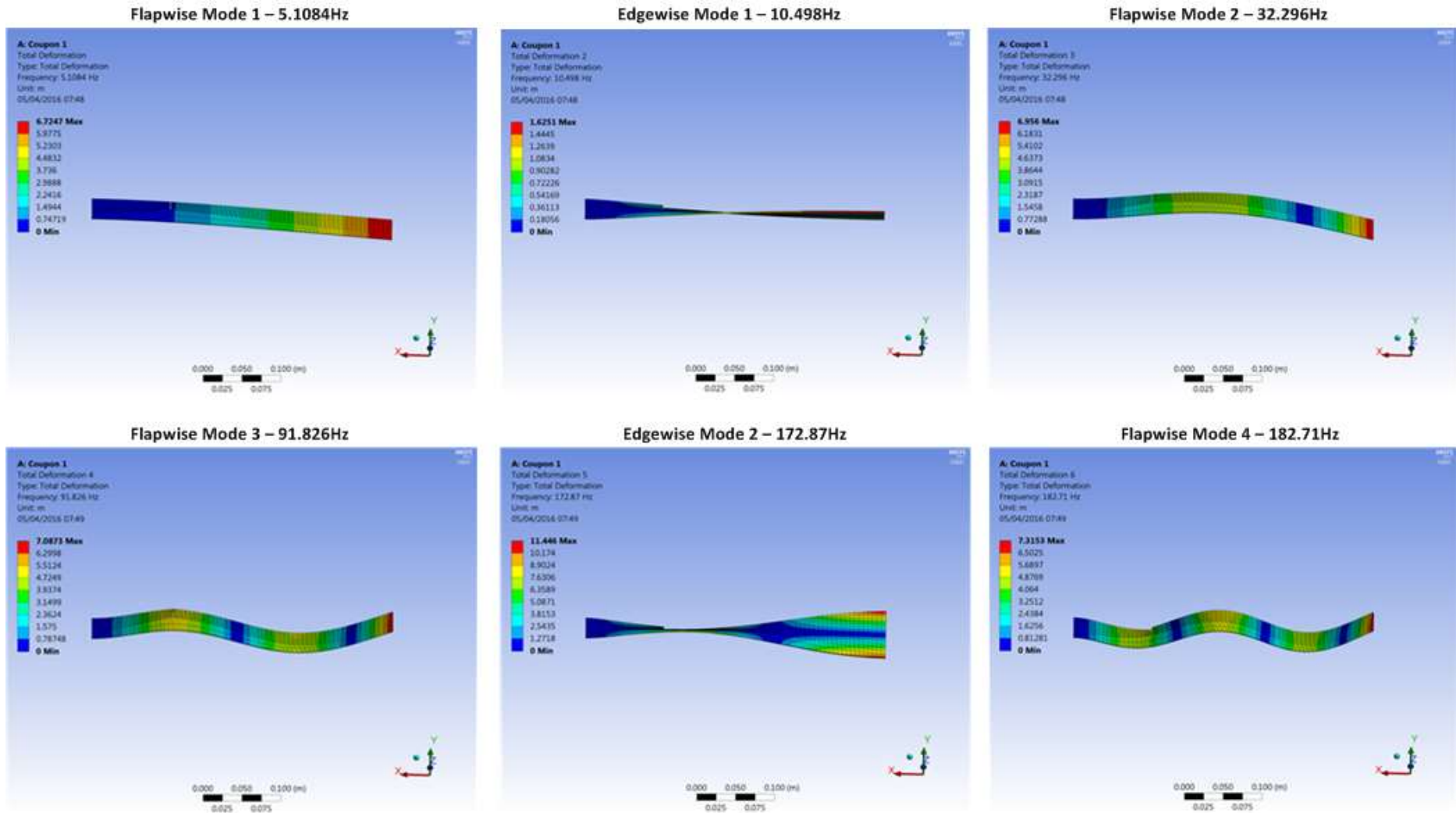
Figure 3.27 Theoretically estimated mode shapes and natural frequencies of Coupon 1(with crack on the left side of fixed end between T1 and T2) using ANSYS.
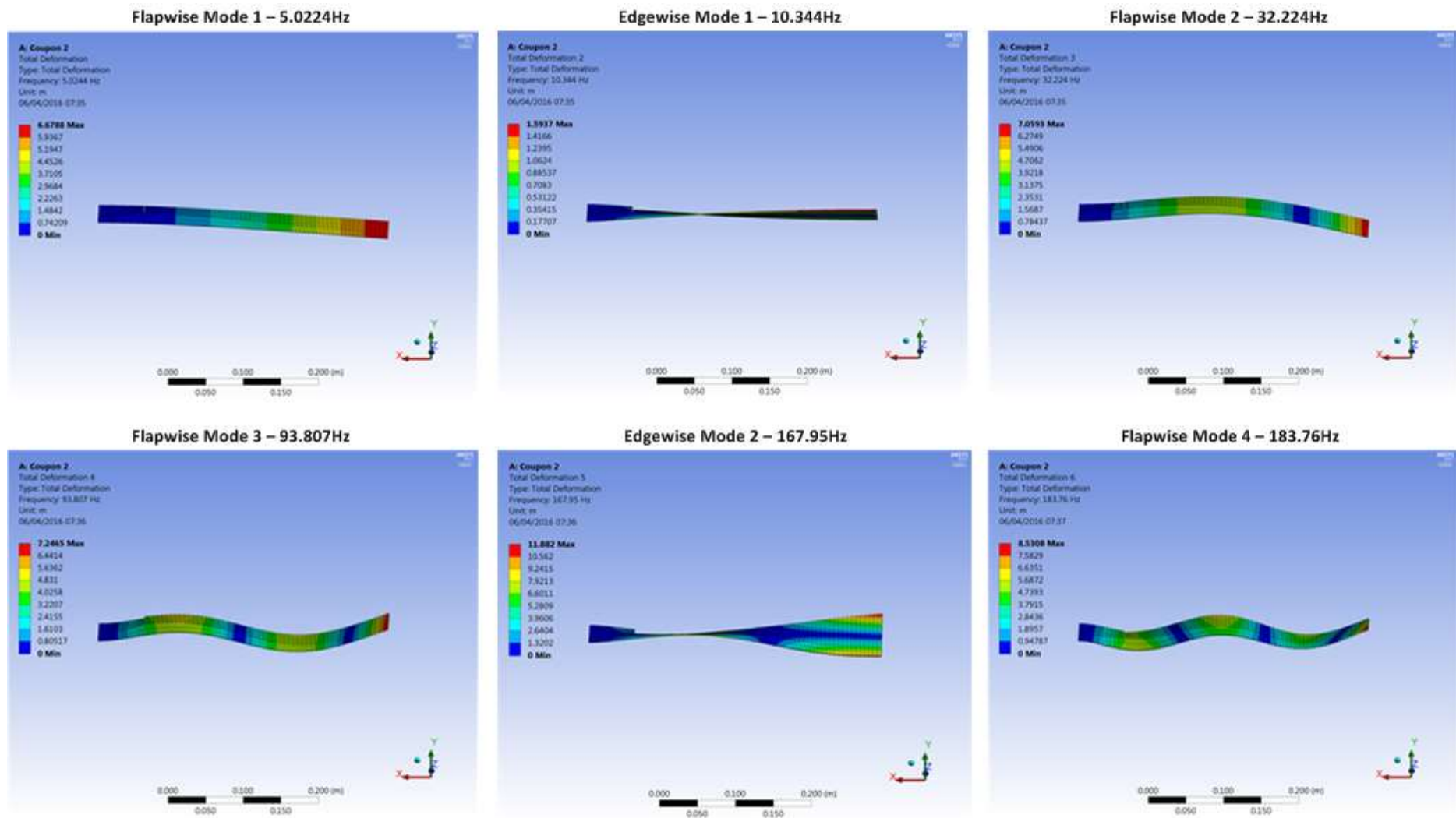
Figure 3.28 Theoretically estimated mode shapes and natural frequencies of Coupon 2 (with crack on the left side of fixed end before T1) using ANSYS.
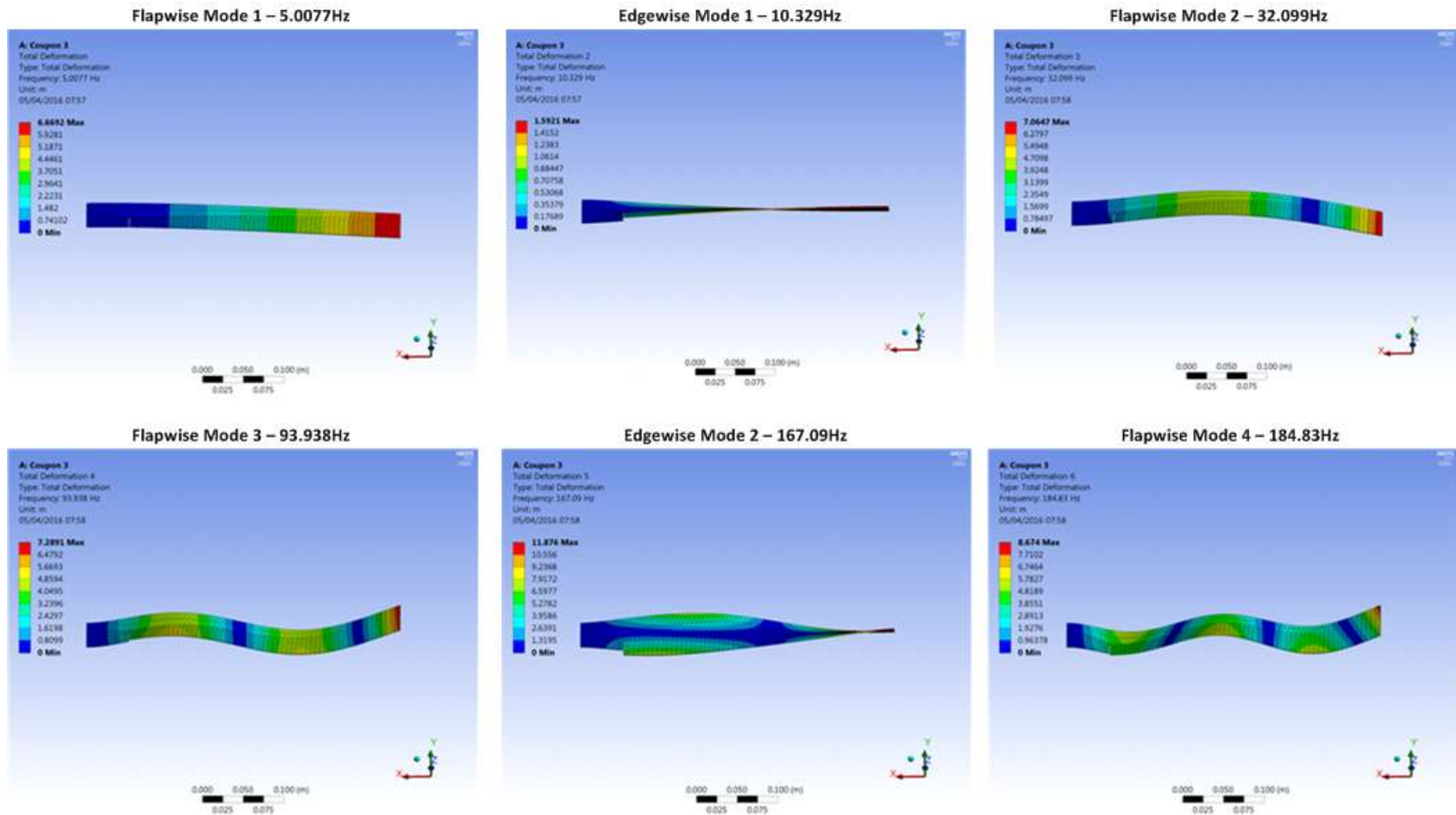
Figure 3.29 Theoretically estimated mode shapes and natural frequencies of Coupon 3 (with crack on the right side of fixed end before T1) using ANSYS.
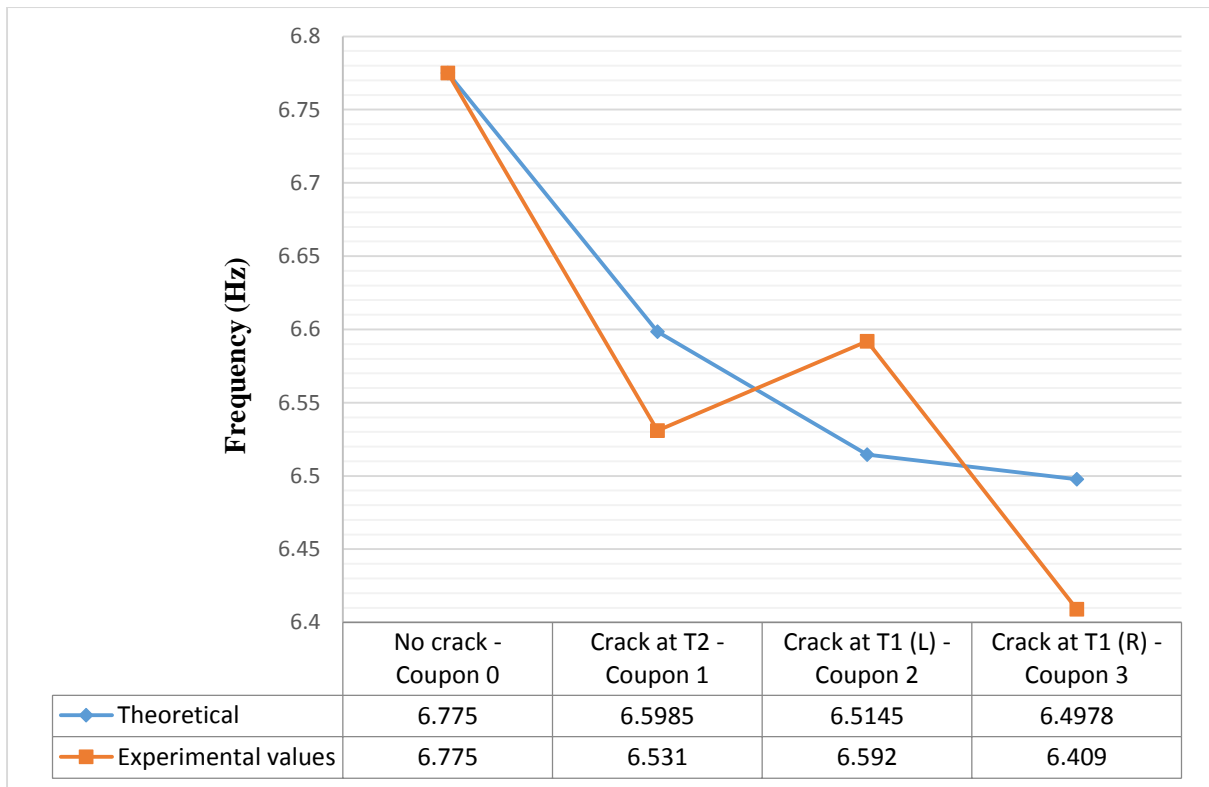
Figure 3.30 Trend plot showing the change in the <u>first</u> mode natural frequency between the four test coupons for the experimentally obtained and normalised ANSYS theoretical measurements.

	No crack - Coupon 0	Crack at T2 - Coupon 1	Crack at T1 (L) - Coupon 2	Crack at T1 (R) - Coupon 3
Theoretical	6.775	6.5985	6.5145	6.4978
Experimental values	6.775	6.531	6.592	6.409
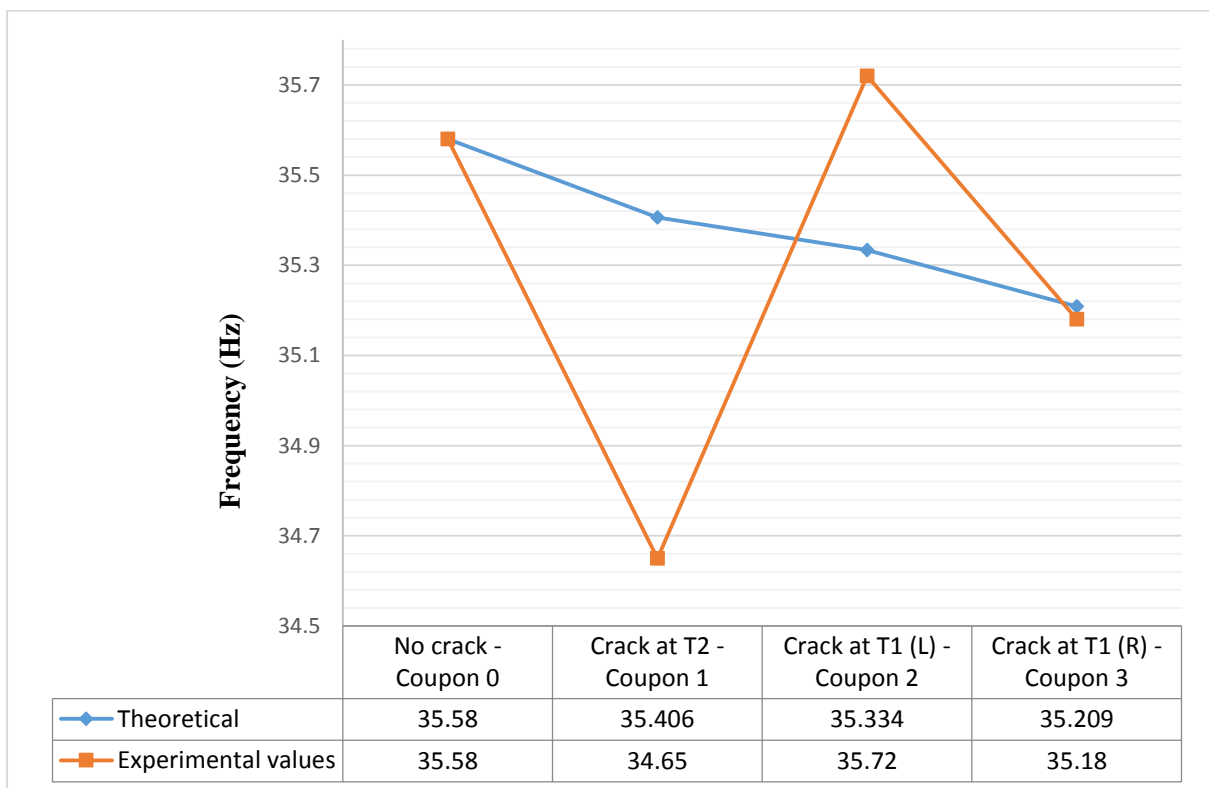
Figure 3.31 Trend plot showing the change in the <u>second</u> mode natural frequency between the four test coupons for the experimentally obtained and normalised ANSYS theoretical measurements.

	No crack - Coupon 0	Crack at T2 - Coupon 1	Crack at T1 (L) - Coupon 2	Crack at T1 (R) - Coupon 3
Theoretical	35.58	35.406	35.334	35.209
Experimental values	35.58	34.65	35.72	35.18
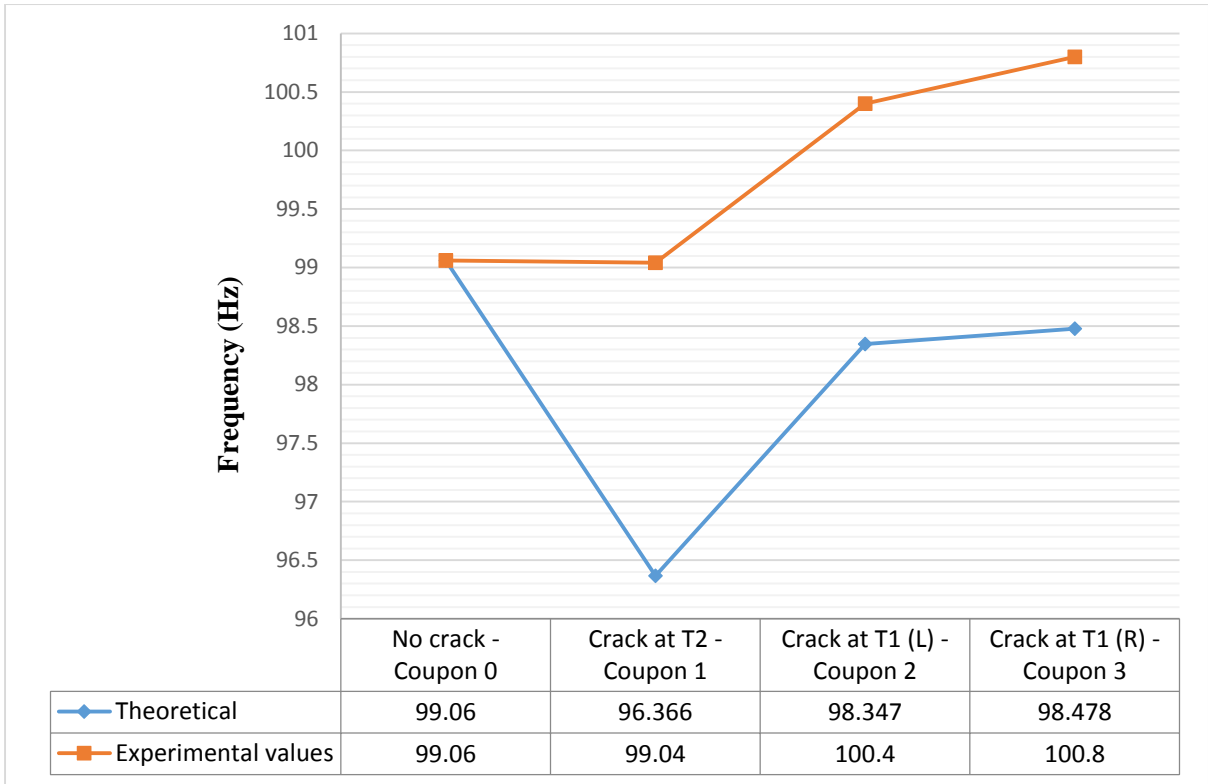
Figure 3.32 Trend plot showing the change in the <u>third</u> mode natural frequency between the four test coupons for the experimentally obtained and normalised ANSYS theoretical measurements.
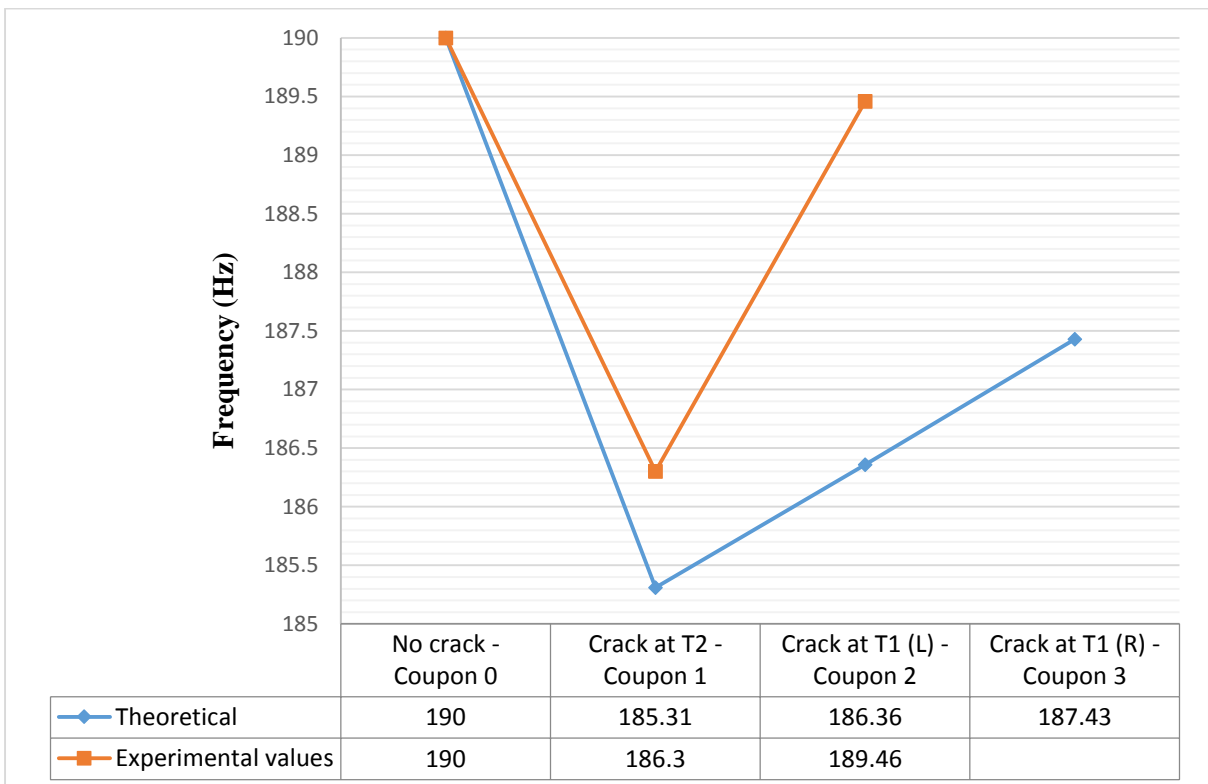
Figure 3.33 Trend plot showing the change in the <u>fourth</u> mode natural frequency between the four test coupons for the experimentally obtained and normalised ANSYS theoretical measurements.

In Figure 3.30 and Figure 3.31, Coupon 2 appears to be the outlier in the measurement trends when theoretical and experimental natural frequency trends are compared. The overall trends were decreasing first and second mode natural frequencies for the other coupons. In Figure 3.32, Coupon 1 appears to be the outlier in the observed trend of increasing natural frequencies for theoretical and experiment results. Perhaps an experiment with gradual crack successions induced, would offer more explanation for the observed trend.

Cracks cause a decrease in the natural frequency of structures up to a point and then it begins to increase. This is particularly the case for cantilevered structures such as the coupons in these experiments. The mass, stiffness and boundary conditions of the test coupons all have an effect on the mode shape and natural frequencies measured. A crack close to the fixed end of the coupon can cause a decrease or an increase in the natural frequency of the coupon depending on the mode number being considered [177]. This is proven in both the experimental and theoretical analysis of results. The introduction of a crack of the same length decreased the natural frequency from the benchmark value in modes 1 and 2 for Coupon 1. However, in Figure 3.32, at the third mode, the natural frequency begins to increase in the experimentally and theoretically obtained measurement.
These results show that damage produces a change in the dynamic behaviour of structures. There is a loss of rigidity due to a crack and the rigidity decrease due to the crack, affects in equal measure, and all bending vibration modes.

3.5 CONCLUSIONS
In the theoretical analysis, the coupon was assumed to be a continuous system i.e. a combination of masses and springs therefore, it has an infinite number of modes and each mode is associated with one mode shape. This means that the coupon will have an infinite number of mode shapes. Note that the mode shapes illustrated are for transverse vibrations. In the ANSYS theoretical analysis, no excitation force was applied to the free end of the coupons as the case was in the experimental analysis of the coupons. ANSYS performs numerical calculations and generates estimates of the modal frequency values.
In reality, compressional and torsional vibrations, as well as a combination of all three types of vibrations may be excited in structures in experimental modal analysis, which are unaccounted for in the theoretically obtained results and plots particularly in Figure 3.11 – Figure 3.15. The vibrations in structures may therefore be exceedingly complex and exact solutions to the differential equations of motion exist only for a few types of simple structures and load configurations [130]. The need for experimental analysis becomes clearer as it provides more realistic information on the structure than the theoretical approach.

The experimental analysis results obtained generally showed that vibration and modal testing are effective methods of diagnosing deviations from normal dynamic characteristics of structures. Regardless of the location of the crack/damage, the natural frequency of the coupons decreased from the benchmark values. The stiffness of the coupon is dependent on the depth of the crack as studied in the literature. The natural frequencies were therefore decreasing because the stiffness of the coupons with cracks (Coupon 1, 2 and 3) was decreasing. Generally, it is known that abnormal loss of stiffness is inferred when measured natural frequencies are substantially lower than expected. Frequencies higher than expected are indicative of supports stiffer than expected or a positive change in the centre of mass of the structure.

Vibration-based condition monitoring of structures is a well-tested and efficient method of detecting damage in structures. This method provides the options of monitoring a structure in the time, frequency or modal domain; a flexibility most other condition monitoring techniques do not provide. Theoretical modal analysis provides an appropriate validation method for experimental modal analysis. Due to assumptions made in theoretical calculations, it is not a perfect fit with experimentally measured data. However, it helps serve as a guide as illustrated in this chapter.

Measuring variations in natural frequencies was the selected vibration-based condition monitoring method applied in the following chapters in this thesis.

This study also showed the effectiveness of in-expensive piezoelectric sounders for vibration analysis. The sounders successfully measured the vibration characteristics of the coupons and suggestions on the coupon physical conditions (i.e. presence or absence of cracks) could be inferred from these measured results. However, the piezoelectric transducer's inability to detect high-order natural frequency modes efficiently was observed. The higher the frequency modes increased, the more difficult an accurate identification of modes could be made. This is because the sensitivity of the piezoelectric transducers decreases slightly with increasing frequency. In addition, many factors, including, material, mechanical and electrical construction, and the external mechanical and electrical load conditions, influence the behaviour of piezoelectric transducers. Generally, low frequency piezoelectric transducers such as the transducers used in the experiments, provide very low-level sensitivity. It is worth noting that dielectric and mechanical losses also affect the efficiency of energy conversion in these piezoelectric transducers [178], [179].

In the following chapters, Micro Electro-Mechanical Systems (MEMS) accelerometers are the introduced sensing devices, replacing the piezoelectric transducers, attempting to overcome the associated drawbacks of the sounder. Nevertheless, knowledge from the use of piezoelectric transducers/sounders in these experiments developed understanding of important issues such as in the mounting of sensing devices.

4 MICRO ELECTRO-MECHANICAL SYSTEMS ACCELEROMETERS

Advancements in embedded systems technologies have seen the introduction of Micro Electro-Mechanical Systems (MEMS) accelerometers. MEMS accelerometers are heavily employed in applications such as navigation systems in smartphones [20], [21] and airbag deployment systems in vehicles [180]–[182]. The widespread use and large scale manufacturing of these accelerometers has dramatically pushed down their cost. Like any other type of accelerometer, a MEMS accelerometer can track motion at the mounting surface of the structure it is attached to, with the added advantage that its presence on the structure does not modify the motion measured.

MEMS accelerometers typically have a built-in signal conditioning unit (in the form of an amplifier and filter), are of low-cost and very small in size. Miniaturisation of these MEMS accelerometers has reduced their cost by decreasing materials used during manufacture. It has also increased the flexibility of MEMS accelerometers as it is possible to position them in places where conventional piezoelectric sensors do not fit physically. These characteristics make MEMS accelerometers suitable for vibration-based condition monitoring of wind turbine blades and therefore, offer a cheaper alternative to the conventional piezoelectric accelerometers used [19]–[22], [142], [183]–[187].

MEMS accelerometers are classified as *piezoresistive* and *capacitive* based accelerometers.

i. **Piezoresistive MEMS:** Conventional piezoelectric accelerometers generally consist of a single-degree of freedom system of a mass suspended on a spring. In piezoresistive MEMS accelerometers, there is typically a cantilever beam with a proof mass located at the tip of the beam and a piezoresistive patch on the beam web. The schematic of a piezoresistive MEMS accelerometer is shown in Figure 4.1. The movement of the proof mass when subjected to vibration, changes the resistance of the embedded piezoresistor. The electric signal generated from the piezoresistive patch due to change in resistance is proportional to the acceleration of the vibrating object [19], [183], [188], [189].
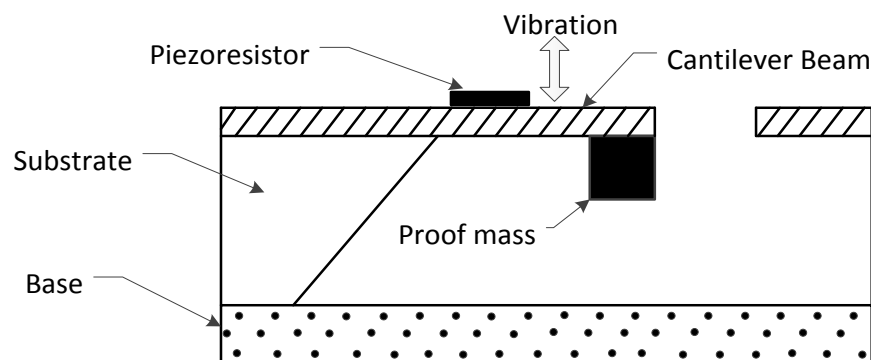
Figure 4.1 A typical MEMS piezoresistive accelerometer using cantilever design, adapted from [19].

Advantages

    a.   These accelerometers tend to have a simple interface.
    b.   Piezoresistive MEMS can survive high shock conditions.
    c.   They have a medium frequency range (~ 10 kHz).
    d.   They can measure very low frequency accelerations.

Disadvantages

    a.   Low sensitivity (10s of mV/g ~ 150mV/g).
    b.   They tend to suffer from acceleration in perpendicular directions.

c. They tend to have higher power consumption. Typically, a Wheatstone bridge is used at the front end.
   d. The resistance exhibits temperature dependence and limits high-temperature uses.
ii. **Capacitive-based MEMS:** The capacitive-based MEMS accelerometers measure acceleration based on a change in capacitance due to a moving plate or sensing element. This is the most commonly implemented MEMS accelerometer because they generally offer more sensitivity (mV/g) and higher resolution than equivalent piezoresistive accelerometers [190]. Capacitive-based MEMS was therefore chosen and used throughout in this thesis. The schematic of a capacitive MEMS accelerometer is shown in Figure 4.2 below [19], [21], [183], [188], [191].
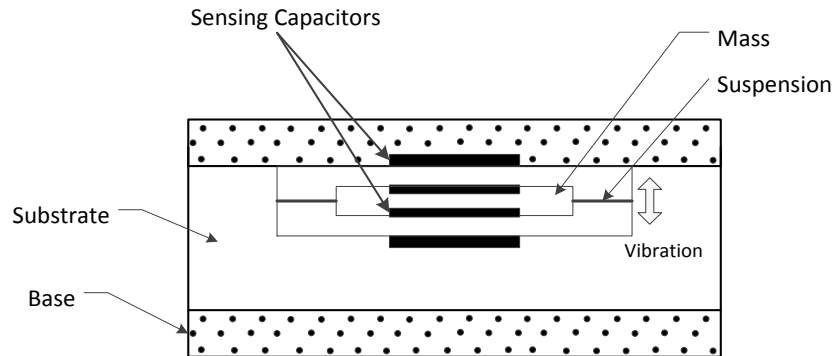
Figure 4.2 A typical capacitive-based MEMS accelerometer based on membrane design, adapted from [183].

Advantages

   a. High sensitivity (50mV/g – 90mV/g)
   b. Low temperature dependence and wide temperature range as the dielectric material is typically air.
   c. Capable of measuring very low frequency accelerations.
   d. Low power circuit interface (10s to 100s of microWatts).
   e. Most common type of MEMS due to a high performance vs cost ratio.

Disadvantage

   a. Low frequency range (natural frequency of a few kHz).

It was assumed in the present research that the lower cost MEMS devices were preferable in terms of cost and thus it was assumed that these devices would be evaluated and deployed. Nevertheless, performance results obtained by other research studies were researched and are discussed below.

Work conducted by Albarbar et al. [19], [21], [183], [192]–[198] observed differences in the vibration signals measured by the MEMS accelerometer in comparison to the conventional accelerometer, although the frequency contents in the spectrum (frequency-domain) of the measured signals were the same for both accelerometers. The difference in measured vibration signal of the MEMS accelerometer was exhibited as a significant deviation in the amplitude and phase in the spectrum when compared to the conventional Integrated Circuit Piezoelectric (ICP) accelerometer. It is, however, stated [193] that an in-depth understanding of the present design used for MEMS accelerometers can offer solutions to the above mentioned deviation problem and can also offer information useful for improving their performance either through modifications in the mechanical design or in the associated electronic circuitry of future MEMS accelerometers.

A study conducted by Badri et al. [193] which involved modelling the internal structure of a capacitive type MEMS accelerometer using finite element modelling (FEM) suggested that errors were introduced possibly in the translation of the finger movement into changes in capacitance and then into output voltage. This study also confirmed that the internal accelerometer plates (referred to as fingers) behave like a cantilever beam which can be considered as one of the major reasons for the error of deviated amplitude and phase observed in vibration measurements. The cantilever type of motion was said by Badri et al. [198] to be causing a non-parallel plates effect in the formed capacitors between the moving and fixed fingers which result in errors in the vibration measurement. Hence, design modifications to the shape of fingers were suggested to remove the cantilever motion and results were shown [193], [198] to improve measurements remarkably.

A correction method involving the development of a filter, based on the characteristic function obtained experimentally from measurements, was also proposed by [21], [194], [195], [197] to address deviations in both amplitude and phase measurements of the MEMS accelerometer in comparison to the conventional ICP accelerometers. This technique appeared to be a success in the time and frequency domains. It was therefore suggested that an appropriate filter, tuned during calibration, could be incorporated in a practical accelerometer unit for applications where reliable and practical signals are required.

Other comparisons [192] have shown that the performance of MEMS accelerometers (type ADXL105 [199]) produce the same quality of spectral vibration data as that of conventional piezoelectric accelerometers (Brüel and Kjær 4370V type [200]). Advantages such as low-cost, ability to measure dc response, better temperature stability and presence of an on-chip conditioning circuit were highlighted. Drawbacks such as the MEMS inability to be used at high temperatures, occurrence of resonance if improperly mounted and higher noise levels in comparison to piezoelectric accelerometers were mentioned.

Regardless, it was emphasised that if proper measures were taken, all these limitations can be overcome and MEMS accelerometers can be used successfully for machine and structure diagnostics. Their low-cost allows permanent placement on multiple measuring points and makes them more economical than conventional accelerometers, to extend to online monitoring, acquiring consistent, reliable accurate data as many of the errors and inconsistences of temporary mounting can be prevented. It has also been suggested [192] that more data could help improve the success of automatic fault diagnostics techniques.

4.1 MEMS ACCELEROMETER: TYPE ADXL335

The ADXL335 [201] accelerometer was the selected MEMS accelerometer type used in all subsequent experiments reported in this thesis. It is a capacitive-based surface micro-machined device with signal conditioned voltage outputs. It is a small, thin, low power device that can measure the static acceleration of gravity in tilt-sensing applications, as well as dynamic acceleration resulting from motion, shock, or vibration. The accelerometers were mounted on printed circuit boards (PCB) which measured 18 mm × 24 mm to allow wires to be connected easily, as the accelerometer package itself measured only 4 mm × 4 mm × 1.45 mm. Figure 4.3 shows the accelerometer size in comparison to a UK £1 coin and its axes of sensitivity. It is worth mentioning that the small size of the ADXL335 accelerometer is ideal for vibration monitoring as it allows for possible integration during manufacture without greatly affecting the blade design and vibration characteristics [185] and retrofitting.
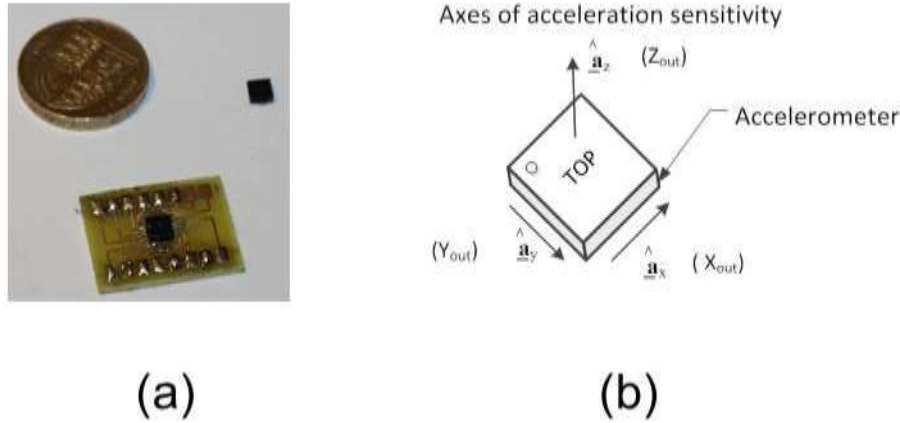
Figure 4.3 ADXL335 MEMS accelerometer

a Stand alone and PCB mounted in relation
b Axes of acceleration sensitivity

The ADXL335 measures acceleration in 3-axes with a full-scale range of ±3 g, (where $g = 9.81$ ms^{-2}) has a typical sensitivity of 300 mV/g, user selective bandwidth with a range of 0.5 Hz to 550 Hz on the Z_{out} and up to 1600 Hz on the X_{out} and Y_{out}, to suit the application using external capacitors across each of the output pins X_{out}, Y_{out} and Z_{out}; has a 150 µg/√Hz rms noise floor across X_{out} and Y_{out} and 300 µg/√Hz rms at Z_{out} and resonant frequency of 5.5 kHz. The power supply is specified at 3.6 V maximum and 1.8 V minimum [201].

The noise floor of the ADXL335 is proportional to the square root of the measurement bandwidth required. As the measurement bandwidth increases, the noise floor increases and the signal to noise ratio (SNR) of the measurement decreases [201]. Therefore, to lower the noise floor and improve the resolution of the ADXL335 accelerometer, low-pass filtering to a bandwidth of 500 Hz was implemented by soldering a 0.01 µF capacitor at each of the output pins. A 0.1 µF capacitor was also soldered at the accelerometer supply pins to decouple the accelerometer from noise on the power supply rails. 500 Hz was selected as the largest common bandwidth for the 3 axes outputs, as not all are identical.

4.1.1 NOISE SENSITIVITY
The noise sensitivity of the ADXL335 accelerometer is ratiometric with the power supply. Using information from the datasheet [201], the typical noise resolution for the accelerometer with a single-pole was calculated as follows:

$$rms\ Noise\ (X_{out}\ and\ Y_{out}) = 150 \times 10^{-6} g/\sqrt{Hz} \times \left(\sqrt{BW \times 1.6}\right)$$

$$Bandwith\ (BW) = 500\ Hz$$

$$\therefore rms\ Noise\ (X_{out} and\ Y_{out}) = 4.24\ mg$$

$$rms\ Noise\ (Z_{out}) = 300 \times 10^{-6} g/\sqrt{Hz} \times \left(\sqrt{BW \times 1.6}\right)$$

$$\therefore rms\ Noise\ (Z_{out}) = 8.49\ mg$$

4.2 APPLICATION OF MEMS ACCELEROMETERS: MICRO –TURBINES

In this section, experimental work conducted involving the application of MEMS accelerometers for measuring micro-turbine blade physical characteristics are described.

4.2.1 METHODOLOGY

Two tapered Marlec Rutland 913 Windcharger turbine blades [162], one new and the other old and damaged in-service at the tip; 335 mm long, 75 mm wide at the root end and 37 mm wide at the tip were cantilevered via screws and bolts to metal blocks, clamped to a work bench. The new blade was obtained from the turbine manufacturers and was the same model as the old blade. The old blade was in operation for over four years and failed in service indicated by extensive surface abrasion and the broken off portion illustrated in Figure 4.4.

Four ADXL335 accelerometers [201] soldered to expansion printed circuit boards to allow wires to be easily connected, were glued to each of the cantilevered blade surfaces in the locations shown in Figure 4.4. The mounting boards were made from FR4 material and measured 18 mm × 24 mm. The blades were impacted with a hammer at the tip end and measurements were simultaneously measured from the accelerometers using a high-precision 16-channel data acquisition system (DAQ), NI USB-6251 [202] and NI LabVIEW SignalExpress software [174]. The DAQ was set to read 16 kSamples of data continuously at a rate of 16 kHz for two seconds. A specific sample quantity was selected in SignalExpress rather than continuous sampling, to avoid data discontinuity error which usually occurs when the buffer is overwritten before the data is read. The DAQ is capable of measuring 1.25 MSamples per second on a single channel and 1 MSamples per second aggregate. Measured data were processed using digital signal processing techniques in MATLAB [144].
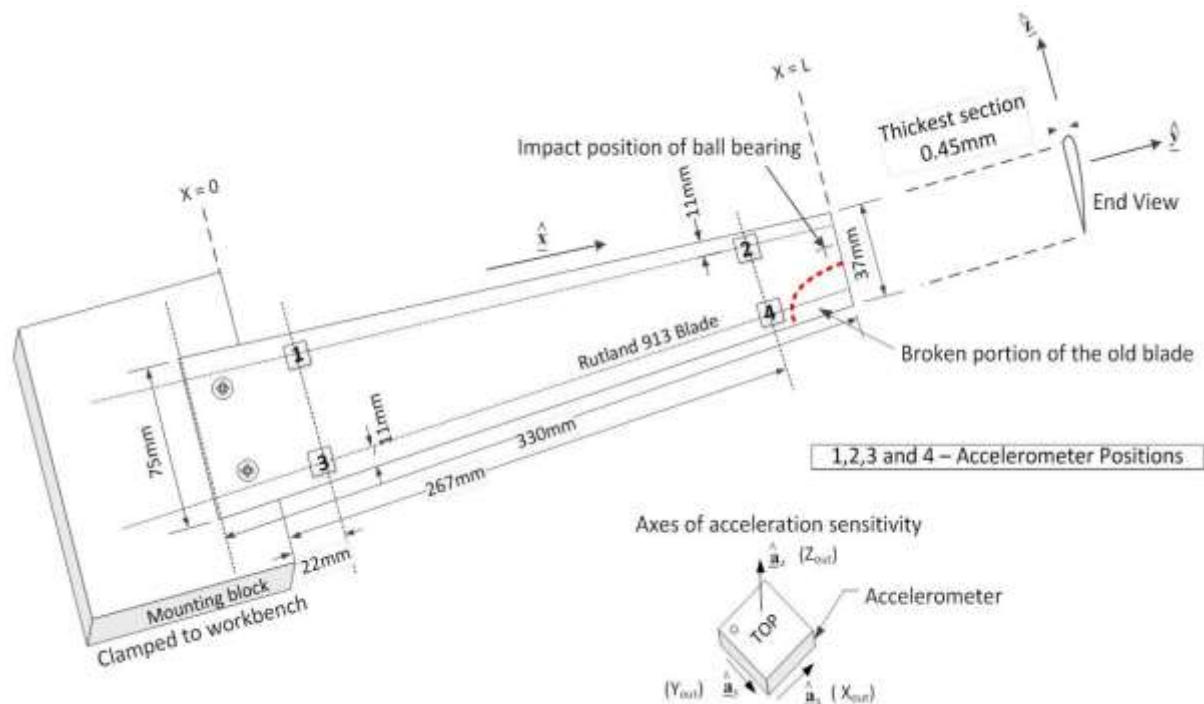
Figure 4.4 Illustration of Marlec Rutland 913 blade experimental set-up.

4.2.2 POST-PROCESSING IN MATLAB

Static measurements were recorded for each accelerometer output axis on each of the blades. These measurements are referred to, as the direct current (DC) *offset* or the *zero g bias level* of the accelerometers. Datasheets for the ADXL335 accelerometers [201] state that these accelerometers have a nominal sensitivity of 300 mV/g of applied acceleration centred on a 1.5 V offset. *Sensitivity* is a scale factor or ratio of change in signal to change in acceleration [203].

Generally, the analogue signals from these MEMS accelerometers are ratiometric to the supply voltage and vary by several hundred millivolts between axes and from device to device. Measuring the DC offset of each accelerometer is therefore crucial for improving the quality and accuracy of the measured data. Further processing of the DC measurements enabled the noise floor of each of the accelerometers to be calculated and represented graphically.

The DC offset measurements obtained from each accelerometer axis were averaged and subtracted from the output data measured during the dynamic acceleration of the blades i.e. when the blades were vibrating in response to the input excitation from the hammer. This removed the DC offset from the measured blade response on each accelerometer. It is worth mentioning that all data recorded from the accelerometers via the DAQ system were acquired as voltages. To convert the measured signal to acceleration (in terms of g), the measured data in terms of Volts (with the DC offset removed), was divided by 300 mV/g, the nominal sensitivity of the output axes of the ADXL335 accelerometer [201]. Later in this thesis a more accurate method for performing a calibration on a rotating blade will be described but for now, we assume the nominal calibration values provided by the device manufacturer. At this point in the thesis, since the main concern is the modal or natural frequency, the lack of an accurate calibration value does not invalidate the work.

The output response measured at each output axis of the accelerometers was plotted in the time domain and the resultant acceleration for each of the four accelerometers was calculated. The calculated resultant acceleration signals were windowed. Windowing reduces errors due to limited duration of the signal when computing the frequency content. A Fast Fourier Transformation (FFT) was conducted on the windowed acceleration signals and various plots of the time domain and frequency domain response were created using MATLAB [144].

Mathematically illustrating the above post-processing procedure, consider the triaxial accelerometer as shown in Figure 4.5 with perpendicular axes X, Y and Z. The vector $\textbf{\textit{R}}$ is the force vector (in g) also called the resultant, that the accelerometer measures, which could be the gravitational force (if static) or the inertial force (if moving) or a combination of both. R_x, R_y and R_z are projections of the R vector on the X, Y and Z axes (in terms of g).

Applying Pythagoras theorem in three dimensions;

$$\textbf{\textit{R}} = \sqrt[2]{R_x{}^2 + R_y{}^2 + R_z{}^2} \qquad \text{Eqn 4.1}$$

Note that the values R_x, R_y and R_z (in terms of g) are linearly related to the output values measured ($X_{measured}$, $Y_{measured}$ and $Z_{measured}$ [in Volts]) by the accelerometer at each respective axis due to dynamic acceleration. The zero-g bias level/ dc offset measured for static acceleration is given as O_x, O_y and O_z.
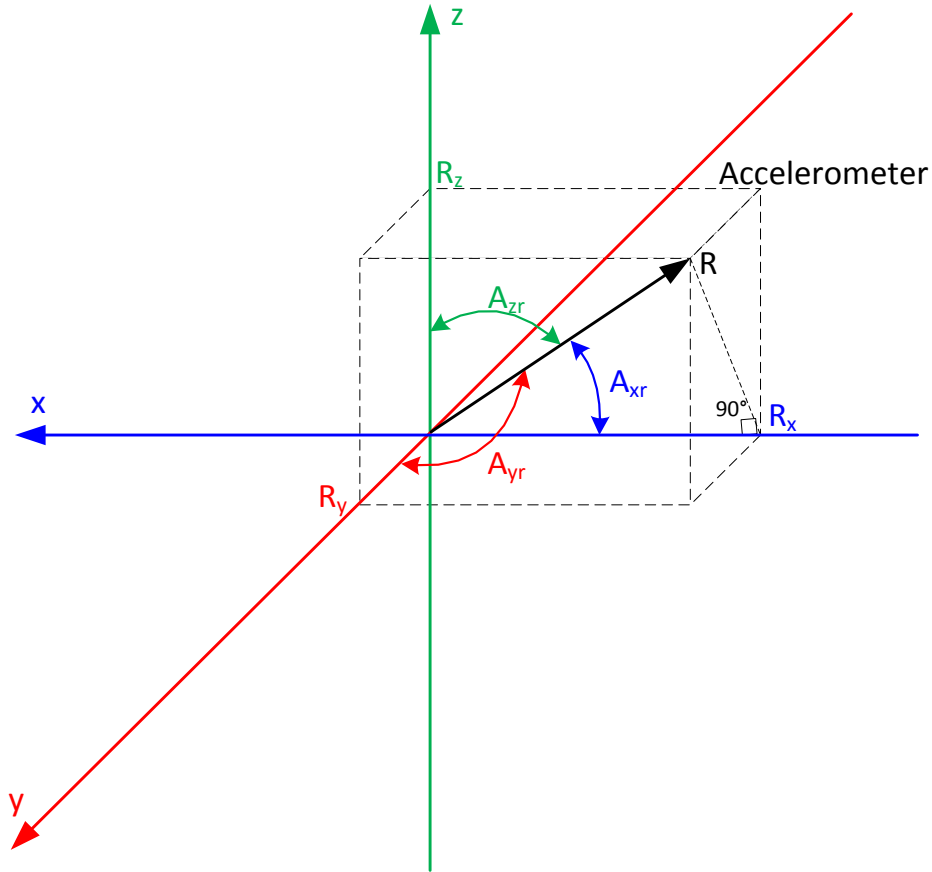
Figure 4.5 A detailed schematic describing the accelerometer axes.

Removing the dc offset from the output measurement, the voltage shift from zero-g voltage can therefore be calculated as follows;

$$\Delta R_x = \left(X_{measured} - mean(O_x)\right) Volts \qquad \text{Eqn 4.2}$$

$$\Delta R_y = \left(Y_{measured} - mean(O_y)\right) Volts \qquad \text{Eqn 4.3}$$

$$\Delta R_z = \left(Z_{measured} - mean(O_z)\right) Volts \qquad \text{Eqn 4.4}$$

Equations 4.2 – 4.4 give the actual accelerometer readings for each axis in terms of Volts. It is still not in terms of g – acceleration due to gravity ($g = 9.81\ ms^{-2}$). To convert to g, the accelerometer sensitivity value was applied, using the nominal value 300 mV/g provided in the ADXL335 datasheet [201]. This simply means that the measured analogue output voltage of the accelerometer will change by 0.3 Volts per 9.81 ms⁻² of acceleration in an ideal scenario.

$$R_x = \left(\frac{\Delta R_x}{0.3}\right) g \qquad \text{Eqn 4.5}$$

$$R_y = \left(\frac{\Delta R_y}{0.3}\right) g \qquad \text{Eqn 4.6}$$

$$R_z = \left(\frac{\Delta R_z}{0.3}\right) g \qquad \text{Eqn 4.7}$$

Equaions 4.5 - 4.7 give the three components of the inertial force vector **R**, and if the accelerometers are static, it can be assumed that this is the direction of the gravitation force vector. The inclination of the accelerometers positioned on the blades, relative to ground can also be derived by calculating the angle A_{zr}, between the resultant **R** and *Z-axis* of the accelerometers. Similarly, the per-axis directions of inclination A_{xr} and A_{yr} can be calculated for the *X* and *Y* axis respectively as shown in Figure 4.5 and illustrated in Equations 4.8 – 4.10 below [204]–[206].

$$\cos(A_{xr}) = \frac{R_x}{R} \qquad \text{Eqn 4.8}$$

$$\cos(A_{yr}) = \frac{R_y}{R} \qquad \text{Eqn 4.9}$$

$$\cos(A_{zr}) = \frac{R_z}{R} \qquad \text{Eqn 4.10}$$

In the modal test experiments conducted, the above angles of inclination were not required for interpreting the output response from the accelerometers and were therefore not calculated.

4.2.3 RESULTS AND DISCUSSIONS

Figure 4.6 and Figure 4.7 show the time domain responses measured from each accelerometer on the new (healthy) and old (damaged) blades respectively.

Figure 4.6 and Figure 4.7 showed that maximum and sustained acceleration was measured at the free end of the blades (measured by accelerometer 2 and 4). This is because the blades were allowed to vibrate freely at the tip with limited restriction. In addition, the profiles of the blades at the tip were more flexible and thinner than at the root end. Therefore, the accelerometers measured easily, the oscillation of the blades in response to the transient excitation forces. Accelerometer 2 on the old blade measured structural ringing excited by the hammer impact. This is indicated by the slightly lower signal-noise ratio (SNR) measured at this position of the old blade, in comparison to the same position on the new blade. The broken-off section on the old blade meant that the impact excitation distribution pattern was different from the new blade.

Accelerometer 1 and 3 were positioned at the root (fixed) end of the blades where the blades are thicker and stiffer. Therefore, little dynamic acceleration was measured at these points. The signals measured were low and the SNR was worse. This prompted an investigation into the noise floor of the MEMS accelerometers used.

Figure 4.8 and Figure 4.9 show the resultant acceleration frequency spectrum of the new and old blades respectively. It also shows the noise floor of each accelerometer. It was observed that for accelerometers 1 and 3, the measured signals were very close to the noise floor, making it difficult to distinguish modal frequencies. However, for accelerometer 2 and 4, the measured resultant acceleration signal was more visible above the noise floor. The deflections measured at accelerometer 4 were used to normalise all measurements for each of the accelerometers on both blades because it measured the maximum acceleration. This scales the measurements and enables magnitude comparisons to be made.
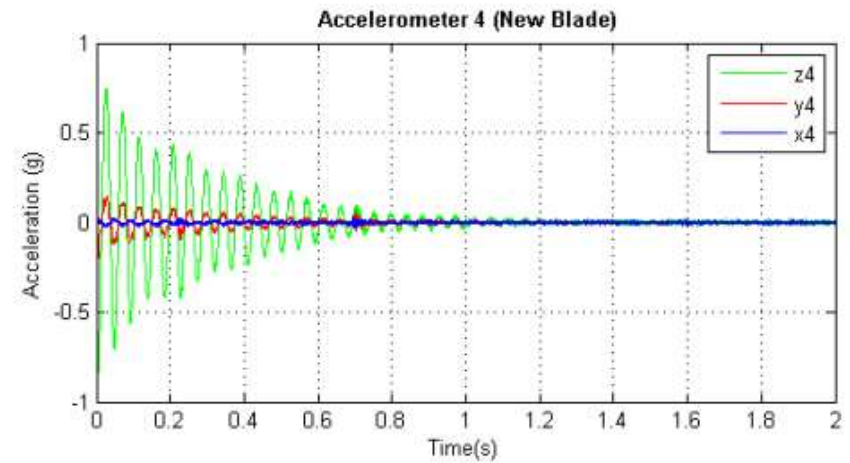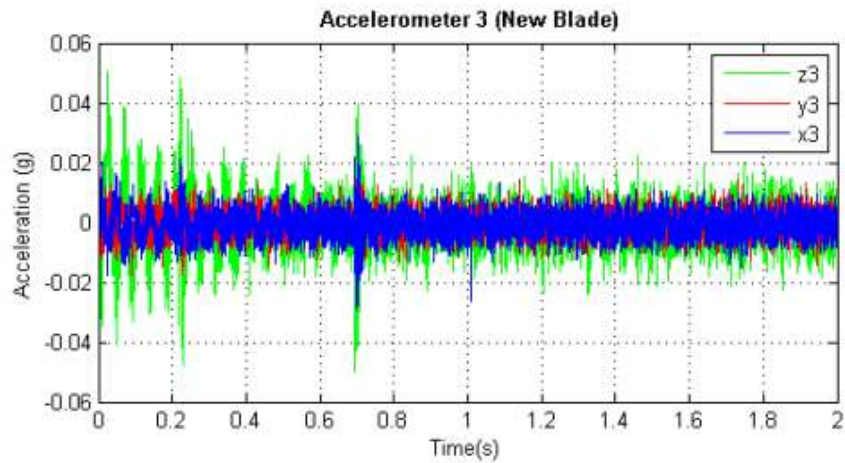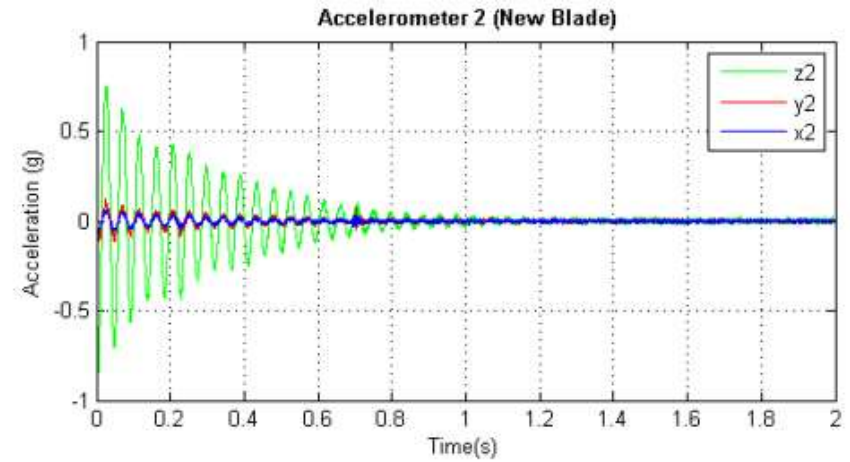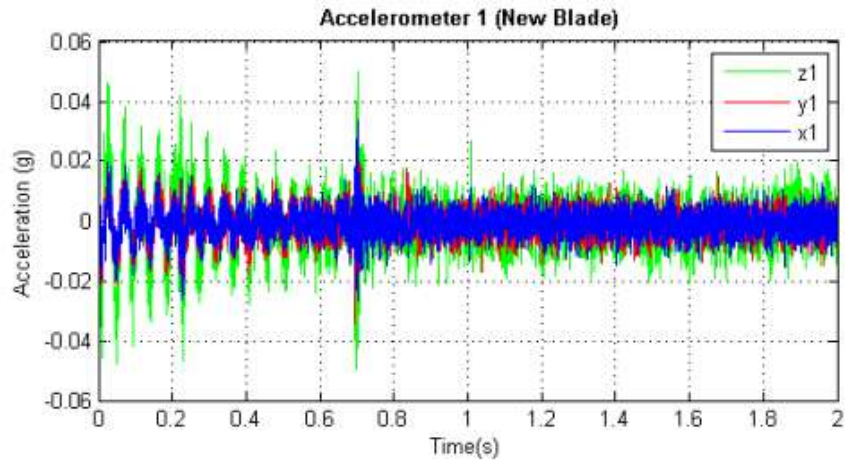
Figure 4.6 Time domain response showing the X_{out}, Y_{out} and Z_{out} from each accelerometer placed on the new (healthy) blade for two seconds of data read at a rate of 16 kSamples per second in response to a transient input excitation from a hammer at the blade tip. Accelerometer 1 and 3 at root end. Accelerometer 2 and 4 at free end.

74
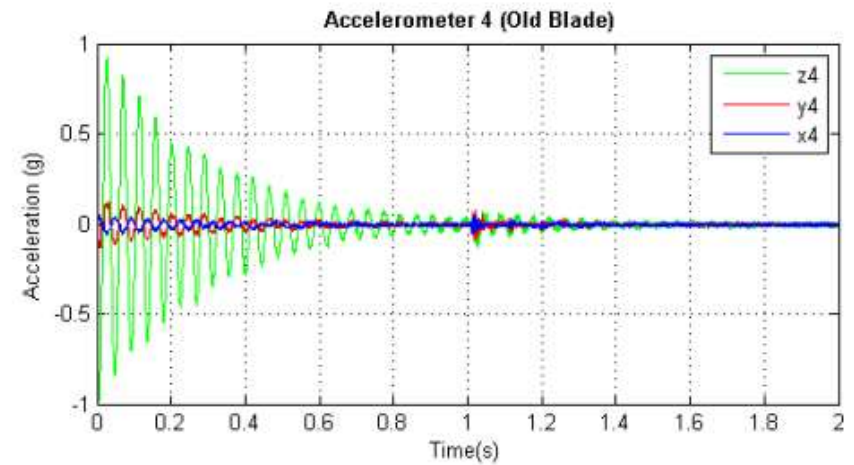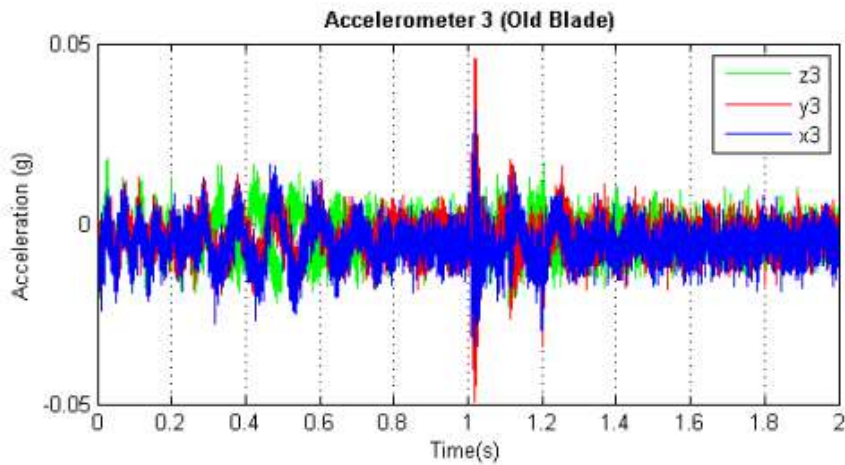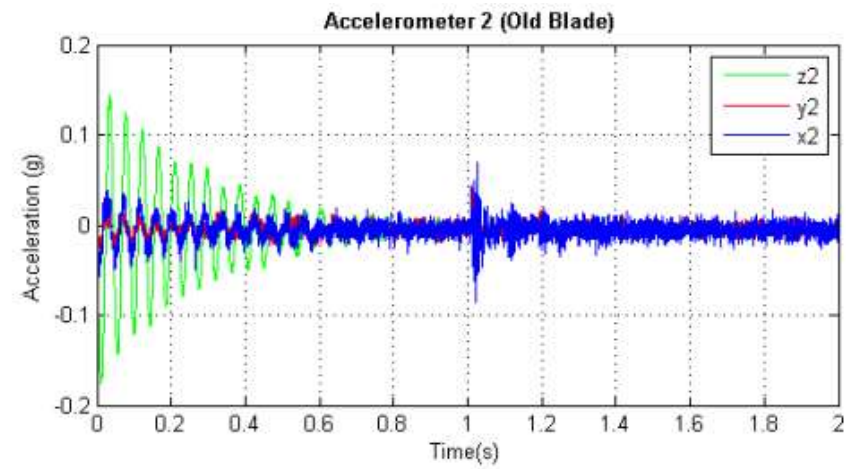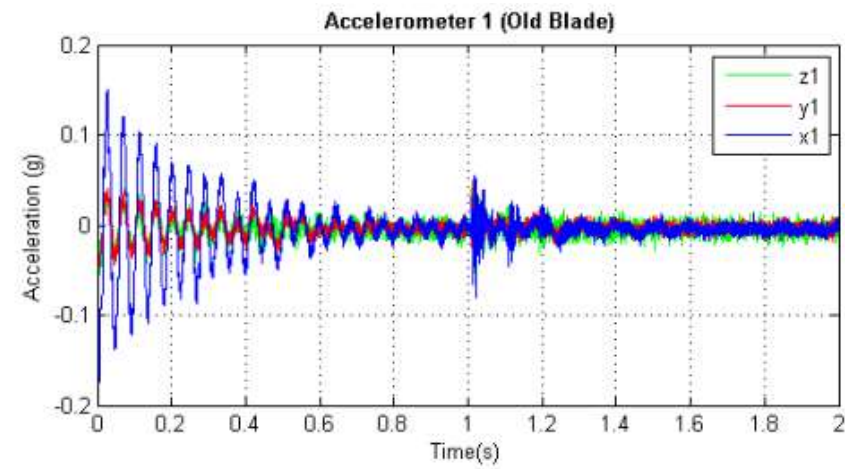
Figure 4.7 Time domain response showing the X_{out}, Y_{out} and Z_{out} from each accelerometer placed on the old, damaged blade for two seconds of data read at a rate of 16 kSamples per second in response to a transient input excitation from a hammer at the blade tip. Accelerometer 1 and 3 at root end. Accelerometer 2 and 4 at free end.
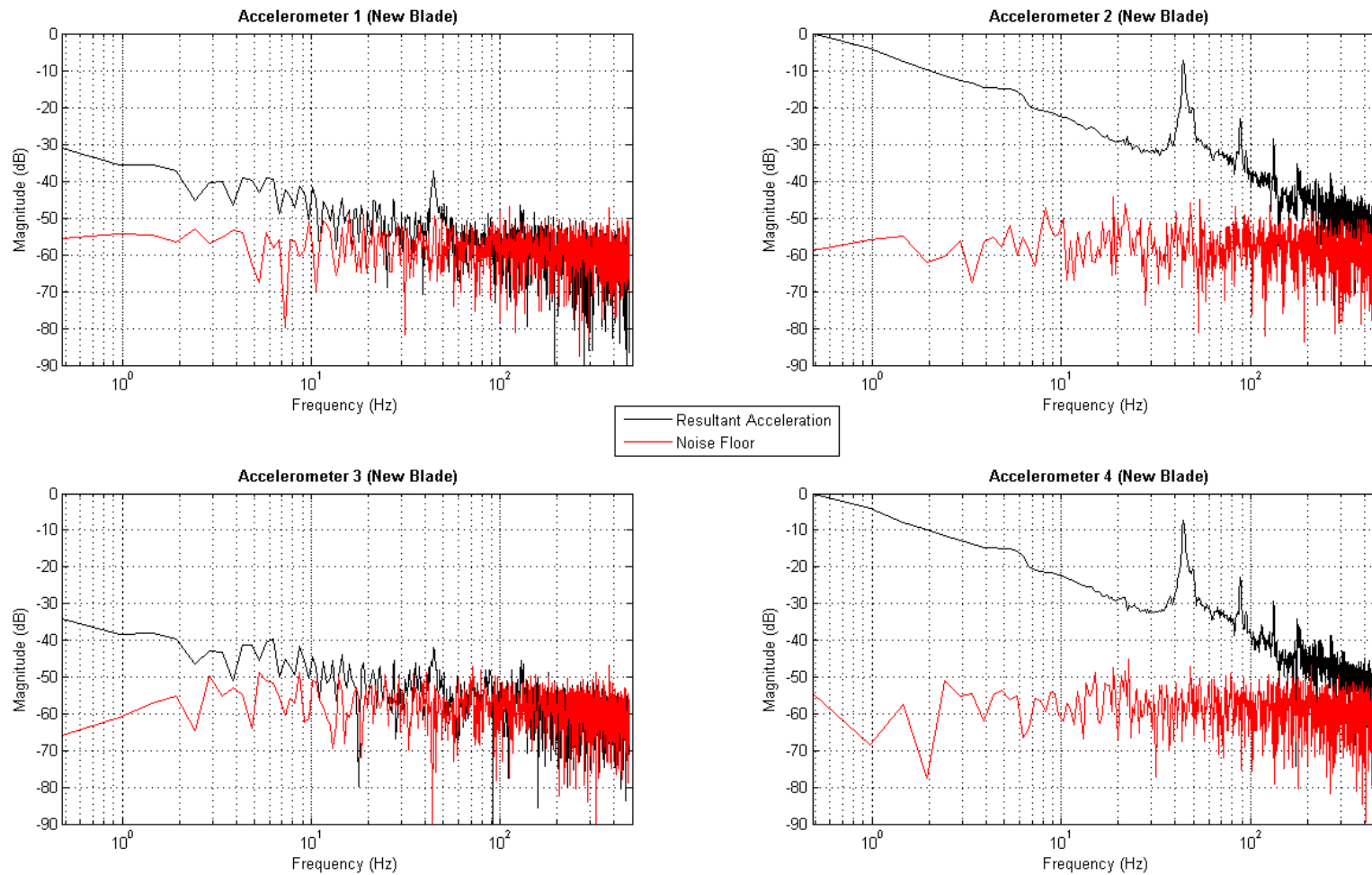
Figure 4.8 Frequency spectra showing the resultant acceleration and noise measurements for each accelerometer position on new blade in response to a transient input excitation from a hammer at the blade tip for two seconds of data read at a rate of 16 kSamples per second, magnitude (dB) relative to the maximum tip deflection at accelerometer 4.
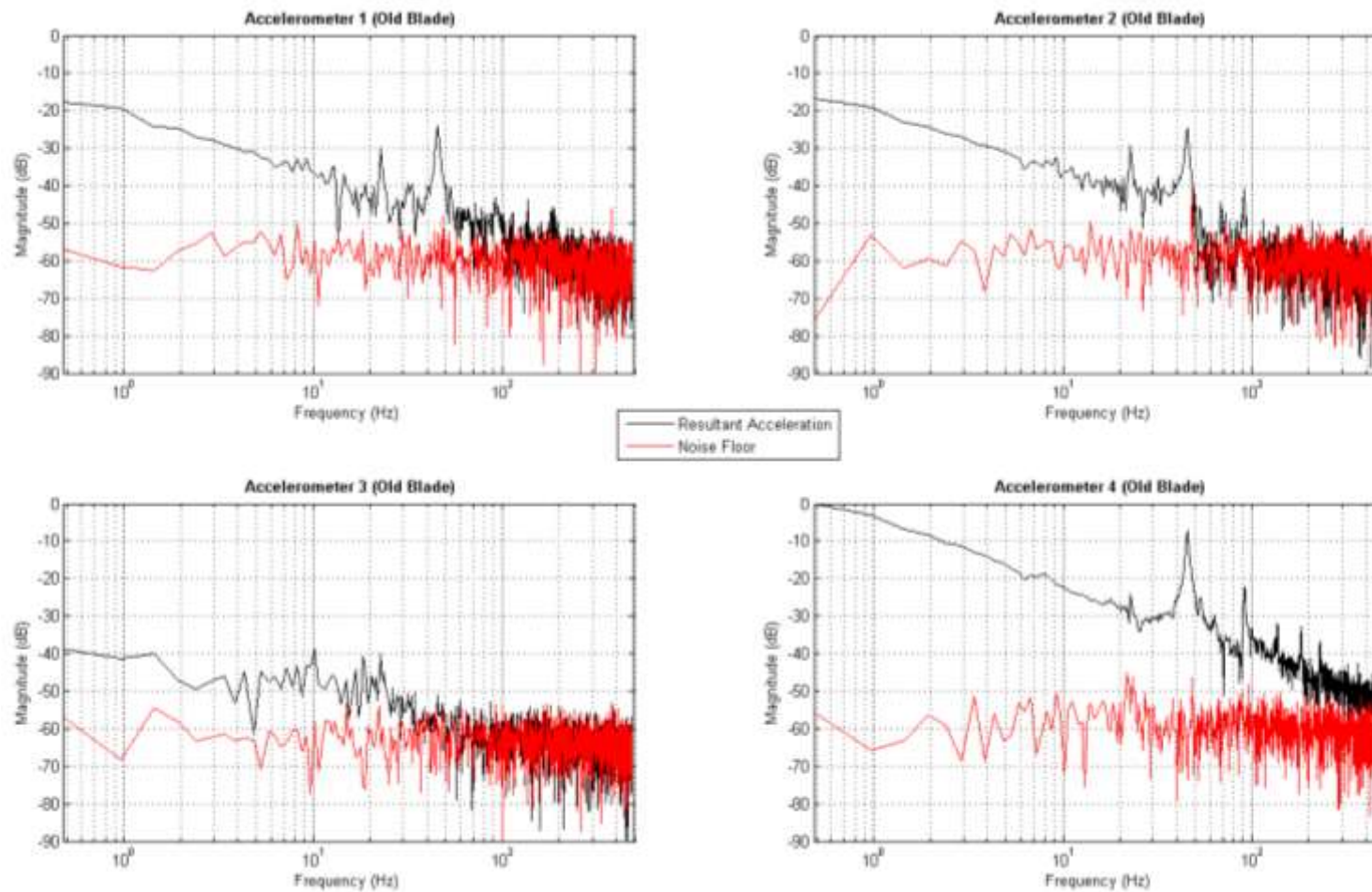
Figure 4.9 Frequency spectra showing the resultant acceleration and noise measurements for each accelerometer position on the old/healthy blade in response to a transient input excitation from a hammer at the blade tip for two seconds of data read at a rate of 16 kSamples per second, magnitude (dB) relative to the maximum tip deflection at accelerometer.
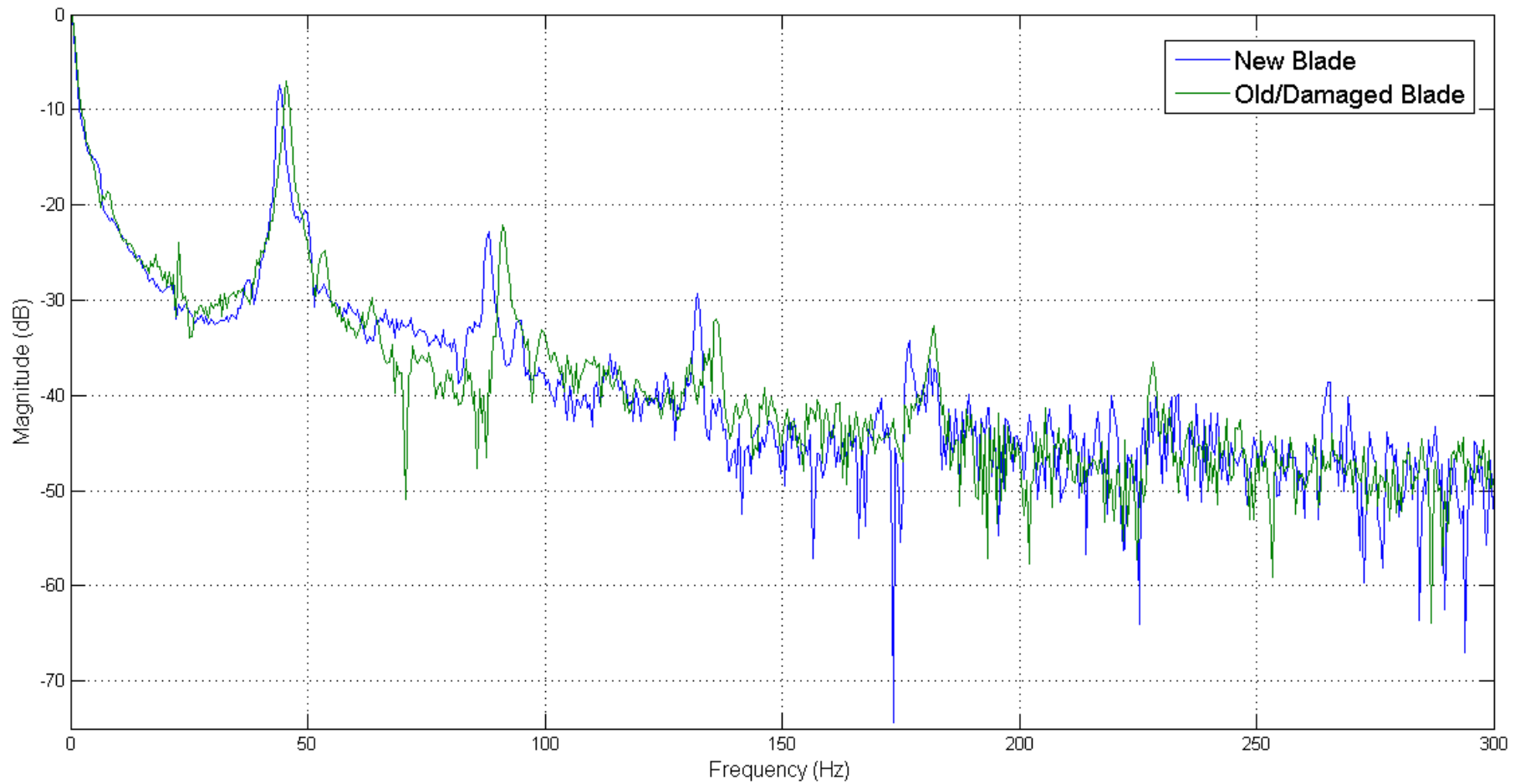
Figure 4.10 Frequency spectrum showing the response at accelerometer position 4 for the new and old/damaged blades for two seconds of data read at a rate of 16 kSamples per second, magnitude (dB) relative to the maximum tip deflection at accelerometer 4 for each of the blades in response to a transient input excitation from a hammer at the blade tip.

Figure 4.10 shows the combined frequency spectrums of the new and old/damaged blades measured at accelerometer 4. Table 4.1 summaries the results for easier comparison.

Table 4.1 Modal frequencies of the new and old/damaged blades.

Mode	Frequency (Hz)		Difference (%)
	New Blade	Old/Damaged Blade	
1st	21.80	22.77	+4.35
2nd	44.08	45.53	+3.24
3rd	88.16	91.07	+1.62
4th	132.20	136.10	+2.91
5th	176.80	182.10	+2.95

Results obtained showed that the old/damaged blade measured higher natural frequencies than the new blade. Analysing the results, the difference in the structural health between both blades was assumed to be the major cause of the measured difference in natural frequencies and potential reasons for these changes are suggested. The natural frequencies of mechanical structures are typically influenced by two main factors: the mass and the stiffness of the structure. A lower mass and/or a stiffer structure increase the natural frequency while a higher mass and/or lower stiffness structure decreases the natural frequency. The weights of the blades were therefore measured using a high precision scale. There was a 0.5% difference in mass between the two blades; the new blade measured 179.5 g and the old/damaged blade measured 178.6 g, consistent with possibly material loss (mass measurements included the glued accelerometers and cables on each of the blades).
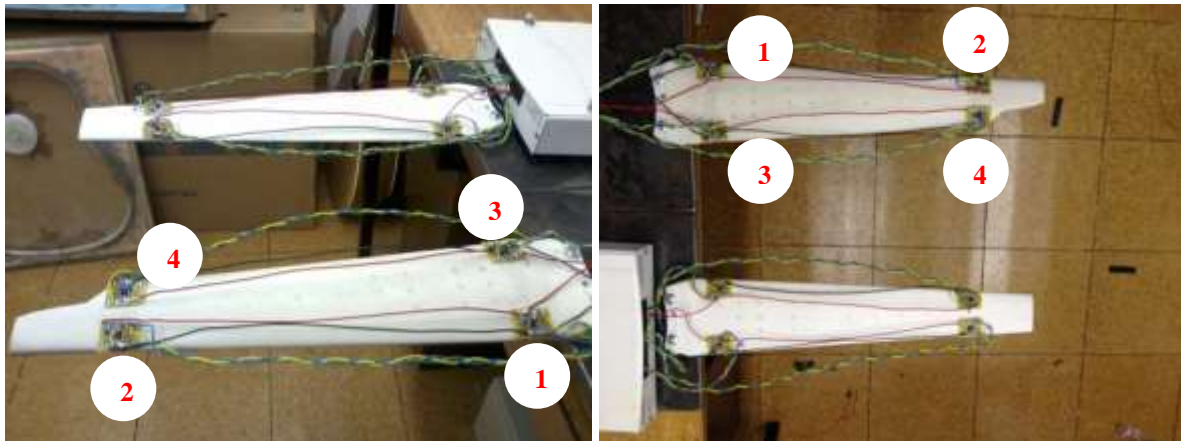
Figure 4.11 Photographs from side and top views, showing the new and old/damaged blades positioned side by side. Note the broken off-section of the old/damaged blade (bottom of the both pictures).

The broken off blade section on the old/damaged blade can be seen in Figure 4.11. A low mass coupled with a shortened length shifts the centre of mass (COM) of the blade towards the root end and mounting block firmly clamped to a workbench, resulting in higher natural frequency measurements in comparison to the new blade. These deductions are supported by various studies summarised in [156], conducted to describe the effects of structural damage on natural frequencies. Frequencies higher than expected are indicative of supports stiffer than expected [207]. To explain these observations, theoretical analysis of the effect of a shift in the centre of mass was explored.

The centre of mass of a structure is a unique location in space that is the average position of the structure's mass. If the distribution of mass along the length of the structure changes, the centre of mass changes [208], [209]. In Figure 4.12, a uniformly tapered blade is considered, to illustrate the shift in the COM due to a circular cut-out section. The tapered blade is symmetric and its mass is

distributed uniformly throughout its volume. Logically, the COM of the intact blade (minus the cut-out), must be at its geometric centre, O.
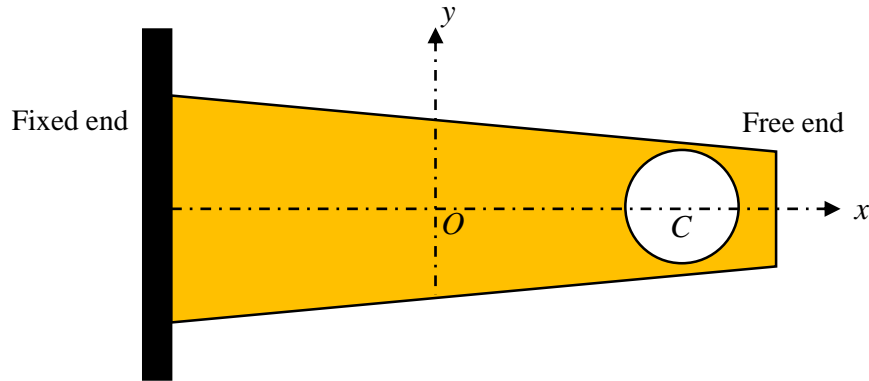
Figure 4.12 A uniformly tapered blade with a circular cut-out to illustrate the shift in the centre of mass (COM).

For continuous systems such as in Figure 4.12, the position of the centre of mass $\boldsymbol{R_{cm}}$ is calculated as [208], [209]:

$$\boldsymbol{R_{cm}} = \frac{\int \boldsymbol{r} dm}{\int dm} = \frac{\int \boldsymbol{r} dm}{M} \qquad \text{Eqn 4.11}$$

Where $\boldsymbol{r}$ is the position vector of each individual mass that makes up the structure and M is the total mass of the structure. Knowing the mass distribution in volume of the structure, each component of the position vector can be obtained as:

$$X_{cm} = \frac{\int x \, dm}{M}, Y_{cm} = \frac{\int y \, dm}{M}, Z_{cm} = \frac{\int z \, dm}{M} \qquad \text{Eqn 4.12}$$

In Figure 4.12, using an *xy*-coordinate system with its origin O at the geometric centre of the blade and the *x*-axis passing through the centre of the cut-out, the new centre of mass must lie somewhere on the *x*-axis since the blade and the cut-out are symmetric about the *x*-axis. Thus, $y_{cm} = 0$. Let m_1 be the mass of the blade with the hole, and m_2 be the mass of the circular cut-out ($m_1 + m_2 = M_{tot}$). M_{tot} is the total mass of the intact blade. The centre of mass of the circular cut-out is at the centre of the circle C. It follows that at the origin of the intact plate:

$$m_1 x_{cm} + m_2 x_C = M_{tot} x_O \equiv 0 \qquad \text{Eqn 4.13}$$

$$\Rightarrow x_{cm} = -\frac{m_2}{m_1} x_C \qquad \text{Eqn 4.14}$$

The centre of mass of the blade has shifted to the left of its origin O towards the fixed end (indicated by the negative sign in Eqn 4.14), by a distance proportional to the ratio of the mass of the cut-out to the mass of the blade. It therefore follows that if the cut-out was below the *x*-axis e.g. at the edge of the free end of the blade, as in Figure 4.11, the centre of mass will shit upwards along the *y*-axis towards the leading edge, and leftwards along the *x*-axis towards the fixed end. Time domain measurements by accelerometer 1 for both blades on the old/damage blade in Figure 4.7 support this theory. Although both blades are generally stiffer at the root end, comparing measurements from accelerometer 1 shows that for the old blade, more vibrations were measured. This indicates movement along the *y*-axis due to a shift in centre of mass.

The mass of the blade in Figure 4.12 decreases by m_2 from M_{tot} to m_1. A follow on effect is the increase in natural frequency because, the square of the natural frequency of any structure, is inversely proportional to its mass as explained in Chapter 3. Therefore, the exact difference a change in mass will shift the natural frequency of the structure by, depends on the position of centre of mass and the stiffness of the structure.

The global mass variation between the two blades was under 1% and the measured maximum percentage difference in modal frequency between the two blades was 4.35% at the first mode. This difference in natural frequency was not constant and decreased for the second and third modes and increased from the third to fifth mode as summarised in Table 4.1.

Although study [210] suggests that it is necessary for the global natural frequencies of a structure to change by about 5% for damage to be detected with confidence, significant changes of up to 5% alone do not automatically imply the existence of damage. Similarly, natural frequency changes less than 5% cannot be disregarded, as changes in modal parameters measured, depend on the nature, location and severity of the damage [156] which may not affect the global parameters of the structure. However, they can be reflected in localised measurements. Accelerometer 4 from which the natural frequency measurements were extracted from was the accelerometer positioned closest to the damage on the old blade. Perhaps this contributed to the clarity in measuring variations between the two blades.

In reality, it is not definitive that the increasing natural frequencies are the results of differences in the structural health of the blades. Natural variations that can occur during the manufacture of both blades could be a potential reason for the results. Although both blades were obtained from the same turbine and were manufactured using the same processes, differences in the structural composition and orientation occur which differentiate structures and can be reflected in the modal properties. In addition, there was no way of ascertaining that natural variations caused the results as no pre-damage results we measured for the old blade for comparison. These results however showed that changes in modal frequencies are valid indicators for measuring variation in structural characteristics and the MEMs accelerometers have the capability of measuring these changes.

Results from this experiment led to further investigations into the measurement of spectral variations of the old/damaged Marlec 913 Windcharger blade using MEMS accelerometers. The experiments are discussed in the following section.

4.3 SPECTRAL ANALYSIS OF CRACKS IN MARLEC 913 WINDCHARGER BLADE

In this section, only the old/damaged blade is considered. Further damage was deliberately inflicted on the blade and measurements were recorded and compared to investigate further:

i.   The effects of the damage on the natural frequency of the blade.
ii. The accuracy with which the MEMS accelerometers detect these natural frequencies.

4.3.1 METHODOLOGY

A Visaton Ex 45 S electrodynamic exciter [211] was introduced to replace the impact hammer used in the previous section, to control the amplitude and frequency of the input excitation signal across all measurements. The exciter can be thought of as a loudspeaker without a membrane. It consists of an oscillating mass, two contact pins for connecting to the amplifier, and the mounting plate to hook up to the surface of the blade as shown in Figure 4.13. By applying a signal to the contact pins, the oscillating mass starts shaking with the frequency of the applied signal and this oscillation is transmitted to the mounting plate and from there, on to the surface of the blade.
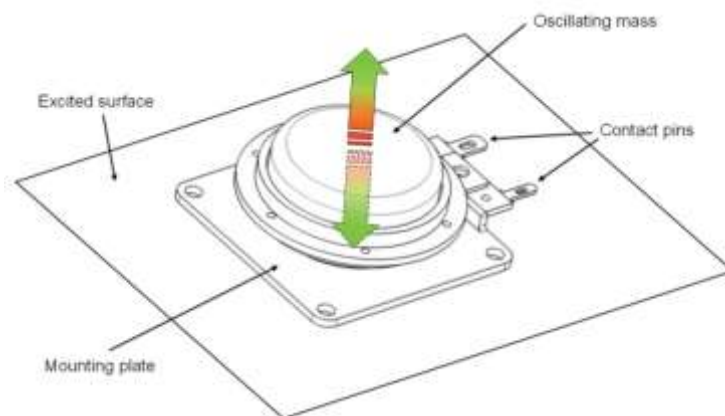
Figure 4.13 The Visaton electrodynamic exciter with a diameter of 45 mm and weight of 0.06 kg from [211].

The exciter was attached firmly, close to the fixed end of the blade. This was the only position that could accommodate the size of the exciter on the blade. A 1V chirp input excitation signal with frequency range 0 - 300 Hz was exerted on the blade using the exciter. This frequency range was selected based on previous experimental results obtained in Section 4.2. The input excitation signal was generated in MATLAB and fed through an analogue output channel on the NI USB-6251 DAQ to an audio power amplifier [212] connected to the two contact pins of the exciter. The chirp input excitation signal propagates towards the free end of the cantilevered blade where it is reflected back towards the exciter. The original signal from the exciter interferes with the reflected waves from the free end of the blades, resulting in a mixture of signals in the output response. The output response is measured by the ADXL335 accelerometers and is strongly dependent on the characteristics of the excited blade [172], [213]–[216].

The resonance of the exciter was measured experimentally prior to its application in these series of tests, as this information was not provided in the data sheet. An ADXL335 accelerometer was fixed to the oscillating mass of the exciter and the transfer function relationship between the two systems was measured. The contact pins of the exciter were connected to a function generator, set to output a 20.6 Vp-p sine wave. The frequency of the sine wave was varied and the output voltage from the exciter and ADXL335 accelerometer attached to the exciter was measured using an oscilloscope. The resonance of the exciter was measured at 90 Hz as shown in Figure 4.14. The purpose of measuring the resonance and establishing a relationship between the exciter and accelerometer was to aid

interpretation of frequency spectrum results measured for the blade and to confidently eliminate frequency contributions from the exciter in final results for improved accuracy.
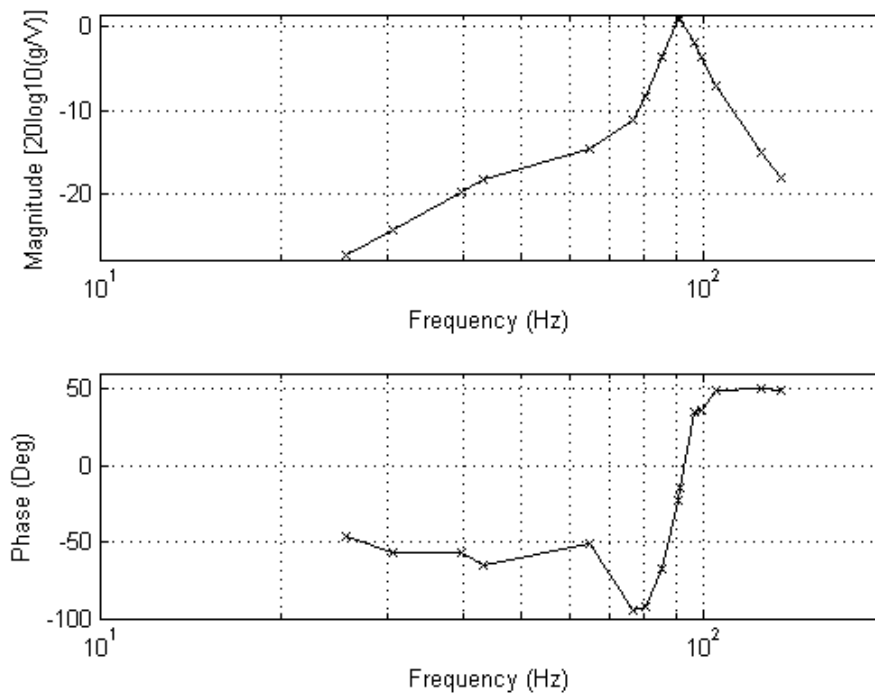
Figure 4.14 Bode plot showing the relationship between the Visaton Ex 45 S exciter and ADXL335 accelerometer. The resonance of the exciter was measured at 90 Hz.

Progressive transverse cracks were induced on the old/damaged blade using a hacksaw along the trailing edge partially mid-way between accelerometer 3 and 4 as shown in Figure 4.15. The cracks were increased from 10 mm to 40 mm with 10 mm intervals.
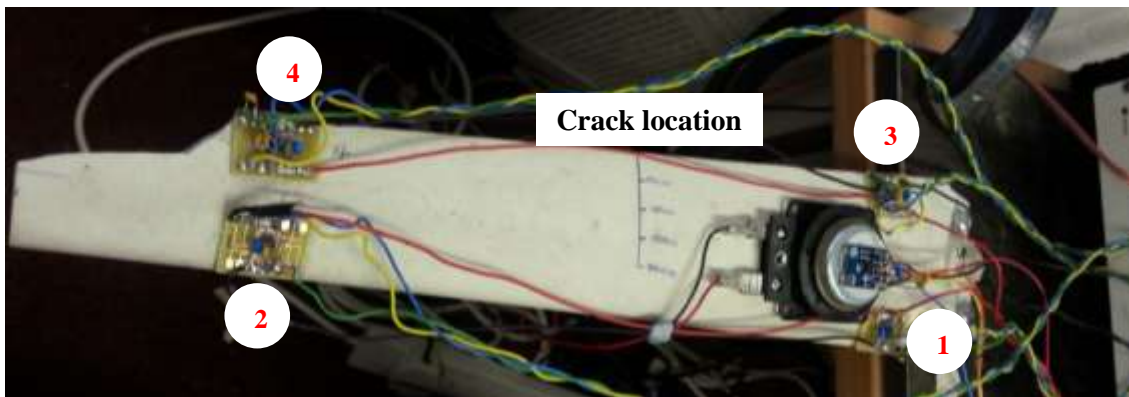
Figure 4.15 Picture showing the old/damaged blade with a broken-off section, clamped at the fixed end. The transverse crack position and the exciter position are also visible. Note the additional accelerometer (referred to as the reference accelerometer) positioned on top of the exciter and the change in exciter impact position from the tip to near the root end of the blade to accommodate the physical size of the exciter.

The input excitation and the responses of the blade at each crack length induced were logged simultaneously for 48 kSamples of data read at a rate of 16 kHz for a period of three seconds using the DAQ. Measurements were analysed in MATLAB where band-pass filtering, windowing (Hanning) and smoothing were applied to the measured signals and the frequency response function relationship between the input and output signals were deduced.

4.3.2 RESULTS AND DISCUSSIONS

Figure 4.16 shows the 1V linear chirp input excitation signal exerted on the blade from the Visaton Ex 45 S exciter. The response of the exciter was measured at its contact pins and via the ADXL335 accelerometer fixed to its oscillating mass.
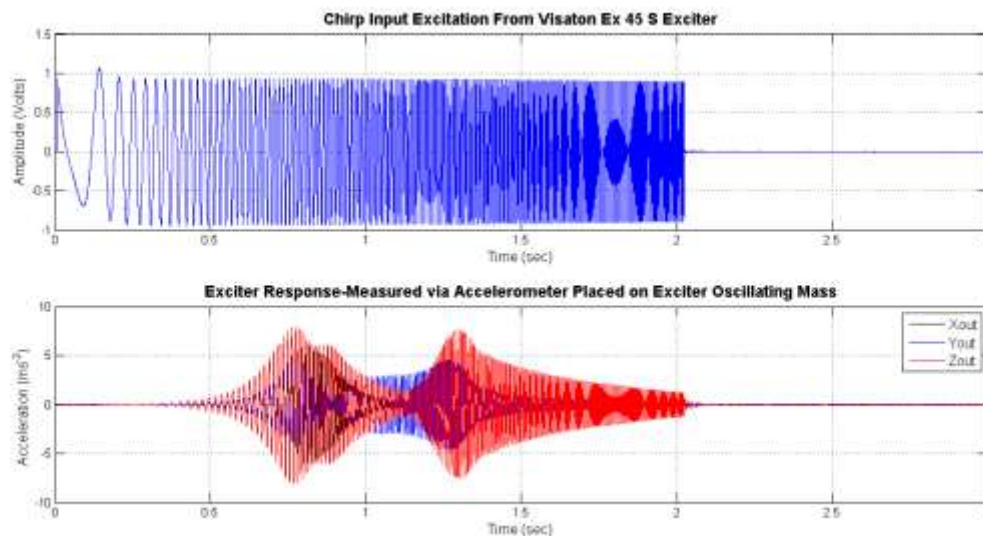
Figure 4.16 Time domain plot showing the input chirp excitation signal from the Visaton Ex 45 S electrodynamic exciter measured at the contact pins (in Volts) and at the accelerometer (in ms^{-2}) for three seconds of data read at a rate of 16 kSamples per second.

The measured response by the accelerometer in Figure 4.16 was used to normalise the output response of the other accelerometers positioned on the blade for each progressing crack. This removed frequency components introduced by the exciter from the spectra, leaving behind the frequency characteristics of the blade for comparisons.

Figure 4.17 shows the measured frequency spectrum at each accelerometer position on the blade for the baseline (without any induced crack) and the crack lengths for the frequency range 0 – 300 Hz. The spectra were different from those measured in the previous section because a continuous input signal was used and the exciter added mass to the blade. In addition, it was observed that frequency components below 50 Hz were attenuated across all accelerometer measurements. This was investigated and it was discovered to be a feature of the audio amplifier used in the experiments. The amplifier induced high-pass filtering on the input signal to the blade and subsequently on the measured response. Nevertheless, as all measurements were recorded under these conditions, this did not affect comparisons of the results. The plots were zoomed in at each of the peaks and the frequency and amplitude measurements were recorded and used to establish trends.
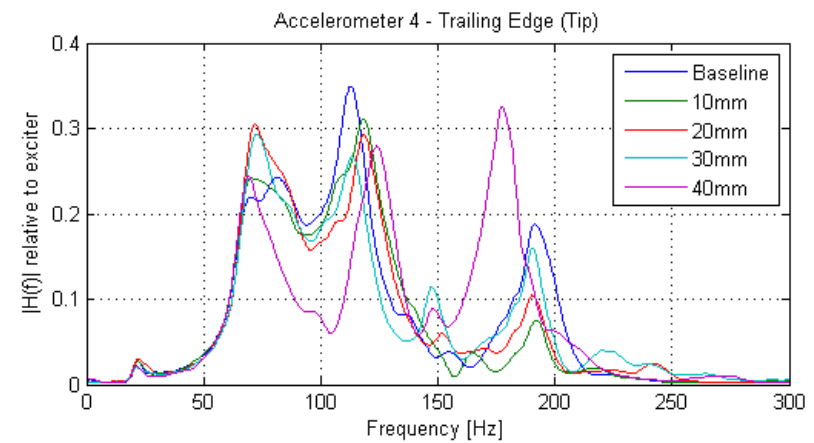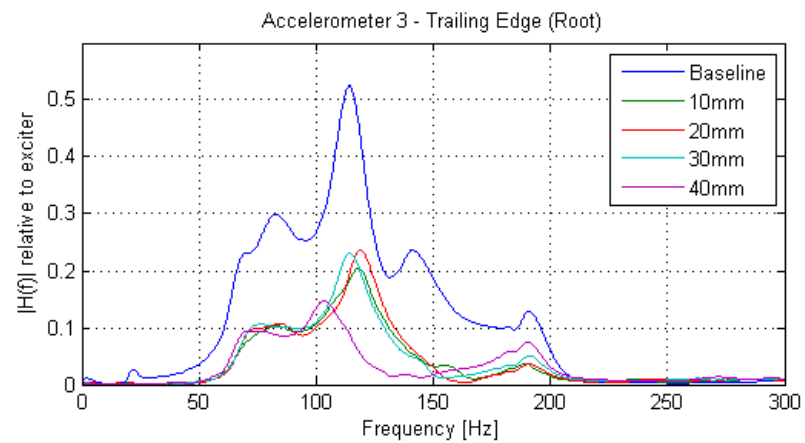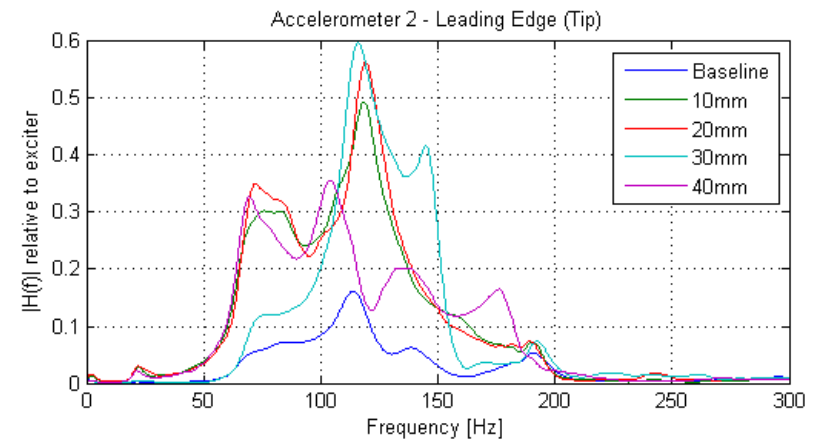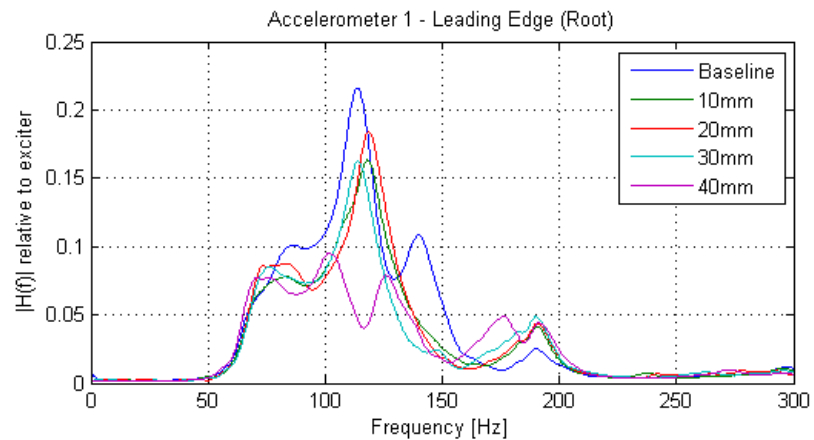
Figure 4.17 Frequency response plots measured at four accelerometer positions for four crack lengths (10 – 40 mm) on the old/damaged Marlec Rutland 913 windcharger blade for data read for three seconds at a rate of 16 kSamples per second.

Theoretical modelling of the effects of progressive transverse cracks on a test coupon, with dimensions as described in Chapter 3, was conducted using ANSYS Workbench [136]. The crack location was similar to the crack position on the old/damaged Marlec blade. Table 4.2 shows the estimated global first six mode frequencies of the coupon for each crack length induced on the coupon. At each mode, the global natural frequency of the coupon decreases for increasing crack length. This information was used to better interpret experimentally obtained measurements from the graphs in Figure 4.17.

Table 4.2 Theoretically estimated global natural frequencies for progressive transverse cracks on a test coupon.

Mode	Crack Lengths				
	No crack	10mm	20mm	30mm	40mm
	Natural Frequency (Hz)				
Mode 1	5.5194	5.5145	5.5002	5.4747	5.4354
Mode 2	34.581	34.413	33.953	33.2	32.153
Mode 3	60.09	59.874	59.182	57.912	56.15
Mode 4	96.854	96.812	96.637	96.166	95.342
Mode 5	182.89	182.19	179.87	175.38	169.12
Mode 6	189.88	189.06	186.94	183.83	180

Experimental results were analysed locally at each accelerometer position. For baseline, (0 mm crack) the first mode frequency measured across all accelerometer positions (accelerometer 1 – 4), was constant at 22.04 Hz. This was a global decrease of 3.21% from the measured value for the same old/damaged blade in the previous experiments in Section 4.2. In the previous section, it was suggested with valid reason, that a higher natural frequency measurement was characteristic of a mass loss and a lower natural frequency was indicative of a mass gain. Therefore, the 3.21% decrease in natural frequency, can be explained as the result of the addition of the exciter (60 grams) positioned at the root end of the old blade.

As the cracks were induced on the blade, the first mode frequency was not detected by both accelerometers (1 and 3) at the root end. However, the accelerometers (2 and 4) at the tip end, measured this mode for every crack length. Figure 4.18 shows the frequency trend measured at the tip end of the blade, for the first mode for increasing crack lengths.

The measured natural frequency of the blade at the first mode was the same for the baseline measurement (0 mm) and for a 10 mm crack. The frequency increased when the crack length was increased to 20 mm. At 30 mm crack length, the frequency decreased rapidly, because the crack length coincides with the width midpoint at that section of the tapered blade, potentially indicating severe structural damage had occurred.
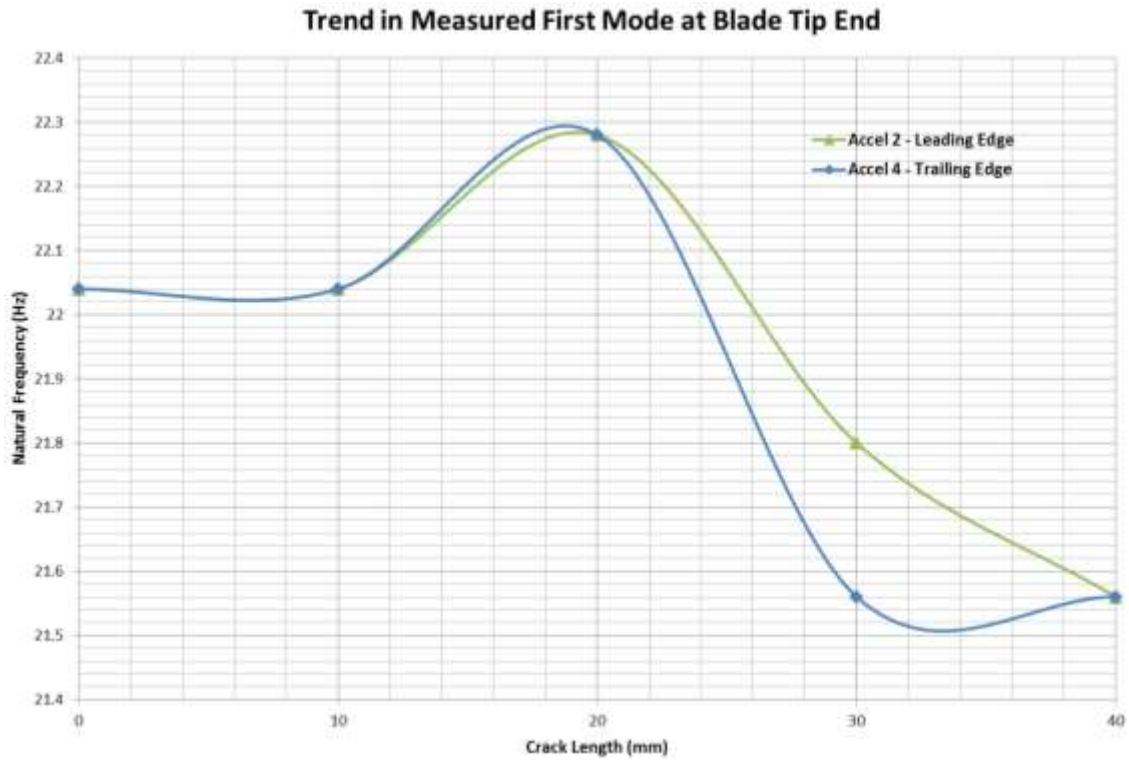
Figure 4.18 First mode frequency measured at the tip end of the old/damaged blade for increasing transverse blade cracks along the trailing edge, measured in response to a 1V chirp input excitation signal at the root end of the blade.
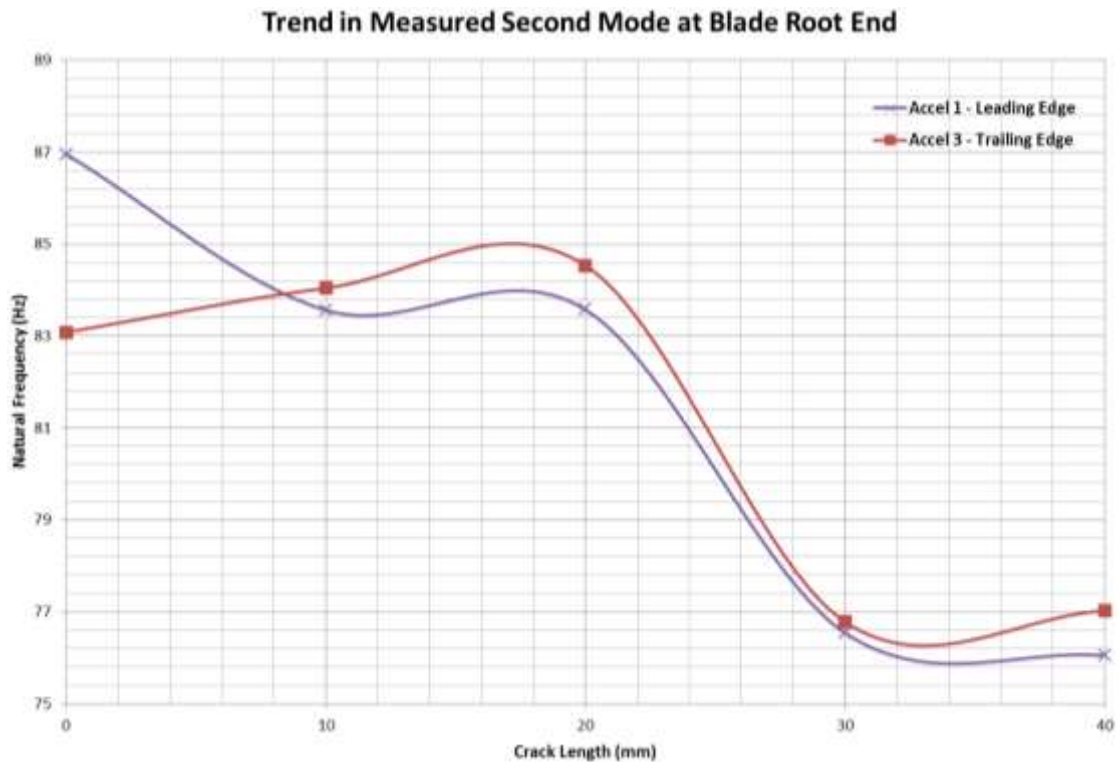
Figure 4.19 Second mode frequency measured at the root end of the old/damaged blade for increasing transverse cracks along the trailing edge, measured in response to a 1Vchirp input excitation signal at the root end of the blade.
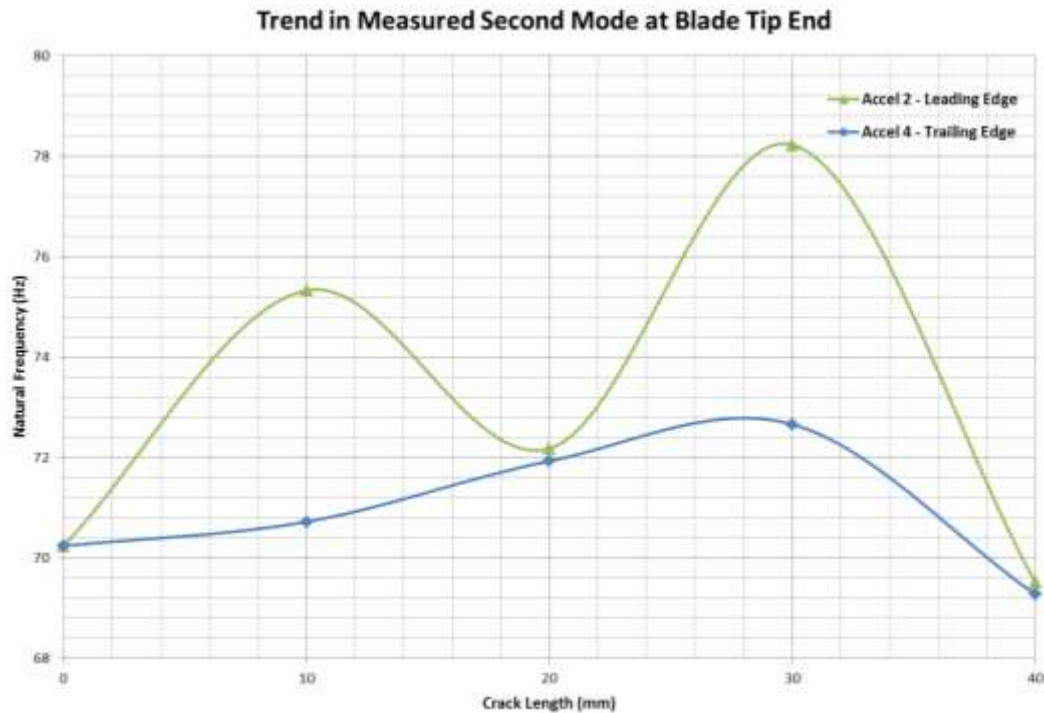
Figure 4.20 Second mode frequency measured at the tip end of the old/damaged blade for increasing transverse cracks along the trailing edge, measured in response to a 1Vchirp input excitation signal at the root end of the blade.

Figure 4.19 and 4.20 shows the trend observed at the second mode frequency of the blade. At the blade tip, both accelerometers measured this mode as 70.24 Hz at baseline (0 mm crack). However, at the root end, it was different for each of accelerometers (86.95 Hz - accelerometer 1 and 83.08 Hz – accelerometer 3). The trend observed also differed between the tip and root end. At the root end, the frequency decreased at 30 mm crack length as observed for the first mode frequency. However, at the tip end of the blade, the two accelerometers measured an increase in natural frequency at the same crack length (30 mm). These inconsistences in measurements across the entire blade at the second mode could not be fully explained. However, the mode occurred close to the resonance of the exciter, measured and shown in Figure 4.14. Although, the purpose of analysing the measured data relative to the reference accelerometer position on the exciter oscillating mass, was to eliminate such frequency contributions. Perhaps the blade and exciter interactions varied at this mode because of the damage at the tip of the blade.
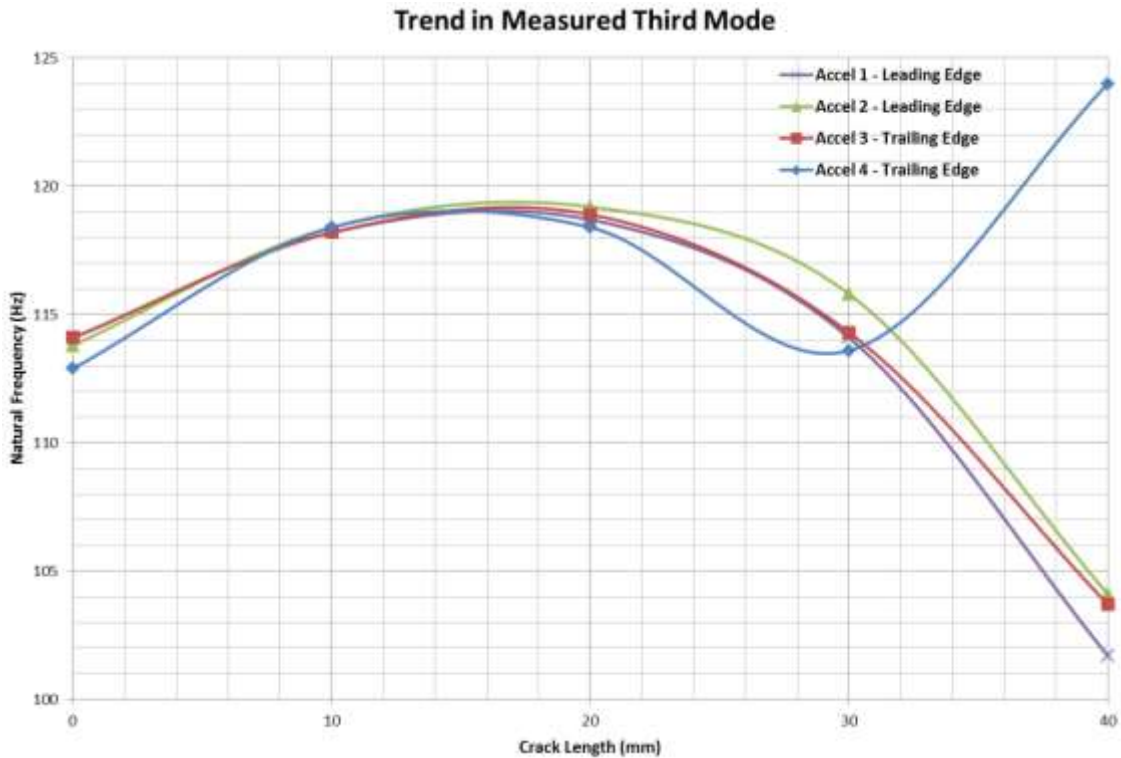
Figure 4.21 Third mode frequency measured at the tip and root ends of the old/damaged blade for increasing transverse cracks along the trailing edge, measured in response to a 1Vchirp input excitation signal at the root end of the blade.

Figure 4.21 shows the measured third mode of the blade for increasing crack lengths. At baseline (0 mm), the third mode of the blade was 113.7 Hz. As the case was for the first and second mode frequencies, the natural frequency of the blade at the third mode increased gradually for 10 mm and 20 mm crack lengths measured at all the accelerometer positions along the blade. Again, at 30 mm crack length, all the accelerometers measured a decrease in the natural frequency of the blade. Further decrease was measured at accelerometer 1, 2 and 3 when the 40 mm crack was induced on the blade. Accelerometer 4 however, measured a 9% increase from baseline measurements in the natural frequency at 40 mm crack length. This could possibly be as a result of the combined effect of the crack and damage at the blade tip at this particular natural frequency mode, or an experiment error.
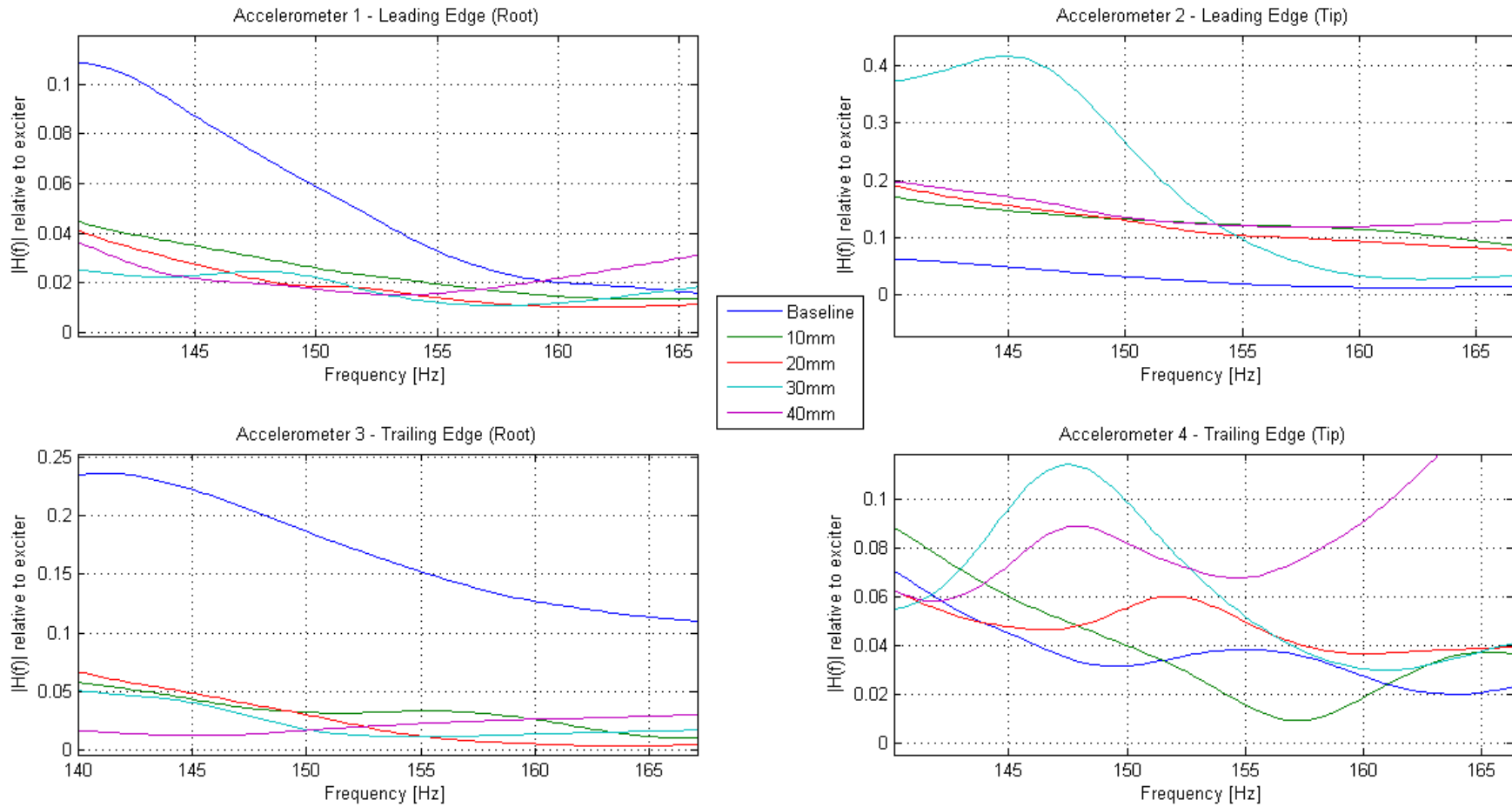
Figure 4.22 Frequency response plots (zoomed in between 140 – 165 Hz) measured at four accelerometer positions for four crack lengths (10 – 40 mm) on the old/damaged Marlec Rutland 913 windcharger blade for data read for three seconds at a rate of 16 kSamples per second.

Trend in Measured "Unique" Mode at Blade Tip End
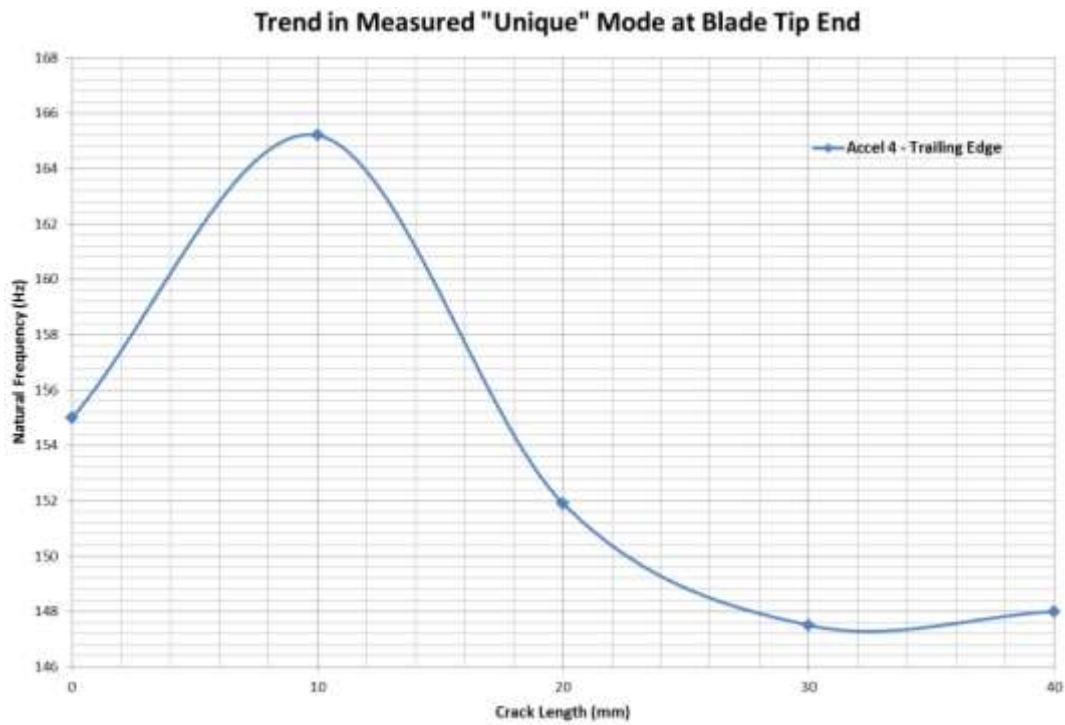
Figure 4.23 "Unique" mode frequency measured by accelerometer 4 at the tip end of the old/damaged blade for increasing transverse cracks along the trailing edge, measured in response to a 1Vchirp input excitation signal at the root end of the blade.

Trend in Measured Fourth Mode
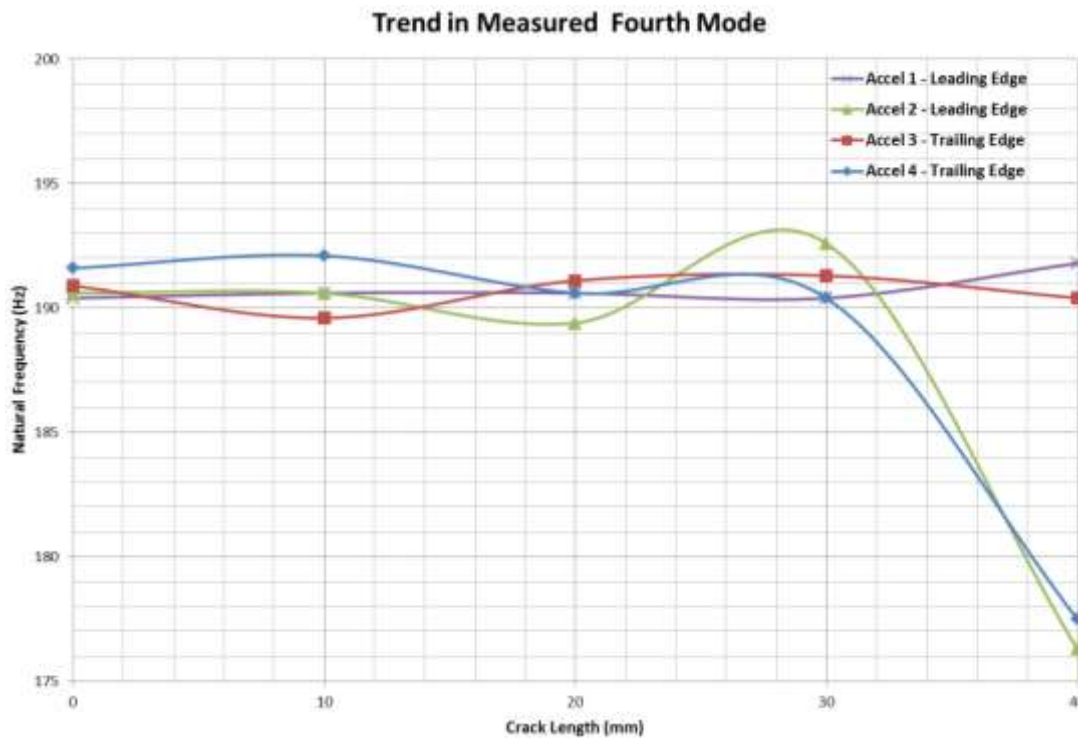
Figure 4.24 Fourth mode frequency measured at the tip and root ends of the old/damaged blade for increasing transverse cracks along the trailing edge, measured in response to a 1Vchirp input excitation signal at the root end of the blade.

A frequency mode unique to only accelerometer 4 was observed between 140 -165 Hz and a zoomed in plot at this mode is shown in Figure 4.22. The mode was measured at the baseline and for each increasing blade length. Figure 4.23 shows the measured trend in the changing natural frequency of this mode for each increasing crack length. The natural frequency increased for the first 10 mm crack length from the baseline. However, it decreased when the crack length was increased to 20 mm until 30 mm. It increased slightly when the 40 mm crack was induced on the blade.

The fourth mode frequency of the blade was at 190.8 Hz (baseline) and Figure 4.24 shows the trend measured at all accelerometer positions on the blade. The overall trend in measurements differed between the root and tip ends of the blade and between accelerometer locations. At the first 10 mm crack length, the measured natural frequency of the blade increased slightly for at all accelerometer locations except at accelerometer 3 (root end and trailing edge). At the 20 mm crack length, the natural frequency measured increased at accelerometers 1 and 3 (root end) only. It decreased for the tip end accelerometers (2 and 4). At 30 mm crack length, the natural frequency decreased slightly at accelerometer 1 and 3(root end) and increased at the accelerometers 2 and 4 (tip end). At 40 mm crack length, the natural frequency decreased at all accelerometer positions except at accelerometer 1 (root end and leading edge), where it increased slightly.

The overall trend in the results obtained showed that the natural frequency of the blade did not decrease immediately a crack was induced. At 10 mm crack length, the accelerometers generally measured an increase in natural frequency irrespective of the accelerometer's proximity to the crack location. However, as the crack length increased beyond this length, the blade responded differently depending on the positions of the accelerometers. 30 mm crack length was observed to be the critical damage point of the blade which predominantly led to a rapid decrease in the natural frequency of the blade. This is consistent with finds in the previous chapter of this thesis (Chapter 3), where 30 mm long cracks were induced on the coupons. The natural frequencies decreased across all the coupons.

These experiments demonstrated the effects the physical properties of the blade such as its mass, had on its natural frequency. It also showed that natural frequencies are valid indicators of changes in the physical conditions of blades. However, as the mode increases, it becomes slightly more difficult to identify damage. It also showed the effectiveness of MEMS accelerometers.

4.4 CONCLUSIONS

Marlec Rutland 913 Windcharger blades are manufactured from composite materials with high stiffness especially at the root end which attaches to the hub of the turbine. Generally, the blades can be described as being brittle; they have high strength but can break without significant deformation prior to breaking when subjected to stress due to bending moments induced by the mean wind and changes in wind speed (turbulence).

Results from experiments conducted in this chapter demonstrated the functionality of MEMS accelerometers. Their miniature size made the task of obtaining modal parameters that describe the blade's condition successful. Overall results from the experiments conducted showed that the natural frequency increased for decreasing mass, and increased for decreasing mass of the blade. It was also shown theoretically, the effects cut-outs and broken-off sections at the tip end had on the centre of mass of the blades. A broken-off section at the tip end shifted the centre of mass in two directions; leftwards towards the root end and upwards towards the leading edge of the blade.

In initial experiments conducted on the new and old blades, structural variations which exist naturally in blades were not considered in the analysis of results. In reality, baseline measurements of the blade's natural frequency will be taken prior to or at the installation phase of the blade on the rotor hub, to account for structural variations between blades and for health comparisons during the blades' lifetime. Regardless, the second set of experiments conducted on the old blade, showed that neglecting the natural structural variations was useful for analytically interpreting the results. In

addition, these results showed that defects such as cracks in blades can be indicated as an increase in natural frequency at its early stage. A decrease in natural frequency could potentially indicate severe damage on the blade. The observation of additional or unique modes at certain locations could also be an indicator of structural damage.

The literature also shows that modal measurements can yield useful performance data about a wind turbine blade condition. Frequency spectrum measurements also proved to be effective for detecting and indicating variations between blades. Perhaps the amplitude at each frequency peak can be used to provide more localised information about the blade but this is dependent on the input excitation impact position, the blade stiffness and accelerometer location. In this study, damaged and undamaged blades were measured with two excitation methods and indeed there were differences in the results. Generally, greater success was encountered with the impulsive excitation from the hammer than from the chirp excitation and this may be due to the loading effect and physical size of the electromagnetic exciter used. However, the exciter offered better input signal control than the hammer and it may be more useful on a larger-scale blade where the exciter weight would be negligible.

The MEMS accelerometer type used in these experiments were of the lowest range to capitalize on their low-cost and modal frequencies were successfully measured that provided information about the conditions of the blades. This shows the potential of these devices for condition monitoring of wind turbine blades.

In the following chapters of the thesis, the use of these MEMS accelerometers on a larger scale study is investigated.

5 CALIBRATION OF MEMS ACCELEROMETERS

Calibration can be described as the process of comparing measured outputs from sensors with known reference information and determining coefficients that force the output to agree with the reference information over a range of output values [217]. It generally improves the accuracy and reliability of sensor measurements.

Sensors such as the triaxial MEMS accelerometers introduced in chapter 4 of this thesis, measure the static acceleration of gravity in tilt-sensing applications, as well as dynamic acceleration resulting from motion, shock, or vibration. They are designed to produce an electrical output signal in Volts that is related to motion (usually in g - acceleration due to gravity where $1 \text{ g} = 9.81 \text{ ms}^{-2}$). Accurate accelerometer calibration is a way of defining the physical meaning to the electrical output and it is a prerequisite for quality measurement.

MEMS accelerometers are not supplied with an accurate calibration like conventional piezoelectric accelerometers. Piezoelectric sensors are extremely stable and their calibrated characteristics do not change over time except when subjected to harsh environmental conditions. In the event that a re-calibration of a piezoelectric accelerometer is required, the accelerometer can be returned to the manufacturer or the user can conduct the re-calibration using a back-to-back comparison calibration method. The accelerometer whose sensitivity is to be measured is mounted in a back-to-back arrangement with a reference accelerometer and the combination is mounted on a suitable vibration source. Since the input acceleration is the same for both devices, the ratio of their outputs is also the ratio of their sensitivities.

Manufacturers of MEMS accelerometers also calibrate the accelerometers by subjecting them to a wide variety of tests to determine the output due to a large number of inputs. Output characteristics commonly measured include sensitivity, resonant frequency, temperature etc. at varying conditions. The difficulty in calibrating these accelerometers is that the number of parameters in shock and vibration measurements is very large and many of these parameters interact, constantly changing from the factory calibration and introducing errors. The miniature size of MEMS accelerometers means that factors such as thermal stress during the soldering of the accelerometers to the printed circuit board, the rotation and orientation of the accelerometer package relative to the printed circuit board and misalignment of the printed circuit board to the structure (wind turbine blade) to which it is attached to, introduce errors to the accelerometer measurements and are generally termed as misalignment error [218]–[220]. *Misalignment error* is defined as the angles between the accelerometer sensing axes and the body axes of the structure or device to which the accelerometer is attached. It describes the coupling of motion in the other two orthogonal system axes into the particular measurement axis [221].

Another significant problem is the drift of the sensitivity and offset which cause output accelerometer measurements to be chaotic and vary. *Sensitivity*, denoted as S and also referred to as *scale factor*, is the ratio of change in signal to change in acceleration and is proportional to the supply voltage in analogue-sensors. *Offset*, denoted as O and also known as the *zero-g bias level*, is the direct current (DC) output level of the accelerometer when it is not in motion or being acted upon by the earth's gravity [201], [203], [205], [222]. It is the average of the accelerometer output over a predetermined time that has no relation to input acceleration or rotation. These two parameters (sensitivity and offset) of each axis on each accelerometer must therefore be characterised to permit accurate conversion from voltage to acceleration.

The calibration parameters of MEMS accelerometers contain scale factors, misalignments, biases, nonlinear coefficients and temperature drifts [223]. Conventionally, the calibration relies on precise inertial test set-up using a mechanical platform, to estimate these parameters according to the input and output reference information. The accelerometer is rotated by the mechanical platform into

several precisely controlled orientations, and the output of the accelerometer is compared with pre-calculated gravity force vector and rotational velocities respectively, at each orientation [217], [224], [225]. However, for mass-market devices, this method of accelerometer calibration is economically inefficient and the mechanical calibration platforms needed are overly expensive further increasing costs. Mass market industries such as mobile phone manufacturers utilise simpler user-calibration procedures [220], [226] to avoid these costs.

This chapter introduces and outlines a novel contribution by the author, for in-use calibration of MEMS accelerometers for application in wind turbine blade condition monitoring. MEMS accelerometers installed in arbitrary positions on a medium-sized wind turbine blade are calibrated using static calibration and least squares approximation methods outlined in further detail in the following sections. The purpose of this method of calibration is to:

a) Discover the adjustment factors of each individual accelerometer positioned on the wind turbine blade and to set the zero point.

b) Ensure that all accelerometers mounted on a single *non-planar* blade, share a common coordinate system for easy and more accurate interpretation of measurements.

A large-scale test was carried out with a medium-sized turbine blade to enable a realistic scenario of the calibration procedure to be studied. The following sections discuss the methodology and then present the application of the technique discussed in the literature to a turbine blade.

5.1 METHODOLOGY

A mechanical support was constructed from steel box-section beams to mimic the hub of a 4.5 m long Carter 25 kW wind turbine blade [227] and form a test fixture (Figure 5.1). This enabled the blade to be suspended above the ground using its existing mechanical fixings and allowed the blade to be rotated manually about its axes. The Carter wind turbine blade was in good working condition and had been in operation for only two months prior to it being obtained on loan for the purpose of non-destructive testing from Beacon Energy [228].

Five PCB-mounted ADXL335 MEMS accelerometers [201] were glued to the blade with their positioning determined based on the discretization of wind turbine blade motions [116], [117], [185] into three degrees of freedom described in Chapter 3 of this thesis. Wind turbine blade motion can be described by three degrees of freedom, which are *flapwise*, *edgewise* and *torsional*. Flapwise motion refers to motion parallel to the axis of rotation of the rotor, typically in the direction of the wind for rotors aligned with the wind. The largest stresses on wind turbine blades are normally due to flapwise bending from thrust forces. Edgewise motion lies in the plane of rotation and refers to motion relative to the blade's rotational motion. Torsional motion refers to motion about the pitch axis [24]. Figure 5.1 shows an annotated picture of the experimental set-up described above.

The output pins of the triaxial ADXL335 accelerometers were band limited to prevent antialiasing and to reduce the noise bandwidth (and hence the rms noise voltage) in measurements. 0.01 μF capacitors were soldered to the three output pins (X_{out}, Y_{out} and Z_{out}) of each accelerometer to implement low-pass signal filtering to a bandwidth of 500 Hz. 0.1 μF capacitors soldered to the supply pins of each accelerometer decoupled noise from the power supply rails. The accelerometers were wired to a 16-channel NI USB-6251 [202] data acquisition system and the cables were taped down securely to the blade to avoid spurious vibrations caused by cable movements.
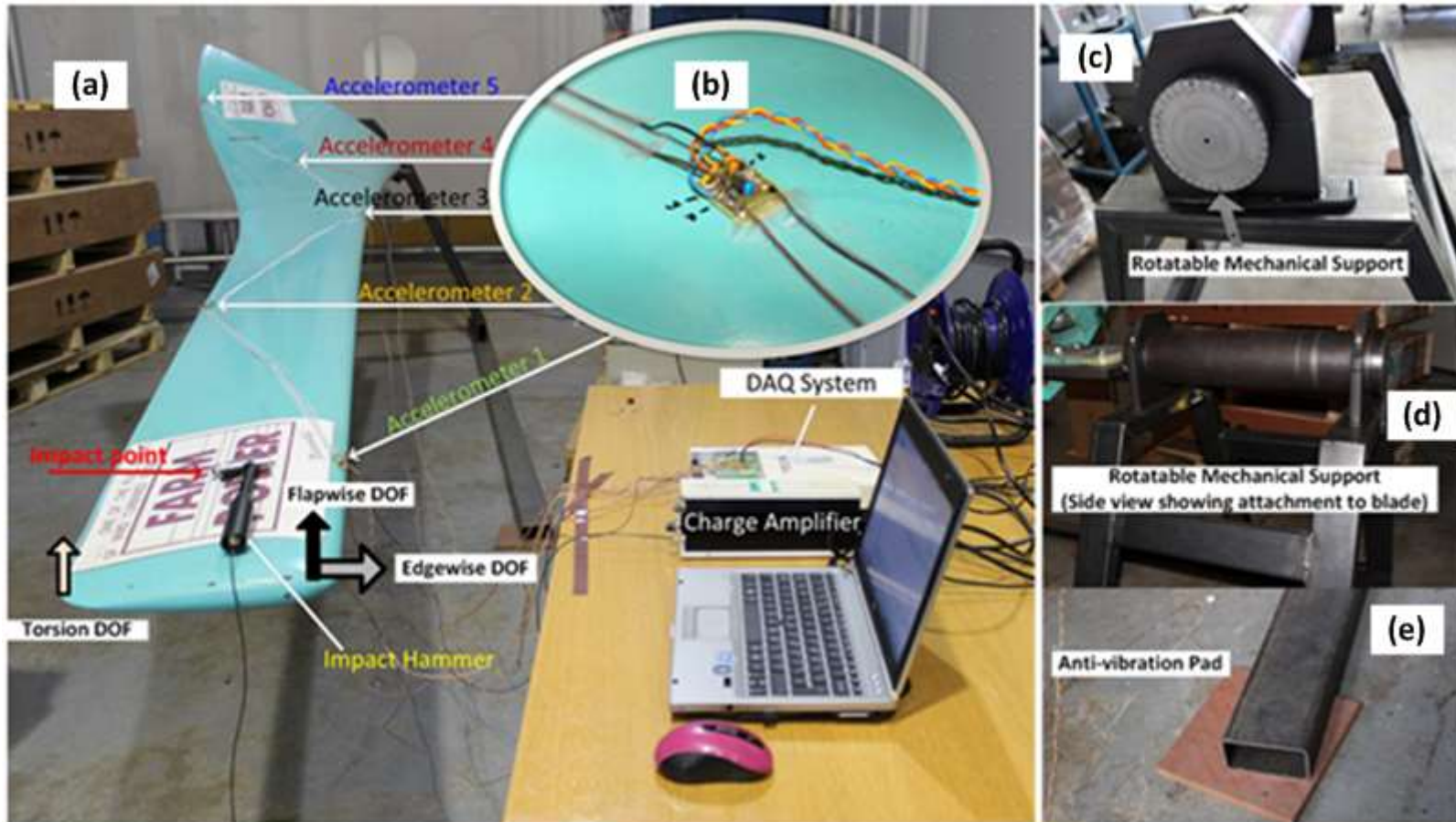
Figure 5.1 An annotated diagram showing the experimental set-up. (a) shows the 4.5 m long Carter 25 kW wind turbine blade, the accelerometer locations, the degrees of freedom and input excitation source (an impact hammer) [20]. (b) shows a zoomed in picture of an accelerometer on the blade. The test fixture is shown in (c), (d) and (e). (c) and (d) shows back and side views respectively, of the rotatable mechanical support mimicking the hub of a turbine blade. (e) shows the anti-vibration pads for absorbing vibrations at the foot of the test fixture.

Static calibration described in the next section, was conducted on the accelerometers while attached to the blade to improve the accuracy of the measurements. This involved rotating the blade through selected angles of orientation, allowing it to be stationary, and then recording static acceleration measurements of the accelerometers via the data acquisition system and LabVIEW SignalExpress software [174]. The decisions behind the choice of orientation angles are also discussed in the following sections. This enabled calibration parameters including the scale factors/sensitivity, misalignments and biases/offsets for each of the accelerometers to be determined.

To verify the calibration procedure employed was effective, dynamic acceleration was induced by exerting a transient input excitation on the blade using a Brüel & Kjær Type 8202 impact hammer [229] which has a built-in force transducer (type 8200). The hammer was connected to a charge amplifier as shown in Figure 5.1, which converted the signal from the force transducer of the hammer into a useful voltage signal measurable, by the data acquisition system. The input excitation signal from the hammer impact was logged simultaneously with the output responses of the accelerometers fixed to the wind turbine blade. The data acquisition system was set to read 10 seconds of data at a rate of 10 kSamples per second using LabVIEW SignalExpress. This was done to enable the vibrations of the blade to diminish to a low value.

In MATLAB [144], the calculated calibration parameters were applied to measured accelerometer responses, replacing post-processing methods employed in previous chapters of this thesis where datasheet values were used and assumed.

5.1.1 STATIC CALIBRATION

Considering a single axis of a MEMS accelerometer (independent of the other two axes), the output voltage is a measure of the angle θ [rad] between this sensitive axis of the device and the direction of gravity in a static calibration. The parameters, sensitivity and offset can be obtained by applying two different but inverse angles to the device (e.g. the accelerometer facing upwards and then facing downwards) thus, two equations with two unknowns are obtained – simultaneous equations which can easily be solved.

Similarly, consider all three axes of the triaxial accelerometer. They could be calibrated by keeping each axis under two different known angles θ with respect to gravity, as shown in Figure 5.2 and summarised in Table 5.1. This yields six possible equations with six unknowns. This is the minimum required set of equations to determine the three different sensitivities S_x, S_y and S_z [in Volts/g] and offsets O_x, O_y and O_z [in Volts] of the an accelerometer [230].
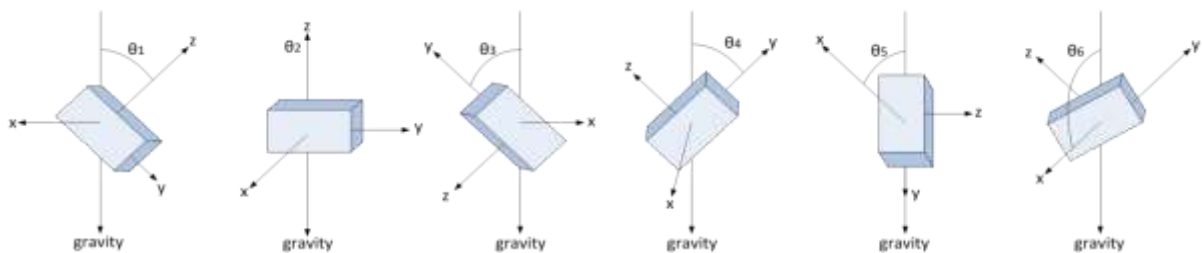
Figure 5.2 Diagram showing the six possible orientations in which the accelerometer can be held in relation to gravity.

Table 5.1 Accelerometer calibration positions from Figure 5.2 and their corresponding normalised acceleration values (where A_x, A_y and A_z are in terms of g-acceleration due to gravity).

Stationary Position	A_x	A_y	A_z
Z_{down} (θ_1)	0	0	$+1g$
Z_{up} (θ_2)	0	0	$-1g$
Y_{down} (θ_3)	0	$+1g$	0
Y_{up} (θ_4)	0	$-1g$	0
X_{down} (θ_5)	$+1g$	0	0
X_{up} (θ_6)	$-1g$	0	0

Pre-calibration of each of the five accelerometers on the 4.5 m long blade using the stationary positions listed in Table 5.1 implies that a minimum of 30 measurements will need to be recorded. Immediately this can be seen as time consuming, inconvenient and costly especially when more accelerometers are required for a larger turbine blade. Typical large-scale wind turbine blades are 25 m long and they are rapidly increasing in length.

Calibrating the accelerometers while they are positioned on the turbine blade is therefore a more efficient approach. However, the curved and non-planar structure of turbine blades means that each accelerometer measurement cannot be compared as they will all have different definitions of x, y and z introducing misalignment errors. This was resolved by generating a global coordinate system (X_G, Y_G and Z_G) which relied on the angle of orientation of the blade θ_G. Fixed along X_G via the rotatable test fixture shown in Figure 5.1, the blade was rotated through the stationary positions along Y_G and Z_G listed in Table 5.2 and shown in Figure 5.3.

Table 5.2 Blade calibration positions and the corresponding values (where A_{GX}, A_{GY} and A_{GZ} are in terms of g - acceleration due to gravity).

Stationary Position	θ_G (°)	A_{GX}	A_{GY}	A_{GZ}
Z_{G_down} (θ_{G1})	0	0	0	$+1g$
Z_{G_up} (θ_{G2})	180	0	0	$-1g$
Y_{G_down} (θ_{G3})	90	0	$+1g$	0
Y_{G_up} (θ_{G4})	270	0	$-1g$	0
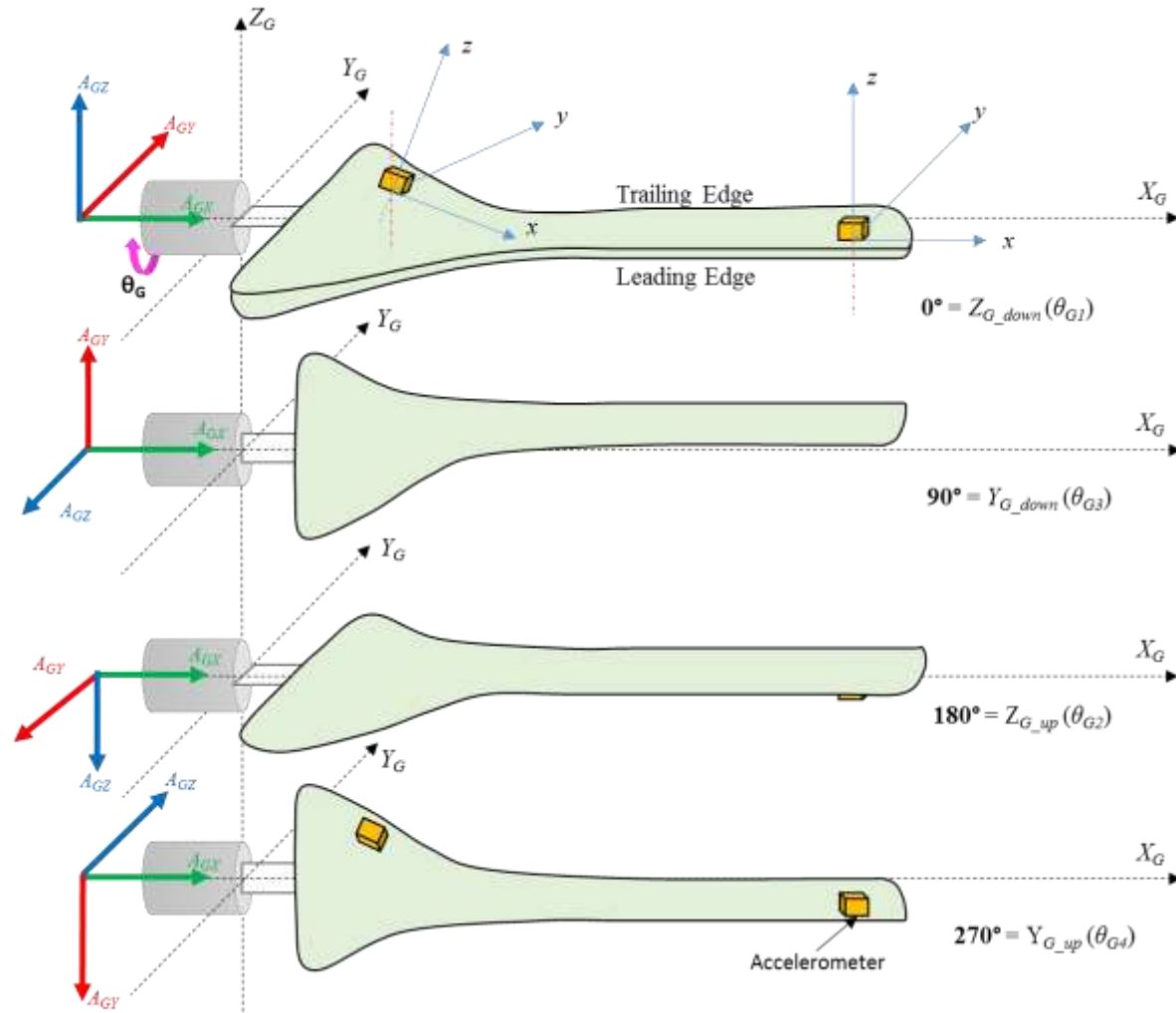
Figure 5.3 Blade calibration positions (θ_{G1}, θ_{G2}, θ_{G3} and θ_{G4}). X_G, Y_G and Z_G represent the global coordinate system. Notice that X_G stays constant for each blade position. The thicker edge of the blade, which houses the main spar, indicates the leading edge and the thin edge, the trailing edge. A_{GX}, A_{GY} and A_{GZ} represent the global normalised acceleration. x_n, y_n and z_n represent the individual accelerometer axes where n denotes the accelerometer position on the blade with $n = 1$ starting at the blade tip.

5.1.2 DESCRIPTION OF CALIBRATION MATHEMATICAL MODEL

As stated in previous sections, MEMS accelerometers measure vibrations in terms of analogue voltages. The relationship between the accelerometer raw measurements in Volts (V_x, V_y and V_z) and the normalised accelerometer measurements in terms of acceleration due to gravity, $g - 9.81$ ms^{-2} (A_x, A_y and A_z) can be expressed as [231]–[233]:

$$\begin{bmatrix} A_x \\ A_y \\ A_z \end{bmatrix} = [A_m]_{3 \times 3} \begin{bmatrix} 1/S_x & 0 & 0 \\ 0 & 1/S_y & 0 \\ 0 & 0 & 1/S_z \end{bmatrix} \begin{bmatrix} V_x - O_x \\ V_y - O_y \\ V_z - O_z \end{bmatrix} \qquad \text{Eqn 5.1}$$

Where:

$[A_m]_{3 \times 3}$ – is a 3×3 misalignment matrix between the accelerometer sensing axes (x, y and z) and the global wind turbine blade axes (X, Y and Z). Calculating the misalignment matrix compensates any misalignment errors.

$S(S_x \, S_y \, S_z)$ – is the sensitivity or scale factor of the accelerometer in terms of its output Volts per g (~ 9.81 ms^{-2}) of acceleration.

$O(O_x \, O_y \, O_z)$ – is the offset or bias of the accelerometer in Volts.

This calibration procedure seeks to establish a relationship and resolve the individual accelerometer measurements (A_x, A_y and A_z) to a global normalised accelerometer measurement coordinate system (A_{GX}, A_{GY} and A_{GZ}) relative to the turbine blade position. Therefore, redefining Eqn 5.1 becomes:

$$\begin{bmatrix} A_{GX} \\ A_{GY} \\ A_{GZ} \end{bmatrix} = [A_m]_{3 \times 3} \begin{bmatrix} 1/S_x & 0 & 0 \\ 0 & 1/S_y & 0 \\ 0 & 0 & 1/S_z \end{bmatrix} \begin{bmatrix} V_x - O_x \\ V_y - O_y \\ V_z - O_z \end{bmatrix} \qquad \text{Eqn 5.2}$$

Eqn 5.2 can be expressed as a simpler expression that combines the unknowns together as shown in Eqn 5.3.

$$\begin{bmatrix} A_{GX} \\ A_{GY} \\ A_{GZ} \end{bmatrix} = \begin{bmatrix} B_{11} & B_{12} & B_{13} \\ B_{21} & B_{22} & B_{23} \\ B_{31} & B_{32} & B_{33} \end{bmatrix} \begin{bmatrix} V_x \\ V_y \\ V_z \end{bmatrix} + \begin{bmatrix} B_{10} \\ B_{20} \\ B_{30} \end{bmatrix} \qquad \text{Eqn 5.3}$$

From Eqn 5.3, it can be seen that the parameters B_{10} to B_{33}, are the calibration parameters that directly relate the raw measurements to the global normalised accelerometer values. Determining these calibration parameters will allow the calibration of any given raw accelerometer measurements at arbitrary positions resulting in:

$$|A| = \sqrt[2]{A_{GX}^2 + A_{GY}^2 + A_{GZ}^2} = 1g \qquad \text{Eqn 5.4}$$

Where:

$|A|$ - is the magnitude of the resultant acceleration as A_{GX}, A_{GY} and A_{GZ} are the normalised acceleration measured per g. Hence, Eqn 5.4 holds true for a fully static body.

5.1.3 LEAST SQUARES APPROXIMATION

Using least squares approximation in MATLAB, Eqn 5.3 was solved. The term *least squares*, describes a frequently used approach to solving over-determined or inexactly specified systems of equations in an approximate sense. Instead of solving the equations exactly, this method seeks only to minimize the sum of the squares of the residuals. The computational techniques for linear least squares problems make use of orthogonal matrix factorisations as well as simple calculus and linear algebra [234], [235].

Consider the equation $q = Dp$ where $D \in R^{m \times n}$ is full rank and (strictly) skinny, i.e., $m > n$ [236]. The matrix has more rows m than columns n. For most q, p cannot be solved, as there are more equations than unknowns. The system cannot be solved exactly therefore, one approach is to find approximate solutions. Choosing a p at random, an error can occur when $q \neq Dp$. The vector $r = Dp - q$ gives the error. A plausible choice (not the only one) is to seek a p with the property that $\|r\|$, the norm or magnitude of the error, is as small as possible. When the error r is zero, p is an exact solution of $q = Dp$. When the length of the error r is as small as possible, p_{ls} is a least squares solution of the equation.

To find p_{ls} the norm of error squared is minimised as:

$$\|r\|^2 = p_{ls}{}^T D^T D p_{ls} - 2q^T D p_{ls} + q^T q \qquad \text{Eqn 5.5}$$

The gradient w.r.t. p is set to zero. Therefore;

$$\nabla_p \|r\|^2 = 2D^T D p_{ls} - 2q^T D p_{ls} = 0 \qquad \text{Eqn 5.6}$$

This yields the normal equations:

$$D^T D p_{ls} = D^T q \qquad \text{Eqn 5.7}$$

Based on invertible matrix I, Eqn 5.7 can therefore be expressed as:

$$p_{ls} = (D^T D)^{-1} D^T q \qquad \text{Eqn 5.8}$$

Eqn 5.8 is a well-known formula for obtaining a Least Squares (approximation) solution, where;

p_{ls} - is a linear function of q.

$p_{ls} = D^{-1}q$ if D is square.

p_{ls} solves $q = Dp_{ls}$ if $q = \in \mathcal{R}(D)$

$D^\dagger = (D^T D)^{-1} D^T$ is called the pseudo-inverse of D

$D^\dagger$ - is a left inverse of (full rank, skinny) D:

$$D^\dagger D = (D^T D)^{-1} D^T D = I \qquad \text{Eqn 5.9}$$

Considering the global normalised accelerometer measurements at the stationary positions, Eqn 5.3 can be rewritten as:

$$[A_{GX} \quad A_{GY} \quad A_{GZ}] = [V_x \quad V_y \quad V_z \quad 1]\begin{bmatrix} B_{11} & B_{21} & B_{31} \\ B_{12} & B_{22} & B_{32} \\ B_{13} & B_{23} & B_{33} \\ B_{10} & B_{20} & B_{30} \end{bmatrix} \qquad \text{Eqn 5.10}$$

Eqn 5.10 can also be further simplified and represented as:

$$\boldsymbol{Y} = \boldsymbol{w}.\boldsymbol{X} \qquad \text{Eqn 5.11}$$

Where:

$\boldsymbol{X}$ – is the matrix representing the 12 calibration parameters matrix that needs to be determined.

$\boldsymbol{w}$ - is the matrix representing raw data collected at the stationary positions and

$\boldsymbol{Y}$ – is the known global normalised earth gravity vector.

Now considering each stationary position,

> At Z_{G_down} position (θ_{G1}), $[A_{GX} \quad A_{GY} \quad A_{GZ}] = [0 \quad 0 \quad 1]$

  Assuming that at Z_{G_down} position, n_1 sets or samples of accelerometer raw data V_x, V_y and V_z have been collected. Then:

$$\boldsymbol{Y_1} = [0 \quad 0 \quad 1]_{n_1 \times 3} \text{ and } \boldsymbol{w_1} = \begin{bmatrix} V_{x\theta_{G1}} & V_{y\theta_{G1}} & V_{z\theta_{G1}} & 1 \end{bmatrix}_{n_1 \times 4} \qquad \text{Eqn 5.12}$$

  Where the matrix $\boldsymbol{Y_1}$ has three identical rows of $[0 \quad 0 \quad 1]$ and matrix $\boldsymbol{w_1}$ contains raw data measured by the accelerometer.

> At Z_{G_up} position (θ_{G2}), $[A_{GX} \quad A_{GY} \quad A_{GZ}] = [0 \quad 0 \quad -1]$

  Assuming that at Z_{G_down} position, n_2 sets or samples of accelerometer raw data V_x, V_y and V_z have been collected. Then:

$$\boldsymbol{Y_2} = [0 \quad 0 \quad -1]_{n_2 \times 3} \text{ and } \boldsymbol{w_2} = \begin{bmatrix} V_{x\theta_{G2}} & V_{y\theta_{G2}} & V_{z\theta_{G2}} & 1 \end{bmatrix}_{n_2 \times 4} \qquad \text{Eqn 5.13}$$

  Where the matrix $\boldsymbol{Y_2}$ has three identical rows of $[0 \quad 0 \quad -1]$ and matrix $\boldsymbol{w_2}$ contains raw data measured by the accelerometer.

> At Y_{G_down} position (θ_{G3}), $[A_{GX} \quad A_{GY} \quad A_{GZ}] = [0 \quad 1 \quad 0]$

  Assuming that at Y_{G_down} position, n_3 sets or samples of accelerometer raw data V_x, V_y and V_z have been collected. Then:

$$\boldsymbol{Y_3} = [0 \quad 0 \quad 1]_{n_3 \times 3} \text{ and } \boldsymbol{w_3} = \begin{bmatrix} V_{x\theta_{G3}} & V_{y\theta_{G3}} & V_{z\theta_{G3}} & 1 \end{bmatrix}_{n_3 \times 4} \qquad \text{Eqn 5.14}$$

Where the matrix Y_3 has three identical rows of $[0 \quad 1 \quad 0]$ and matrix w_3 contains raw data measured by the accelerometer.

➤ At Y_{G_up} position (θ_{G4}), $[A_{GX} \quad A_{GY} \quad A_{GZ}] = [0 \quad -1 \quad 0]$

Assuming that at Y_{G_up} position, n_4 sets or samples of accelerometer raw data V_x, V_y and V_z have been collected. Then:

$$Y_4 = [0 \quad -1 \quad 0]_{n_4 \times 3} \text{ and } w_4 = \begin{bmatrix} V_{x\theta_{G4}} & V_{y\theta_{G4}} & V_{z\theta_{G4}} & 1 \end{bmatrix}_{n_4 \times 4} \qquad \text{Eqn 5.15}$$

Where the matrix Y_4 has three identical rows of $[0 \quad -1 \quad 0]$ and matrix w_4 contains raw data measured by the accelerometer.

Combining Eqn 5.13 to 5.15 and assuming $n = n_1 + n_2 + n_3 + n_4$ then Eqn 5.11 becomes, measured by the accelerometer.

$$Y_{n \times 3} = w_{n \times 4} \, X_{4 \times 3} \qquad \text{Eqn 5.16}$$

Where $Y = \begin{bmatrix} Y_1 \\ Y_2 \\ Y_3 \\ Y_4 \end{bmatrix}_{n \times 3}$ and $w = \begin{bmatrix} w_1 \\ w_2 \\ w_3 \\ w_4 \end{bmatrix}_{n \times 4}$

Therefore, the calibration parameter matrix X can be determined by the least squares method as:

$$X = [w^T w]^{-1} w^T Y \qquad \text{Eqn 5.17}$$

Where:

w^T - means matrix transpose and $[w^T w]^{-1}$ means matrix inverse [226], [237].

Solving the above equations in MATLAB (See code in Appendix 10.1) generated the global calibration parameters for the accelerometers on the Carter wind turbine blade. These static calibration parameters can be applied to any raw accelerometer measurements at arbitrary blade positions by simply calculating the product of the calibration parameter and the raw measurements.

Eqn 5.18 shows the calibration parameter matrices, X_1 –X_5 deduced at each accelerometer location along the blade.

In the next section, results obtained by applying the above calibration parameter matrices to raw accelerometer measurements are investigated.

$$
X_1 = \begin{bmatrix} 0 & 0.3384 & 0.2454 \\ 0 & -2.6962 & 1.6511 \\ 0 & 1.6961 & 2.8424 \\ 0 & 0.9893 & -7.4664 \end{bmatrix}
$$

$$
X_2 = \begin{bmatrix} 0 & 0.3082 & -0.0135 \\ 0 & -3.1424 & -0.3372 \\ 0 & -0.3421 & 3.2366 \\ 0 & 5.0317 & -4.5986 \end{bmatrix}
$$

$$
X_3 = \begin{bmatrix} 0 & 0.6343 & 0.2472 \\ 0 & -2.6809 & 1.5782 \\ 0 & 1.5581 & 2.7799 \\ 0 & 0.7525 & -7.2419 \end{bmatrix} \qquad \text{Eqn 5.18}
$$

$$
X_4 = \begin{bmatrix} 0 & -0.4316 & 0.3249 \\ 0 & -3.1954 & -0.1816 \\ 0 & -0.1853 & 3.2517 \\ 0 & 6.0199 & -5.4825 \end{bmatrix}
$$

$$
X_5 = \begin{bmatrix} 0 & -0.6292 & 1.3393 \\ 0 & -2.9444 & 0.4045 \\ 0 & 0.7716 & 2.9077 \\ 0 & 4.3985 & -7.3783 \end{bmatrix}
$$

5.2 RESULTS AND DISCUSSIONS

Applying the determined calibration parameters to raw accelerometer measurements (V_x, V_y and V_z), Figure 5.4 shows the time domain plot of the normalised accelerometer measurements (A_x, A_y, A_z) obtained at each accelerometer position in response to an impulse excitation induced by a force hammer when the turbine blade was orientated at a position θ_{G1} (0°).

At 0° (see Figure 5.3), the expected static global normalised accelerometer measurement (A_{GX}, A_{GY}, A_{GZ}) is [0 0 1] in units of g. Observing Figure 5.4, it can be seen that the individual acceleration measurements (A_x, A_y, A_z) have been resolved to a global normalised measurement (A_{GX}, A_{GY}, A_{GZ}) independent of the accelerometer location on the turbine blade and the curved blade surface profile i.e.

$$
[A_x \, A_y \, A_z] \approx [A_{GX} \, A_{GY} \, A_{GZ}] = [0 \quad 0 \quad 1]
$$

At all accelerometer positions on the turbine blade, it is clear in Figure 5.4, that the resultant acceleration measured for the blade positioned at $\theta_{G1} = 0°$ was along the Z_G axis. The spikes above $1g$ in the measured acceleration signal indicate the period when the MEMS accelerometers are measuring dynamic acceleration experienced by the blade, induced by a 6 N transient input excitation signal from the force hammer. By visual inspection, accelerometer 2 measured the highest acceleration magnitude, consistent with its location on the trailing (thin) edge near the impact excitation point close to the blade tip.

Some vibrations were measured along the Y_G axis, which was centred on $0g$ acceleration. Along X_G, no dynamic acceleration was measured, as this axis was static during measurements. In a real life scenario on a wind turbine rotating blade, acceleration along X_G, will not be $0g$ because the axis will not be static. Implementing this calibration routine on an operating wind turbine blade could help wind farm operators easily identify and investigate further, accelerometer measurements that may potentially suggest blade damage, by simple visual inspection of the time domain response. In addition, faulty accelerometers can be identified and replaced if necessary.

As further evidence proving the effectiveness of the calibration procedure, Figure 5.5 – 5.9 present time domain plots of the normalised accelerometer measurements for blade orientations at 90°, 180°, 270°, 30° and 60° respectively.
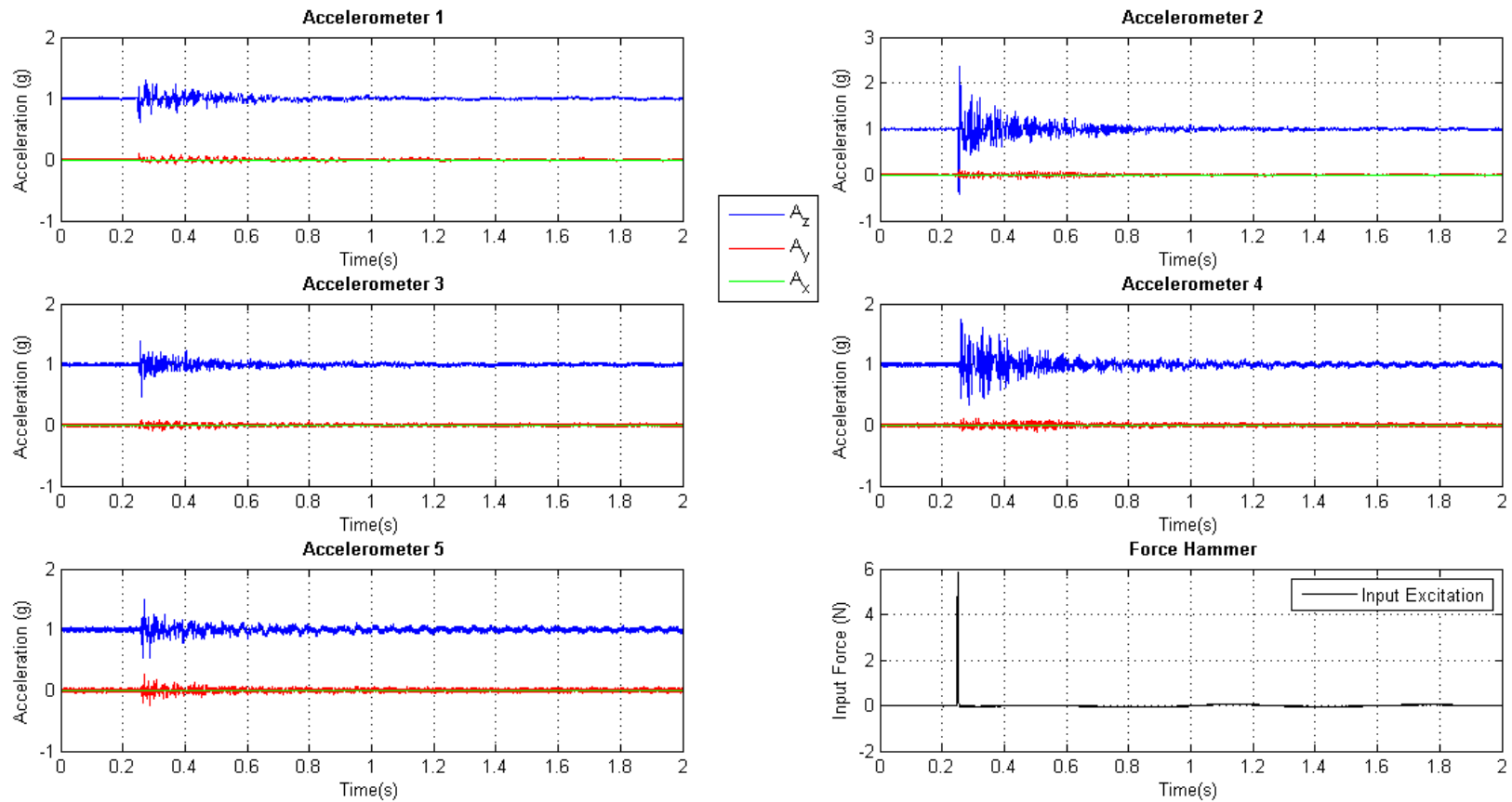
Figure 5.4 Time domain plots showing the measured accelerometer response to a 6 N transient input excitation induced by a force hammer on the Carter wind turbine blade, orientated at ($\theta_{GI} = 0°$). The data were read at a rate of 10 kHz for 10 seconds to allow the output signal to die-out. The plot is zoomed-in for the first two seconds. Accelerometer 1 is nearest the tip, 5 is nearest the root.
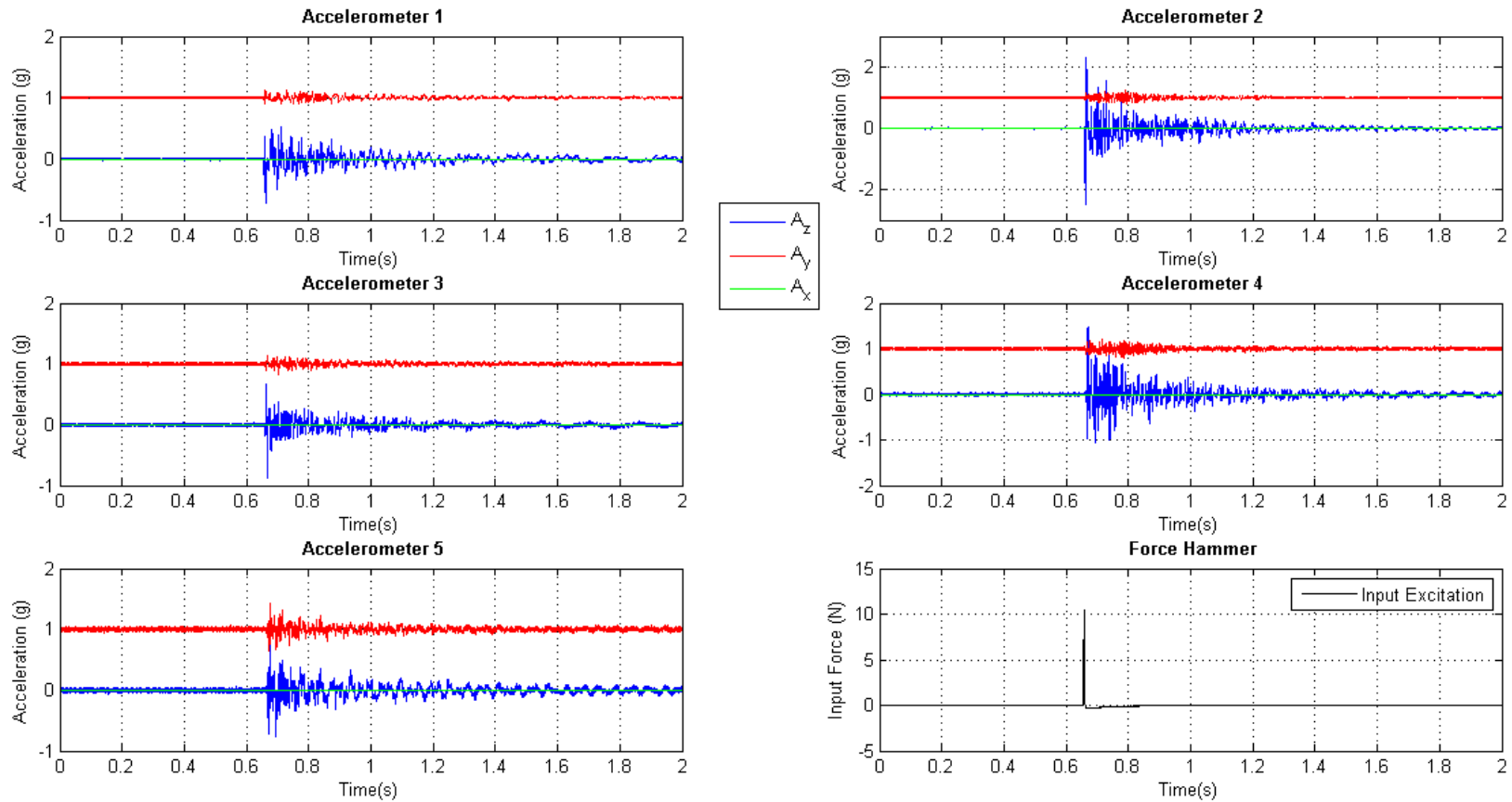
Figure 5.5 Time domain plots showing the measured accelerometer response to a 10 N transient input excitation induced by a force hammer on the Carter wind turbine blade, orientated at ($\theta_{G3} = 90°$). The data were read at a rate of 10 kHz for 10 seconds to allow the output signal to die-out. The plot is zoomed-in for the first two seconds. Accelerometer 1 is nearest the tip, 5 is nearest the root.
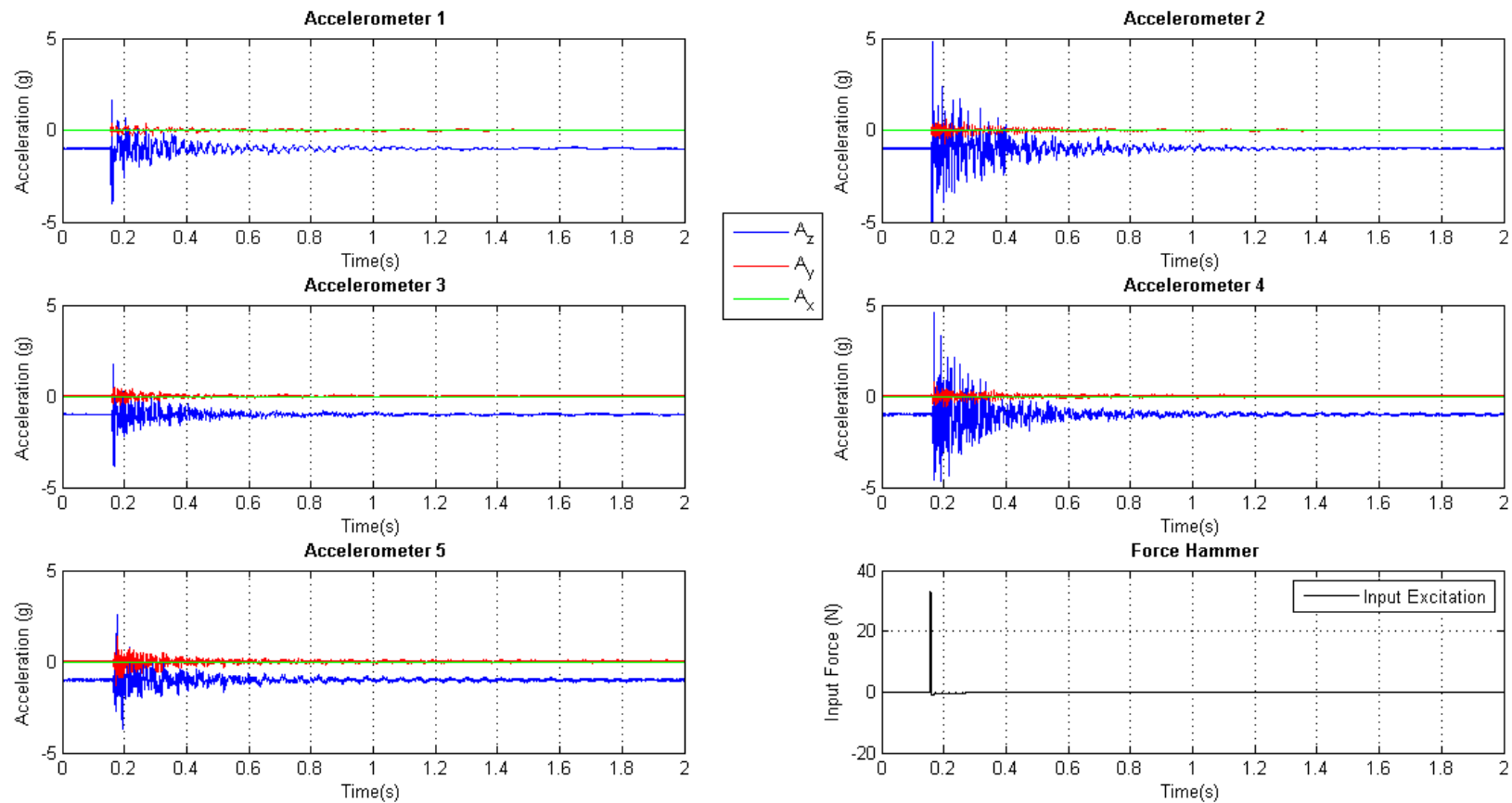
Figure 5.6 Time domain plots showing the measured accelerometer response to a 30 N transient input excitation induced by a force hammer on the Carter wind turbine blade, orientated at ($\theta_{G2} = 180°$). The data were read at a rate of 10 kHz for 10 seconds to allow the output signal to die-out. The plot is zoomed-in for the first two seconds. Accelerometer 1 is nearest the tip, 5 is nearest the root.
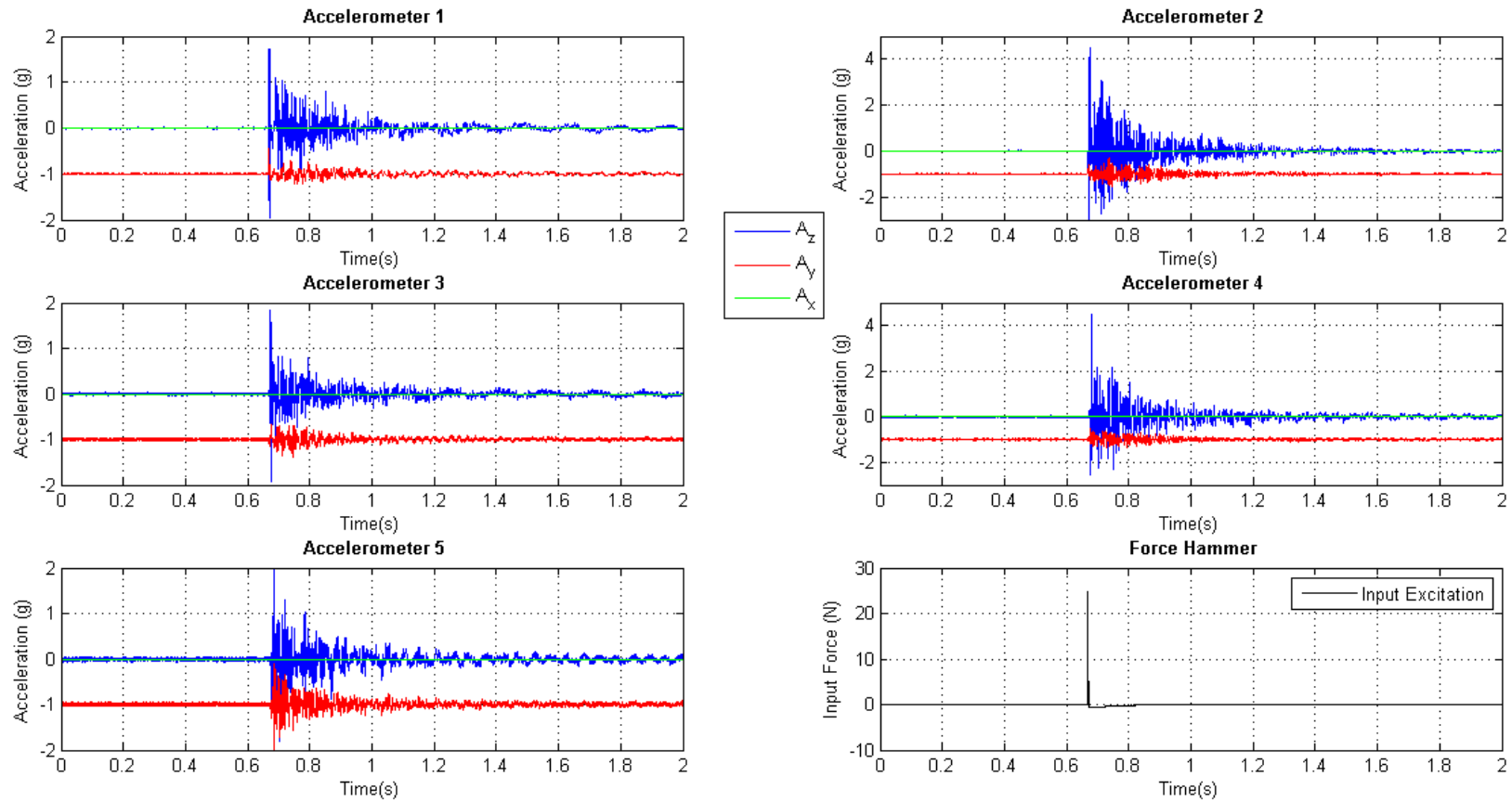
Figure 5.7 Time domain plots showing the measured accelerometer response to a 24 N transient input excitation induced by a force hammer on the Carter wind turbine blade, orientated at ($\theta_{G4} = 270°$). The data were read at a rate of 10 kHz for 10 seconds to allow the output signal to die-out. The plot is zoomed-in for the first two seconds. Accelerometer 1 is nearest the tip, 5 is nearest the root.
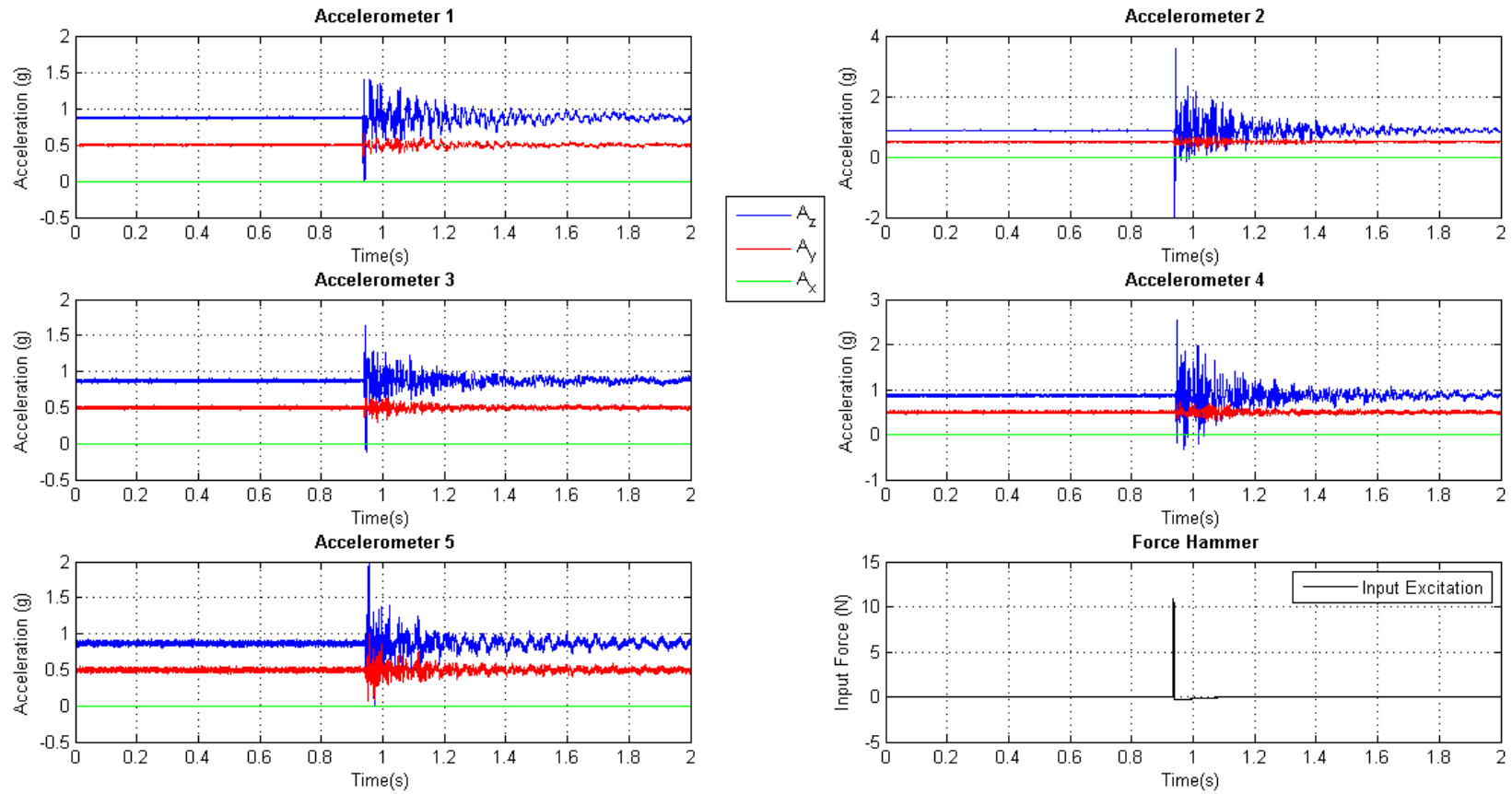
Figure 5.8 Time domain plots showing the measured accelerometer response to an 11 N transient input excitation induced by a force hammer on the Carter wind turbine blade, orientated at ($\theta = 30°$). The data were read at a rate of 10 kHz for 10 seconds to allow the output signal to die-out. The plot is zoomed-in for the first two seconds. Accelerometer 1 is nearest the tip, 5 is nearest the root.
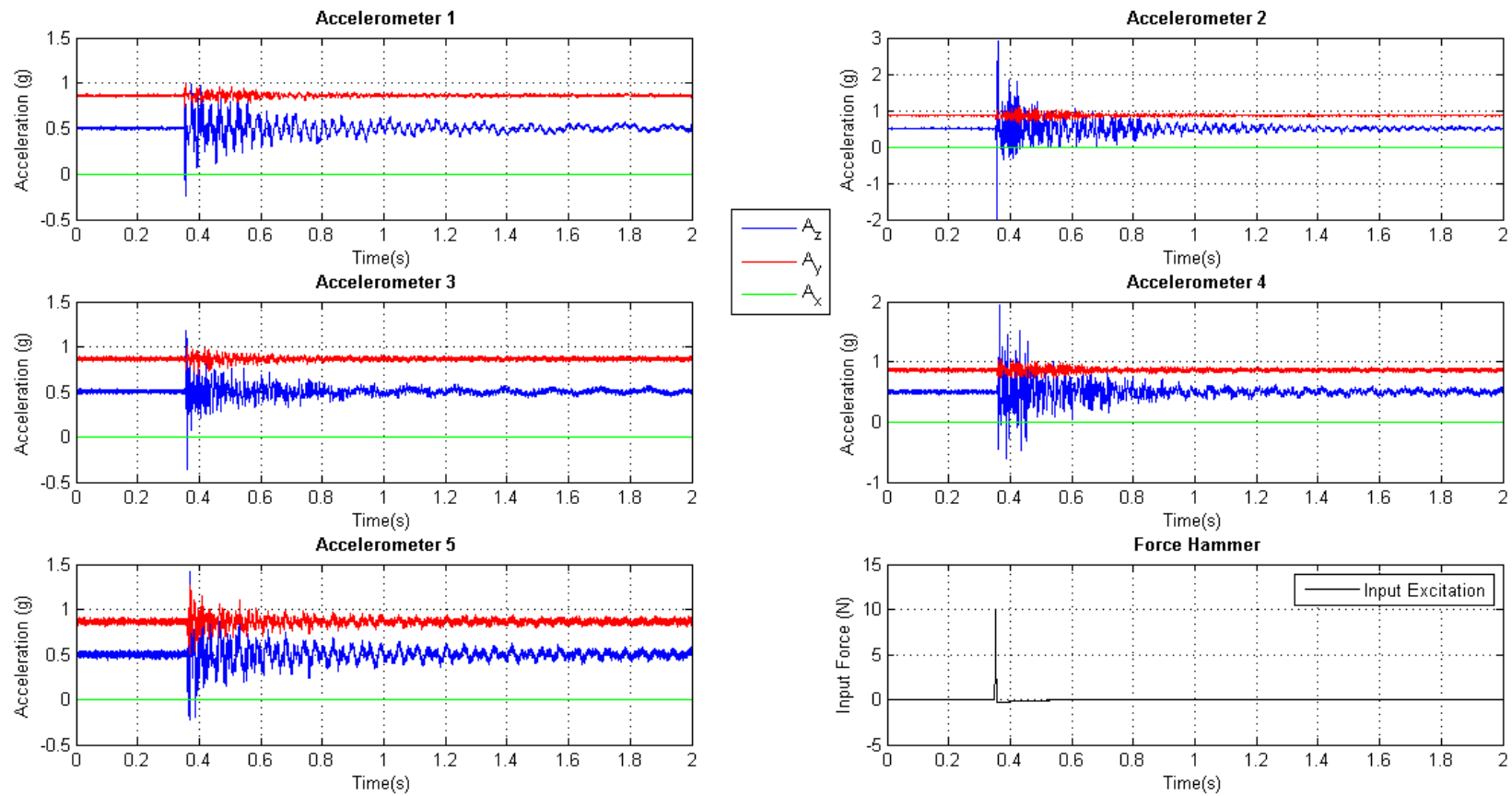
Figure 5.9 Time domain plots showing the measured accelerometer response to an 11 N transient input excitation induced by a force hammer on the Carter wind turbine blade, orientated at ($\theta = 60°$). The data were read at a rate of 10 kHz for 10 seconds to allow the output signal to die-out. The plot is zoomed-in for the first two seconds. Accelerometer 1 is nearest the tip, 5 is nearest the root.

In the Figures above, it can be observed that as the output along X_G stays constant at $0g$, the measured acceleration along Y_G and Z_G switch positions continuously as the blade orientation θ_G is changed.

The frequency spectrum of the Carter wind turbine blade was extracted using Fast Fourier Transformation methods from the time domain data measured and calibrated when the blade was orientated at 0° (θ_{G1}). Figure 5.10 shows the extracted frequency spectrum measured at each accelerometer position along the blade. It also shows the frequency spectrum of the force hammer. The fundamental frequency/resonance of the blade was measured as 1.831 Hz and was measured by all accelerometers. This correlated with the estimated value of 1.6 Hz obtained by releasing the blade from rest in the flapwise direction and timing the period for it to settle.

Impact testing from the force hammer blow has the frequency content limited by length of the impact; the shorter the pulse, the higher the frequency range [238]. Therefore, the force hammer impact produces a broadband frequency range. To ensure that the frequency spectrum measured was solely of the wind turbine blade, the frequency response function was calculated in MATLAB at each accelerometer position by dividing the output frequency response at that point, by the input frequency response from the force hammer. The magnitude of the FRF was then plotted as shown in Figure 5.10.

Generally, all of the accelerometers measured similar resonance frequencies. However, the magnitudes of each resonance frequency varied for each accelerometer. For instance, accelerometers 4 and 5 measured higher magnitudes at 19.07 Hz in comparison to the accelerometers towards the tip of the turbine blade. Results also showed that the blade fed back to the force hammer at 1.984 Hz, close to its natural frequency.
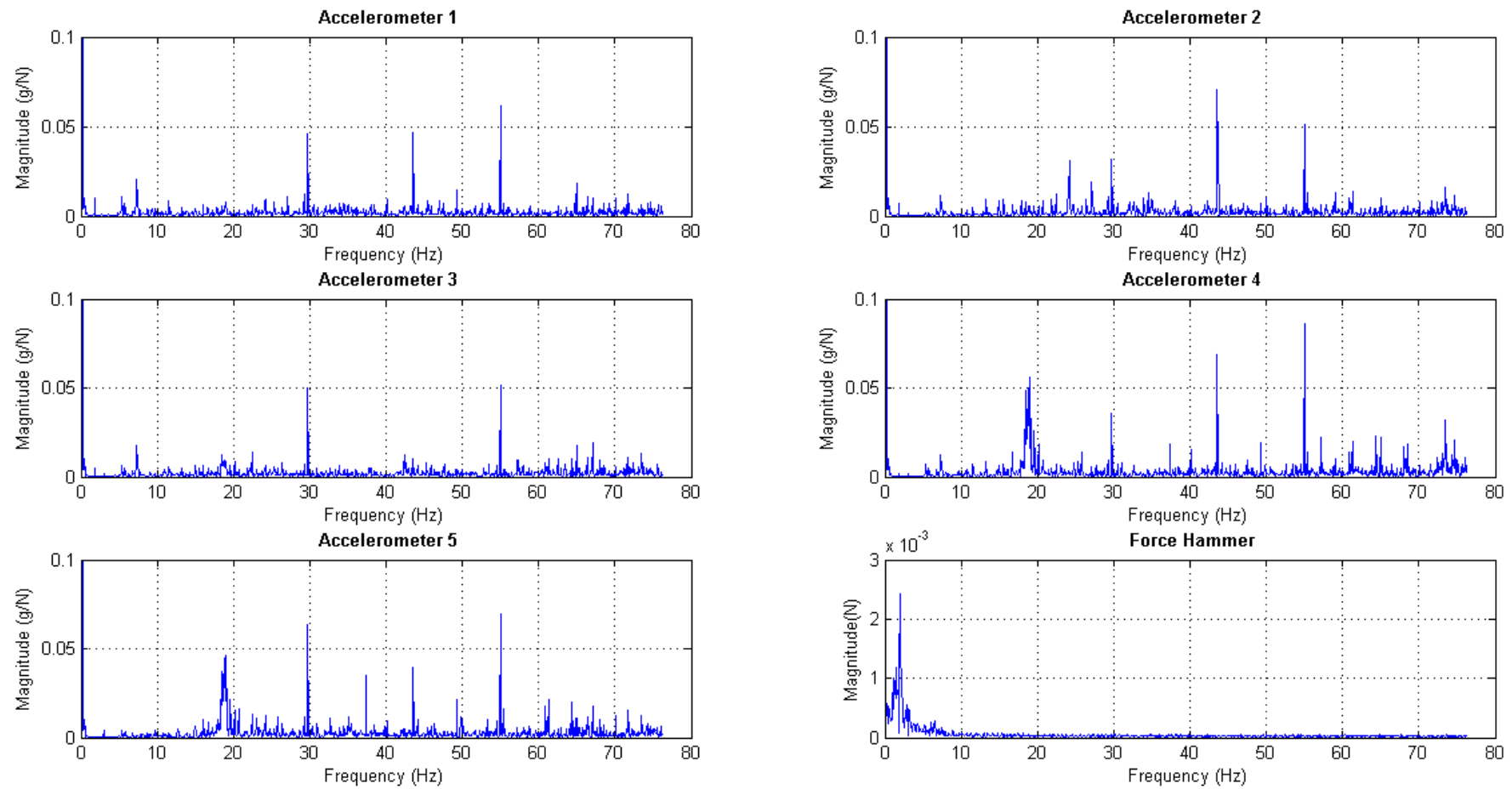
Figure 5.10 Frequency spectrum showing the response at each accelerometer position on the 4.5m long Carter wind turbine blade for ten seconds of data read at a rate of 10 kSamples per second, when the blade is orientated at an angle of ($\theta_{G1} = 0°$) (flapwise direction). Accelerometer 1 is nearest the tip, 5 is nearest the root. The plot also shows the input excitation exerted on the blade.

5.3 CONCLUSIONS

In this chapter, details of further evidence for the potential for MEMS accelerometers to be integrated into a condition monitoring system were presented. A novel static calibration procedure was described and applied to measured data from a real wind turbine blade. The author successfully demonstrated the application of MEMS accelerometers to a real medium-sized turbine blade in a laboratory test. Static calibration was applied to the devices in situ and conversion of the local coordinates for each 3-axis device to a global coordinate system relevant to the blade was shown to make the measurements from the different devices comparable.

Most wind turbine blades have non-linear and curved surfaces with varying and obscure shapes to capture as much energy in the wind as possible and specifically towards the root end of the blade to attach easily and efficiently on to the hub. Calibrating these accelerometers provides a physical meaning to the electrical output signals typically measured in Volts in relation to motion. It allows uniformity in simultaneous measurement across accelerometers in-use. The calibration procedure saves time on individual calibration of accelerometers and potential associated costs when these accelerometers are applied in-field on operating wind turbine blades. In a real life scenario on an operating wind turbine, the blade can easily be stopped for a short period at chosen positions to allow the installed accelerometers to be calibrated.

6 APPLICATION OF MEMS ACCELEROMETERS: ICE LOADING SIMULATION

The Carter [227] wind turbine blade was obtained on loan and therefore no physical damage could be inflicted on the blade to investigate the accelerometer capabilities under different damage conditions. Therefore, ice loading, a common and frequent occurrence on turbine blades, was simulated on the medium-sized Carter blade using attached weights, to investigate the capability of the MEMS accelerometers in detecting loads.

Wind turbine blades are the most affected components of ice accretion caused by the wind speed and the relative wind speed due to rotation of the blades [239]. Ice accretions on the blades even in small amounts have been found to deteriorate the blades' aerodynamic performance [240]–[242]. The weight of the ice causes aerodynamic imbalances that lead to an increase in wear and the consequent shortening of the blades' lifetime, causing reduction in energy production. Generally, wind turbines are shut down during severe icing events, which also leads to loss of energy production and consequently, economic losses. Traditional ice detection methods use meteorological equipment e.g. wind gauges, anemometers, temperature change measurements using thermometers and or thermocouples etc., to detect conditions for icing. However, these methods do not detect ice on blades. There are also several ice detection instruments on the market but studies [242]–[246] suggest that improvements and enhancements in measurement sensitivity and accuracy of these instruments are needed. There are therefore strong and urgent needs for new and reliable icing measurement instruments at the blades of wind turbines especially for point measurements.

MEMS accelerometers were therefore examined in this section as potential new introductions into the ice loading detection and measurement market. The medium-sized wind turbine blade was loaded at the tip using a specially designed and constructed frame and attached weights. The blade responses were measured via the accelerometers. The blade tip was specifically chosen for measurements because research studies from experiments and simulation [84], [88], [247], [248] show that the sections near the tip of the blade where the blade chord length and thickness is less, is where ice accretion occurs the most. Icing is less severe both in terms of local ice mass and in terms of ice thickness towards the root end of the blades, where the blades' profiles are larger and thicker. The effect of temperature variation is also more significant for the blade area from the tip to the centre.

Changes in blade resonant frequencies have been identified as an indirect ice detection method [242], [244], [246]. Therefore, the blade was excited using a Visaton exciter [211] and frequency response measurements were deduced for comparing increasing loads induced on the blade. A chirp input excitation signal was exerted on the blade, mimicking continuous or sustained periods of vibration induced by the wind on operating turbine blades during icing events.

Overall, the tests outlined in this section, aimed to:

(a) Test the exciter as an excitation source.
(b) To use this to further investigate whether ice loading could be detected.

6.1 METHODOLOGY

A special loading frame was designed and built using wood, foam and bolts. Wood was used because it is light in weight. The frame weighed 1.6 kg and a hook which weighed 1.2 kg was attached to the frame, to suspend the loads. Two bolts were used to sandwich and clamp the two sides of the wooden frame together as illustrated in the sketch in Figure 6.1a and the photograph in Figure 6.1b. Thick foam layers were used to line the inner walls of the wooden frame to protect the blade and provide padding against surface abrasion and scratches.

(a)

(b)
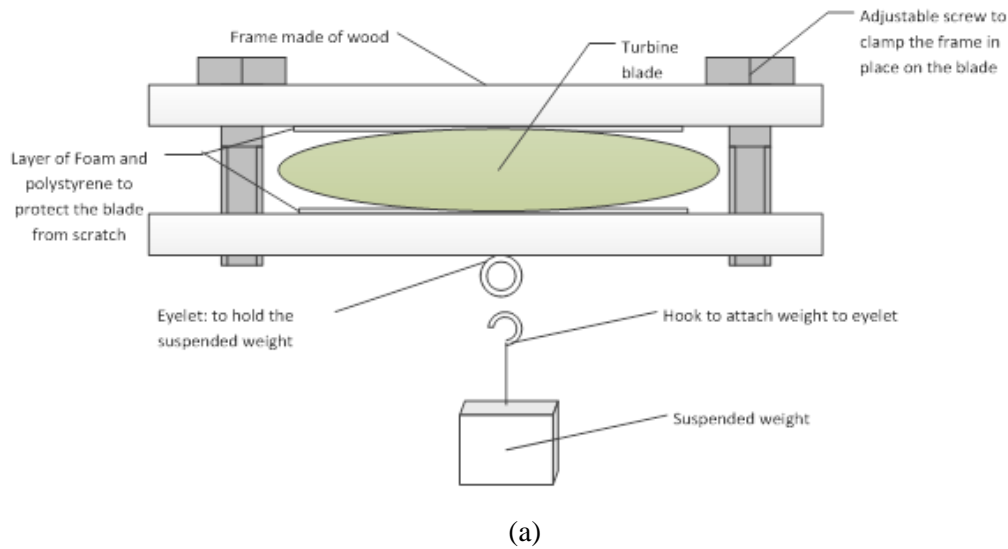
Figure 6.1 (a) An annotated diagram illustrating the frame design used to suspend varying weights from the Carter wind turbine blade. (b) Photograph of frame as-built and the hook.

The measurements in this chapter represent point loading and not full loading of the wind turbine blade. However, the effect of the point loading on the full blade length is investigated. Using density, mass and volume relationships, and an assumed thickness of 5 mm accretion on the turbine blade, the maximum weight of ice was estimated as follows:

Consider the measurement distance along the entire blade length, L = 4.5 m and the tip width, b = 0.3 m at the point of loading, the surface area, $A = 2Lb$ was calculated as 2.7 m². Assuming a 5 mm ice accretion thickness with a density of 900 kg/m³ [249], the volume of 5 mm of ice accretion was determined as 13.5×10^{-3} m³. Therefore, the maximum weight of ice for a 5 mm accretion was calculated as 12.2 kg. This was set as the maximum weight not to be exceeded during measurements (including the frame). Metal weights shown in Figure 6.2 were therefore attached at the bottom of the frame. The weight sizes were 1 kg and 2.5 kg and combinations of the weights were used to obtain loads of 3.5 kg, 5 kg, 6 kg and 7 kg. The weights were increased gradually to simulate the changing phases in ice loading and accretion on wind turbine blades. 7 kg was the maximum load exerted on the blade to avoid exceeding the blades loading limit and subsequently damaging the blade.
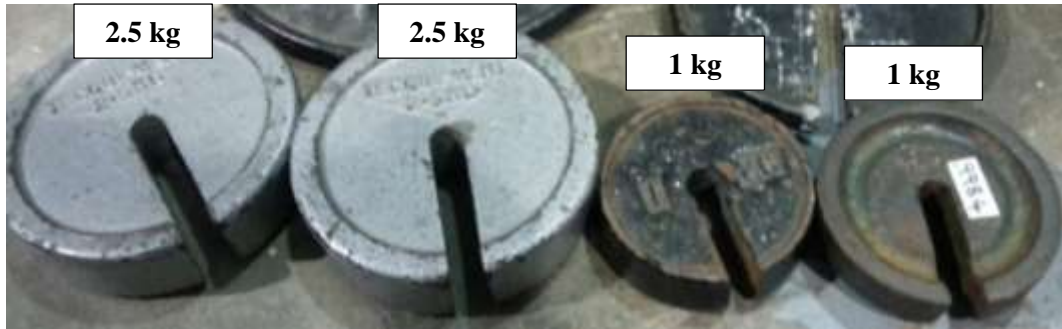
Figure 6.2 Picture showing the weights used to load the blade.

Considering the frame and hook which have a combined mass of 2.8 kg and published material [249], the equivalent type of accreted ice for each of the weights 1 – 7 kg were deduced as follows;

Table 6.1 Typical properties of accreted atmospheric ice [249] relative to applied weights.

| Type of Ice | Typical Density (kg/m^3) | Adhesion and Cohesion | General Appearance | | Point Loading Weight (kg) | * Estimated Density for 5 mm ice thickness (kg/m^3) |
			Colour	Shape		
Glaze	*900*	*Strong*	*Transparent*	*Evenly distributed/icicles*	*12.2*	*900*
Hard rime	600 - 900	Strong	Opaque	Eccentric, pointing windward	7.0 6.0	725.92 651.85
Wet snow	300 - 600	Weak (forming) Strong (frozen)	White	Evenly distributed/eccentric	5.0 3.5 2.5	577.78 466.67 392.59
Soft rime	200 - 600	Low to medium	White	Eccentric, pointing windward	1.0 0	281.48 207.41

* *Calculated using the combined weight of the mounting frame, hook and attached weights 1 – 7 kg.*

Ten additional ADXL335 MEMS accelerometers were attached (glue mounted) to the 4.5 m long blade to fully characterise the blade's vibration and modes. With increased measurement points, it becomes easier to animate the blade movement and response to input excitations. Figure 6.3 shows the positions of all accelerometers on the blade. Accelerometer 1 was used as the reference accelerometer for all measurements conducted on the blade. All measurements were conducted with the turbine blade orientated at $\theta_{G1} = 0°$ (flapwise direction) as shown in Figure 6.3.

Limited by the number of channels on the 16-channel NI-USB 6251 [202] data acquisition system, measurements were taken in sections for each weight suspended on the blade as shown in Figure 6.3. The blade length was divided into five sections (0.5 m from the tip for section 1 and then 1 m divided each section after). Accelerometer output responses were logged using this sectioning method but accelerometer 1 was kept as the reference in all measurements. Using LabVIEW SignalExpress software [174], 48 kSamples of data were read at a rate of 16 kHz for three seconds for each weight attached for each section.
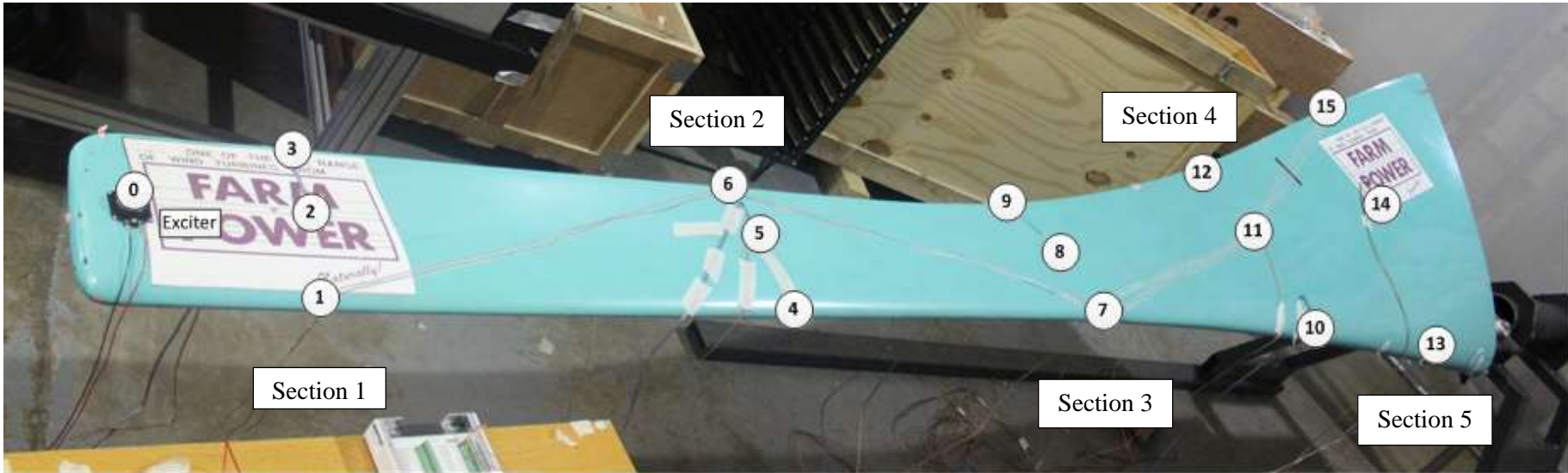
Figure 6.3 An annotated picture showing the accelerometer positions along the Carter wind turbine blade, the electromagnetic exciter location and the measurement sections.

6.1.1 ELECTROMAGNETIC EXCITER TEST

A Visaton Ex 60 S electromagnetic exciter [211] was positioned close to the tip of the blade as shown in Figure 6.3 and was used to induce a 0.9 V chirp signal with 0 - 300 Hz start and stop frequency. The signal was generated in MATLAB [144] and fed through to the exciter via its contact pins connected to an audio amplifier [212] connected to an analogue-output channel on the 16-channel NI-USB 6251 data acquisition system. The exciter was glued to the turbine blade for rigidity and was used because it offers a fully self-contained unit that could potentially be used in a real system to trigger measurement by the accelerometer. It weighed 0.12 kg and had a diameter of 60 mm.

Figure 6.4 shows an annotated diagram of the electromagnetic exciter and its characteristic graph which was obtained by varying the input frequency of a 20.6 Vp-p sine wave on a function generator and measuring the exciter output via an oscilloscope at its output pins.
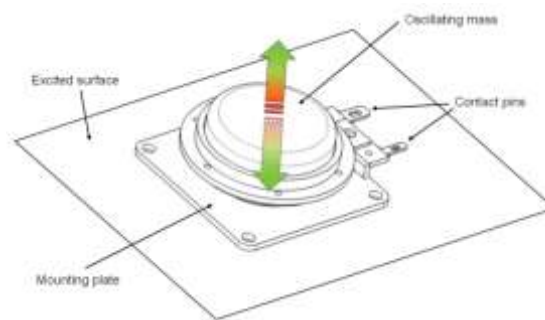
(a)
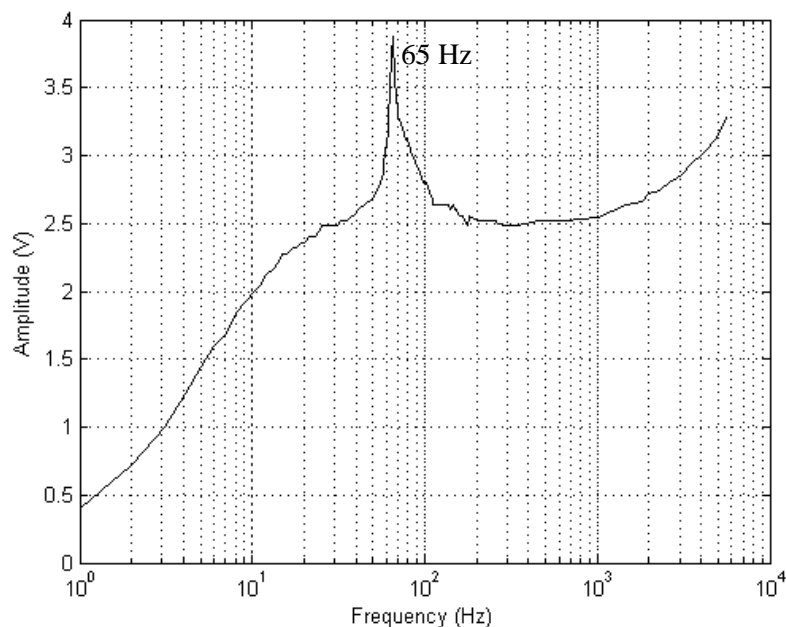
(b)

Figure 6.4 (a) An annotated diagram showing the Visaton exciter used to excite the blade. The exciter had a diameter of 60 mm diameter, 8 Ω impedance and weighed 0.12 kg.
(b) A characteristic plot of the Visaton Ex 60 S exciter which shows its measured resonance at 60 Hz.

The blade was loaded 16.5 cm away from the tip between the exciter and accelerometer 1 position as shown in the picture in Figure 6.5. Baseline measurements without the frame and hook attached to the turbine blade were taken to make comparisons and to investigate any variations as the blade was loaded. Figure 6.6 shows an example of the weights hanging from the turbine blade.
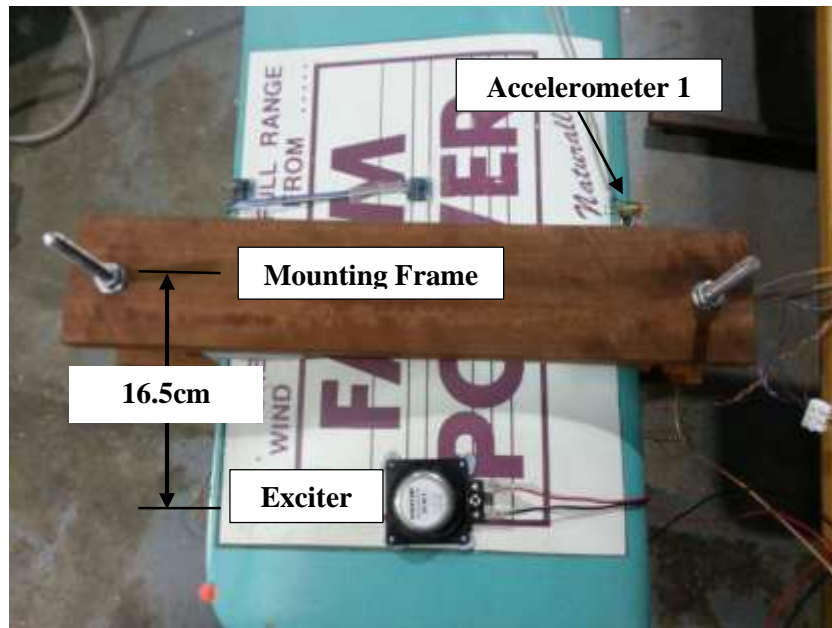
Figure 6.5 Picture showing the exciter and loading frame on the turbine blade.
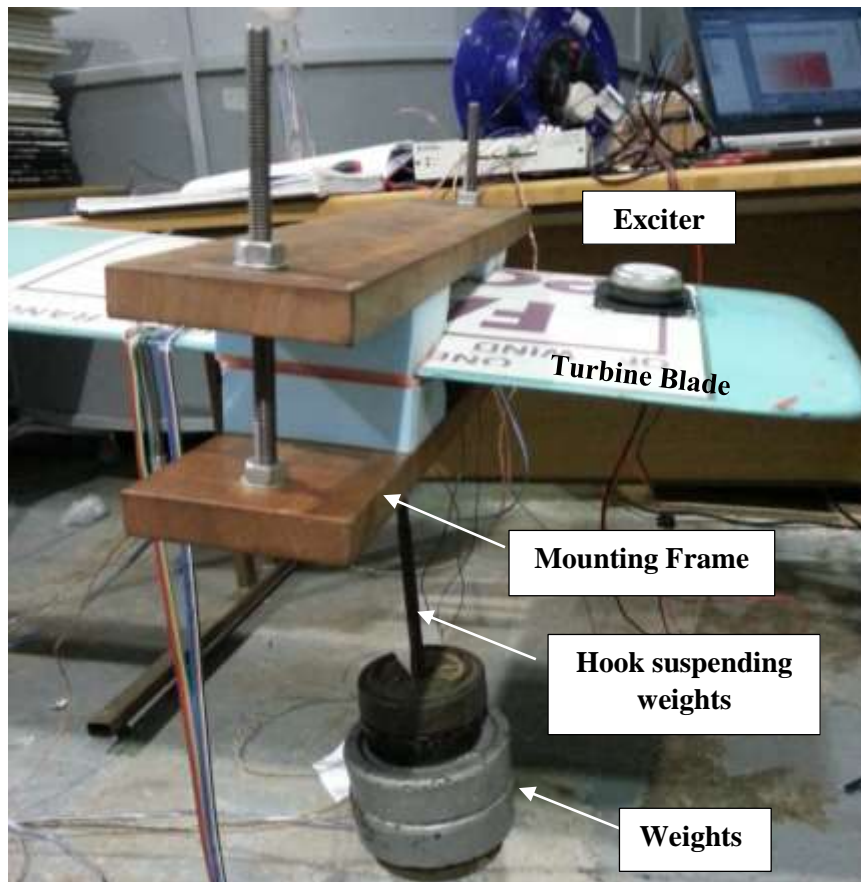
Figure 6.6 Picture showing 7 kg weight suspended from the medium-sized turbine blade at the tip end.

6.2 RESULTS AND DISCUSSIONS

Figure 6.7 shows the input chirp excitation signal applied to the wind turbine blade via the exciter. The initial peak at 1 V signifies the active point of the exciter i.e. the exciter and amplifier system are switched on to excite the blade and log data. The sudden change causes the voltage to rise and it quickly settles to an amplitude of 0.9 V. The signal was allowed to die out after two seconds of continuous excitation with frequency varying from 0 – 300 Hz.
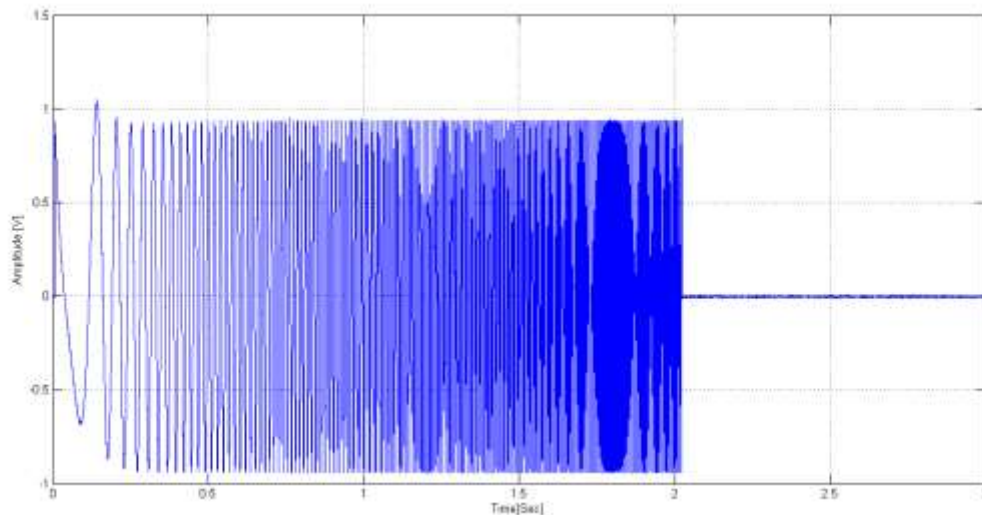
Figure 6.7 Plot showing the chirp input excitation signal exerted on the wind turbine blade via the Visaton exciter for 48 kSamples read at a rate of 16 kHz for three seconds.

Figure 6.8 – Figure 6.21 show the frequency spectra measured for each accelerometer position (from 2 at tip end -15 at root end) at the different loads applied to the turbine blade. In the graphs below, Baseline represents the measured frequency response when nothing is attached to the blade. 0 kg represents measurements taken when the frame and hook are attached to the blade but without any load attached. The remaining measurements 1 kg – 7 kg simply represent loads attached to the blade using the frame and hook.
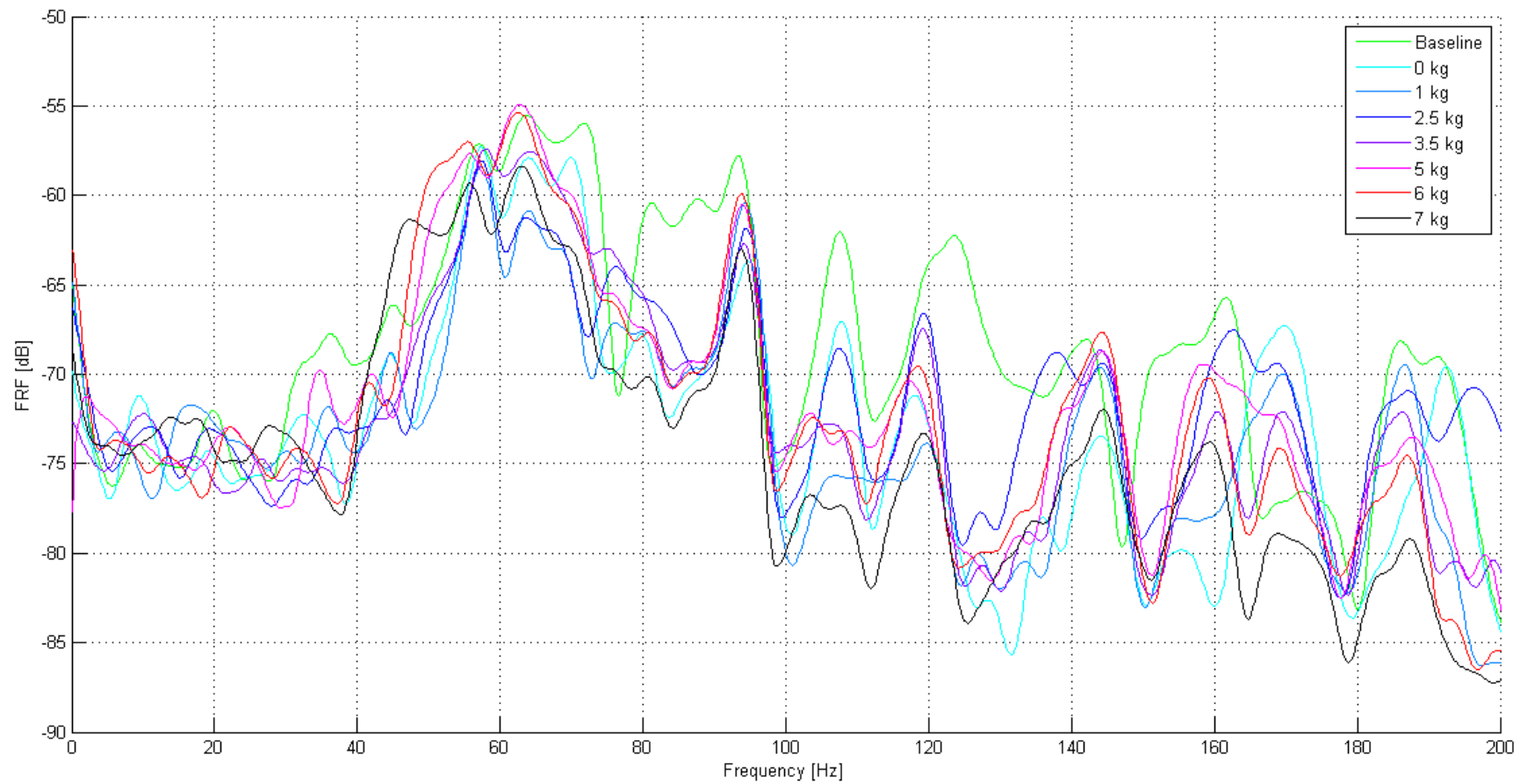
Figure 6.8 Frequency spectrum showing the frequency response function (FRF) measured at accelerometer 2 (tip end – section 1) relative to the reference position, accelerometer 1 for 48 kSamples read at a rate of 16 kHz for three seconds.
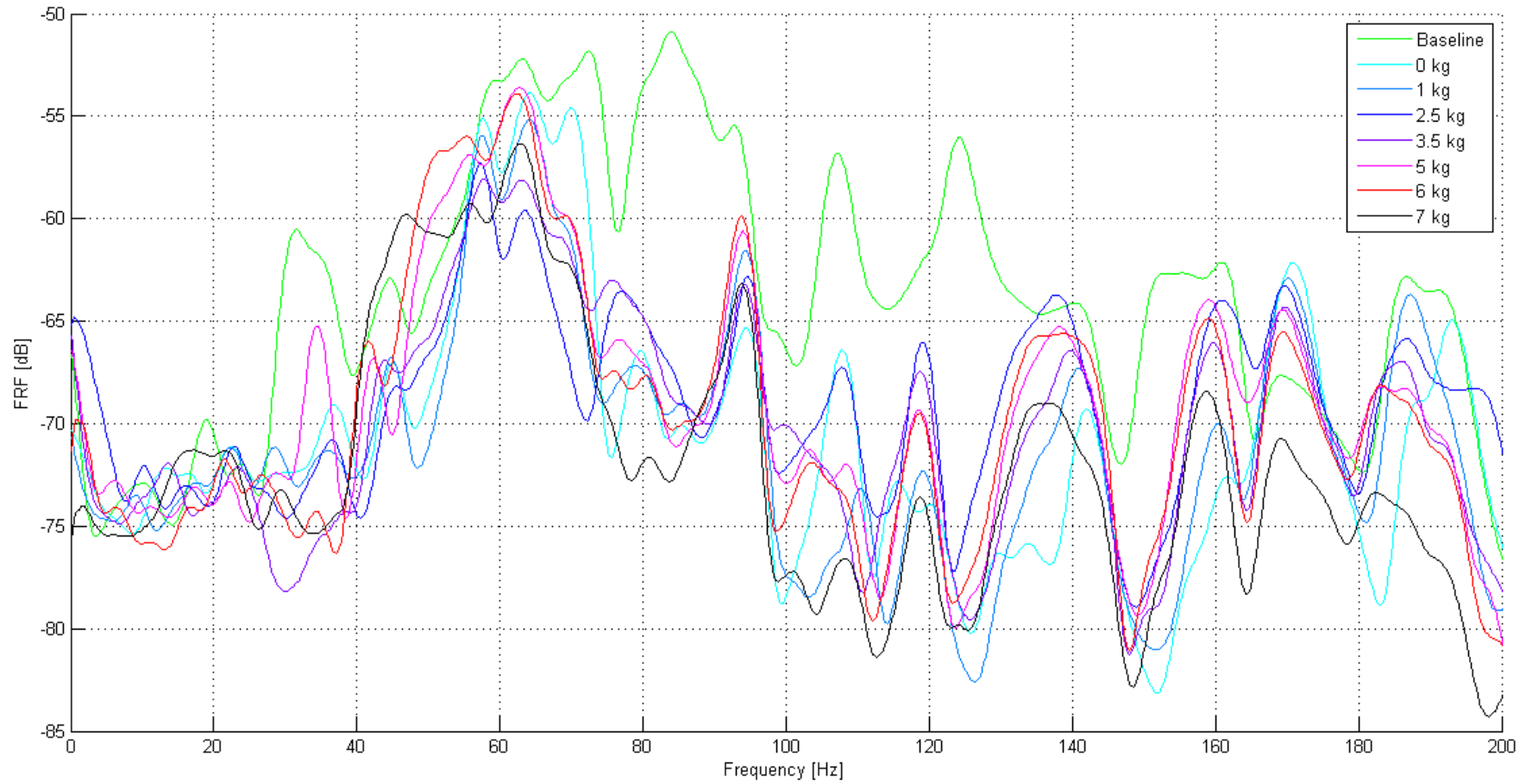
Figure 6.9 Frequency spectrum showing the frequency response function (FRF) measured at accelerometer 3 (tip end – section 1) relative to the reference position, accelerometer 1 for 48 kSamples read at a rate of 16 kHz for three seconds.
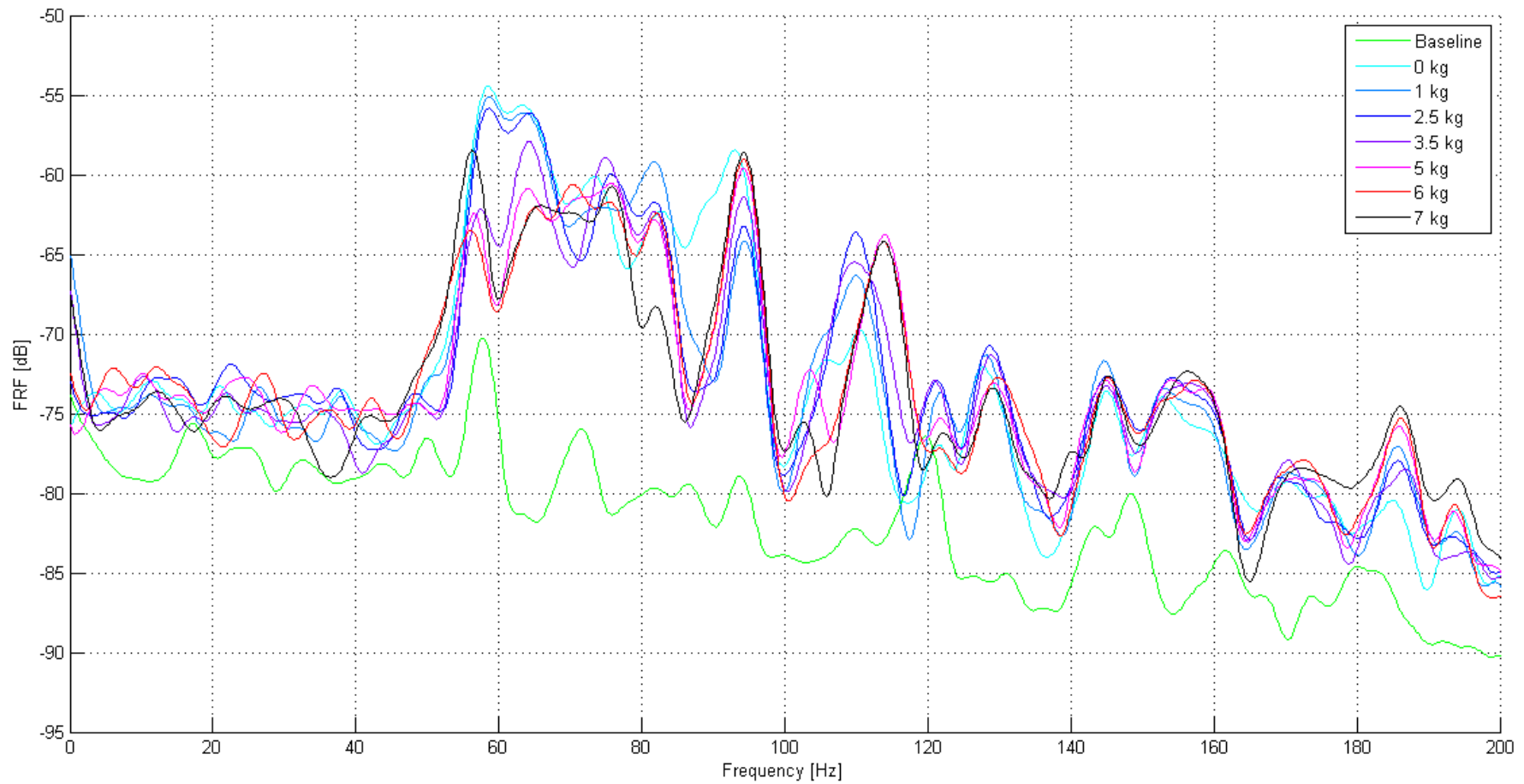
Figure 6.10 Frequency spectrum showing the frequency response function (FRF) measured at accelerometer 4 (tip end – section 2) relative to the reference position, accelerometer 1 for 48 kSamples read at a rate of 16 kHz for three seconds.
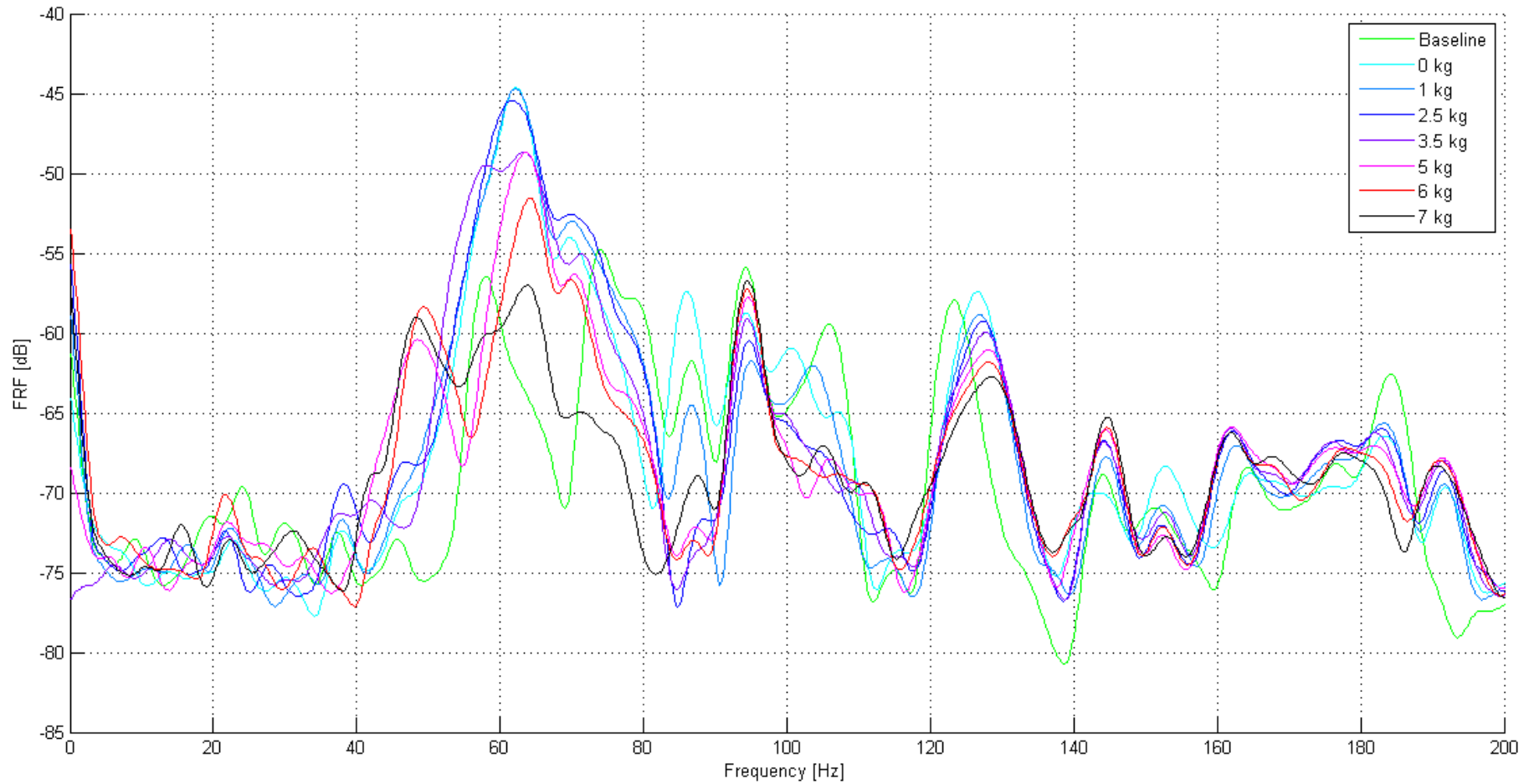
Figure 6.11 Frequency spectrum showing the frequency response function (FRF) measured at accelerometer 5 (tip end – section 2) relative to the reference position, accelerometer 1 for 48 kSamples read at a rate of 16 kHz for three seconds.
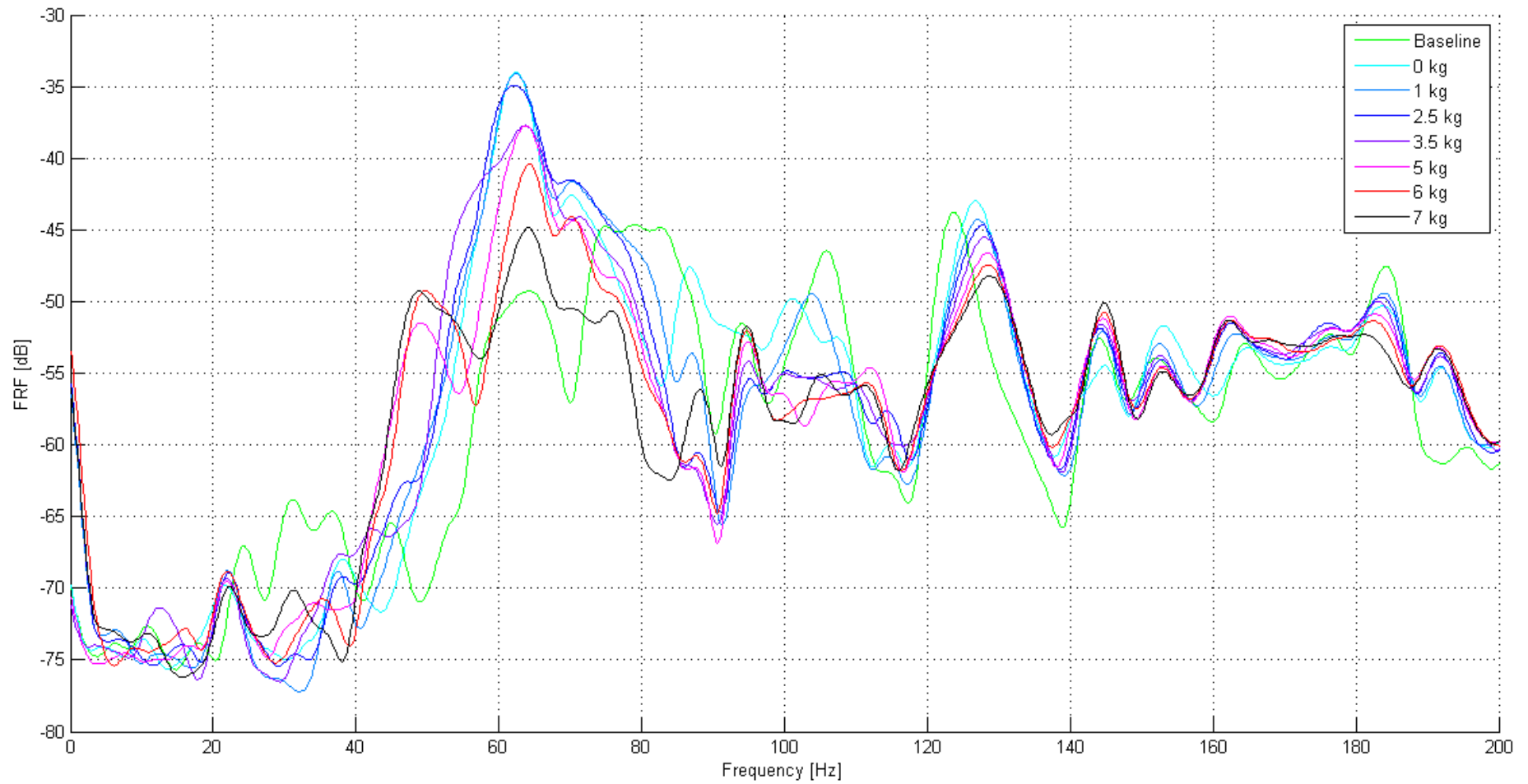
Figure 6.12 Frequency spectrum showing the frequency response function (FRF) measured at accelerometer 6 (tip end – section 2) relative to the reference position, accelerometer 1 for 48 kSamples read at a rate of 16 kHz for three seconds.
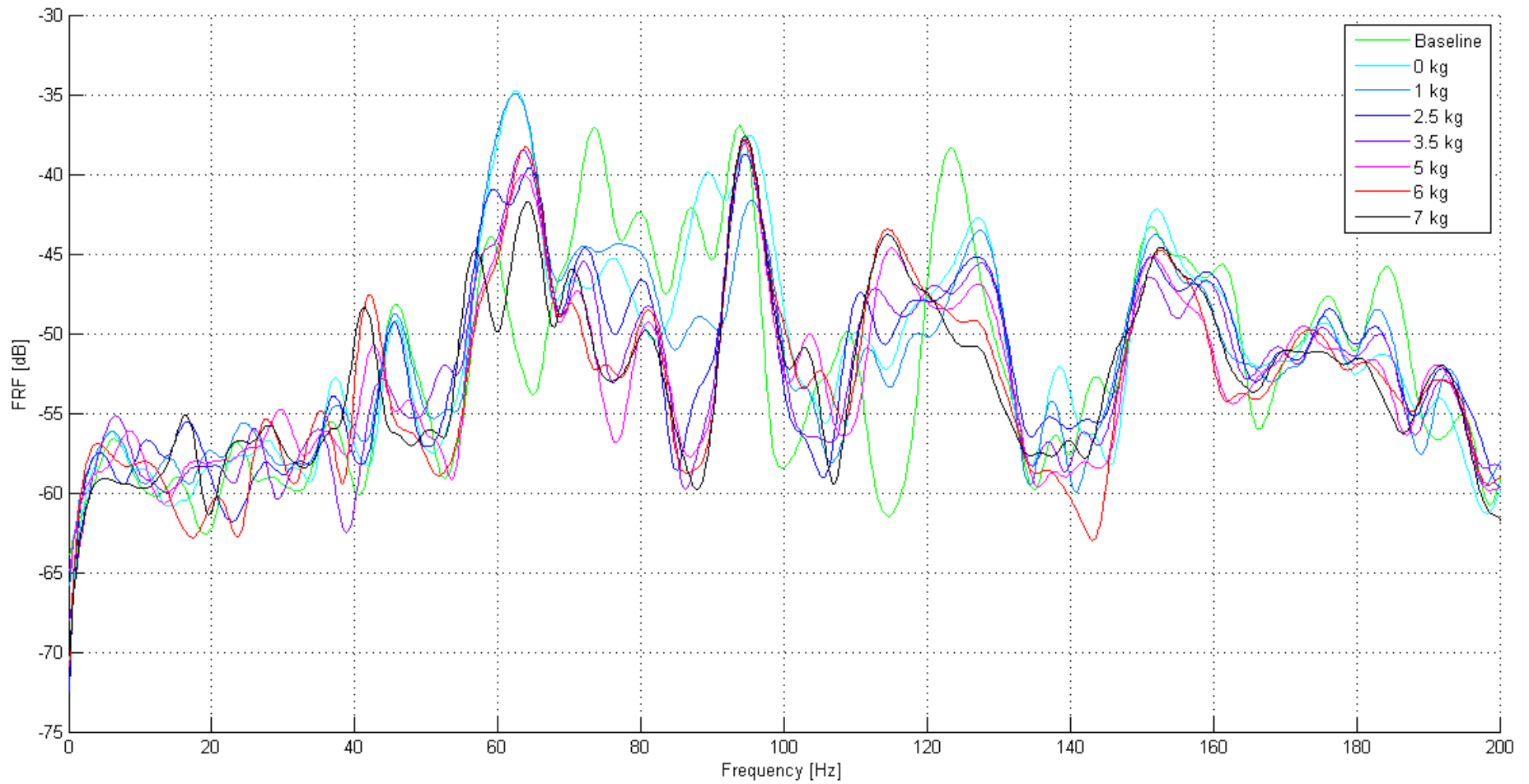
Figure 6.13 Frequency spectrum showing the frequency response function (FRF) measured at accelerometer 7 (middle – section 3) relative to the reference position, accelerometer 1 for 48 kSamples read at a rate of 16 kHz for three seconds.
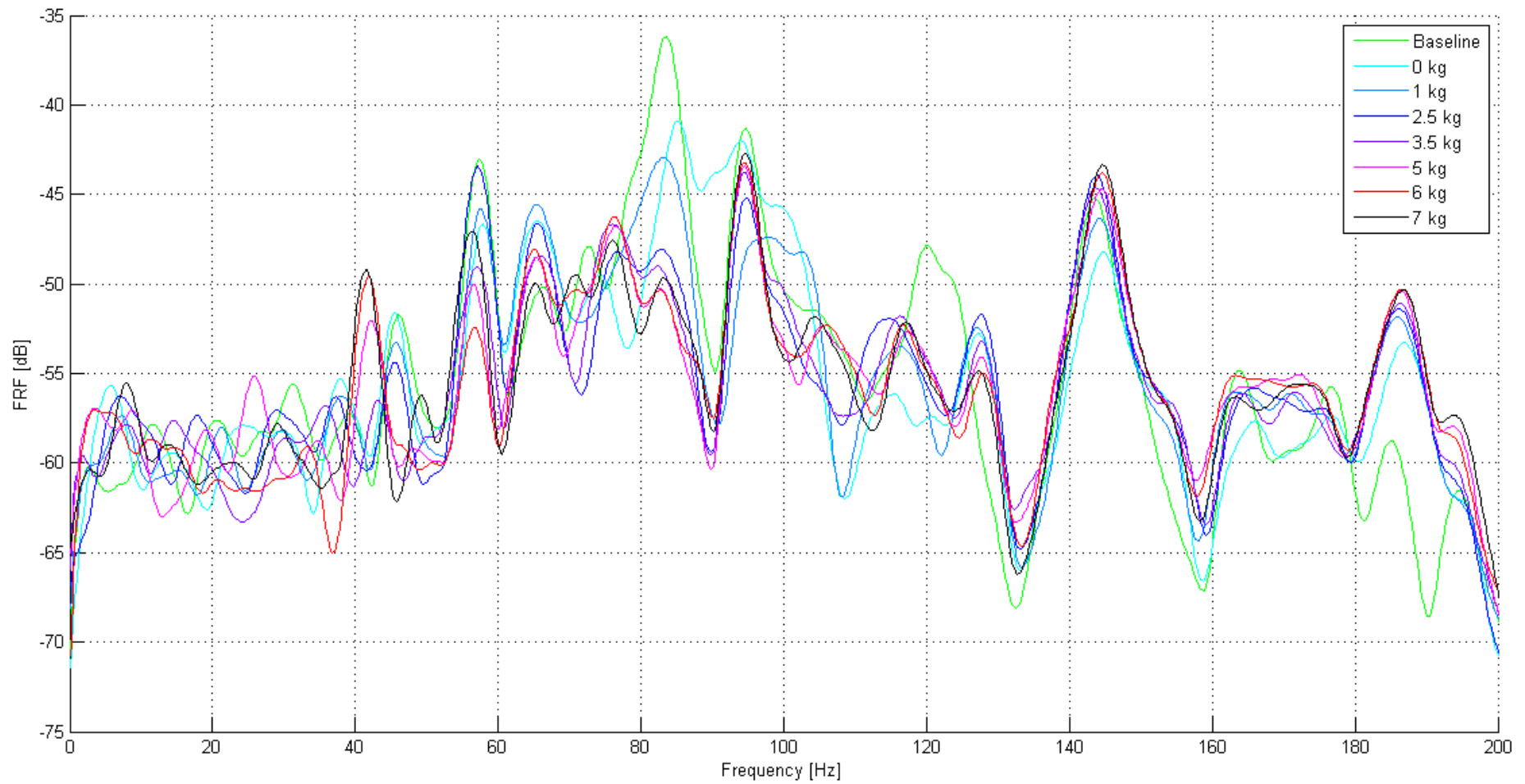
Figure 6.14 Frequency spectrum showing the frequency response function (FRF) measured at accelerometer 8 (middle – section 3) relative to the reference position, accelerometer 1 for 48 kSamples read at a rate of 16 kHz for three seconds.
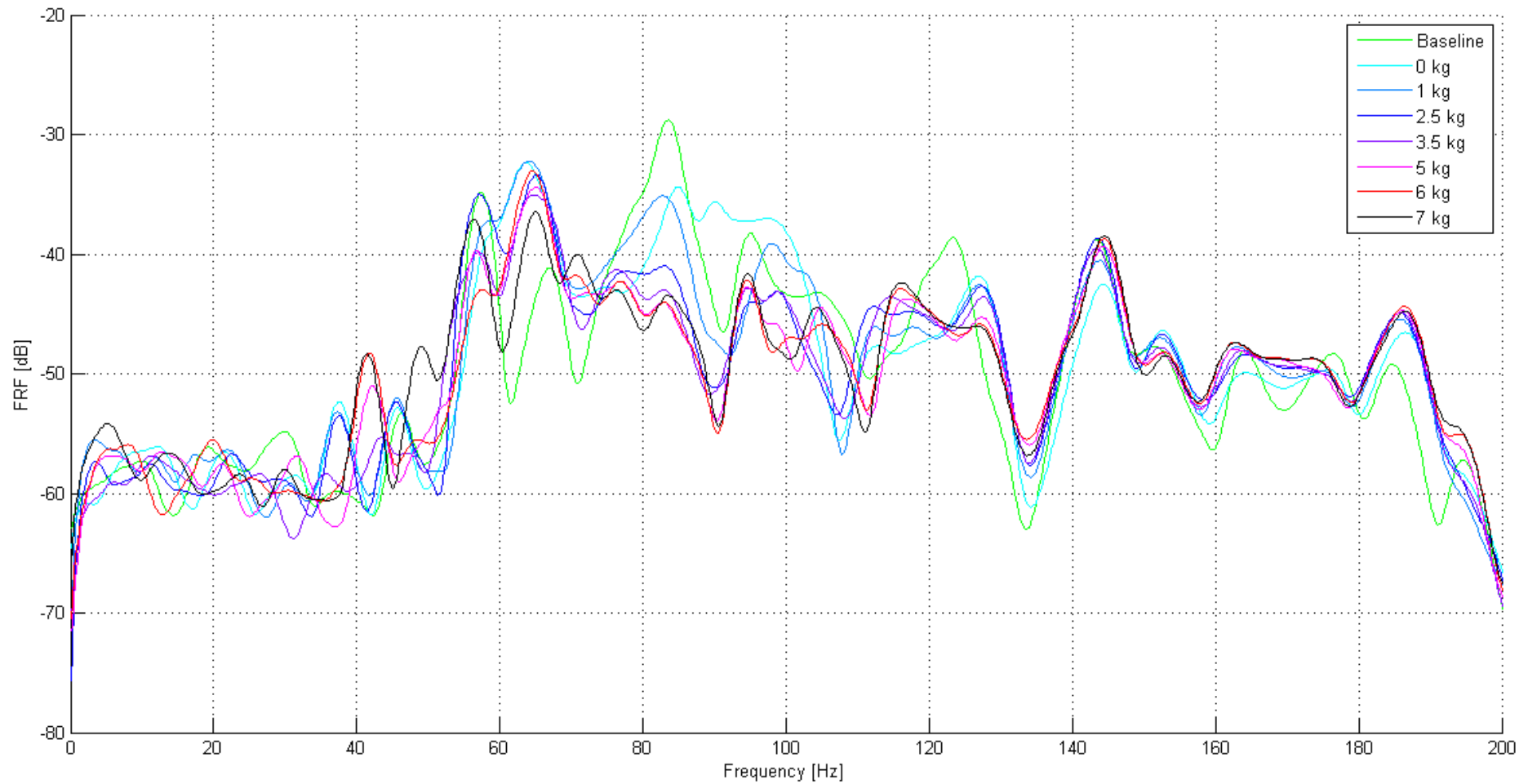
Figure 6.15 Frequency spectrum showing the frequency response function (FRF) measured at accelerometer 9 (middle – section 3) relative to the reference position, accelerometer 1 for 48 kSamples read at a rate of 16 kHz for three seconds.
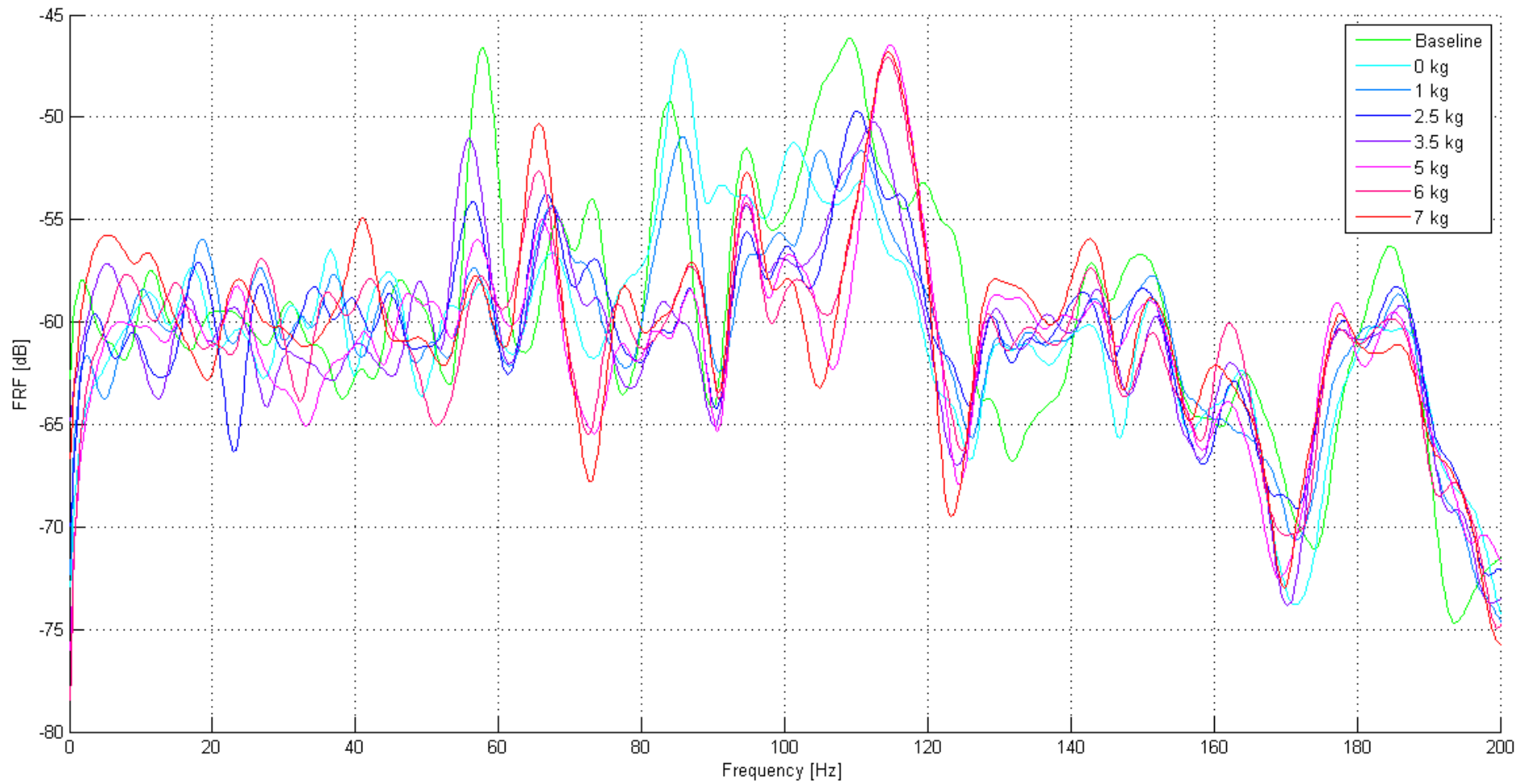
Figure 6.16 Frequency spectrum showing the frequency response function (FRF) measured at accelerometer 10 (root end – section 4) relative to the reference position, accelerometer 1 for 48 kSamples read at a rate of 16 kHz for three seconds.
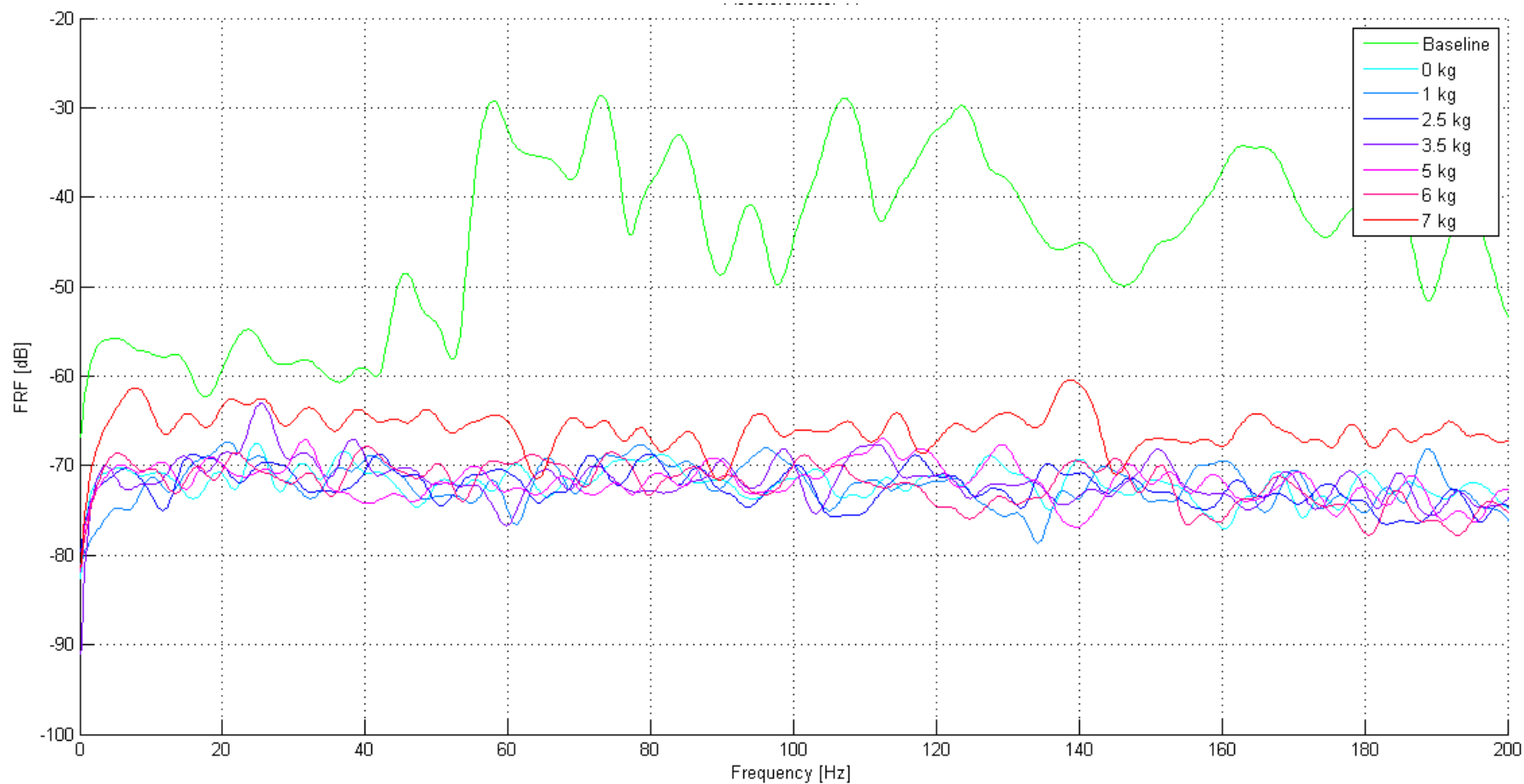
Figure 6.17 Frequency spectrum showing the frequency response function (FRF) measured at accelerometer 11 (root end– section 4) relative to the reference position, accelerometer 1 for 48 kSamples read at a rate of 16 kHz for three seconds.
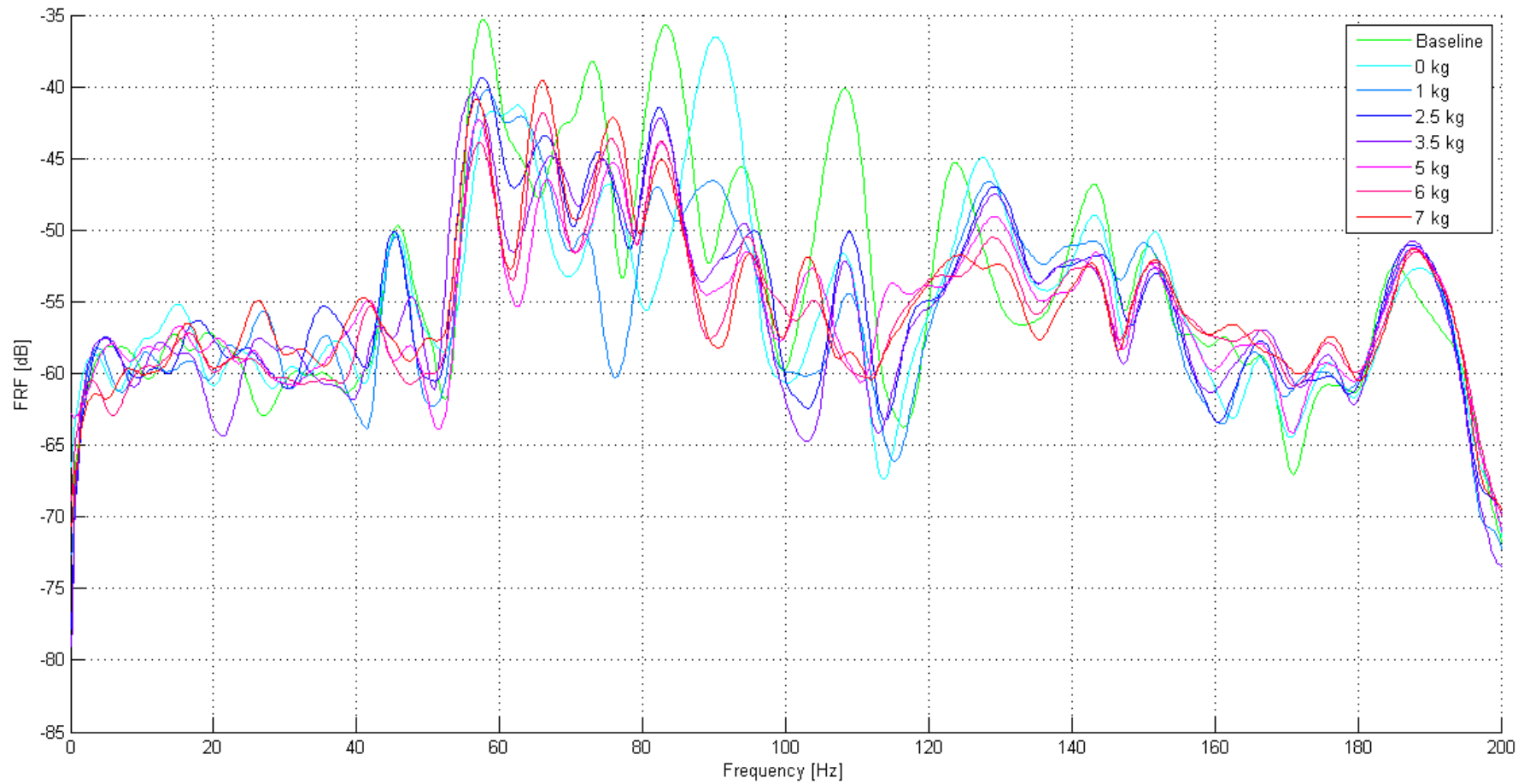
Figure 6.18 Frequency spectrum showing the frequency response function (FRF) measured at accelerometer 12 (root end– section 4) relative to the reference position, accelerometer 1 for 48 kSamples read at a rate of 16 kHz for three seconds.
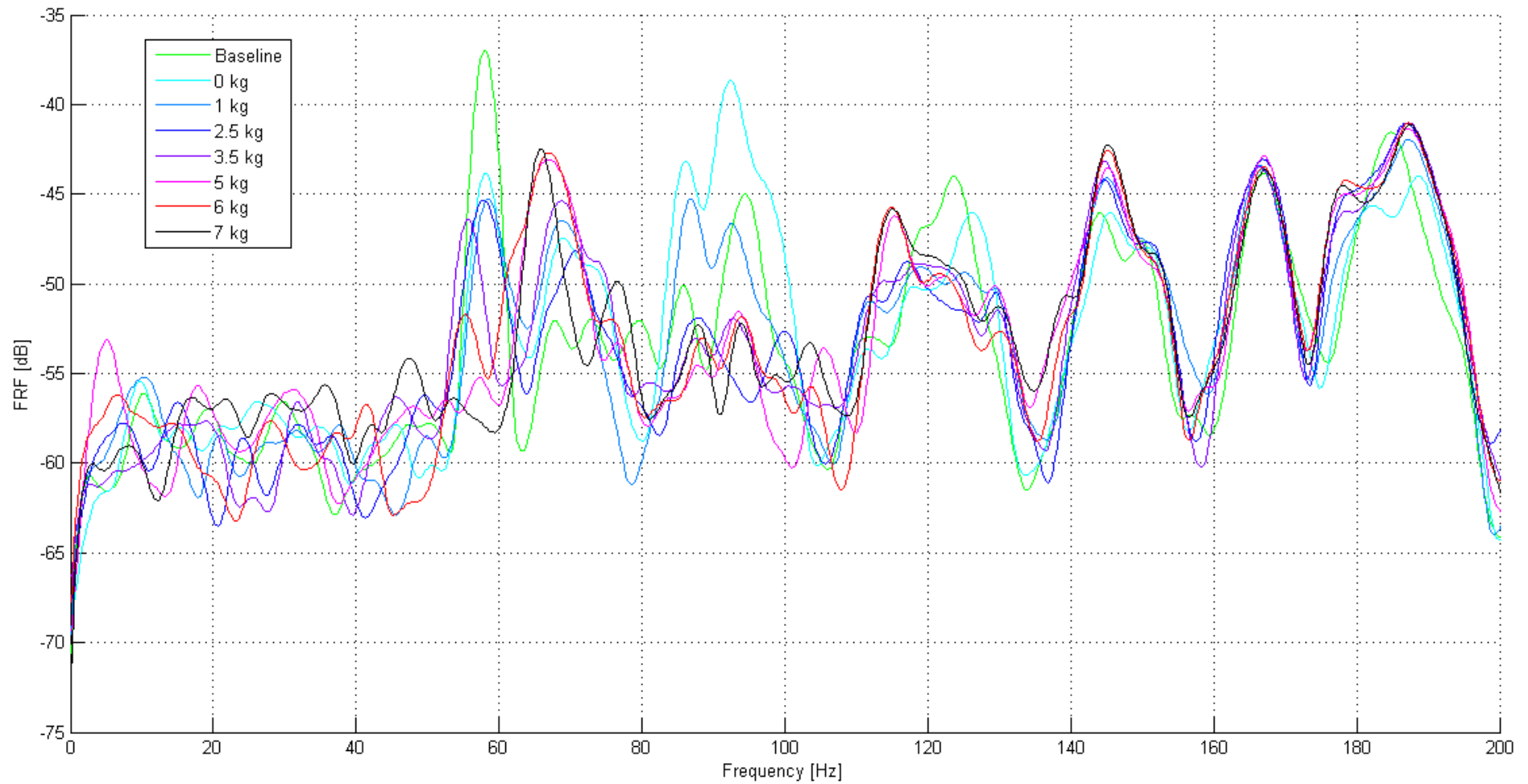
Figure 6.19 Frequency spectrum showing the frequency response function (FRF) measured at accelerometer 13 (root end– section 5) relative to the reference position, accelerometer 1 for 48 kSamples read at a rate of 16 kHz for three seconds.
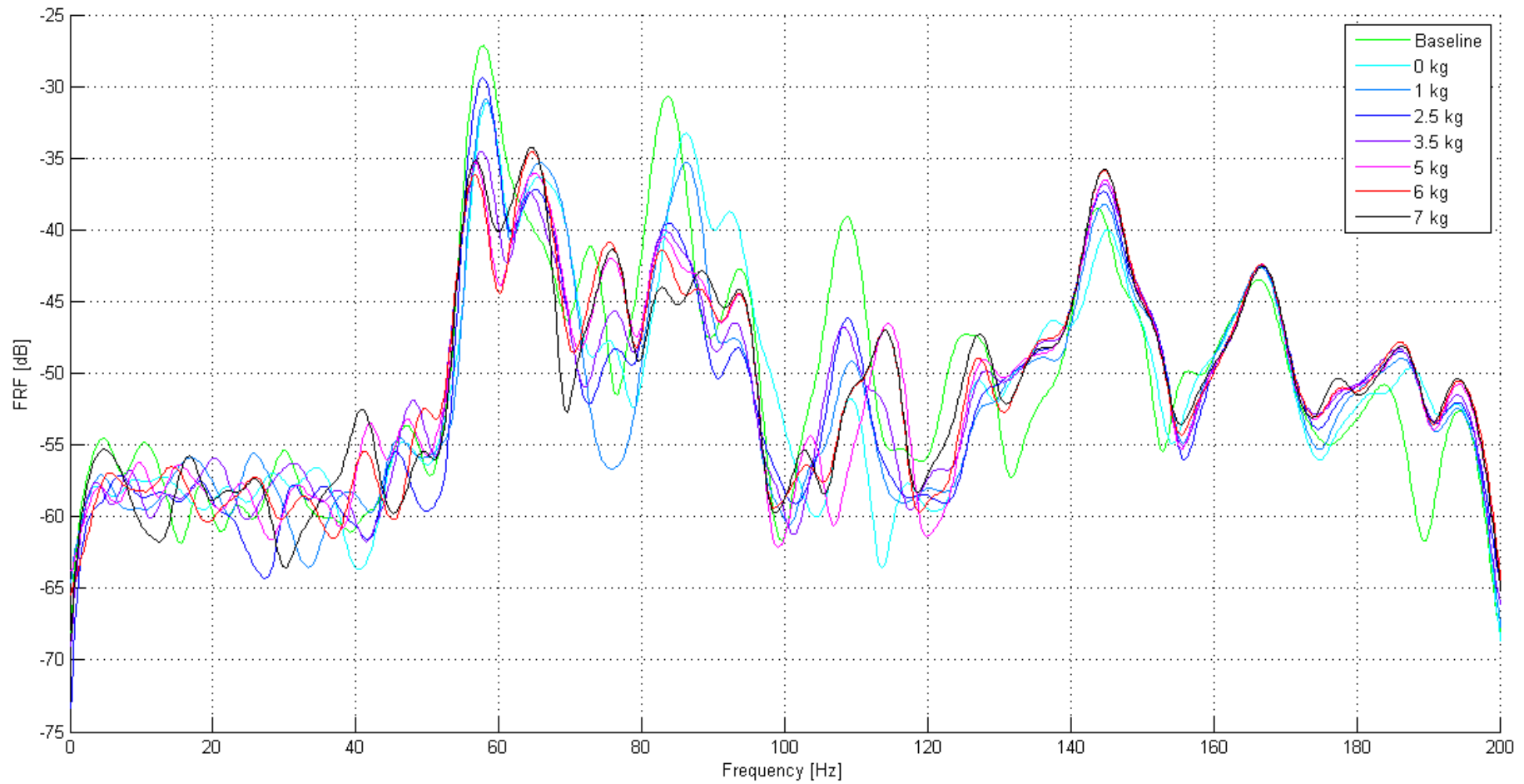
Figure 6.20 Frequency spectrum showing the frequency response function (FRF) measured at accelerometer 14 (root end– section 5) relative to the reference position, accelerometer 1 for 48 kSamples read at a rate of 16 kHz for three seconds.
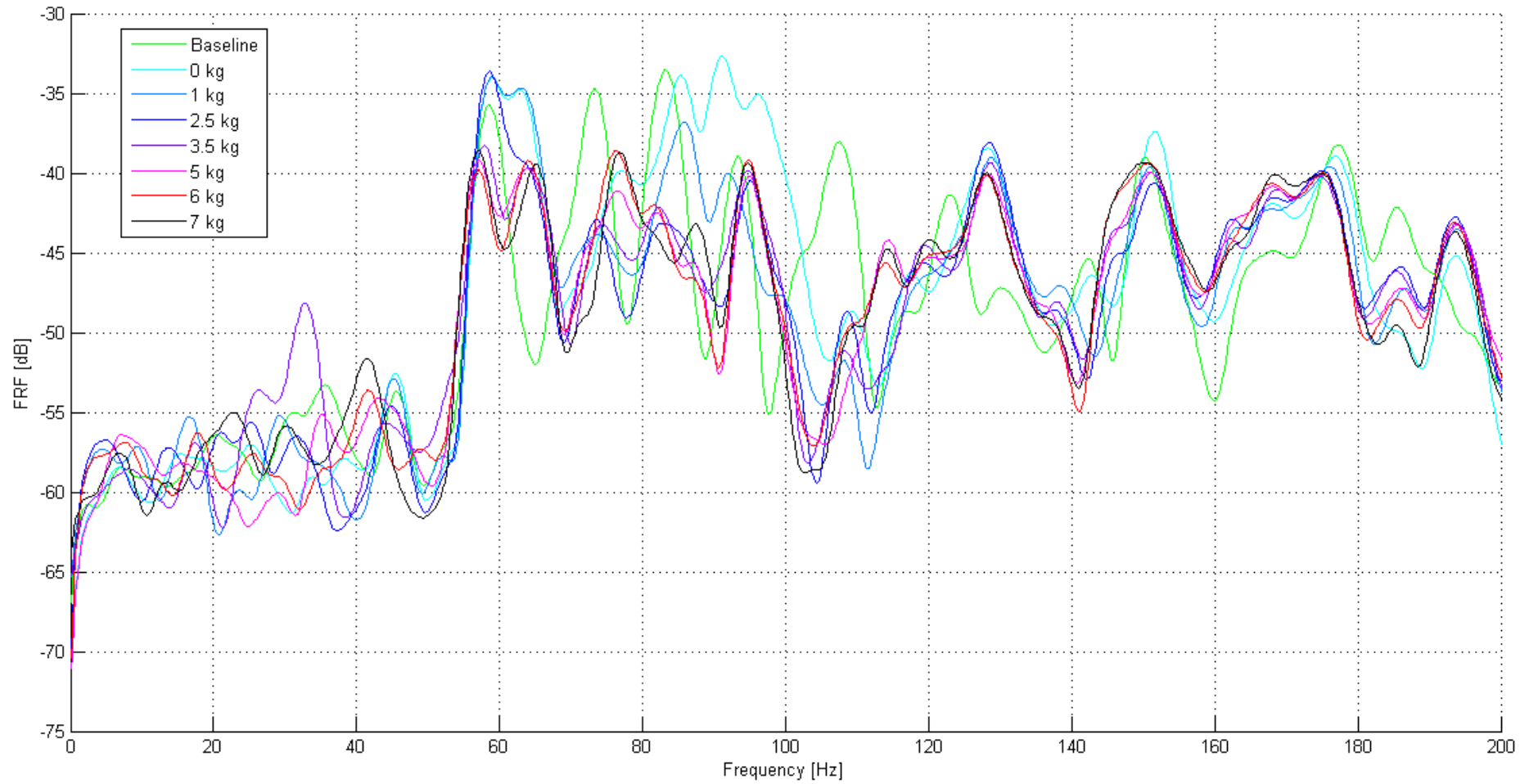
Figure 6.21 Frequency spectrum showing the frequency response function (FRF) measured at accelerometer 15 (root end– section 5) relative to the reference position, accelerometer 1 for 48 kSamples read at a rate of 16 kHz for three seconds.

The frequency response functions were plotted for each accelerometer output relative to the reference accelerometer, accelerometer 1, in response to the chirp input excitation from the electromagnetic exciter. To improve the signal to noise ratio of the measurements, smoothing was applied in MATLAB. Measurements below 50 Hz were attenuated in all spectra. Again, this effect was caused by the audio amplifier which induced high-pass filtering on the input signal to the blade and subsequently on the measured response. Nevertheless, as all measurements were recorded under these conditions, this did not affect comparisons of the results. The plots were zoomed in at each of the peaks and the frequency and amplitude measurements were recorded and used to establish trends. Zoomed in plots of the frequency peak at 90 - 98 Hz are shown for each of the accelerometers in Figure 6.22 (a) – (o).
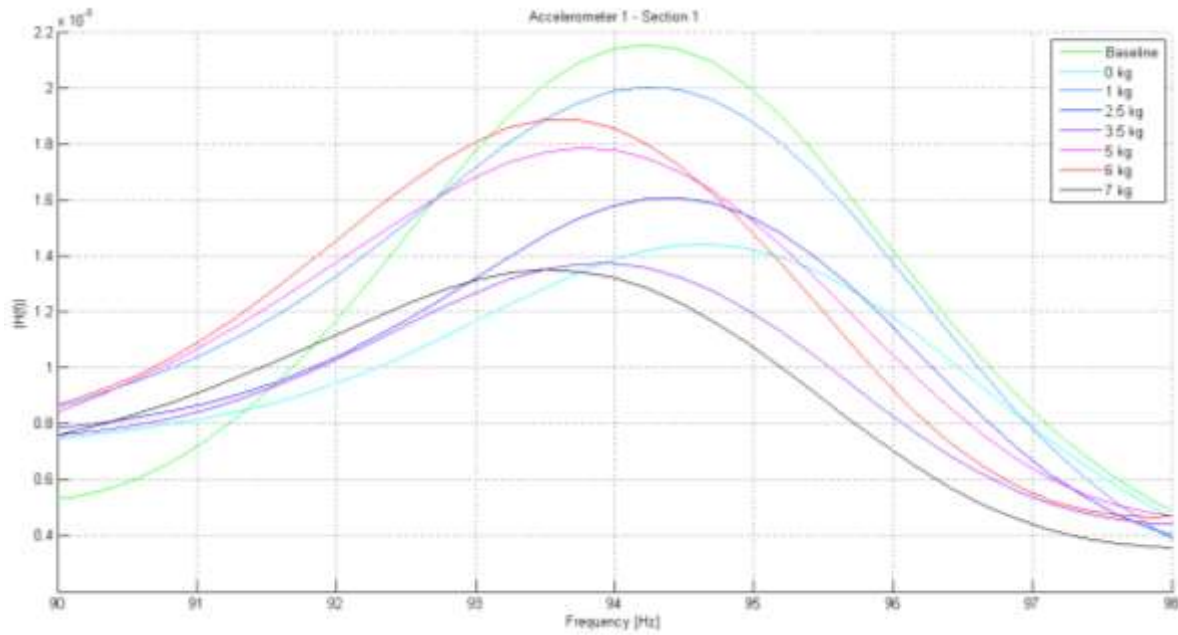
(a) Accelerometer 1 – Blade Tip End
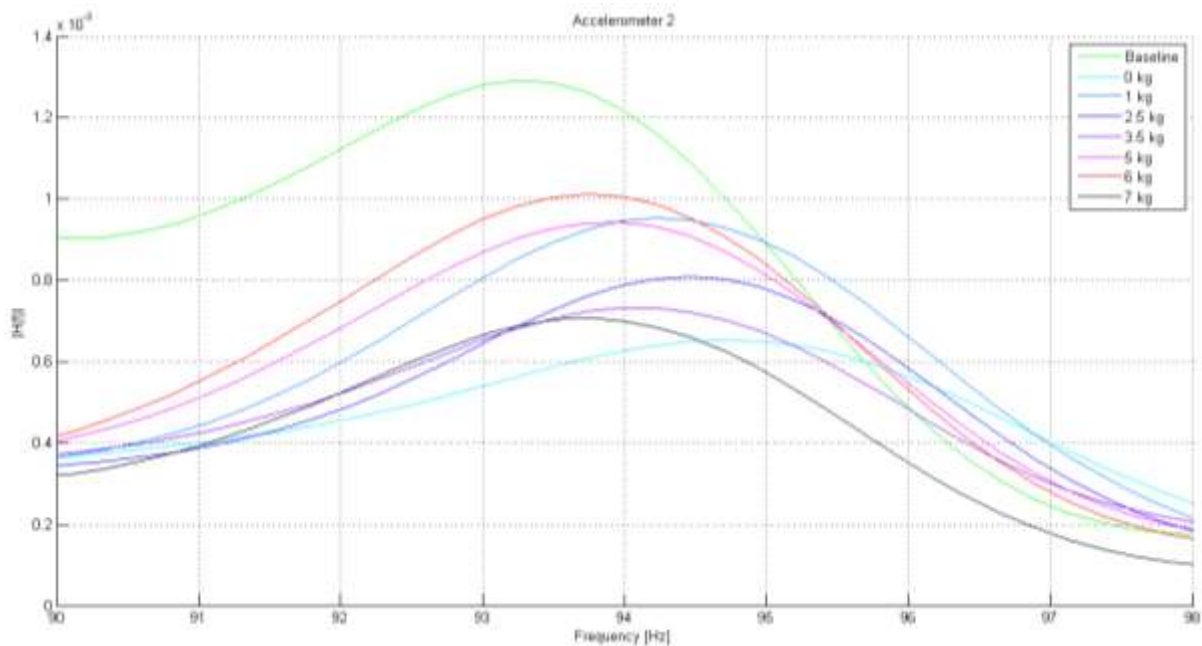
(b) Accelerometer 2
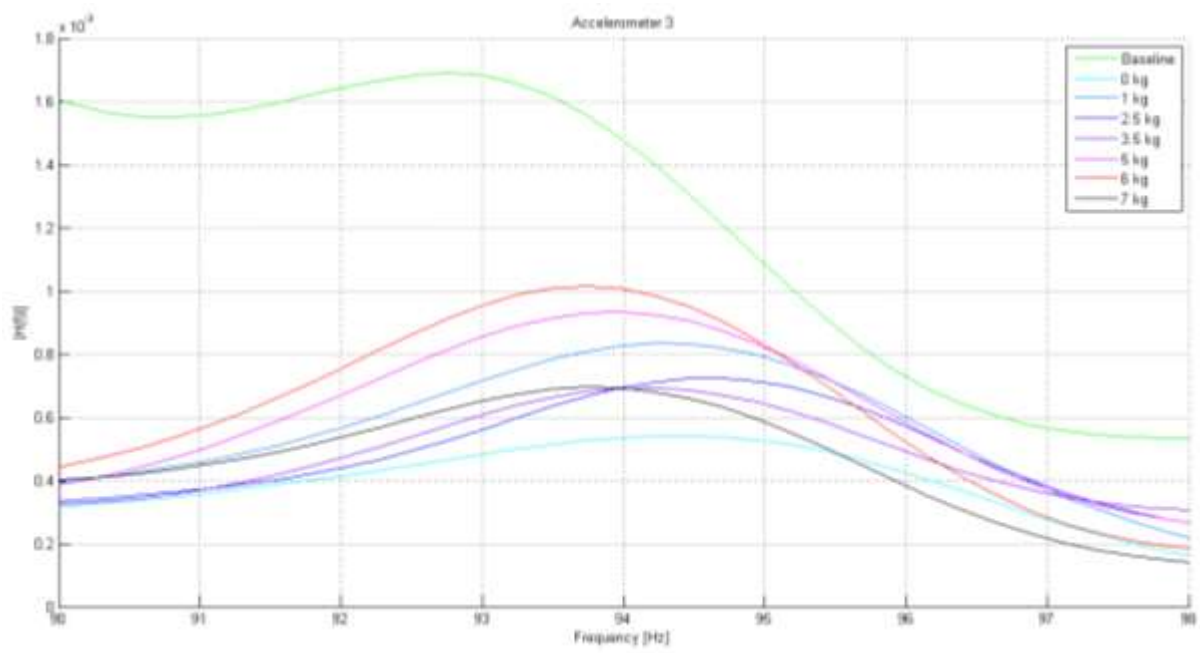
(c) Accelerometer 3
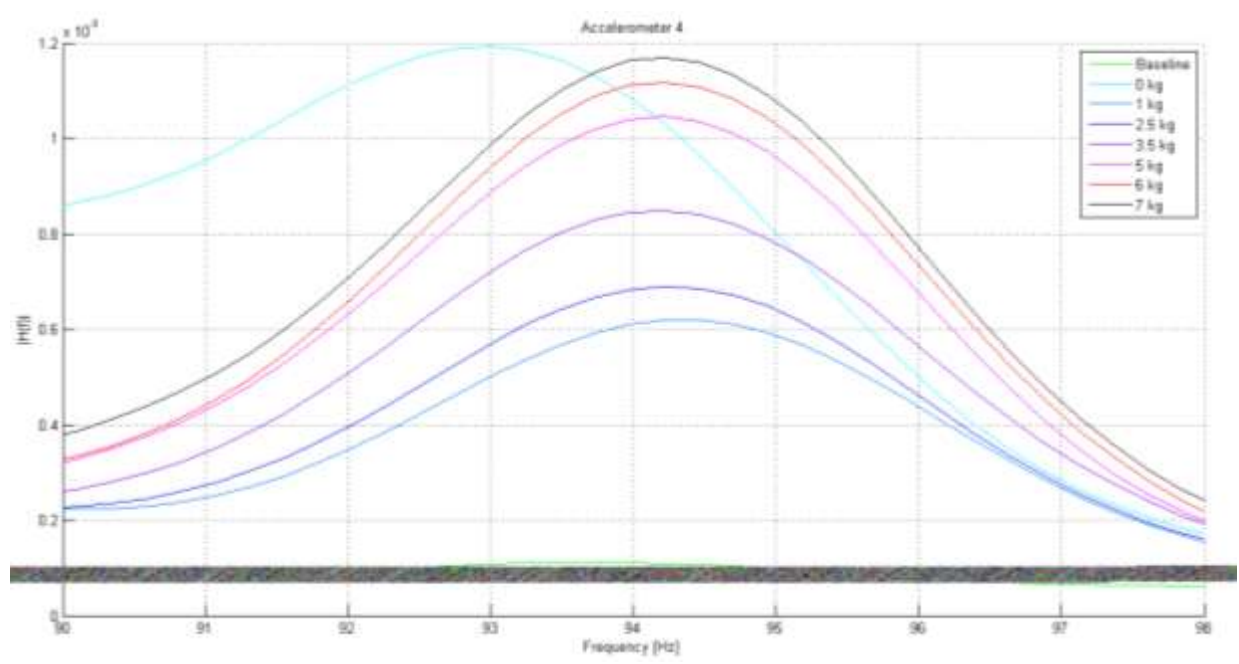
(d) Accelerometer 4
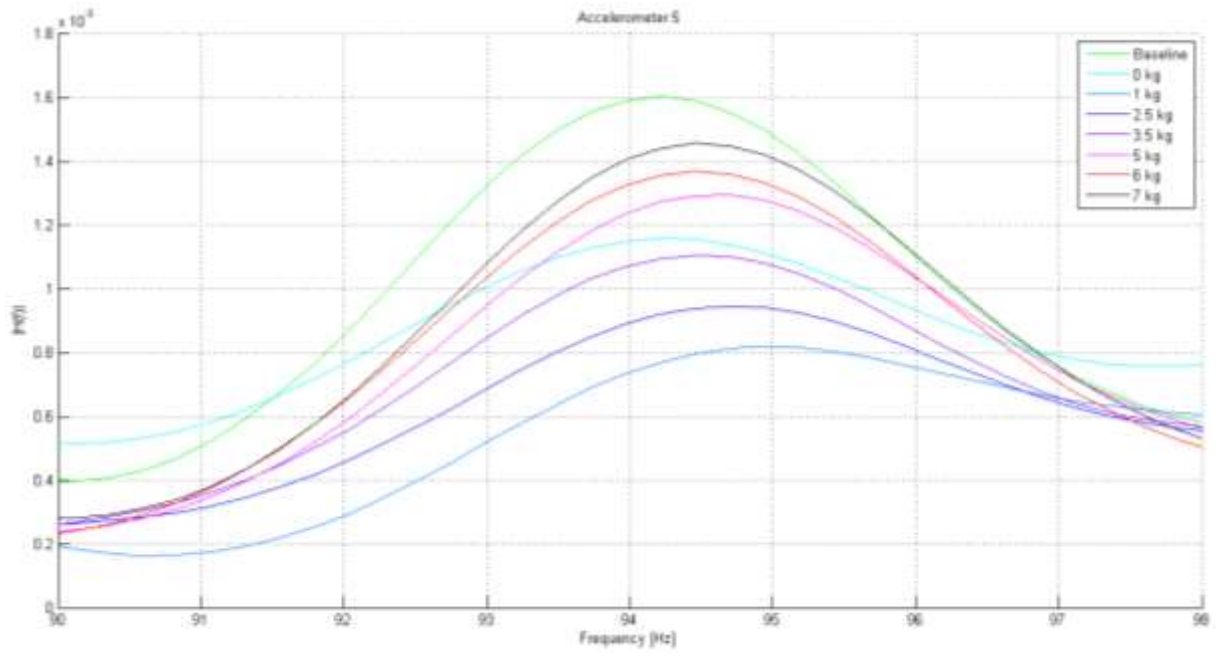
(e) Accelerometer 5
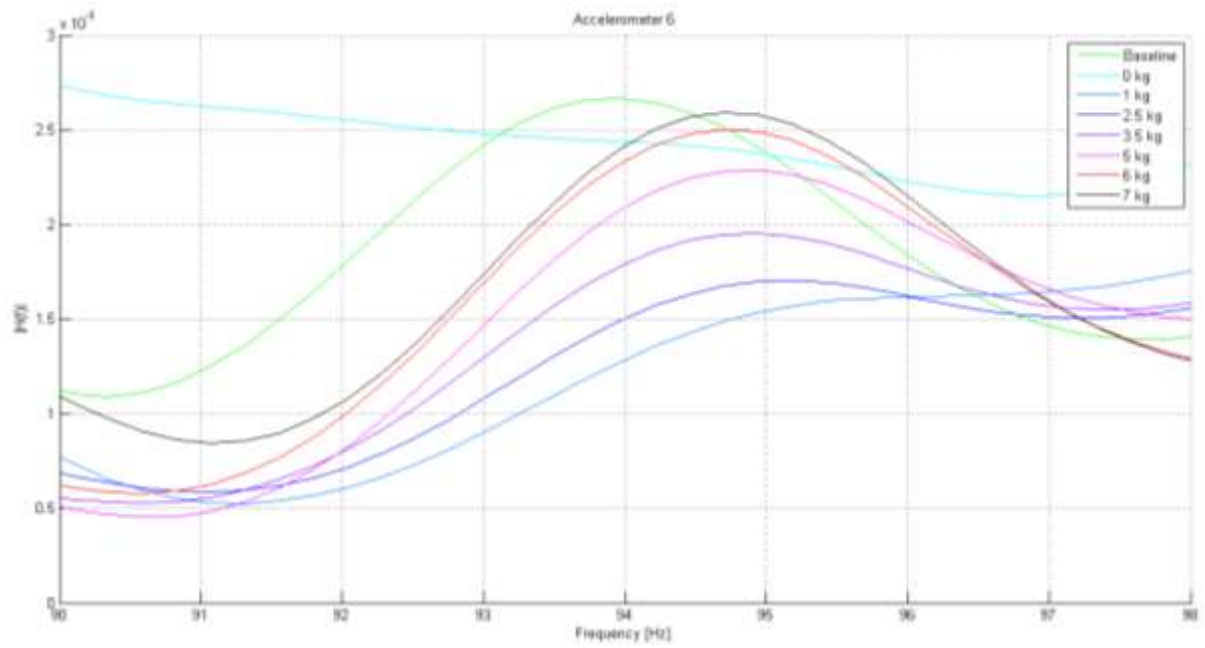
(f) Accelerometer 6
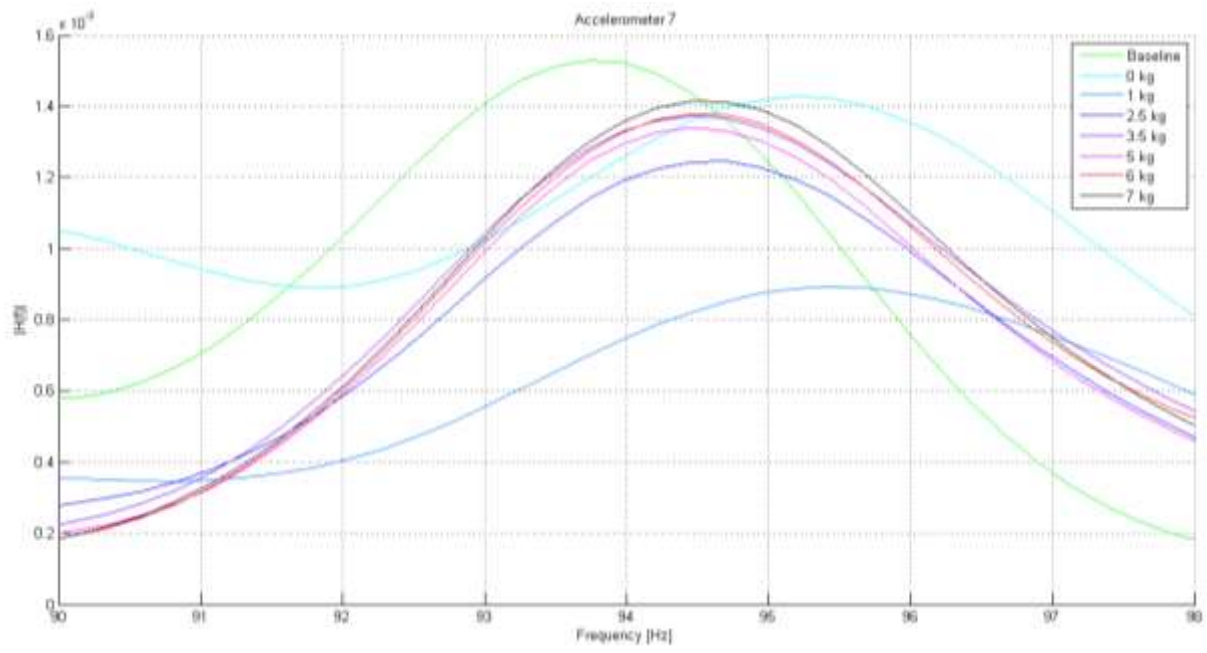
(g) Accelerometer 7
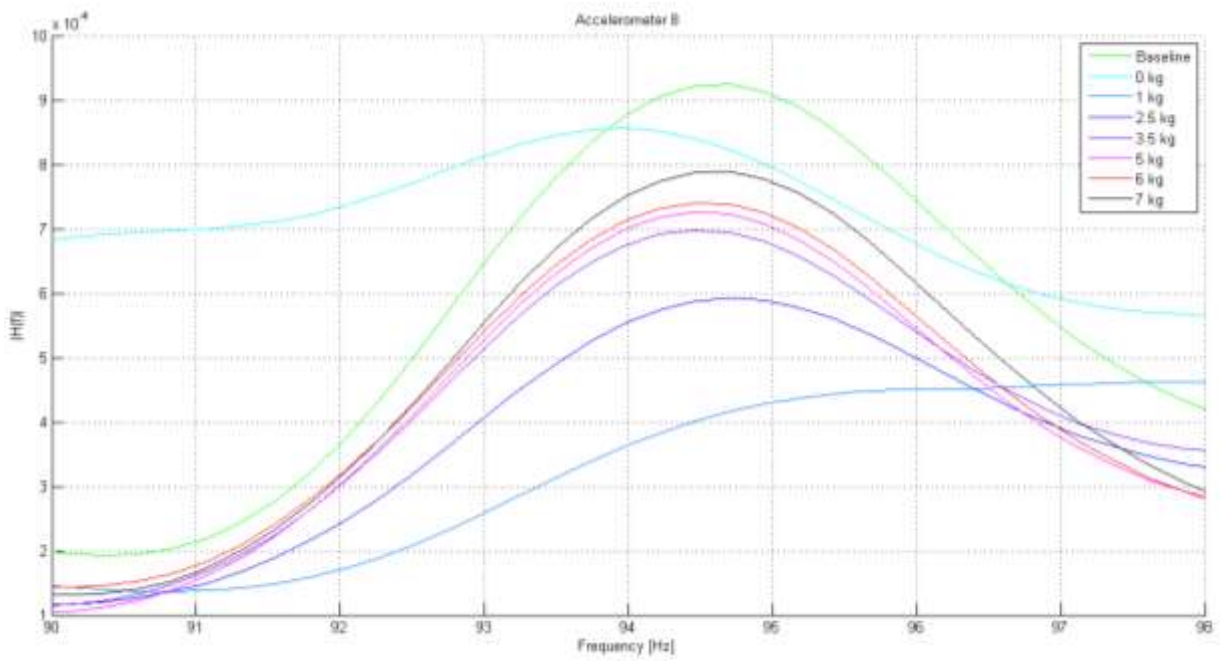
(h) Accelerometer 8
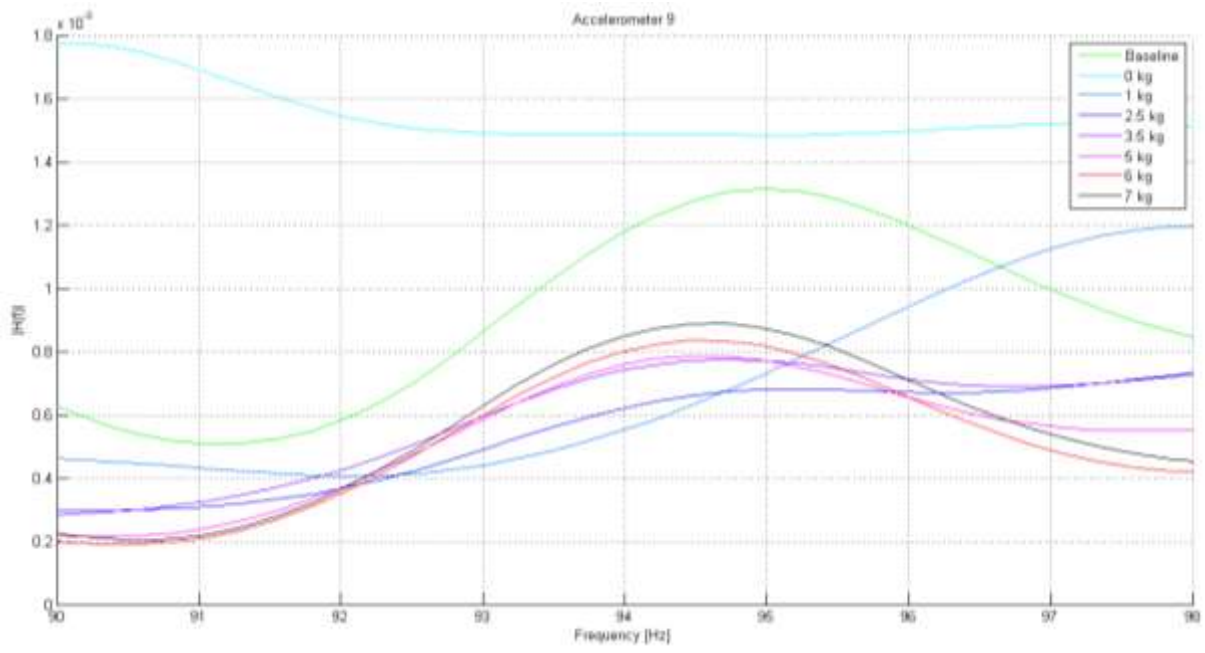
(i) Accelerometer 9
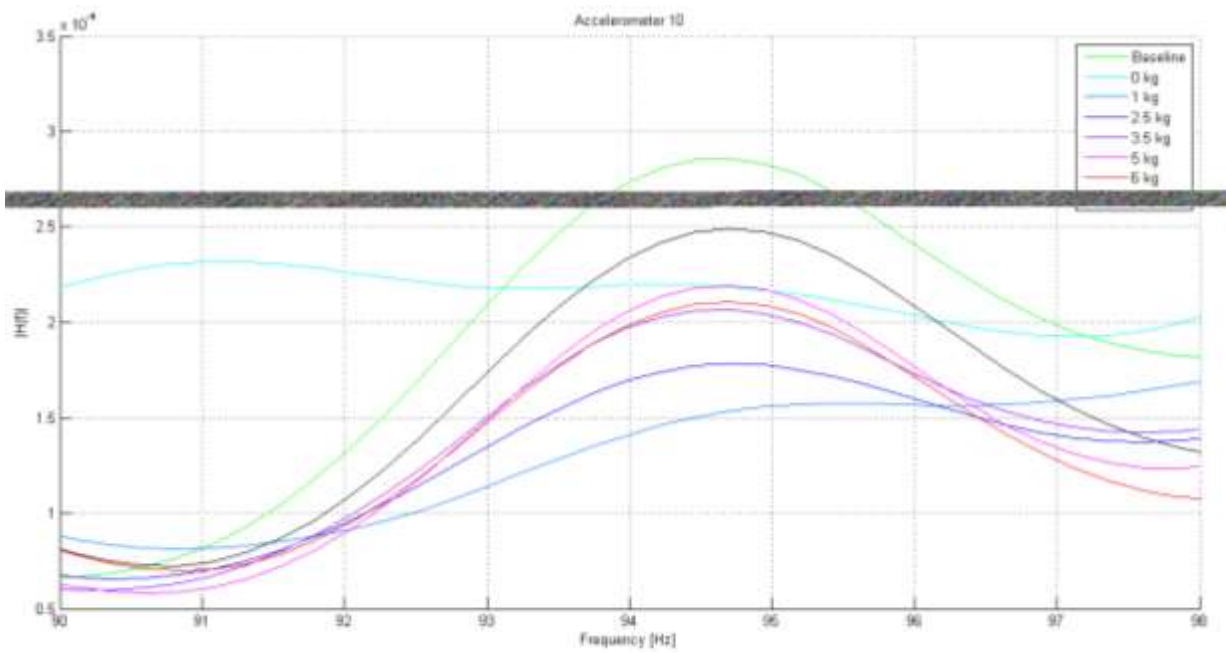
(j) Accelerometer 10

139
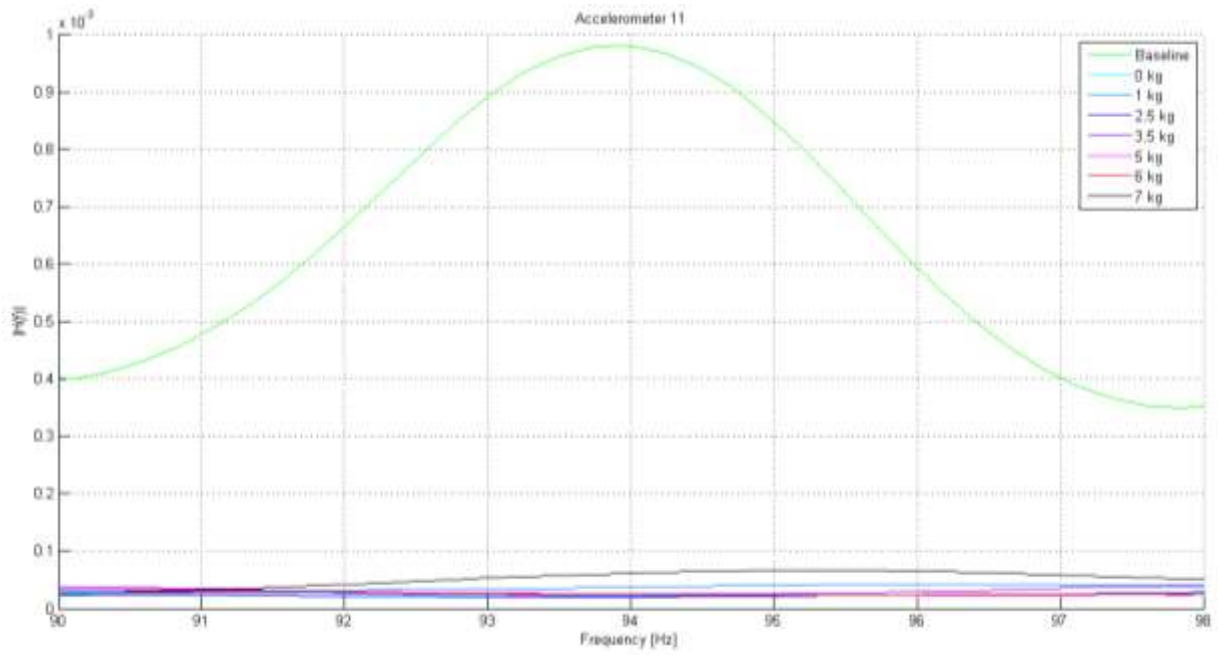
(k) Accelerometer 11
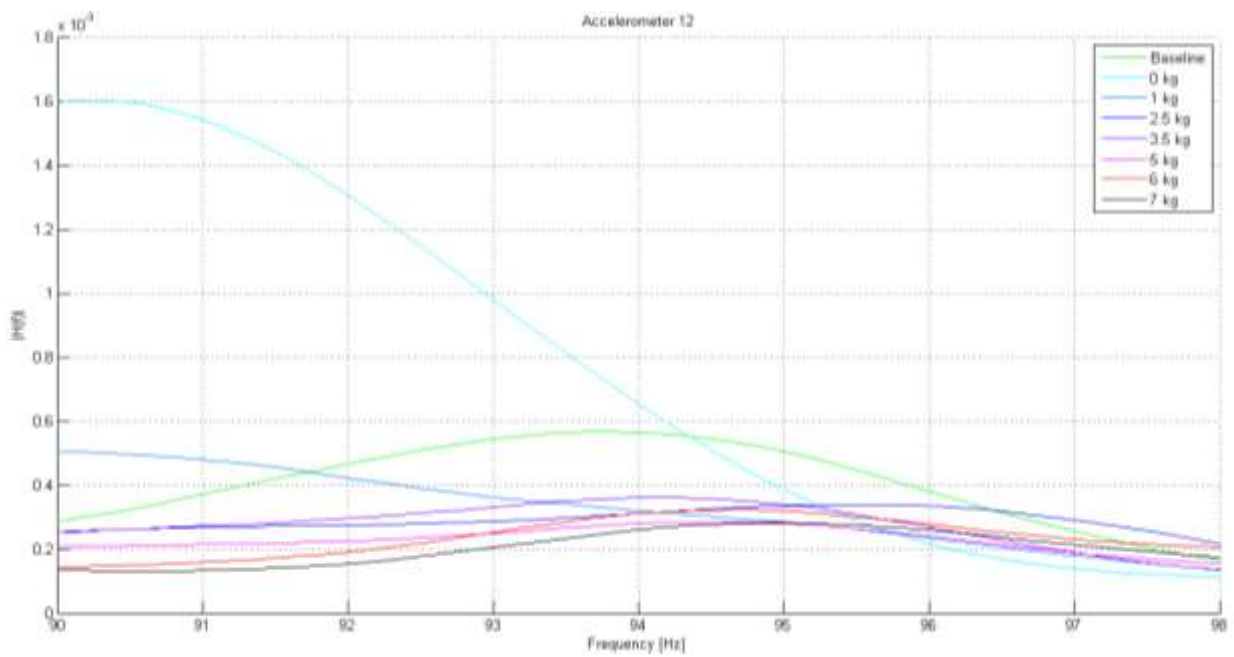
(l) Accelerometer 12

140
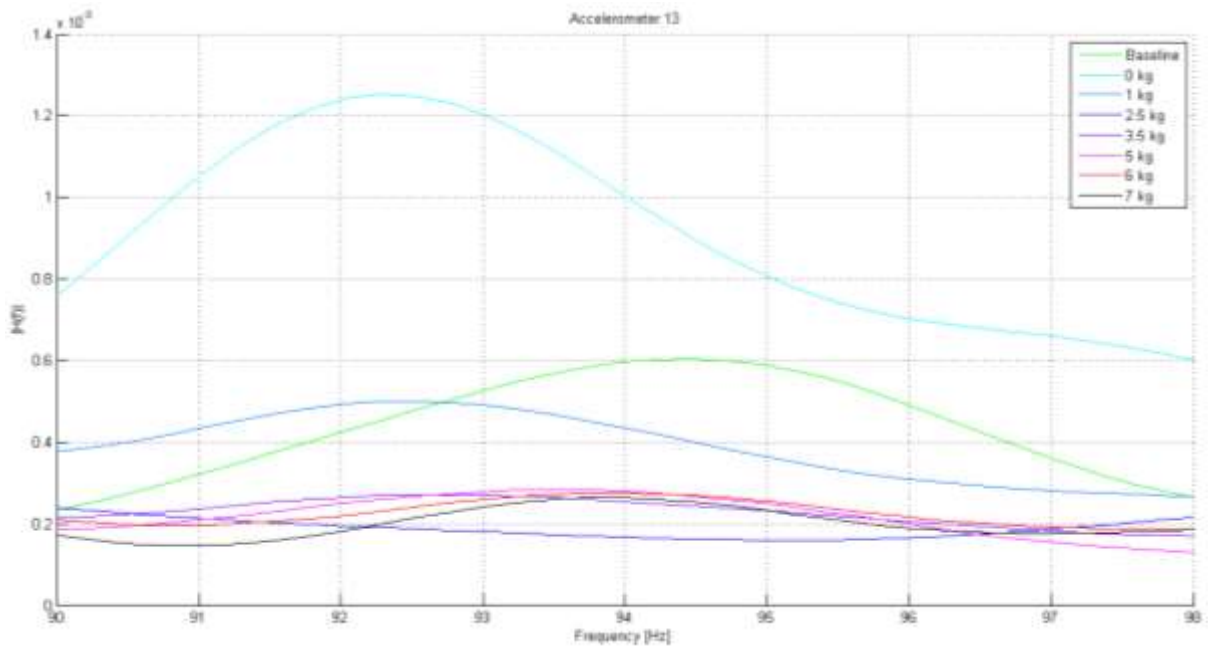
(m) Accelerometer 13
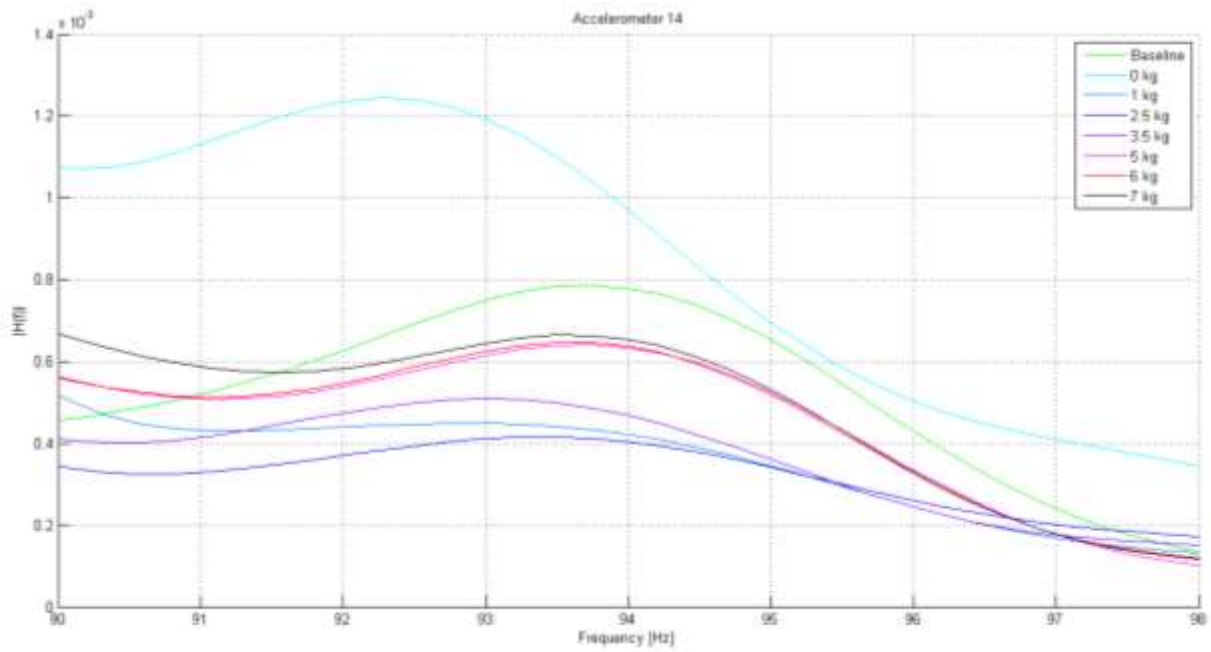
(n) Accelerometer 14
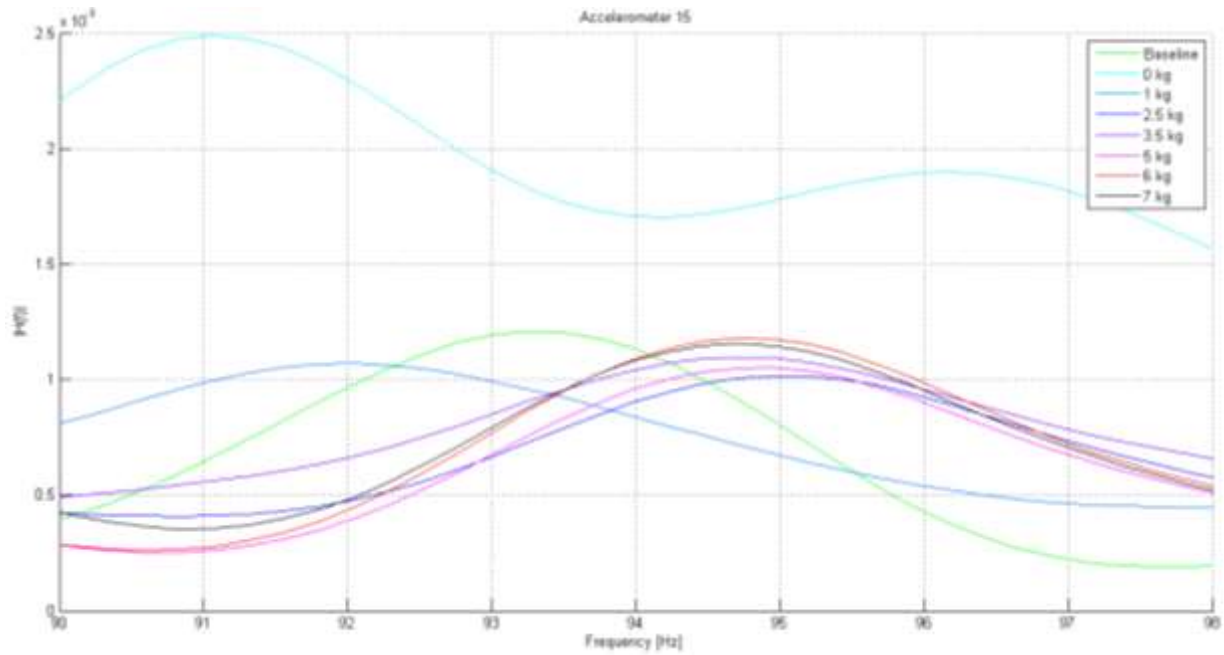
(o) Accelerometer 15

Figure 6.22 (a) – (o) Frequency spectra showing the frequency response functions measured from tip to root end at accelerometers 1 – 15, zoomed in at 90 – 98 Hz for 48 kSamples of data read at a rate of 16 kHz for three seconds.

By way of theoretical modelling in ANSYS Workbench [136], the frequency peak observed between 90 – 98 Hz, was identified as the ninth mode frequency of the Carter blade. Due to the old age and production halt of Carter wind turbines, the manufacturers had only hard copy designs of the Carter wind turbine blade. The blade was therefore modelled in Siemens NX7 engineering design software [250], using measured dimensions. The design file generated, was imported into ANSYS Workbench and modal analysis was conducted. Table 6.2 summaries the material properties assumed in the design and Table 6.3 summaries the theoretically estimated mode frequencies of the blade for point mass loading.

Table 6.2 Assumed material properties of Carter wind turbine blade in ANSYS Workbench theoretical simulation.

Material Type	Elasticity	Density (kgm^{-3})	Young's Modulus (GPa)	Shear Modulus (GPa)	Poisson's Ratio
Composite Material Epoxy e-Glass Wet	Orthotropic	1850	35	4.7	0.28

Figure 6.23 shows the baseline (no load or frame attached) theoretically estimated ninth torsional mode frequency of the blade. At this mode, the blade can be seen to be twisting about its long axis, particularly at the tip end where the mounting frame was mounted in experimental tests. The theoretical analysis provided valuable information that contributed to the interpretation of the experimentally measured results.

Table 6.3 Theoretically estimated mode frequencies for the Carter wind turbine blade.

Mode	Frequency (Hz)								Mode Type
	Baseline	0 kg	1 kg	2.5 kg	3.5 kg	5 kg	6 kg	7 kg	
1	1.3262	1.2779	1.2619	1.2389	1.2243	1.2033	1.1899	1.1769	Flapwise
2	6.1571	5.9819	5.9221	5.8351	5.7789	5.6971	5.6442	5.5925	Edgewise
3	9.2823	9.1983	9.172	9.1359	9.1137	9.0828	9.0638	9.0458	Flapwise
4	25.894	25.862	25.852	25.838	25.828	25.815	25.807	25.799	Flapwise
5	41.266	41.229	41.217	41.201	41.19	41.175	41.166	41.157	Flapwise
6	53.548	53.511	53.498	53.479	53.467	53.449	53.437	53.426	Edgewise
7	58.536	58.441	58.411	58.368	58.341	58.302	58.278	58.255	Torsional
8	79.981	79.878	79.842	79.789	79.754	79.703	79.669	79.635	Flapwise
9	92.202	91.964	91.889	91.782	91.715	91.621	91.563	91.506	Torsional
10	110.26	110.11	110.06	109.98	109.93	109.86	109.81	109.76	Flapwise
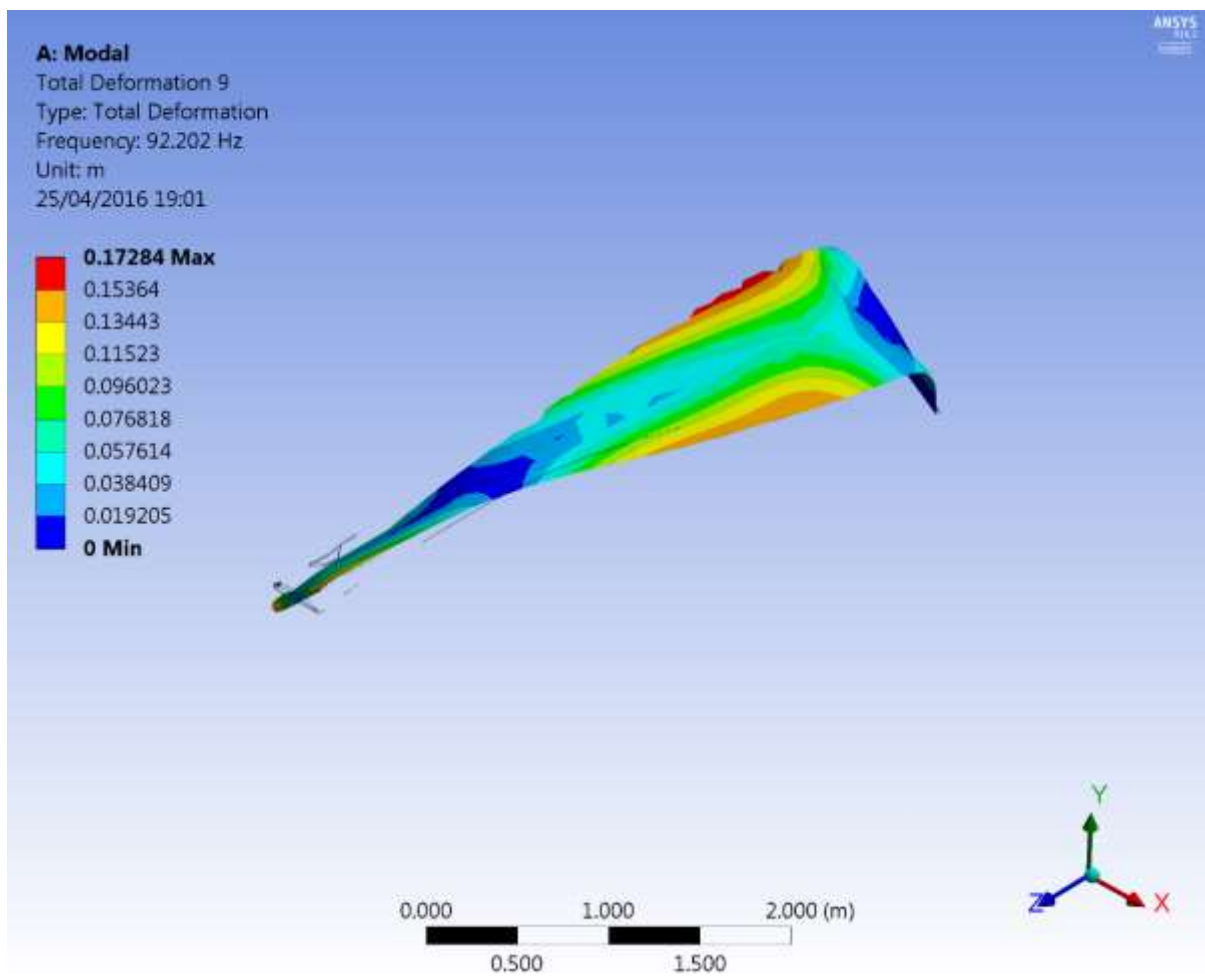
Figure 6.23 Theoretically estimated ninth natural frequency mode of the Carter wind turbine blade. Blade lines indicated the blade's undeformed position.

Theoretically measured natural frequency show a decreasing trend in the natural frequency of the Carter blade for point loading at the tip end. However, in experiments conducted, the frame that supports the masses, acts as a support and potentially increases stiffness at that point on the blade. In the following section, the stiffness of the blade and the effect on measured results are considered mathematically.
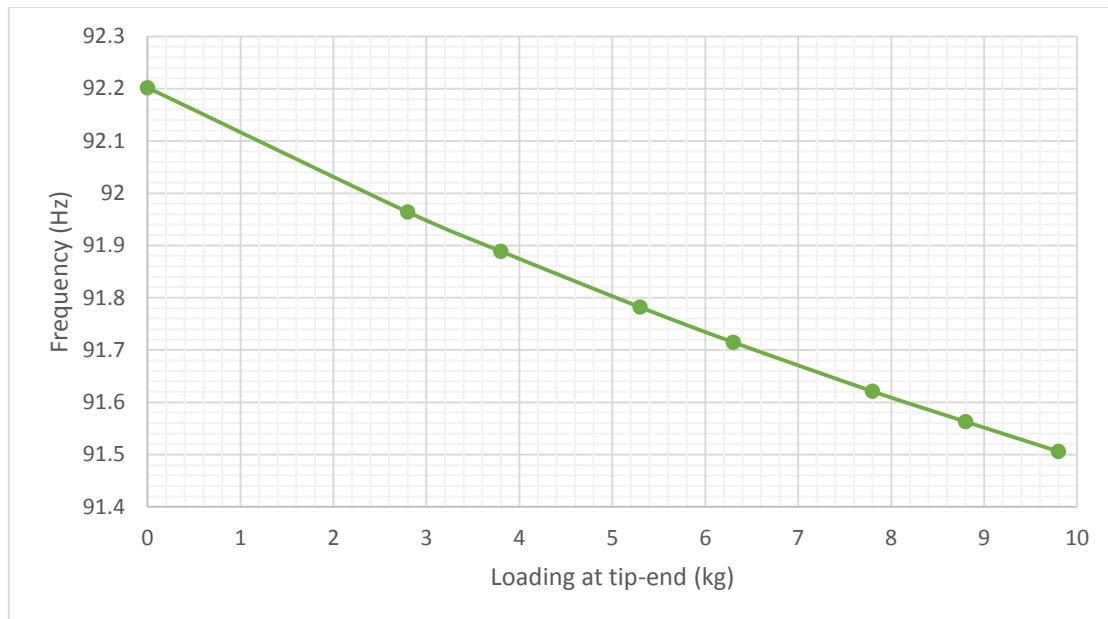
Figure 6.24 Plot showing the ninth mode natural frequencies of the blade, obtained at each point loading in ANSYS Workbench.

The blade frequency at baseline for the selected mode for investigation in the experimental results, was *94.22 Hz*. This was measured from the reference point - accelerometer 1 (at the tip end of the blade). Assuming the blade to be a uniform cantilever beam (boundary conditions applied), Euler-Bernoulli beam assumptions can be applied to estimate the stiffness of the blade from the following equation:

$$f(in\ Hz) = \frac{1}{2\pi}\sqrt[2]{\frac{k}{(m_0 + m)}}$$

Eqn 6.1

Where;

f – Resonant frequency (measured in Hz)

k – Blade stiffness (measured in N/m)

m – Blade mass (50 kg)

m_o – Applied load at blade tip (measured in kg)

The blade stiffness was estimated because it is ideally, supposed to be the only constant structural parameter of the blade at baseline (without the frame), as the blade did not suffer any damage during testing. The stiffness was estimated as *17.5 MN/m* at baseline (zero weight and no frame suspended from the blade). Using the estimated stiffness of the blade and Eqn 6.1, mathematical expected change in frequency with increasing applied mass was calculated for the experimental weights and the values obtained are summarised in Table 6.4 below and plotted in Figure 6.25.

According to the laws of classical mechanics, assuming constant stiffness, the natural frequency of the blade's vibration should decrease with increasing loads applied to the blade and this is demonstrated in the graph shown in Figure 6.24 and Figure 6.25. Now considering experiment results summarised in Figure 6.26, which shows the measured trend in frequency change for each blade loading condition across the five measurement sections of the blade; the graphs for all sections can be seen to plateau out at the right end similar to the theoretically and mathematically expected trend in Figure 6.24 and 6.25.

144

Table 6.4 Mathematically estimated change in frequency for applied loads. 0 kg represents baseline with no frame or load attached and 2.8 kg represents the addition of the loading frame on the blade.

Frequency (Hz) f	Type of ice simulated	Added Mass, m_o (kg)	Total Mass, $(m_o + m)$ (kg)	Stiffness, k (N/m)
94.22	No ice	0.00	50.00	
91.69	Soft rime	2.80	52.80	
65.39		3.80	53.80	
64.62	Wet snow	5.30	56.30	1.75E+07
63.58		6.30	59.80	
62.18		7.80	64.80	
60.62	Hard rime	8.80	70.80	
58.93		9.80	77.80	

Suggestions for the varying trend at the left end of the graph in Figure 6.26 were considered. Applying the frame (2.8 kg) to the blade in section 1 increased the measured frequency of the blade from its baseline measurement. This could be due to a change in the blade boundary condition. The loading frame acts as a restriction and increases the stiffness of the blade, pre-empting the blade from oscillating freely when acted on by the exciter. From the theoretical model, the blade will tend to twist in the torsional degree of freedom, but the frame prevents this free motion, restricting the blade. Although the frame is modelled as and considered to be an added tip mass to the blade, which should decrease the natural frequency of the blade, the component due to stiffness added by the frame at this section, appears to be greater. Therefore, the counteracting effects between added mass and stiffness due to the frame at section 1 of the blade results in a positive frequency shift.

The other sections of the blade do not immediately experience the imposed stiffness at the addition of the frame because they are far away in distance from the frame attachment position. Also, towards the root end of the blade, the second moment of area of the blade is increasing. Therefore, a greater amount of stiffness will need to be imposed at the tip end to be measured at the root end or the loading point will have to be closer to the fixed end of the blade. Hence, it can be said that the positive component due to stiffness and the negative component due to applied mass are potentially counteracting each other and the applied mass is dominant in the other sections resulting in the MEMS accelerometers measuring a decrease in natural frequency at the other sections, when the frame is attached.

Figure 6.27 shows the estimated stiffness of the blade plotted against the added tip mass for each of the measurement sections. The stiffness was estimated using Eqn 6.1, and the average measured frequencies at each section, by the MEMS accelerometer, for each load applied. In the plots, sections 1 and 2 have similar stiffness, generally lower than sections 3, 4 and 5. This is in agreement with studies conducted in NREL [251] which suggest that the flapwise stiffness of wind turbine blades, decreases from the root to the point just before maximum chord location and then increases a little at maximum chord due to more material and resin at the root to accomplish safe securing of the blade at the root. From the maximum chord, to the tip of the blade, flapwise stiffness is not linear but is more or less an exponential decay i.e. closer to the tip, the stiffness is lower. Note that the flapwise stiffness also depends largely on the locations of the internal spars, thereby increasing the resistance to bending.

In these experiments, the Carter blade has its maximum chord at its root end (section 5) and the chord decreases from root to tip end of the blade. It is therefore expected that the stiffness of the blade will decrease from root to tip end exponentially as observed in Figure 6.27.
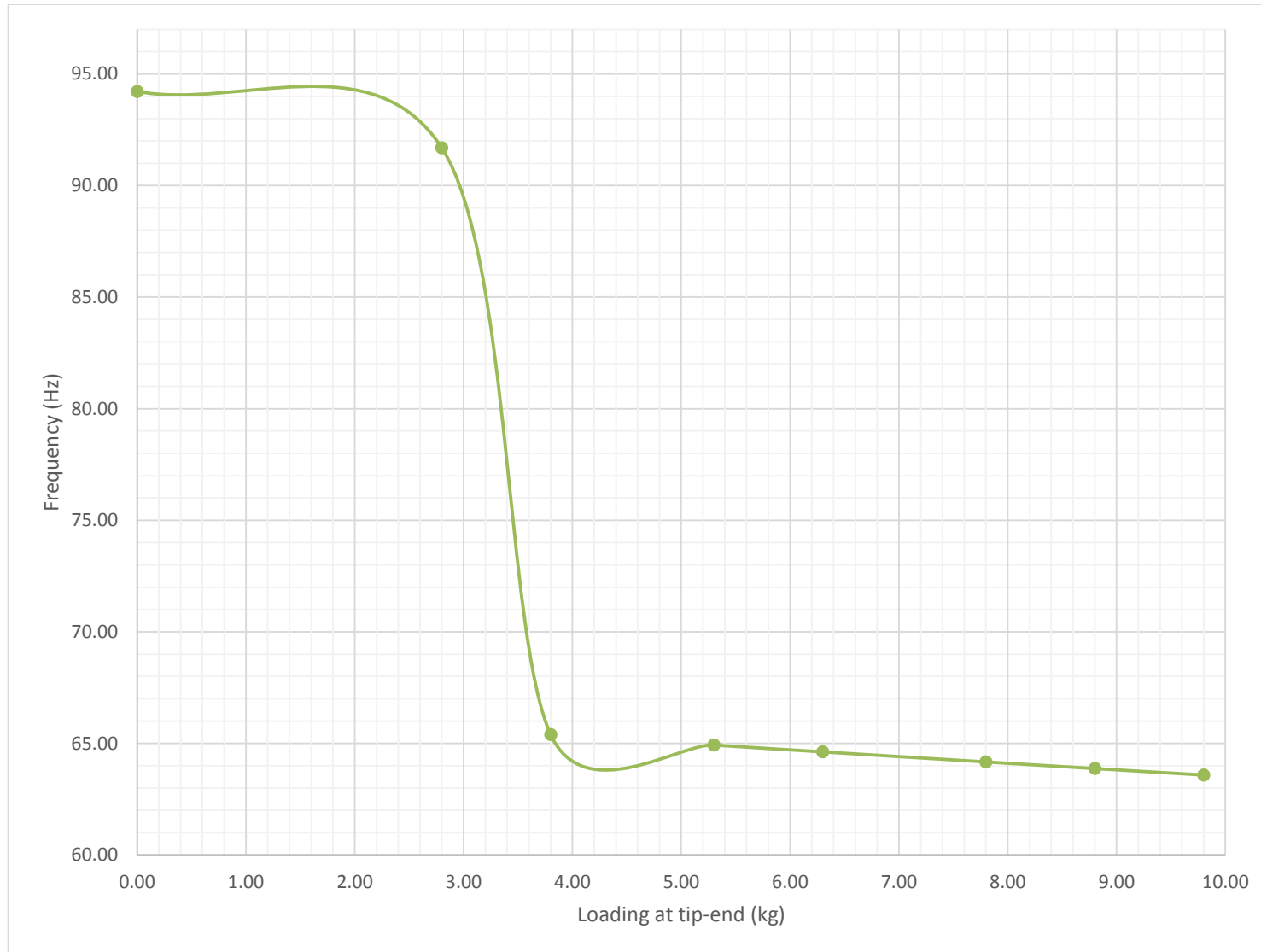
Figure 6.25 Graph showing the theoretically estimated trend in frequency change for increasing ice load on the 50 kg Carter wind turbine blade.
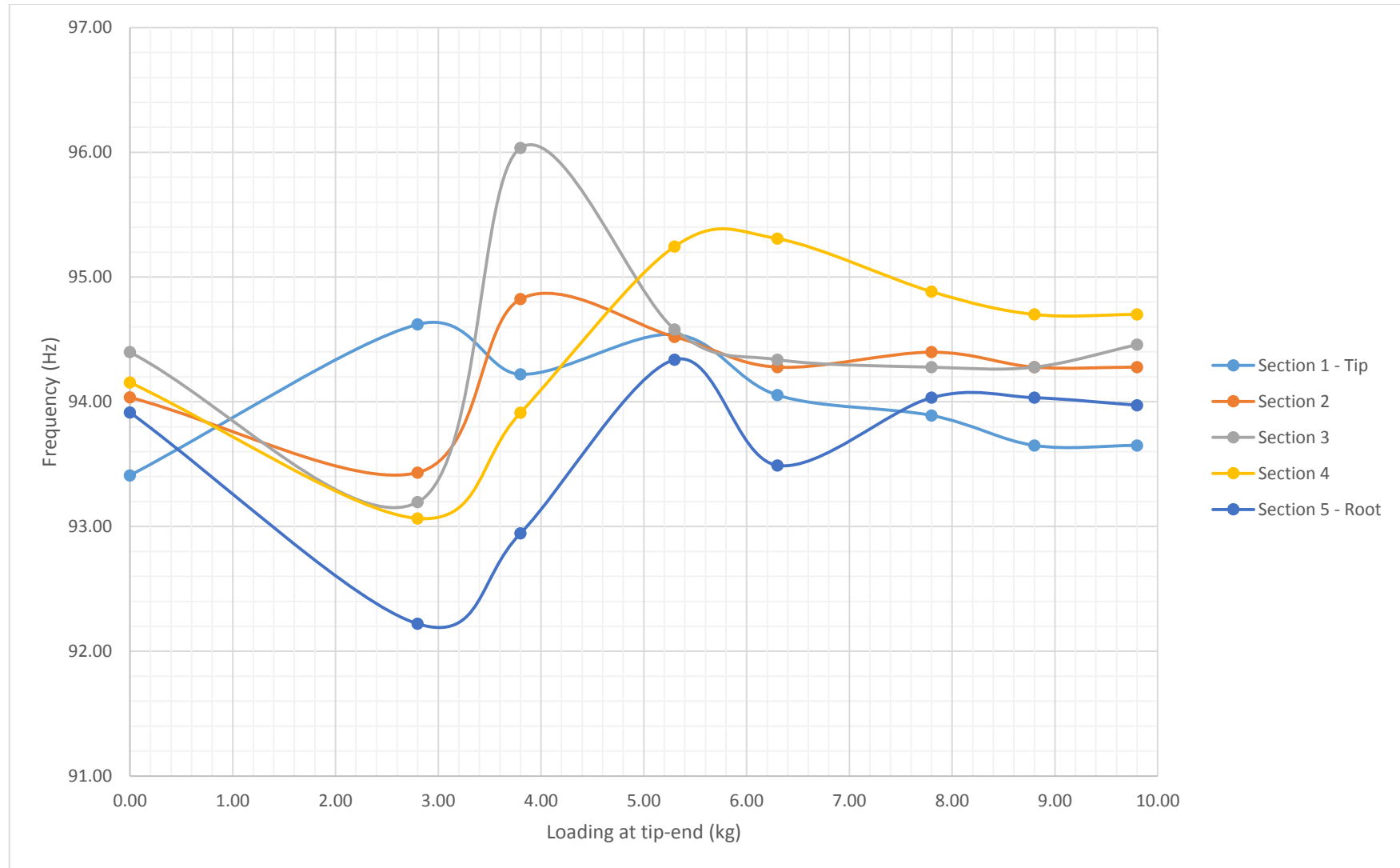
Figure 6.26 Graph showing the average experimentally measured trend in frequency change for increasing load on the blade across each measurement section, where measurements at 0 kg represent baseline measurements when the mounting frame and hook are not attached to the blade.
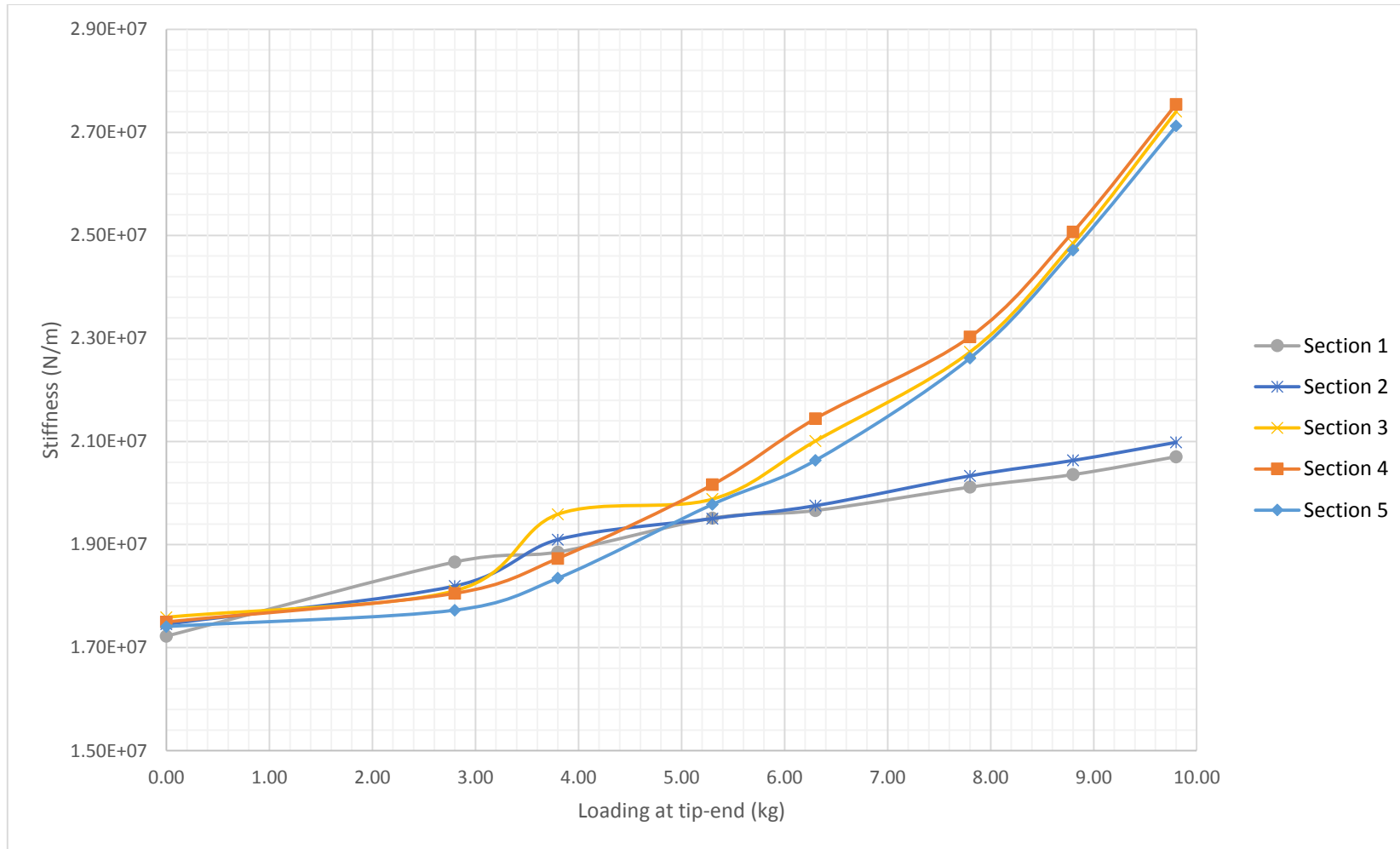
Figure 6.27 Graph showing the estimated blade stiffness plotted against load added at blade tip-end.

Going back to Figure 6.26, it can therefore be argued with reason that the peaks occurring later at the other sections of the blade (sections 2-5) are as a result of the blade's stiffness becoming higher than the negative mass applied at the tip end. Nevertheless, beyond this peak in frequency, the frequency of the blade decreases as the applied mass at the tip end is increased.

The theoretically and mathematically expected trends shown in Figure 6.24 and Figure 6.25 do not directly match experimentally obtained graphs in Figure 6.26 because they do not take into account, the dimensions and restraining physical size of the mounting frame system. This demonstrates that the MEMS accelerometers have been able to measure the characteristics of the blade to some degree of accuracy as demonstrated in the graphs and graph analysis.

Additionally, complex interactions between the exciter and the blade as well as the exciter and mounting frame, could be contributing to the increasing frequency and deviation from the theoretical and mathematical expected trends.

These experiments generally showed that the different sections and points along the wind turbine blade responded differently to increasing point loading at the tip end. It also showed the complexity in measuring the dynamic properties of the blade using continuous excitation. However, the MEMS accelerometers were able to detect and measure these changes, reemphasising their potential for use in detecting icing on wind turbine blades, as changes in resonant frequencies are considered to be indirect detection methods of icing.

From published literature [242], [244], [246], there is strong and urgent need for new and reliable icing measurement instruments at the blades of wind turbines, especially point measurements. Icing measurements can be categorised into accretion rate/intensity, persistence and ice load. The MEMS accelerometers could possibly be implemented for accretion rate and ice load measurements, helping wind farm operators to interpret and understand icing on wind turbine blades.

6.3 CONCLUSIONS

In this chapter, ice loading on wind turbine blades was explored from published literature and simulated experimental testing. Forced excitation using a chirp signal fed from a commercially-available exciter was conducted on a real turbine blade with success. The exciter drove the blade and measurements for increasing load were successfully measured by the MEMS accelerometers. Experimental testing of the exciter was conducted prior to its use on the turbine blade to fully describe its resonant characteristics. This is important as the exciter can be integrated into a condition monitoring system for a real turbine and understanding its functionality will enable its best use. It can also be considered for internal installation in the turbine blade and used to actively excite the blade or trigger vibration measurements by MEMS accelerometers when necessary. Exciting the blade with a known force or input can make interpretation of measured responses easier to analyse and potentially further improve measured data for condition monitoring. It also eliminates human error to some extent in the excitation of the blade in laboratory controlled environments like in the experiments conducted in this chapter.

Loading tests showed changes in the blade resonant frequencies which were detectable by the MEMS accelerometers. Experiments mimicked ice loading on wind turbine blades, an area in urgent need of reliable icing measurement instruments. The natural frequency of the blade decreased as the load at the tip of the blade was increased, showing the potential of MEMS accelerometers for icing measurements. Further experiments however need to be conducted perhaps using a different loading system, to distribute the loading on the blade to replicate real life icing conditions along the blade.

In the following chapter, the concept for applying these MEMS accelerometers for condition monitoring of wind turbine blades is explored. An autonomous condition monitoring system is proposed and the different elements that will comprise the system are investigated.

7 CONCEPTUALISATION OF AN IN SITU AUTONOMOUS CONDITION MONITORING SYSTEM

The importance of condition monitoring of wind turbine blades to wind farm operators and insurers has been discussed and emphasised in previous chapters throughout this thesis. Micro Electro-Mechanical Systems (MEMS) accelerometers have been investigated as potential sensors for vibration-based condition monitoring of wind turbine blades at marginal costs. In continuation, this chapter takes a systems approach to conceptualise the design of an autonomous monitoring system that can potentially be built, implemented and installed within a wind turbine blade. The system was not built. However, various functionalities and design specifications were considered. They include:

a) The device will be fully self-contained and installable at blade manufacture.

b) It will be self-powered.

c) The device will have signal processing capabilities.

d) It will be able to transmit data concerning the condition of the blade measured by the MEMS accelerometers to a base station on the ground i.e. operate remotely.

e) It will contain electromagnetic exciters similar to the ones used in experiments in previous chapters to excite the blade and trigger measurements.

Some commercially available components that have the potential to fulfil the design specifications listed above, were investigated. MEMS accelerometers were considered for detecting vibrations, a microcontroller for processing measured signals, a wireless transmitter for transmitting processed signals and energy harvesting and storage for powering the device. Figure 7.1 below shows the architecture of the proposed system.

Such a system has various technical challenges, such as the provision of a power supply that can outlast the service life of the blade and the availability and location of the accelerometers deployed within the structure to measure the various properties of the blade during operation. In addition to the power and electronic requirements, a strategy for monitoring and signal processing the received data is also worthy of consideration. Energy harvesting methods considered for the autonomous low-cost system are detailed whilst exploring the energy requirements necessary to acquire frequency domain statistics such as Fast Fourier Transforms (FFTs) and transmit this vibration data measured via sensors and microcontrollers affixed to the wind turbine blades internally or retrofitted externally.

Literature explored for the different design specifications of the proposed autonomous condition monitoring system and experimental results obtained from the analysis of identified electronic components to make-up the system are discussed in this chapter.
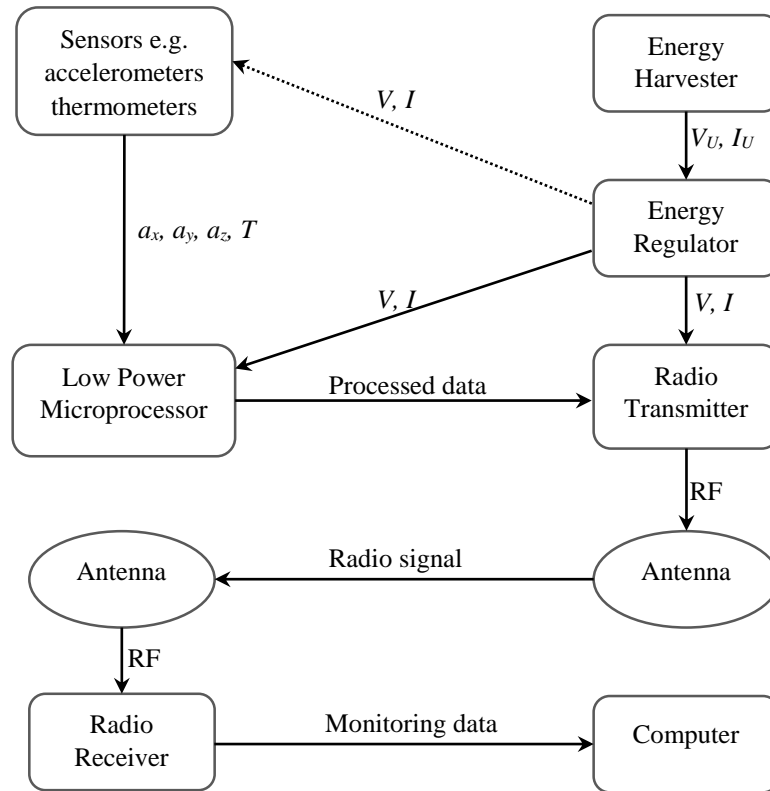
Figure 7.1 Architecture of the wireless monitoring system for in situ wind turbine monitoring. Dotted link indicates a necessary link for active sensors such as packaged MEMS accelerometers. Subscript *U* indicates unregulated voltages and currents that may be ac or dc quantities.

7.1 POWER CONSUMPTION ESTIMATION

Power consumption of each of the off-the-shelf electronic components considered for the design of the autonomous wireless condition monitoring system was investigated. The figures in Table 7.1 below show the measured current at the rated voltage of each device.

Table 7.1 Measured current consumption of typical devices that can be used in the autonomous system.

Device	Current Consumption (A)	Voltage (V)	Comments
Accelerometer	$355\ \mu$	3.00	ADXL335
Microcontroller	$287\ \mu$	3.27	dsPIC33FJ128MC802
RF Transmitter	$8\ m$	3.00	433.92 Hz, 8Kbps

The total power consumption was estimated at 26 mW. However, the microcontroller was not executing any program when the current measurement was taken. During intense computation, such as during the FFT computation, the current consumption of the microcontroller could increase to 50 – 65 mA [252].

In a particular application, it would be necessary to consider how much processing is required by the monitoring system or alternatively, the data may be transmitted to the ground station for post processing where fewer power constraints apply. It is clearly challenging to make generalisations about the system beyond the architecture, except to observe that some typical readily available commercial components offer low power consumption and the possibility to exercise close control of

data processing and transmission plus an idle mode where the circuit can remain in a very low power state until the energy harvested is adequate to perform the system's main functions.

The power consumption of the MEMS accelerometers will be relatively constant during operation and will typically depend on the supply from the microcontroller. In addition, the volume of data being transmitted can have an effect on the power consumption of the transmitter. Therefore, the power consumption must be topmost priority in choosing these systems. The following sections therefore discuss the power consumption factors to be considered when final decisions are made, on the microcontroller and transmitter to be integrated into the autonomous system.

7.1.1 MICROCONTROLLER

Understanding the power for a particular system has significance in minimising power consumption and in the choice of microcontroller. This process is known as 'Power Budgeting' [253].

The total power consumption of microcontrollers can be broken into two broad categories: dynamic power and static power.

a. **Dynamic power** is the power consumed when the microcontroller is running and performing its programmed tasks such as Fast Fourier Transform sampling or calibrating measured data and is affected by the frequency at which these tasks are performed. For example, if data are sampled every second, it will demand more power in comparison to every five seconds for the same amount of data. Data-logging, peripheral and active powers are examples within this category. Peripheral power allows the microcontroller to communicate with the accelerometer measuring analogue signals and the transmitter.

b. **Static power** is the power consumed, when the microcontroller is not running code but simply applies voltage to a device. Standby power, which is the power, consumed when the microcontroller is waiting for an internal or external event to wake-up to process data, make decisions and communicate with the receiver is an example of static power. In typical microcontroller applications, the majority of their product life is spent in this mode which can consume large amounts of energy if not correctly understood and mitigated [254].

The total energy consumed by a microcontroller is the sum of the energy during dynamic or active mode and the energy consumed during the static or standby mode [253]–[256]. That is:

$$Total\ Energy = Energy_{dynamic} + Energy_{static} \qquad \text{Eqn 7.1}$$

$$Time \times I \times V = Time_{dynamic} \times I_{dynamic} \times V + Time_{static} \times I_{static} \times V \qquad \text{Eqn 7.2}$$

From the above equations, it can immediately be seen that voltage is constant and is not under the influence of the microcontroller. Therefore, voltage can be excluded from further calculations so that the average current is the focus.

For remote sensing applications such as the autonomous system proposed, the activity profile was assumed as follows to investigate the power consumption.

Table 7.2 Autonomous condition monitoring device activity profile.

Component	Application activity
Peripheral	500 samples of single blade vibration data measured via MEMS accelerometers.
Active	Process analogue inputs- calibrate data using algorithm.
Data	Conduct FFT and produce two column data (frequency and amplitude) ready for transmission every cycle.
Peripheral	Transmit 16 bytes of two column data via transmitter each cycle.
Standby	Wakes once every 3 seconds to run the program, maintain real-time clock (RTC), capable of wake up on input-output (IO) interrupt.

It is common to consider the active processing power of the microcontroller first. However, the power the microcontroller consumes when it is not operating is often more important than active processing power. With the assumption that the system typically wakes up from standby mode at set time intervals to record and process vibration measurements carried out by the accelerometers as detailed in Table 7.2, it can be estimated that the microcontroller will spend most of its time in the standby mode. In addition, as no program has been written for execution, it was the viable option to consider as a starting point.

Table 7.3 below uses the typical specifications provided in the datasheet for dsPIC33FJ128MC802 [252] with a 48 mA standby mode current to illustrate the impact of standby power on total microcontroller power across varied active time to standby time ratios:

Table 7.3 Impact of $I_{standby}$ on total power based on ratio of active to standby time. ($I_{standby} = 48mA$ obtained from the summation of I_{Idle}- CPU and Core is OFF and CLOCK is ON; I_{power_down} − Current consumed during when powering down plus watchdog timer current if enabled; and I_{doze} − Current consumed in doze mode). All values were selected at ambient temperature of +25°C and 3.3 V [252], [257].

Active to Standby Ratio	% Time in Standby	$Time_{active}$ x I_{active} (mAs)	$Time_{standby}$ x $I_{standby}$ (mAs)	Total Charge (mAs)	% Impact of $I_{standby}$ to Total Power
1:10	90%	100	480	580	82.76%
1:100	99%	100	48	148	32.43%
1:1000	99.9%	100	4.8	104.8	4.58%

Table 7.3 demonstrates that as the ratio of active to standby exceeds 1:100, standby current of the microcontroller begins to account for very little of the overall system power. This proves to some degree, the suitability of the suggested microcontroller dsPIC33FJ128MC802 for the autonomous condition monitoring system as the device is expected to be in standby power majority of its projected lifespan. The microcontroller can stay in standby mode and only become active when required without massively affecting the system power.

Ideally, creating a power profile for the microcontroller will be the most effective method in planning and determining the energy supply for the autonomous condition monitoring system. This involves accurately measuring the static and dynamic power using ammeters, capacitors and/or oscilloscopes and the purpose is to provide a clear image of where the primary sources of power use are in the system so that it can be optimized [253], [258]. The profile will indicate which states of the system consume the most power and efforts can be focused on reducing the power states or optimising the

energy supply to the system. This would have a direct effect on the functionality of the proposed system especially in deciding whether the device will process and store the blade vibration data or transmit the raw measurements to an on-site computer, to be Fast Fourier Transformed.

To create a power profile the following steps will be followed:

a) Breakdown the application into states based on varying power consumption (see Figure 7.2).
b) Measure the power and execution time of each state.
c) Determine the total energy consumed in each state by calculating the product of power and time.
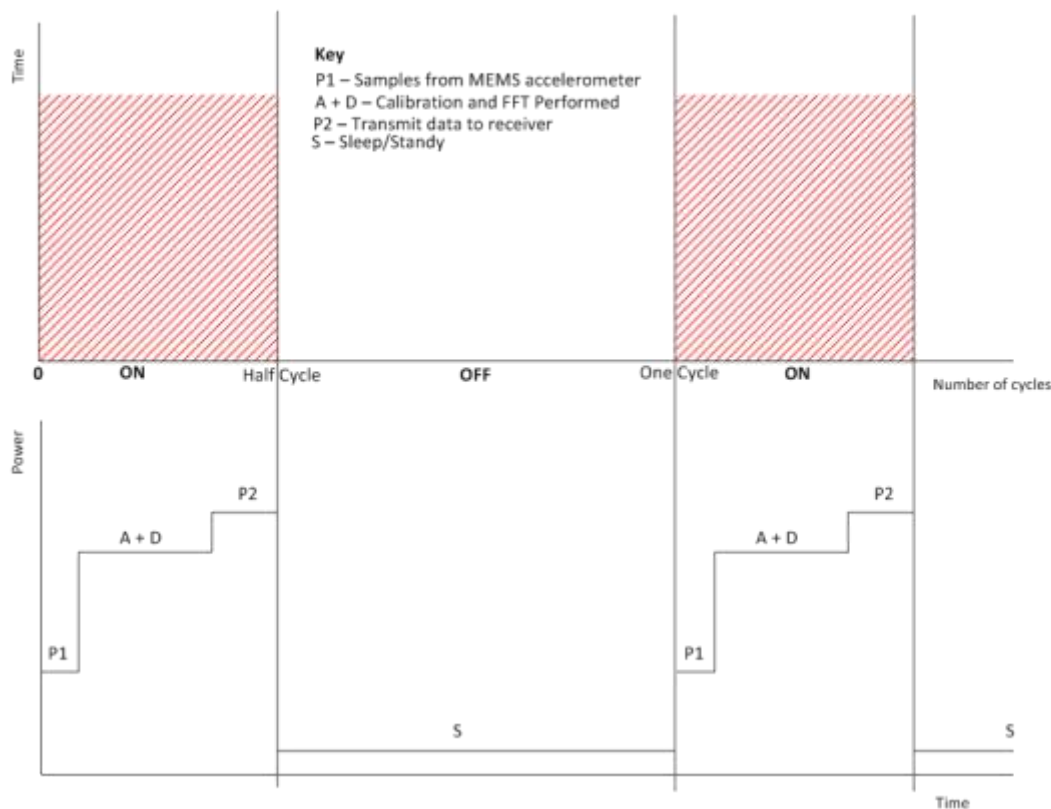
Figure 7.2 Flow diagram showing the states for the autonomous condition monitoring device.

7.1.2   RADIO CHANNEL LINK BUDGET

Link budget is the method of accounting for all the gains and losses from a transmitter, through the medium (free space, waveguide, fibre, cable etc.) in which it is to operate, to the receiver in a communication system. It helps account for the attenuation of transmitted signal due to propagation as well as the antenna gains, feed line and miscellaneous losses. Environmental conditions, receiver sensitivity, available bandwidth and available and permitted output power are some of the major factors that may impact system performance [259].

The transmitter to be used in this application will be positioned on the wind turbine blade - a moving and rotating part of the turbine. This could have significant effects on the propagation of the signal to be transmitted to the receiver and a knock-on effect on the power consumption of the transmitter. Link budgeting enables considerations on how far the signal from the transmitter can go and if the estimated received power relative to the receiver sensitivity is sufficient for sending data.

154
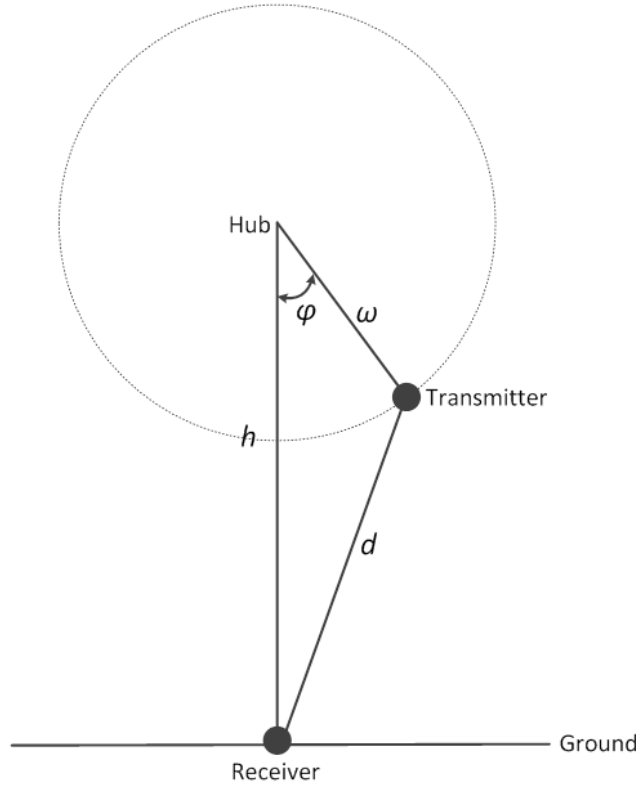
Figure 7.3 Link budget calculation for a blade-mounted transmitter.

Consider the system shown in Figure 7.3. The power at the ground-based receiver is thus:

$$P_R = P_T + G_T - L_T - L_{FS} - L_M + G_R - L_R \qquad \text{Eqn 7.3}$$

Where P_R is the received power in dBm. G_T and G_R are the antenna gains of the transmitter and receiver in dBi, L_R and L_M are loss factors in dB for miscellaneous mechanisms such a polarization mismatch between transmitter and receiver. The term L_{FS}, is the free space loss and is a function of transmit frequency and the distance of the link. If frequency, f, is measured in MHz and the distance, d, is in metres the loss in dB is given as:

$$L_{FS} = -27.55 + 20 \log_{10}(f) + 20 \log_{10}(d) \qquad \text{Eqn 7.4}$$

Derived from: $20 \log_{10} \left(\frac{4\pi d f}{c} \right) = 20 \log_{10}(d) + 20 \log_{10}(f) + 20 \log_{10} \left(\frac{4\pi}{c} \right)$ Eqn 7.5b
where c is the speed of light in vacuum 3×10^8 ms^{-1}

A practical choice for the antenna in a rotating system is an antenna with pattern symmetry in one of its cardinal planes, in order that when it undergoes rotation as the blade turns; the received signal is not adversely affected. Here we assume a monopole which meets that requirement with a gain $G_T = 5.19$ dBi. The receive antenna can be of various types, however, a commonly used patch antenna with a unidirectional pattern and G_R of approximately 9 dBi would seem a reasonable choice due to its beam shape.

The distance d for the link is not a fixed value and varies according to the blade's angular position. Thus, the link budget will vary accordingly. For an assumed hub height of 95 m and rotor diameter of 90 m, 50 m $< d <$ 140 m. The free space loss variation during a full cycle with the receiver directly under the hub is $20 \log_{10}(140) - 20 \log_{10}(50) = 8.94 \ dB$. The receiver deployed in such a system must be able to handle this dynamic range and these distances.

To determine the transmit power, and hence, the radio energy requirement, it is necessary to assume a particular receiver sensitivity. A typical benchmark figure for receiver sensitivity would be -70 dBm; although, in some frequency bands and devices, it may be -110 dBm or even better. Taking the worst figure of -70 dBm, a frequency of 2.45 GHz and the dimensions given above, the transmit power can be determined:

$$P_T = P_R - G_T + L_T + L_{FS} + L_M - G_R + L_R \qquad \text{Eqn 7.6}$$

If we assume that the connector/mismatch losses and miscellaneous losses are negligible and by substituting from Eqn 7.4 then,

$$P_T = P_R - G_T - 27.55 + 20 \log_{10}(f) + 20 \log_{10}(d) - G_R \qquad \text{Eqn 7.7}$$

Hence for the given quantities and the largest value for d we get the transmit power to be approximately -1.04 dBm. This corresponds to a power of 0.787 mW delivered into a 50Ω load.

The analysis assumes the worst case of the transmitter and receiver being at the greatest value of d. If some sort of power control could be affected on the transmitter, there is the possibility of modulating the output power according to the position of the blade at a given time. Turning attention back to Figure 7.3, the distance can be calculated by taking the blade radius, ω and the hub height, h and performing a simple geometrical calculation. It can be shown that:

$$d(\varphi) = \sqrt[2]{h^2 + \omega^2 - 2h\omega \cos(\varphi)} \qquad \text{Eqn 7.8}$$

and the average distance between transmitter and receiver is calculated from:

$$d_{av} = \frac{1}{\pi} \int_{\varphi=0}^{\varphi=\pi} d(\varphi) \; d\varphi \qquad \text{Eqn 7.9}$$

which can be calculated numerically. In the case of the example where h = 95 m and ω = 45 m, the calculation gives an average value of $\underline{d_{av}}$ = 100.4 m. The average transmit power required is therefore calculated as before but using d_{av} in place of d giving -3.93 dBm which is 0.405 mW. Thus, there is a potential saving of approximately a half if power control can be achieved in the radio system. Note that this calculation assumes that the transmitter remains in the main beam of the receive antenna which is a reasonable assumption given the range of the receiver in all of its possible positions and the $\approx 65°$ beam width of the patch antenna. The system might be conceived with different frequencies of operation taken from the Industrial, Scientific and Military (ISM) bands that offer an unlicensed radio spectrum. A selection of these bands along with their bandwidths and worst-case transmit powers are included in Table 7.4.

As would be expected from Eqn 7.6, the power required is lower at lower frequencies, however it must be borne in mind that lower frequencies are associated with larger antennas (for a given antenna efficiency and bandwidth) and hence, there may be a trade-off between the power consumption and the physical dimensions of the device.

Table 7.4 Approximate transmit power and available bandwidth for a receiver sensitivity of -70 dBm at $d = 140$ m.

Frequency (MHz)	Power (mW)	Bandwidth (MHz)
27.12	0.0001	0.326
40.68	0.0002	0.04
433.92	0.0247	1.74
915	0.1099	26
2450	0.7881	100
5800	4.4168	150

7.2 ENERGY SOURCES

Powering the autonomous condition monitoring system is paramount to the successful functioning and operation of the entire system. This section describes the energy sources considered for the system, which has been subdivided into harvesting, storage and regulation. Batteries were the first consideration in the thought process of developing the concept of the autonomous device. However, issues such as the lifespan of the battery expiring before the projected lifetime of the autonomous device dismissed this idea as the sole energy source for the system. In addition, the environmental impact associated with the continued and necessary disposal of the old batteries meant additional costs would be added to the maintenance of the system affixed on the blade to decrease operation and maintenance costs. It defeated the purpose of the autonomous system, which is to decrease wind turbine blade maintenance costs.

Energy harvesting is the process by which low-density ambient energy is captured, converted and stored (where necessary) to provide low-power (from micro Watts to a few Watts) generation for powering electronic devices [260], [261]. Solar, thermal, mechanical energy and electromagnetic radiation are the most common sources for harvesting electrical energy from the environment. Sources such as solar and thermal energy are not readily available at all times and therefore, storage of the energy after capture will benefit these sources of energy. Battery power density and lifespan are limited, however, energy harvesting can help extend battery life and in some cases replace batteries, eliminating the environmental effects of battery disposal.

Advancements in sensor and integrated circuits (ICs) instrumentation and design, have introduced micro-scale devices capable of capturing these energy sources and converting them into electrical energy. The benefits of these devices due to their miniature size are: their ease of installation, flexibility, suitability for retrofitting and avoidance of added weight and cost (especially in scenarios where access to mains electricity is problematic) [260], [262], [263].

7.2.1 HARVESTING

Several energy harvesting methods were considered for the autonomous low-cost wireless monitoring system. In this section, their operation, advantages and disadvantages for application in the autonomous system are discussed.

   a. **Photovoltaic (PV) cells**: PV cells convert sunlight into electricity with power ratings in the order of milli Watts for a single cell to hundred Watts for a large module [264]–[266].
     Advantages
       i.   Cells have a relatively long lifetime with no moving parts.
      ii.   They can be easily attached to a turbine blade, particularly if they are of flexible thin film type.
     iii.   Cells are light and size is scalable.
     iv.   The cost is modest even for small-scale application (£2– 4 per Watt).
      v.   The output is dc.

Disadvantages

i. The output is highly variable as the cells do not operate during night-time and the power is reduced during cloudy conditions.

ii. The cells cannot be mounted inside the blade.

iii. On a blade that rotates attached to a turbine, which yaws into the wind, the cell will frequently not be in an optimal position relative to the sun.

iv. If the cell projects too far from the blade surface, it may affect the aerodynamics of the turbine blade.

v. Fouling of the cell over time will reduce efficiency and performance will naturally degrade with time.

b. **Piezoelectric Device:** Piezoelectric devices make use of a resonant beam which generates electricity when subjected to strain caused by vibration or motion, thereby generating a voltage [267]–[269].

Advantages

i. Devices available are generally lightweight.

ii. Energy harvesting efficiency is well maintained over a long period (unless the maximum tip-to-tip displacement is exceeded).

iii. The frequency of vibration of the beam can be adjusted or tuned to suit the wind turbine blade.

iv. Devices are available in various sizes and can be positioned in/on the wind turbine blade easily.

Disadvantages

i. Output is ac that needs to be rectified.

ii. The devices flex and can thus fatigue over time.

iii. As the piezoelectric harvester feeds off the vibrations of the turbine blade, they can only work when there is sufficient wind (although this is generally when there is greatest need to monitor the blade).

iv. They are relatively expensive at current prices (~ £3,500 per Watt based on a peak power output of 10mW for a ~ £35 device.).

c. **Electromagnetic Harvester:** These devices also convert vibration energy into electrical energy. The relative motion of a magnetic mass in the transducer with respect to a coil causes a change in the magnetic flux. This generates an AC voltage across the coil [267], [270].

Advantages

i. Electromagnetic energy harvesters can be placed in/on wind turbine blades easily with no connection problems.

Disadvantages

i. Such devices are bulky, which could interfere with the aerodynamics of the blade if externally mounted.

ii. The output power is low from some devices.

ii. Moving parts are susceptible to fatigue and failure.

d. **Thermal Energy Harvester:** Thermal energy harvesters such as a thermocouples operate based on the Seebeck effect, i.e. when two junctions made of two dissimilar conductors are kept at different temperatures, an open circuit voltage develops between them [267]. Heat loss due to mechanical friction within the nacelle (which houses the gearbox etc.) of a wind turbine blade could be harvested using thermal energy harvesters.

Advantages
  i.   Devices are relatively low cost.
  ii.   They are light.
  iii. The energy dissipated in the nacelle provides a constant source of energy.
Disadvantages
  i.   Thermal energy harvester output will be variable due to the variance in temperature in the nacelle.
  ii.   Connection through the hub to the accelerometers adds to complexity and cost.

e. **RF Energy Harvester:** Radio frequency energy available through public telecommunication services (e.g., GSM and WLAN frequencies) is converted to electrical energy [267], [271], [272]. The technology is restricted to a band where there is sufficient ambient power, for example 902 – 928 MHz [273].
  Advantages
    i.   Devices are potentially low cost.
    ii.   They can be placed easily on (or in) the wind turbine blade.
  Disadvantages
    i.   The power density available is small requiring a large antenna aperture to capture even small amounts of power.
    ii.   Wind turbines are located far away from areas of high population density; therefore, there will be little RF energy to harvest.
    iii. The power output is low.

Based on the above discussion, photovoltaic and piezoelectric energy harvesters were seen as the most viable options to power an autonomous blade CM system. Electromagnetic energy harvesters were a possible consideration, however, they are difficult to utilize and limited technology is available on the market at present.

7.2.2 STORAGE

Storing the excess energy generated by the harvesters is essential to ensure uninterrupted operation of the microcontroller when performing operations such as turning on the transmitter, acquiring or signal processing the data. Voltage, charge storage capacity, charge cycling, lifetime, cost, size and weight were examined to identify the most suitable choice for the storage of energy. Energy storage methods and techniques for the autonomous low-cost wind turbine blade condition monitoring system are considered below.

a. **Chemical Storage**: Batteries are the most widely used chemical storage of electrical energy. Rechargeable batteries may be charged by the energy harvester to power the autonomous CM system. Numerous battery chemistries are available however, the most widely deployed and readily available are lithium ion batteries [274]. The energy densities available from batteries are significantly higher than capacitors. However, batteries are only capable of a finite number of charge/discharge cycles. Some battery chemistries are also affected by the memory effect (e.g. Nickel-Cadmium) which can degrade performance if they are not deep cycled periodically, whilst others (e.g. Lithium Ion) prefer not to be deep cycled. The microcontroller if required could manage this.
  Advantages
    i.   They provide high charge capacity per unit volume at a reasonable cost.
    ii.   There is a large choice available in terms of size, voltage and capacity.

Disadvantages
    i.   They can be bulky and degrade over time.
    ii.   Disposal of batteries contributes to environmental waste.
   iii.   The lifetime of the battery may be a limiting factor.

b. **Charge Storage:** Capacitors or supercapacitors could provide a modest amount of electrical energy storage, when the energy harvesting device generates insufficient power for a limited period.
Advantages
    i.   They are lightweight.
    ii.   There is a large choice available in terms of capacity and voltage.
Disadvantages
    i.   Cost is high per unit energy stored.
    ii.   Capacity is quite limited.

c. **No Storage:** Potentially, the energy harvesting device could be directly coupled to the autonomous condition monitoring device without any energy storage.
Advantages
    i.   This is a low cost, simple solution, which avoids the limited longevity associated with batteries.
Disadvantages
    i.   This method may constrain the choice of energy harvester to be used.
    ii.   Loss of data can be expected when the harvester is unable to provide enough power for the condition monitoring device.

In conclusion, the preferred solution is to use capacitors as the storage medium due to their long service life, however due to the energy density and cost of such devices, batteries will be considered in the remainder of the thesis as in previous sections.

7.2.3 REGULATION

In order to charge the storage units and to provide an output at a constant voltage suitable for operating the sensors, microcontroller and transmitter, a regulator must be provided. Linear regulator ICs are one option as low dropout devices are available. However, generally they are suitable for higher power applications.

Commercial regulators designed for power harvesting are available and these are the preferred option, since apart from being optimised for low power operation, they also provide control pins ($\overline{SHDN}$ and *PGood*) which interface with the microcontroller. Internally, the devices consist of a switching regulator and are designed specifically for a particular harvesting technology. An example of such a regulator circuit showing the device and its external component is given in Figure 7.4.
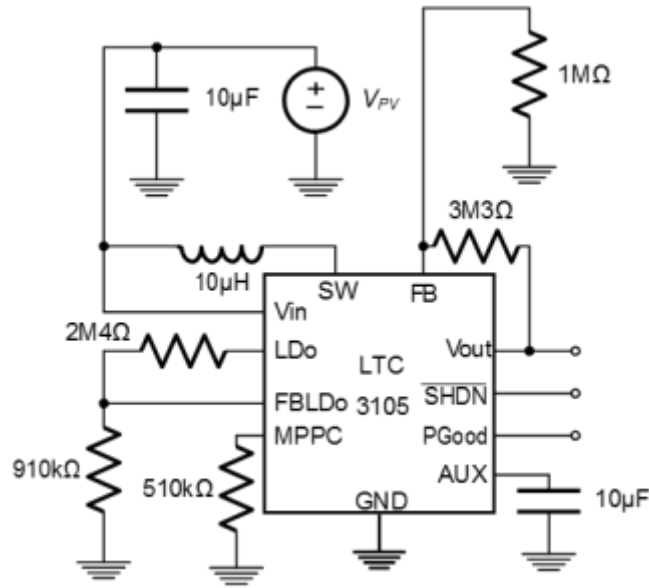
Figure 7.4 Schematic of the photovoltaic circuit adapted from [275]. *Vout, $\overline{SHDN}$* and *PGood* signals are all routed to the microcontroller.

7.3 EVALUATION OF COMMERCIAL ENERGY SOURCES

7.3.1 PHOTOVOLTAIC PANEL

A SLMD481H10L photovoltaic cell [276] was selected as a typical high performance mono-crystalline device with an efficiency of approximately 22%.
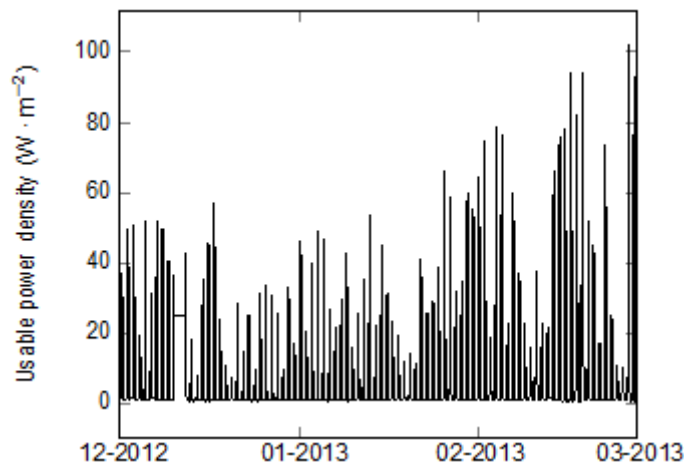
Figure 7.5 Usable solar power from panel in the UK (Midlands) during the winter of 2012 – 2013.

Figure 7.5 shows the measured power density during the winter period 2012 -2013 based on data acquired in the UK midlands for a horizontal planar device. The average power that would be received by the device chosen (SLMD481H10L [276]) would be 38 W per m². Taking into account the device efficiency and area (5.963×10^{-3} m²), this equates to an average power output of 50 mW assuming an optimal solar cell orientation. This is approximately double the power requirement of the system currently measured as 26 mW as stated earlier in this chapter.

7.3.2 PIEZOELECTRIC ENERGY HARVESTER

A Midé Volture (type V21BL) [277] piezoelectric vibration energy harvester was investigated (see Figure 7.6). It comprises of two electrically isolated piezowafers, which may be used independently or bridged for increased voltage (series configuration), or current output (parallel configuration). A

parallel configuration was used because higher current was preferred for the regulator configuration chosen for the system.
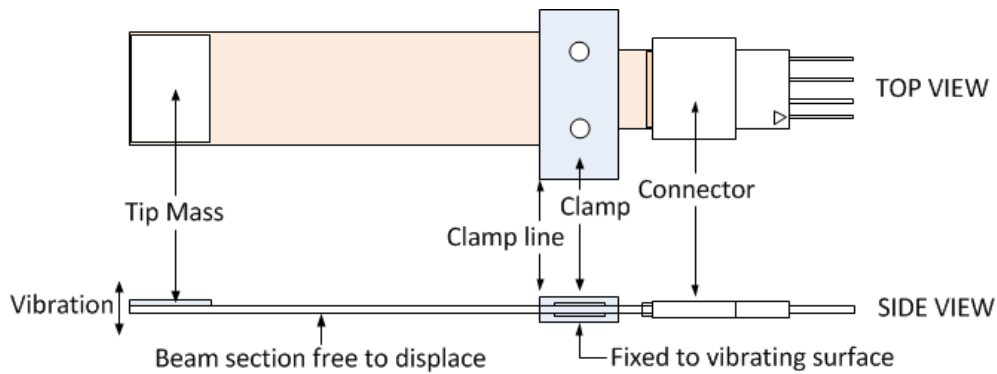
Figure 7.6 Diagram of the Midé Volture piezoelectric energy harvester [277].

One restriction of cantilever devices is that they have distinct resonances that have to be matched to frequency bands where there is sufficient energy in the vibrating structure. Tuning of the device can be achieved by attaching a small mass to the tip of the device.

An experiment was devised to measure the effect of tip loading on a mounted V21BL device. Figure 7.7 shows the experiment set-up.
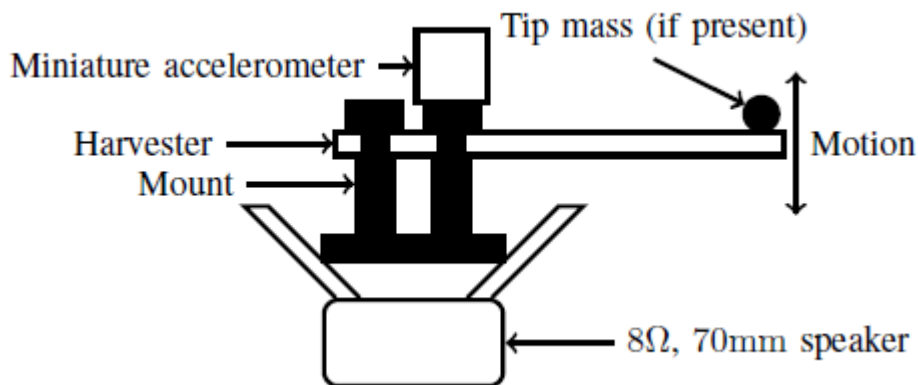
Figure 7.7 Experimental set-up for measuring the piezoelectric energy harvester simulating wind turbine vibrations.

The arrangement was driven from a variable frequency sinusoidal voltage source and feedback from the accelerometer was used to maintain constant peak acceleration of 4.2 ms^{-2} across the frequency range of interest, which was 20 – 120 Hz. The data were subsequently normalised with respect to the displacement seen at the accelerometer, obtained by double integrating the acceleration. In addition, the data were normalised with respect to the area of the device to represent the power harvested. The result of loading can be seen in Figure 7.8. As would be expected, the natural frequency of the device was successfully lowered.

Generally, large scale wind turbine blades (i.e. 40 m and above in diameter) have their first natural frequencies in the range of 0.5 Hz to 15 Hz [116]. In addition, the turbulent characteristics of the wind produce higher frequency, forcing vibrations some of which may excite higher order vibrational modes. This therefore means that the piezoelectric energy harvester should be tuned to suit the vibrational characteristics of each individual blade.

Consider Figure 7.9, which shows the spectrum of the Carter wind turbine blade [227] investigated in the previous chapter of this thesis. It can be seen that the modal frequencies of the blade extend considerably above the fundamental. In particular, there is a mode at 70–80 Hz, which is within the tuneable range of the harvester characterised in Figure 7.8. The piezo can be positioned at the blade root and tuned to harvest energy at that frequency.

In further tests, by varying the loading and by utilising a compatible voltage regulator optimised for piezoelectric energy harvesting, such as the type LTC3588EMSE [278], a maximum power output of 10 mW can be achieved at $1g$ acceleration. This meets the 1 mW power requirement for each MEMS accelerometer. However, a cluster of these piezoelectric energy harvesters would be needed to meet the autonomous low-cost wireless condition monitoring system requirements. During experiments, the manufacturer's suggested maximum limit of 4 mm deflection at the tip was not exceeded, something, which would have to be carefully considered if such a system, were deployed in the field.
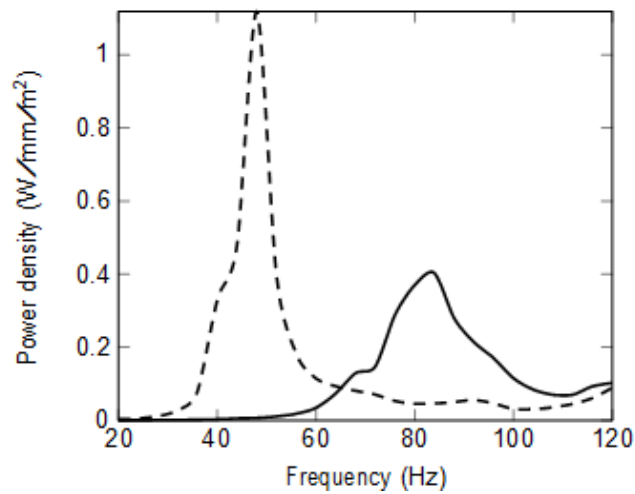
Figure 7.8 Power density achieved for type V21BL device expressed per mm of displacement of the affixed mass. Comparison between untuned device frequency response (solid line) and the tuned frequency response for a $1g$ tip mass (dotted line). The test was conducted with a constant 4.2 m/s^2 peak acceleration.
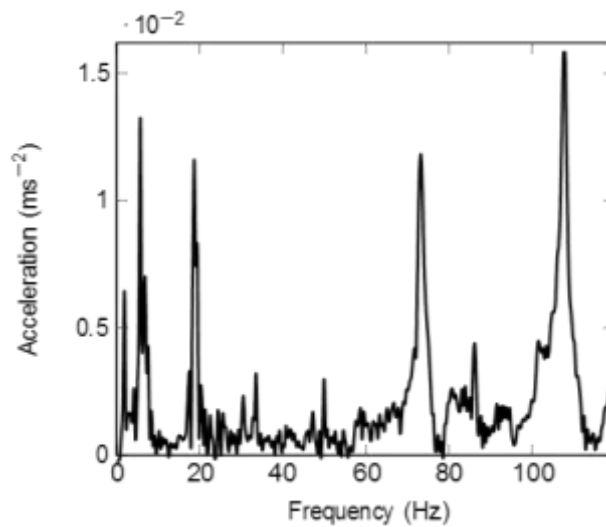
Figure 7.9 Frequency response of 4.5 m long blade from a 25 kW Carter wind turbine measured near to the blade root. The excitation was applied using a force hammer near to the blade tip.

7.4 CONCLUSIONS

This chapter has introduced the concept of a fully autonomous monitoring system for a wind turbine blade that has its own in-built power source. The major power requirement of such a system is to provide radio frequency transmission power from the blade to ground. A link budget has been presented to quantify this, which takes into account the rotating machine. A microprocessor and the sensors from which the data are to be collected, consume the remainder of the power budget. From the power supply options evaluated in more detail, the photovoltaic cell provides the highest power density per unit area of device (50 mW) compared to the piezoelectric harvester (10 mW).

For the latter device, it has been demonstrated that higher order vibration modes of a wind turbine blade could be coupled into the harvester with selection of an appropriate device and by tuning. It is difficult to make a true like-for-like comparison between the harvesting technologies as they draw energy from two sources that are different in nature- the PV panel being active in fair weather with sunshine and the piezoelectric device being active in windy weather. Either technology is likely to require a period to charge energy storage devices until there is sufficient energy available to make an energy transmission.

The system can therefore be envisaged as an aperiodic rather than continuous device. There seems a strong argument that a piezoelectric system has a major advantage over the PV since it does not require any external changes to a standard turbine blade design and operation. In addition, the piezoelectric device can harvest energy when the turbine experiences the highest mechanical loading, which is likely to be coincident with the times that the other sensors such as accelerometers are also active. In generally windy and possibly dull weather, the system would consequently be capable of performing the monitoring functions with the shortest period between samples.

8 CONCLUSIONS AND FUTURE WORK

In this chapter, the research novelty, key findings and opportunities for future work in the research, are discussed.

The main aim of this thesis was to investigate the potential for installing low-cost consumer electronics for vibration-based wind turbine blade condition monitoring in a laboratory-controlled environment. This has been accomplished and demonstrated through theoretical, mathematical and experimental measurements outlined in this thesis. As stated in Chapter 1 and demonstrated in Chapters 2 - 7, the novel contributions made by the author were:

- A review of vibration based condition monitoring for natural frequency identification.

- The application of MEMS accelerometers for condition monitoring of wind turbine blades in laboratory experiments.

- Development of an in-service calibration technique for arbitrarily positioned MEMS accelerometers on a wind turbine blade.

- The validation of low-cost modal analysis techniques on a medium sized wind turbine blade in laboratory experiments.

- The measurement of vibration characteristics using MEMS accelerometers due to mimicked ice loading on a real wind turbine blade.

- Detailed systems approach to the design of a novel embedded monitoring system that can be installed at manufacture, is self-powered, has signal processing capability and can operate remotely.

8.1 KEY RESULTS AND FINDINGS

In this section, key research results and findings described in detail in each chapter of this thesis are reemphasised.

In Chapter 2, the characteristics of wind turbines, their blades, failures and their causes, as well as existing condition monitoring techniques from published literature were introduced. Horizontal axis wind turbines were selected as the focus for the work outlined in the thesis. However, the work can also be applied to vertical axis wind turbines but more study of these systems is required. Published literature on the complexity in turbine blade design was also studied which presented knowledge about loading on blades and helped identify keep mounting positions for experimental measurements. Identification of blade defects and failure from published literature enabled their categorisation into production and operational defects. In addition, the comparison of the different condition monitoring methods from published literature helped identify vibration-based method as the most suitable for use in the rest of the thesis.

In Chapter 3, detailed explanations of vibration-based condition monitoring was given and modal analysis was introduced in the thesis. The relationship between the calculated and measured frequency response of a mechanical structure and its physical properties was established from published literature and conducted experiments. Theoretical and experimental modal analysis methods were presented and investigated as part of a pilot study. Test coupons that mimicked micro wind turbine blades of a Marlec Rutland 913 Windcharger, were analysed using both methods (theoretical and experimental). The first five natural frequencies of the test coupons were distinguished and

comparisons were made between the theoretically obtained calculations and the experimentally obtained measurements further proving the validity in vibration and modal testing methods. Cracks were induced on the test coupons and low-cost sensing piezoelectric sounders with proof masses (brass discs), were used to detect and measure the coupons' responses. This chapter also explained the use of different excitation methods and in particular, impulse excitations from a hammer and snapback methods were investigated in experiments. Overall, this chapter demonstrated the possibility to use low-cost sensing devices for vibration based condition monitoring in laboratory experiments.

In Chapter 4, MEMS accelerometers and their categories (piezoresistive and capacitive- based types) were introduced. Previous applications of these accelerometers were described from published literature and their advantages for application in wind turbine blade condition monitoring were outlined. It was assumed in the research that the lower cost MEMS devices were preferable in terms of cost and they were therefore evaluated and deployed in laboratory experiments. MEMS accelerometers' performance results in comparison to conventional accelerometers obtained from published literature were also presented in this chapter. The results from published literature for the MEMS accelerometers showed deviations in the amplitude and phase in the spectrum when compared to the conventional Integrated Circuit Piezoelectric accelerometers. The literature studies suggested that in-depth understanding of the internal design and possibly effective user-calibration of the MEMS accelerometers can contribute towards improving the identified deviations. Modifications to the mechanical design or in the associated electrical circuity of the MEMS accelerometers were suggested avenues for increased efficiency of the accelerometers if the latter methods were unachievable.

ADXL335 accelerometers were introduced and instrumented for experimental laboratory vibration measurements on micro wind turbine blades of the Marlec Rutland 913 Windcharger. Analogue and digital filtering techniques were applied to improve the resolution of the measured signal output of the accelerometers and the noise floor was considered in Chapter 4. The capability of these accelerometers to distinguish physical properties and characteristics of the micro blades was also demonstrated by comparing frequency response results measured for a new blade with that of an old/damaged blade (previously in operation and had a broken off section). It was demonstrated that higher natural frequencies were measured for the old blade than the new blade. It was also shown that the natural frequencies of the blades were influenced by their mass and stiffness. The positioning of some of the accelerometers and the response they measured also suggested that MEMS accelerometers are capable of measuring localised damage especially close to the tip of the micro blades.

Also in chapter 4, the frequency spectral variation due to induced cracks/damage on the old blade was examined. The use of chirp input signal excitation using an electromagnetic exciter was introduced and measurements from accelerometers were normalised. Results from experiments in this chapter emphasised the complexity involved in performing point-to-point measurements. The natural frequency did not decrease immediately with the introduction of cracks. The effects physical properties of the blades such as mass and stiffness had on the natural frequency were demonstrated. However, it was demonstrated that there was potential for the MEMS accelerometers to be used to determine characteristics of the micro blades.

In chapter 5, a specially designed test fixture was described, manufactured from steel box-section to mimic the hub of a 4.5 m long Carter 25 kW wind turbine blade (medium-sized). A novel calibration technique was introduced for calibrating arbitrarily positioned MEMS accelerometers on a real medium-sized turbine blade. The calibration technique enabled the discovery of the acceleration factors of each individual accelerometer positioned on the turbine blade and set the zero point using samples over time. The calibration technique also enabled the aligning of coordinates of the accelerometers positioned on the blade to the blade's (global) coordinate system. This ensured that all accelerometers mounted on the non-planar blade shared a common coordinate system allowing for

easier and more accurate interpretations of measurements. The effectiveness of the calibration technique was demonstrated experimentally and its benefits for application on a mass-market product such as the accelerometers were discussed. In chapter 6, ice loading, a common factor that affects wind turbine blade operation and subsequently failure, was simulated by attaching weights to the medium-sized blade. The results obtained from experiments showed that the MEMS accelerometers are capable of detecting point loading on wind turbine blades. The uses of electromagnetic exciters as potential sources of excitations as part of the autonomous system were also investigated.

Chapter 7 presented a systems design approach towards developing an in situ autonomous condition monitoring system that incorporated MEMS accelerometers. Conceptualisation of an autonomous system that could be installed at manufacture, is self-powered with signal processing capability and operates remotely was demonstrated. The device was not built however; some commercially available products that could potentially be components of the proposed autonomous system were investigated. Literature was explored for the different design specifications of the proposed system and experimental results obtained from their analysis was presented. Energy harvesting methods, storage and regulation were also considered for the autonomous system and reasons for concluding recommendations to be adopted in the system were clearly demonstrated.

In summary, it was demonstrated in the thesis that MEMS accelerometers can be instrumented to measure the vibrations of wind turbine blades in the laboratory and they do have the potential to be applied for blade condition monitoring in the field.

8.2 FUTURE WORK

Further investigations are required into the implementation of MEMS accelerometers on an operating wind turbine blade. Measurements demonstrated in this thesis focused strictly on controlled-environments obtainable in the laboratory. For initial measurements, the accelerometers can be positioned on the operating blades and calibrated using the calibration technique described in Chapter 5 in the current thesis. The blades could be actively excited using electromagnetic exciters as described in the thesis and measurements for known inputs can be measured and analysed. A further step will be that ambient forces such as the wind, will excite the blades naturally and the capability of the MEMS accelerometers to measure the blades' responses will be investigated. The measured data can be analysed using experimental modal analysis methods as described and demonstrated in the thesis in Chapters 3 - 6.

The conceptualisation and description of the autonomous system in chapter 7 allows for further investigation into a wider scope of commercially available components that could be used to develop the device. The device can be built and implemented in a laboratory controlled environment and could be tested in field on an operating wind turbine blade. Onshore and offshore testing could be conducted and improvements and or adjustments to enable adaptability of the device to the various operating environments can be investigated. Investigations into the design and physical appearance of a commercial product could also be conducted as well as its adaptation to suit various climates (within and outside Europe).

Further validation of MEMS accelerometers is needed. More low-cost MEMS accelerometers have become available since the start of the research described in the current thesis. These accelerometers offer higher ranges and better quality that compensate for the shortcomings of the ADXL335 MEMS accelerometers used for experiments. These various accelerometers can be tested on turbine blades applying the same methodology outlined in this thesis and performance comparisons can be researched and studied. These accelerometers can also be investigated for use on other components of a wind turbine besides the blade and can also be considered for condition monitoring of other mechanical structures such as ships in the marine, oil and gas industries to name a few.

Bench studies that directly compare commercially deployed piezoelectric accelerometers with MEMS accelerometers need to be conducted. The current thesis explored the cost benefits of deploying MEMS accelerometers over the conventional piezoelectric systems. However, like-for-like performance comparisons and findings from experiments in a controlled-laboratory environment will provide additional evidence and/or areas for improvements; strengthening the campaign to follow through with the deployment of MEMS accelerometers for wind turbine blade condition monitoring applications.

Finally, a key and crucial area for development will be the instrumentation and implementation of the MEMS measurements to a wind turbine supervisory control and data acquisition system (SCADA). This is the control mechanism that links all condition monitoring data from various components of the wind turbine. It is very useful and effective for managing large amounts of data ultimately making it easier for wind farm operators to manage the measured data output and maintain the turbine blades as one system.

9 REFERENCES

[1] MSc CREST Flexible and Distance Learning Series, "The Wind Turbine," in *MSc in Renewable Energy Systems Technology Study Notes for Wind 1 2011/12*, Loughborough, 2009, pp. 2–9.

[2] D. Wroblewski, "Wind Turbines," *Boston University College of Engineering*, 2008. [Online]. Available: http://people.bu.edu/dew11/turbinetypes.htmlhttp://people.bu.edu/dew11/turbinetypes.html.

[3] K. K. Borum, M. McGugan, and P. Brøndsted, "Condition monitoring of wind turbine blades," in *27th Risø International Symposium on Materials Science: Polymer Composite Materials for Wind Power Turbines*, 2006, pp. 139–145.

[4] J. G. McGowan, R. W. Hyers, K. L. Sullivan, J. F. Manwell, S. V. Nair, B. McNiff, and B. C. Syrett, "A review of materials degradation in utility scale wind turbines," *Energy Mater. Mater. Sci. Eng. Energy Syst.*, vol. 2, no. 1, pp. 41–64, Mar. 2007.

[5] B. Lu, Y. Li, X. Wu, and Z. Yang, "A review of recent advances in wind turbine condition monitoring and fault diagnosis," *2009 IEEE Power Electron. Mach. Wind Appl.*, pp. 1–7, Jun. 2009.

[6] Risø DTU (National Laboratory for sustainable energy), "Failure modes," 2010. [Online]. Available: http://www.risoe.dtu.dk/research/sustainable_energy/wind_energy/projects/vea_structural_blade_design/failure_modes.aspx?sc_lang=en.

[7] A. Ghoshal, M. J. Sundaresan, M. J. Schulz, and P. F. Pai, "Structural health monitoring techniques for wind turbine blades," *J. Wind Eng. Ind. Aerodyn.*, vol. 85, no. 3, pp. 309–324, Apr. 2000.

[8] R. W. Hyers, J. G. Mcgowan, K. L. Sullivan, J. F. Manwell, and B. C. Syrett, "Condition monitoring and prognosis of utility scale wind turbines," *Energy Mater. Mater. Sci. Eng. Energy Syst.*, vol. 1, no. 3, pp. 187–203, 2006.

[9] F. B. Sørensen, E. Jørgensen, P. C. Debel, M. F. Jensen, M. H. Jensen, K. T. Jacobsen, and M. K. Halling, "Improved design of large wind turbine blade of fibre composites based on studies of scale effects (Phase 1) - Summary Report (Risø-R-1390(EN))," Denmark, 2004.

[10] M. J. Sundaresan, M. J. Schulz, and A. Ghoshal, "Structural health monitoring static test of a wind turbine blade Subcontract Report NREL/SR-500-28719," Colorado, USA, 2002.

[11] F. B. Sørensen, L. Lading, P. Sendrup, M. McGugan, P. C. Debel, J. D. O. Kristensen, G. Larsen, A. M. Hansen, J. Rheinlander, J. Rusborg, and D. J. Vestergaard, "Fundamentals for remote structural health monitoring of wind turbine blades - a preproject Risø-R-1336(EN)," Riso-R-1336(EN) Report, Denmark, 2002.

[12] Sinclair Knight Merz, "Condition Monitoring of Wind Turbines," Glasgow, United Kingdom, 2006.

[13] E. Wiggelinkhuizen, T. Verbruggen, H. Braam, L. Rademakers, J. Xiang, and S. Watson, "Assessment of Condition Monitoring Techniques for Offshore Wind Farms," *J. Sol. Energy Eng.*, vol. 130, no. 3, p. 031004, 2008.

[14] J. R. McEwan and BHR Group Limited, *Condition Monitoring:Proceedings of the 3rd International Conference (Windsor, UK, 15-17 October 1990)*, Illustrate. Essex, England: Elsevier Applied Science, 1991.

[15] Z. Hameed, Y. S. Hong, Y. M. Cho, S. H. Ahn, and C. K. Song, "Condition monitoring and fault detection of wind turbines and related algorithms: A review," *Renew. Sustain. Energy Rev.*, vol. 13, no. 1, pp. 1–39, Jan. 2009.

[16] S. Ganeriwala and J. Yang, "Using Modal Analysis for Detecting Cracks in Wind Turbine Blades," *Sound & Vib.*, vol. 45, no. 5, pp. 10–13, 2011.

[17]   B. Schwarz and M. Richardson, "Experimental modal analysis," in *CSI Reliability Week*, 1999, vol. 35, no. 1, pp. 1–12.

[18]   Rexroth Bosch Group, "Rotor Blade Condition Monitoring Systems," *BLADEcontrol*. [Online].   Available: http://www.boschrexroth.com/corporate/sub_websites/industries/windenergie_portal/en/wind_ components/products/blade-control/index.jsp.

[19]   A. Albarbar, A. Badri, and J. K. Sinha, "Performance evaluation of MEMS accelerometers," *J. Meas.*, vol. 42, no. 5, pp. 790–795, 2009.

[20]   K. S. Tee, M. Awad, A. Dehghani, D. Moser, and S. Zahedi, "Triaxial Accelerometer Static Calibration," in *World Congress on Engineering (WCE)*, 2011, vol. III, no. 2, pp. 6–9.

[21]   A. Badri, J. K. Sinha, and A. Albarbar, "A Method to Calibrate the Measured Responses by MEMS Accelerometers," *J. Strain*, vol. 47, no. Supplement s2, pp. 242–257, Dec. 2010.

[22]   A. Ghosh, *Introduction to Measurements and Instrumentation*, Third Edit. New Delhi: PHI Learning Private Limited, 2009.

[23]   H.-J. Wagner and J. Mathur, *Introduction to Wind Energy Systems*. Berlin, Heidelberg: Springer Berlin Heidelberg, 2009.

[24]   J. Manwell, J. McGowan, and A. Rogers, *Wind Energy Explained: Theory, Design and Application*, Second Edi. Chichester: John Wiley & Sons, Ltd, 2009.

[25]   E. Sesto and C. Casale, "Exploitation of wind as an energy source to meet the world ' s electricity demand," *J. Wind Eng. Ind. Aerodyn.*, vol. 76, pp. 375–387, 1998.

[26]   E. Sesto and D. F. Ancona, "Present and prospective role of wind energy in electricity supply," in *New Electricity 21*, 1995.

[27]   Vestas, "World's most powerful wind turbine now operational," *Vestas News*, 2015. [Online]. Available: http://www.vestas.com/en/media/news#!150612_nr_uk_vws. [Accessed: 05-May-2015].

[28]   T. Ackermann and L. Söder, "An overview of wind energy-status 2002," *Renew. Sustain. Energy Rev.*, vol. 6, no. 1–2, pp. 67–127, Jan. 2002.

[29]   J. Flint, M. Hargreaves, R. Davison, and A. Croft, "Engineering application 2.1," in *Engineering Mathematics: A Foundation for Electronic, Electrical, Communications and Systems Engineers*, Fourth Edi., Essex, England: Pearson Education Limited, 2013, pp. 68–69.

[30]   M. Ragheb and A. M. Ragheb, "Wind Turbines Theory - The Betz Equation and Optimal Rotor Tip Speed Ratio," *Fundam. Adv. Top. Wind Power*, vol. 1, no. 1, 2011.

[31]   F. Blaabjerg, Z. Chen, R. Teodorescu, and F. Iov, "Power electronics in wind turbine systems," *Conf. Proc. - IPEMC 2006 CES/IEEE 5th Int. Power Electron. Motion Control Conf.*, vol. 1, pp. 46–56, 2007.

[32]   BiGGAR Economics, "Onshore Wind: Direct & Wider Economic Impacts," 2012.

[33]   R. Smith, "Vertical-Axis Wind Turbines," *Symscape*, 2007. [Online]. Available: http://www.symscape.com/blog/vertical_axis_wind_turbine.

[34]   R. Smith, "Anatomy of a Horizontal-Axis Wind Turbine," *Symscape*, 2007. [Online]. Available: http://www.symscape.com/blog/anatomy_horizontal_wind_turbine#.UJDxgsV96So.

[35]   TeacherGeek, "Types of Wind Turbines," *TeacherGeek.com*, 2006. [Online]. Available: http://www.teachergeek.org/wind_turbine_types.pdf.

[36]   C. B. Meyers, "Types of Wind Turbines," *Centurion Energy*, 2013. [Online]. Available: http://centurionenergy.net/types-of-wind-turbines.

[37]   C. B. Meyers, "Wind Turbine History," *Centurion Energy*, 2013. [Online]. Available: http://centurionenergy.net/wind-turbine-history.

[38] C. B. Meyers, "How Wind Turbines Work," *Centurion Energy*, 2012. [Online]. Available: http://centurionenergy.net/how-wind-turbines-work.

[39] E. Eggleston and AWEA Staff, "What Are Vertical-Axis Wind Turbines (VAWTs)," *American Wind Energy Association*, 1998. [Online]. Available: http://www.soe-townsville.org/external_atmosphere/verticle_wind_axis.html. [Accessed: 24-Apr-2014].

[40] M. Robinson, M. Hand, D. Simms, and S. Schreck, "Horizontal axis wind turbine aerodynamics: three-dimensional, unsteady, and separated flow influences," in *FEDSM99 3rd ASME/JSME Joint Fluids Engineering Conference*, 1999, no. April, pp. 1–11.

[41] I. Golub, R. Tarko, W. Skomudek, and M. Wawrzyniak, "Wind Power Generation – A Review," *Acta Energetica*, 2013. [Online]. Available: http://actaenergetica.org/en/science/innovations/wind-power-generation-–-a-review.

[42] Clean Energy Brands Technology Support, "Wind Turbines," *Knowlegde Base*, 2013. [Online]. Available: http://www.cleanenergybrands.com/shoppingcart/knowledgemanager/questions/157/101+Small+Wind+Turbines.

[43] B. Hayman, J. Wedel-Heinen, and P. Brøndsted, "Materials challenges in present and future wind energy," *Mater. Res. Soc. Bull.*, vol. 33, no. 04, pp. 343–353, Jan. 2008.

[44] J. W. Holmes, B. F. Sørensen, and P. Brøndsted, "Reliability of Wind Turbine Blades : An Overview of Materials Testing," in *Wind Power Shanghai*, 2007, vol. 2007, no. November, pp. 1–6.

[45] C. Skamris, B. Vestergaard, J. Wedel-Heinen, K. M. Halling, O. Sønderby, J. J. Kristensen, B. Pedersen, P. Brøndsted, C. L. Thomsen, and E. T. D. Bjerregaard, "Type Approval Scheme for Wind Turbines. Recommendation for Design Documentation and Test of Wind Turbine Blades," Copenhagen, Denmark, 2002.

[46] C. C. Ciang, J.-R. Lee, and H.-J. Bang, "Structural health monitoring for a wind turbine system: a review of damage detection methods," *Meas. Sci. Technol.*, vol. 19, no. 12, p. 122001, Dec. 2008.

[47] P. Brøndsted, H. Lilholt, and A. Lystrup, "Composite Materials for Wind Power Turbine Blades," *Annu. Rev. Mater. Res.*, vol. 35, no. 1, pp. 505–538, Aug. 2005.

[48] K. T. Jacobsen, "Joining Structural Parts of Composite Materials for Large Rotorblades," in *27th Risø International Symposium on Materials Science*, 2006, pp. 69–82.

[49] B. Sørensen, H. Toftegaard, and K. Branner, "Improved design for large wind turbine blades of fibre composites (Phase 4)-Summary report," vol. 1734, no. June, 2010.

[50] K. S. Babu, M. S. Reddy, N. V. S. Raju, and N. D. Rao, "The Material Selection for Typical Wind Turbine Blades Using a MADM Approach & Analysis of Blades," in *The 18th International Conference on Multiple Criteria Decision Making*, 2006, pp. 1–12.

[51] F. M. Jensen, H. Stang, and K. Branner, "Ultimate strength of a large wind turbine blade," Technical University of Denmark, Department of Civil Engineering, Section for Structural Engineering, 2008.

[52] W. Musial, "Wind Turbine Testing and Certification," in *Wind Turbine Blade Workshop*, 2004, pp. 1–23.

[53] J.-S. Chou, C.-K. Chiu, I.-K. Huang, and K.-N. Chi, "Failure analysis of wind turbine blade under critical wind loads," *Eng. Fail. Anal.*, vol. 27, pp. 99–118, Jan. 2013.

[54] E. Sagol, M. Reggio, and A. Ilinca, "Issues concerning roughness on wind turbine blades," *Renew. Sustain. Energy Rev.*, vol. 23, pp. 514–525, Jul. 2013.

[55] P. Weiss, "Insects in the Wind Lead to Less Power," *Science News: Magazine of the Society for Science & the Public*, Jul-2001. [Online]. Available: https://www.sciencenews.org/article/insects-wind-lead-less-power.

[56] Kelly Aerospace, "Wind Turbine Ice Protection System," *Thermal Systems*, 2011. [Online]. Available: http://www.kellyaerospace.com/wind_turbine_deice.html.

[57] A. C. Hansen and C. P. Butterfield, "Aerodynamics of Horizontal-Axis Wind Turbines," *Annu. Rev. Fluid Mech.*, vol. 25, no. 1, pp. 115–149, Jan. 1993.

[58] M. R. Soltani, A. H. Birjandi, and M. Seddighi Moorani, "Effect of Surface Contamination on the Performance of a Section of a Wind Turbine Blade," *Sci. Iran.*, vol. 18, no. 3, pp. 349–357, Jun. 2011.

[59] C. Berggreen, C. Jensen, and B. Hayman, "Buckling strength of square composite plates with geometrical imperfections: Preliminary results," in *Advancements in Marine Structures - Proceedings of MARSTRUCT, The 1st International Conference on Marine Structures*, 2007, pp. 413–420.

[60] B. T. Astrom, *Manufacturing of Polymer Composites*, Illustrate. London: CRC Press, 1997.

[61] G. . Short, F. . Guild, and M. . Pavier, "The effect of delamination geometry on the compressive failure of composite laminates," *Compos. Sci. Technol.*, vol. 61, no. 14, pp. 2075–2086, Nov. 2001.

[62] S.-F. Hwang and S.-M. Huang, "Postbuckling behavior of composite laminates with two delaminations under uniaxial compression," *Compos. Struct.*, vol. 68, no. 2, pp. 157–165, Apr. 2005.

[63] G. . Short, F. . Guild, and M. . Pavier, "Delaminations in flat and curved composite laminates subjected to compressive load," *Compos. Struct.*, vol. 58, no. 2, pp. 249–258, 2002.

[64] K. Branner, P. Berring, and C. Berggreen, "Buckling strength of thick composite panels in wind turbine blades—part II: effect of delamination," in *4th International Conference of Composites Testing & Model Identification*, 2008.

[65] C. Berggreen and B. Simonsen, "Non-uniform Compressive Strength of Debonded Sandwich Panels - II. Fracture Mechanics Investigation," *J. Sandw. Struct. Mater.*, vol. 7, no. 6, pp. 483–517, Nov. 2005.

[66] A. Nokkentved, C. Lundsgaard-Larsen, and C. Berggreen, "Non-uniform Compressive Strength of Debonded Sandwich Panels - I. Experimental Investigation," *J. Sandw. Struct. Mater.*, vol. 7, no. 6, pp. 461–482, Nov. 2005.

[67] H. S. Toft, K. Branner, P. Berring, and J. D. Sørensen, "Defect distribution and reliability assessment of wind turbine blades," *Eng. Struct.*, vol. 33, no. 1, pp. 171–180, Jan. 2011.

[68] M. G. Khalfallah and A. M. Koliub, "Effect of dust on the performance of wind turbines," *Desalination*, vol. 209, no. 1–3, pp. 209–220, Apr. 2007.

[69] G. P. Corten and H. F. Veldkamp, "Insects can halve wind-turbine power," *NATURE*, vol. 412, no. July, London, pp. 42 – 43, Jul-2001.

[70] G. Corten and H. Veldkamp, "Insects Cause Double Stall," in *European Wind Energy Conference (EWEC)*, 2001, pp. 2–5.

[71] C. Spruce, "Power Performance of Active Stall Wind Turbines with Blade Contamination," in *European Wind Energy Conference (EWEC) Conference*, 2006, pp. 1–8.

[72] M. C. Robinson, M. M. Hand, D. A. Simms, and S. J. Schreck, "Horizontal Axis Wind Turbine Aerodynamics: Three-Dimensional, Unsteady, and Separated Flow Influences," in *3rd ASME/JSME Joint Fluids Engineering Conference*, 1999, no. April, pp. 1–11.

[73] M. Hansen, *Aerodynamics of Wind Turbines*, Second Edi. Earthscan, 2008.

[74] H. A. Madsen and Forsløgsanslåd Risø, *Aerodynamics of a Horizontal-Axis Wind Turbine in Natural Conditions*. Denmark: Risø National Laboratory, 1991.

[75] C. Bak, H. A. Madsen, P. Fuglsang, and F. Rasmussen, "Double stall," Roskilde, Denmark, 1998.

[76] H. Snel, G. P. Corten, J. W. M. Dekker, J. de Boer, M. Francke, P. K. Chaviaropoulos, and S. Voutsinas, "Progress in the Joule Project: Multiple Stall Levels," in *European Wind Energy Conference (EWEC)*, 1999, pp. 142 – 145.

[77] G. V. Lachmann, "Aspects of Insect Contamination in Relation to Laminar Flow Aircraft," London, 1960.

[78] G. Petrone, C. De Nicola, D. Quagliarella, J. Witteveen, and G. Iaccarino, "Wind Turbine Performance Analysis Under Uncertainty," in *49th AIAA Aerospace Sciences Meeting including the New Horizons Forum and Aerospace Exposition*, 2011, no. January, pp. 1 – 18.

[79] M. B. Bragg, a. P. Broeren, and L. a. Blumenthal, "Iced-airfoil aerodynamics," *Prog. Aerosp. Sci.*, vol. 41, no. 5, pp. 323–362, Jul. 2005.

[80] M. Walsh, "Accretion and Removal of Wind Turbine Icing in Polar Conditions," Aalto University School of Science and Technology, 2010.

[81] A. Ilinca, "Analysis and Mitigation of Icing Effects on Wind Turbines," in *Wind Turbines*, I. Al-Bahadly, Ed. Rimouski, Canada: InTech, 2011, pp. 177 – 215.

[82] C. René, R. Markus, and R. Gabriela, "Four years of monitoring a wind turbine under icing conditions," in *13th International Workshop on Atmospheric Icing of Structures (IWAIS XIII)*, 2009, pp. 6–10.

[83] W. Jasinski, S. Noe, M. Selig, and M. Bragg, "Wind turbine performance under icing conditions," *J. Sol. Energy Eng. Trans. ASME*, vol. 120, no. February, pp. 60 – 65, 1998.

[84] M. C. Homola, M. S. Virk, T. Wallenius, P. J. Nicklasson, and P. a. Sundsbø, "Effect of atmospheric temperature and droplet size variation on ice accretion of wind turbine blades," *J. Wind Eng. Ind. Aerodyn.*, vol. 98, no. 12, pp. 724–729, Dec. 2010.

[85] A. G. Kraj and E. L. Bibeau, "Phases of icing on wind turbine blades characterized by ice accumulation," *Renew. Energy*, vol. 35, no. 5, pp. 966–972, May 2010.

[86] X. Wang, "Convective Heat Transfer and Experimental Icing Aerodynamics of Wind Turbine Blades," University of Manitoba, 2008.

[87] N. Davis, A. N. Hahmann, N.-E. Clausen, and M. Žagar, "Forecast of Icing Events at a Wind Farm in Sweden," *J. Appl. Meteorol. Climatol.*, vol. 53, no. 2, pp. 262–281, Feb. 2014.

[88] N. Dalili, a. Edrisy, and R. Carriveau, "A review of surface engineering issues critical to wind turbine performance," *Renew. Sustain. Energy Rev.*, vol. 13, no. 2, pp. 428–438, Feb. 2009.

[89] L. Rempel, "Rotor blade leading edge erosion—real life experiences," *Wind Systems Magazine*, pp. 22–24, Oct-2012.

[90] A. Sareen, C. A. Sapre, and M. S. Selig, "Effects of leading edge erosion on wind turbine blade performance," *Wind Energy*, vol. 17, no. 10, pp. 1531–1542, Oct. 2014.

[91] ORE Catapult, "At The Leading Edge," *Circuit*, no. 5, pp. 1 –9, 2015.

[92] M. H. Keegan, D. H. Nash, and M. M. Stack, "On erosion issues associated with the leading edge of wind turbine blades," *J. Phys. D. Appl. Phys.*, vol. 46, no. 38, p. 383001, Sep. 2013.

[93] E. Sanderson, A. Morrison, E. Taylor, E. Paramasivam, and R. CME, "Study and Development of a Methodology for the Estimation of the Risk and Harm to Persons from Wind turbines," London, 2013.

[94] T. Brown, "Lightning Protection and Radar Cross-Section Minimisation," in *Sepergen wind Wind Energy Technology*, 2010, no. March.

[95] S. Yokoyama, Y. Yasuda, M. Minowa, S. Sekioka, K. Yamamoto, N. Honjo, and T. Sato, "Clarification of the mechanism of wind turbine blade damage taking lightning characteristics into consideration and relevant research project," *2012 Int. Conf. Light. Prot.*, pp. 1–6, Sep. 2012.

[96] A. Kusiak, Z. Zhang, and A. Verma, "Prediction, operations, and condition monitoring in wind

energy," *Energy*, vol. 60, pp. 1–12, Oct. 2013.

[97]   A. Brown and L. Rashid, "Wind Turbines and Radar Interaction," 2011. [Online]. Available: http://www.supergen-wind.org.uk/docs/presentations/2011-04-20_8_TonyBrown_General Assembly_Radar.pdf. [Accessed: 20-Oct-2011].

[98]   A. Brown and L. Rashid, "Radar and Wind Farms," 2010. [Online]. Available: http://www.supergen-wind.org.uk/docs/presentations/2010-09-24_8_2_Rashid_radar.pdf. [Accessed: 20-Oct-2011].

[99]   F. P. García Márquez, A. M. Tobias, J. M. Pinar Pérez, and M. Papaelias, "Condition monitoring of wind turbines: Techniques and methods," *Renew. Energy*, vol. 46, pp. 169–178, Oct. 2012.

[100] J. M. Pinar Pérez, F. P. García Márquez, A. Tobias, and M. Papaelias, "Wind turbine reliability analysis," *Renew. Sustain. Energy Rev.*, vol. 23, pp. 463–472, Jul. 2013.

[101] F. P. García Márquez, J. Pinar Pérez, M. Papaelias, and R. Ruiz Hermosa, "Wind Turbines Maintenance Management Based on FTA and BDD," in *International Conference on Renewable Energies and Power Quality (ICREPQ'12)*, 2012, pp. 4–6.

[102] R. F. Stapelberg, *Reliability, Availability, Maintainability and Safety in Engineering Design*, 2009 Editi. Girona, Spain: Springer, 2009.

[103] D. McMillan and G. W. Ault, "Condition Monitoring Benefit for Onshore Wind Turbines: Sensitivity to Operational Parameters," *Renew. Power Gener. IET*, vol. 2, no. 1, pp. 60–72.

[104] H. Guo, S. Watson, P. Tavner, and J. Xiang, "Reliability analysis for wind turbines with incomplete failure data collected from after the date of initial installation," *Reliab. Eng. Syst. Saf.*, vol. 94, no. 6, pp. 1057–1063, Jun. 2009.

[105] J. Nilsson and L. Bertling, "Maintenance Management of Wind Power Systems Using Condition Monitoring Systems—Life Cycle Cost Analysis for Two Case Studies," *IEEE Trans. Energy Convers.*, vol. 22, no. 1, pp. 223–229, Mar. 2007.

[106] P. Tavner, J. Xiang, and F. Spinato, "Improving the Reliability of Wind Turbine Generation and its Impact on Overall Distribution Network Reliability," in *18th International Conference on Electricity Distribution*, 2005, no. 4, pp. 1–4.

[107] B. Hahn, M. Durstewitz, and K. Rohrig, "Reliability of Wind Turbines," in *Wind Energy*, J. Peinke, P. Schaumann, and S. Barth, Eds. Berlin, Heidelberg: Springer Berlin Heidelberg, 2007, pp. 329–332.

[108] M. Lange, M. Wilkinson, and T. Van Delft, "Wind Turbine Reliability Analysis," 2011.

[109] G. Van Bussel and M. Zaaijer, "Reliability, Availability and Maintenance aspects of large-scale offshore wind farms, a concepts study," in *Proceedings of Marine Renewable Energies Conference (MAREC)*, 2001, pp. 119–126.

[110] G. Van Bussel and M. Zaaijer, "Estimation of Turbine Reliability Figures within the DOWEC Project," Copenhagen, Denmark, 2003.

[111] J. Ribrant and L. M. Bertling, "Survey of failures in wind power systems with focus on Swedish wind power plants during 1997-2005," in *IEEE Transactions on Energy Conversion*, 2007, vol. 22, no. 1, pp. 167–173.

[112] F. Spinato, P. J. Tavner, G. J. W. van Bussel, and E. Koutoulakos, "Reliability of wind turbine subassemblies," *IET Renew. Power Gener.*, vol. 3, no. 4, p. 387, 2009.

[113] Y. Amirat, M. E. H. Benbouzid, E. Al-Ahmar, B. Bensaker, and S. Turri, "A brief status on condition monitoring and fault diagnosis in wind energy conversion systems," *Renew. Sustain. Energy Rev.*, vol. 13, no. 9, pp. 2629–2636, 2009.

[114] B. S. Nivedh, "Major failures in the wind turbine components and the importance of periodic inspections," *www.windinsider.com*, 2014. [Online]. Available: http://www.dewi.de/dewi_res/fileadmin/pdf/papers/WindInsider_November_2014.pdf.

[Accessed: 16-Jun-2015].

[115]   P. Smith, "Data : Component fault rates analysed," *WINDPOWER Monthly*, 2014. [Online]. Available: http://www.windpowermonthly.com/article/1302791/data-component-fault-rates-analysed. [Accessed: 15-Jun-2015].

[116]   G. C. Larsen, M. H. Hansen, A. Baumgart, and I. Carlen, "Modal Analysis of Wind Turbine Blades (Risø -R-1181(EN))," Denmark, 2002.

[117]   H. B. Pedersen and O. D. Kristensen, "Applied modal analysis of wind turbine blades (Risø -R-1388(EN))," Denmark, 2003.

[118]   C. J. Crabtree and P. J. Tavner, "Condition Monitoring of Wind Turbines," in *5th PhD. Seminar on Wind Energy in Europe*, 2009, pp. 1–4.

[119]   G. Marsh, "In-service Monitoring of Turbine Blades," *Reinf. Plast.*, vol. 52, no. 5, pp. 24–27,29, 2008.

[120]   P. J. Tavner, C. J. Crabtree, and M. Wilkinson, "Cost-Effective Condition Monitoring for Wind Turbines," *IEEE Trans. Ind. Electron.*, vol. 57, no. 1, pp. 263–271, Jan. 2010.

[121]   Moog, "Blade sensing sytems," 2010. [Online]. Available: http://www.moog.com/markets/energy/wind-turbines/blade-sensing-system/.

[122]   Renewable Energy Focus, "Risoe embeds smart sensor sytems for offshore wind farms," 2010. [Online]. Available: http://www.renewableenergyfocus.com/view/6519/ris-embeds-smart-sensor-systems-for-offshore-wind-turbines/. [Accessed: 09-Dec-2011].

[123]   E. P. Carden and P. Fanning, "Vibration Based Condition Monitoring : A Review," *Struct. Heal. Monit.*, vol. 3, no. 4, pp. 355–377, 2004.

[124]   LMS Siemens, "Modal Analysis," *Testing Solutions Technical Notes*, 2013. [Online]. Available: http://www.lmsintl.com/modal-analysis.

[125]   M. P. Norton, *Fundamentals of noise and vibration analysis for engineers*. Melbourne: Cambridge University Press, 1989.

[126]   D. J. Ewins, *Modal Testing: Theory and Practice*, 2nd ed. London: John Wiley & Sons, INC, 1984.

[127]   P. Avitabile, "Mechanical Vibrations Overview of Experimental Modal Analysis."

[128]   Maia, Silva, Lieven, He, Skingle, Lin, To, and Urgueira, *Theoretical and Experimental Modal Analysis*. Hertfordshire: Research Studies Press Ltd.

[129]   J. He and Z.-F. Fu, *Modal Analysis*. Oxford: Butterworth-Heinemann, 2001.

[130]   J. T. Broch, *Mechanical Vibration and Shock Measurements*, 2nd ed. Denmark: Brüel & Kjær, 1980.

[131]   G. B. Warburton, *The Dynamic Behaviour of Structures*, Second. Nottingham: Pergamon Press, 1976.

[132]   J. D. Den Hartog, *Mechanical Vibrations*, Fourth. New York: McGraw-Hill, 1956.

[133]   MathWorks, "Finite Element Method (FEM) Basics," *Partial Differential Equation Toolbox*, 2013. [Online]. Available: http://www.mathworks.co.uk/help/pde/ug/basics-of-the-finite-element-method.html.

[134]   J. Chessa, "Programing the Finite Element Method with Matlab A Few Words on Writing Matlab Programs," no. October, pp. 1–45, 2002.

[135]   Ross, *Finite element techniques in structural mechanics*. 1935.

[136]   ANSYS, "ANSYS Workbench Platform." ANSYS, 2016.

[137]   Autodesk, "Mechanical Simulation and Modelling," *Features for Simulation Mechanical*, 2013. [Online]. Available: http://www.autodesk.co.uk/products/autodesk-simulation-family/features/simulation-mechanical.

[138] J. F. Skov and M. D. Ulriksen, "Damage Identification in Wind Turbine Blades - A Modal and Wavelet Analysis-based Approach," Aalborg University Esbjerg, 2014.

[139] Y. Wang, M. Liang, and J. Xiang, "Damage detection method for wind turbine blades based on dynamics analysis and mode shape difference curvature information," *Mech. Syst. Signal Process.*, vol. 48, no. 1–2, pp. 351–367, 2014.

[140] P. Berring, D. Tcherniak, K. Branner, and G. C. Larsen, "Effect of a Damage To Modal Parameters of a Wind Turbine," in *Le Cam, Vincent and Mevel, Laurent and Schoefs, Franck. EWSHM - 7th European Workshop on Structural Health Monitoring*, 2014, pp. 261–269.

[141] M. D. Ulriksen, D. Tcherniak, P. H. Kirkegaard, and L. Damkilde, "EWSHM 2014: Operational modal analysis and wavelet transformation for damage identification in wind turbine blades," *Struct. Heal. Monit.*, 2015.

[142] O. O. Esu, J. A. Flint, and S. J. Watson, "Integration of Low-cost Accelerometers for Condition Monitoring of Wind Turbine Blades," in *Proc. European Wind Energy Association (EWEA) Conference*, 2013, pp. 1–4.

[143] National Instruments, "LabVIEW System Design Software," *Products*. [Online]. Available: http://www.ni.com/labview/.

[144] MathWorks, "MATLAB: The Language of Technical Computing." [Online]. Available: http://www.mathworks.co.uk/products/matlab/.

[145] S. M. Kay and S. L. Marple, "Spectrum Analysis-A Modern Perspective," vol. 69, no. 11, 1981.

[146] National Instruments Corporation, "Understanding FFTs and Windowing," 2015. [Online]. Available: http://www.ni.com/white-paper/4844/en/. [Accessed: 06-Jun-2015].

[147] S. Doebling, C. Farrar, M. Prime, and D. Shevitz, "Damage identification and health monitoring of structural and mechanical systems from changes in their vibration characteristics: A literature review," California, 1996.

[148] E. P. Carden, "Vibration Based Condition Monitoring: A Review," *Struct. Heal. Monit.*, vol. 3, no. 4, pp. 355–377, Dec. 2004.

[149] H. Banks, D. Inman, D. Leo, and Y. Wang, "An experimentally validated damage detection theory in smart structures," *J. Sound Vib.*, vol. 191, no. 5, pp. 859–880, 1996.

[150] S. Alampalli, G. Fu, and E. Dillon, "Signal versus noise in damage detection by experimental modal analysis," *J. Struct. Eng.*, vol. 123, no. 2, pp. 237–245, 1997.

[151] M. Friswell and J. Penny, "Is damage location using vibration measurements practical?," in *EUROMECH 365 International Workshop: DAMAS 97, Structural Damage Assessment Using Advanced Signal Processing Procedures*, 1997, no. July 1997, pp. 1–8.

[152] U. Lee and J. Shin, "A frequency response function-based structural damage identification method," *Comput. Struct.*, vol. 80, no. 2, pp. 117–132, Jan. 2002.

[153] R. D. Adams, P. Cawley, C. J. Pye, and B. J. Stone, "A vibration technique for non-destructively assessing the integrity of structures," *Arch. J. Mech. Eng. Sci. 1959-1982 (vols 1-23)*, vol. 20, no. 2, pp. 93–100, Apr. 1978.

[154] M. Samman and M. Biswas, "Vibration testing for nondestructive evaluation of bridges. I: theory," *J. Struct. Eng.*, vol. 120, no. 1, pp. 269–289, 1994.

[155] M. Samman and M. Biswas, "Vibration testing for nondestructive evaluation of bridges. II: results," *J. Struct. Eng.*, vol. 120, no. 1, pp. 290–306, 1994.

[156] O. S. Salawu, "Detection of structural damage through changes in frequency: a review," *Eng. Struct.*, vol. 19, no. 9, pp. 718–723, Sep. 1997.

[157] P. H. Kirkegaard and A. Rytter, "Vibration Based Damage Assessment of Civil Engineering Structures Using Neural Networks," in *Presented at the 1st Workshop of the European Group*

for Structural Engineering Applications of Artificial Intelligence, 1994, pp. 1–15.

[158] L. Wang and T. H. T. Chan, "Review of Vibration-Based Damage Detection and Condition Assessment of Bridge Structures using Structural Health Monitoring," in *The Second Infrastructure Theme Postgraduate Conference : Rethinking Sustainable Development: Planning, Engineering, Design and Managing Urban Infrastructure*, 2009, no. March.

[159] P. Gipe, "Evaluating the Technology - What Works and What Doesn't," in *Wind Power: Renewable Energy For Home, Farm and Business*, Completely., White River Junction, Vermont: Chelsea Green Publishing Company, 2004, pp. 83 – 146.

[160] Guirt, "Wind Turbine Blade Aerodynamics," *Wind Energy Handbook*, 2012. [Online]. Available: http://www.gurit.com/files/documents/2_aerodynamics.pdf.

[161] H. Wang and W. Worley, "Tables of natural frequencies and nodes for transverse vibration of tapered beams," Washington, D. C., 1966.

[162] Marlec Renewable Power, "Rutland 913 Windcharger." [Online]. Available: http://www.marlec.co.uk/products/windchargers/rutland-913-windcharger/.

[163] W. C. Young and R. G. Budynas, *Roark's Formulas for Stress and Strain*, Seventh Ed. New York: McGraw-Hill, 2002.

[164] Sakshat Virtual Labs, "Free Vibration of a Cantilever Beam (Continuous System)," *Indian Institute of Technology*, 2012. [Online]. Available: http://iitg.vlab.co.in/?sub=62&brch=175&sim=1080&cnt=1.

[165] S. Whittney, "Vibrations of Cantilever Beams: Defelction, Frequency and Research Uses," *University of Nebraska-Lincoln*, 1999. [Online]. Available: http://emweb.unl.edu/Mechanics-Pages/Scott-Whitney/325hweb/Beams.htm.

[166] Suranaree University of Technology, "Moments of Inertia," 2009. [Online]. Available: http://www.sut.ac.th/engineering/Civil/courses/410201/section_01/pdf/09_review.pdf.

[167] The Geometry Center, "Beams, Bending and Boundary Conditions," 1996. [Online]. Available: http://www.geom.uiuc.edu/education/calc-init/static-beam/boundary.html.

[168] M. Bayat and I. Pakar, "Analytical study on the vibration frequencies of tapered beams," *Lat. Am. J. Solids …*, vol. 8, pp. 149–162, 2011.

[169] C. Felippa, "ASEN 2003 : Introduction to Dynamics and Systems," *Introduction to Aerospace Engineering Sciences, University of Colorado at Boulder*, 2003. [Online]. Available: http://www.colorado.edu/ASEN/ASEN_SOPH/ASEN2003/ASEN2003.Appdedix.C.pdf.

[170] O. A. Bauchau and J. I. Craig, "Euler-Bernoulli Beam Theory," in *Structural Analysis Part II*, O. A. Bauchau and J. I. Craig, Eds. Georgia: Springer Netherlands, 2009, pp. 173 – 221.

[171] Maplin, "3V Ceramic Piezo Transducer 27/1.8," *Product Catalogue*. [Online]. Available: http://www.maplin.co.uk/p/3v-ceramic-piezo-transducer-2718-yu87u.

[172] S. S. Rao and Y. F. Fah, "Vibration Measurement and Applications," in *Mechanical Vibrations*, Fifth., no. 1824, Singapore: Prentice Hall Inc, 2011, pp. 870–938.

[173] National Instruments Corporation, "User Guide and Specifications NIUSB-6008/6009," 2012. [Online]. Available: http://www.ni.com/pdf/manuals/371303m.pdf.

[174] National Instruments Corporation, "NI LabVIEW SignalExpress," 2012. [Online]. Available: http://www.ni.com/labview/signalexpress/.

[175] Granta Design, "CES EduPack," 2012. [Online]. Available: http://www.grantadesign.com/education/.

[176] National Instruments, "Basic Information about AC and DC Coupling," *NI Support*, 2012. [Online]. Available: http://digital.ni.com/public.nsf/allkb/0F81C33977056A7D862566F1005CAA71.

[177] G.-R. Gillich, N. M. M. Maia, I.-C. Mituletu, Z.-I. Praisach, M. Tufoi, and I. Negru, "Early

structural damage assessment by using an improved frequency evaluation algorithm," *Lat. Am. J. Solids Struct.*, vol. 12, no. 12, pp. 2311–2329, 2015.

[178] NDT Education Resource Center, "Characterisitics of Piezoelectric Transducers," *NDT Course Material*, 2001. [Online]. Available: https://www.nde-ed.org/EducationResources/CommunityCollege/Ultrasonics/EquipmentTrans/characteristicspt.htm.

[179] APC International, "Behavior of a Piezo Element," *Knowledge Center: Piezo Theory*, 2014. [Online]. Available: https://www.americanpiezo.com/knowledge-center/piezo-theory/behavior.html.

[180] C. Ratcliffe, D. Heider, R. Crane, C. Krauthauser, M. K. Yoon, and J. W. Gillespie, "Investigation into the use of low cost MEMS accelerometers for vibration based damage detection," *Compos. Struct.*, vol. 82, no. 1, pp. 61–70, Jan. 2008.

[181] S. W. Yoon, "Vibration Isolation and Shock Protection for MEMS," Michigan, 2009.

[182] C. Hammerschmidt, "STMicroelectronics rolls MEMS-based airbag sensor," *EE Times Europe*, 10-Nov-2010. [Online]. Available: http://www.automotive-eetimes.com/en/stmicroelectronics-rolls-mems-based-airbag-sensor.html?cmp_id=7&news_id=222901196. [Accessed: 22-Oct-2013].

[183] A. Albarbar, S. Mekid, A. Starr, and R. Pietruszkiewicz, "Suitability of MEMS Accelerometers for Condition Monitoring: An experimental study," pp. 784–799, 2008.

[184] P. Batista, C. Silvestre, P. Oliveira, and B. Cardeira, "Accelerometer Calibration and Dynamic Bias and Gravity Estimation: Analysis, Design, and Experimental Evaluation," *IEEE Trans. Control Syst. Technol.*, vol. 19, no. 5, pp. 1128–1137, Sep. 2011.

[185] O. O. Esu, J. A. Flint, and S. J. Watson, "Condition Monitoring of Wind Turbine Blades Using MEMS Accelerometers," in *Proc. Renewable Energy World Europe (REWE)*, 2013, pp. 1–12.

[186] H. Die, Z. Chunnian, and L. Hong, "Autocalibration method of MEMS accelerometer," in *2011 International Conference on Mechatronic Science, Electric Engineering and Computer (MEC)*, 2011, pp. 1348–1351.

[187] M. Sipos, P. Paces, J. Rohac, and P. Novacek, "Analyses of Triaxial Accelerometer Calibration Algorithms," *IEEE Sens. J.*, vol. 12, no. 5, pp. 1157–1165, May 2012.

[188] B. Minhang, *Analysis and Design Principles of MEMS Devices*. Amsterdam, The Netherlands: ELSEVIER B. V., 2005.

[189] J. a. Plaza, a. Collado, E. Cabruja, and J. Esteve, "Piezoresistive accelerometers for MCM package," *J. Microelectromechanical Syst.*, vol. 11, no. 6, pp. 794–801, Dec. 2002.

[190] A. Beliveau, G. T. Spencer, K. a. Thomas, and S. L. Roberson, "Evaluation of MEMS capacitive accelerometers," *IEEE Des. Test Comput.*, vol. 16, no. 4, pp. 48–56, 1999.

[191] H. Xie and G. K. Fedder, "A CMOS z-axis capacitive accelerometer with comb-finger sensing," in *Proceedings IEEE Thirteenth Annual International Conference on Micro Electro Mechanical Systems (MEMS)*, 2000, pp. 496–501.

[192] S. Thanagasundram and F. S. Schlindwein, "Comparison of integrated micro-electrical-mechanical system and piezoelectric accelerometers for machine condition monitoring," *Proc. Inst. Mech. Eng. Part C J. Mech. Eng. Sci.*, vol. 220, no. 8, pp. 1135–1146, Aug. 2006.

[193] A. Badri and J. Sinha, "Dynamics of MEMS Accelerometer," in *The 17th International Congress on Sound & Vibration*, 2010, no. July, pp. 2253–2261.

[194] A. E. Badri and J. K. Sinha, "IMPROVEMENT IN MEASURED SIGNALS OF MEMS," in *3rd International Conference on Integrity, Reliability and Failure*, 2009, no. July, pp. 1–7.

[195] A. Badri and J. K. Sinha, "Correcting Amplitude and Phase Measurement of Accelerometer in Frequency Domain," in *The 5th International Conference on Condition Monitoring and Machinery Failure Prevention Technologies (CM 2008 and MFPT 2008)*, 2008, pp. 94 –100.

[196] A. E. Badri, J. K. Sinha, and A. Albarbar, "A typical filter design to improve the measured signals from MEMS accelerometer," *J. Meas.*, vol. 43, no. 10, pp. 1425–1430, Dec. 2010.

[197] A. Badri, J. K. Sinha, and A. Albarbar, "Enhancing the Frequency Range of Measurement for an Accelerometer," *Noise Vib. Worldw.*, vol. 40, no. 6, 2009.

[198] A. E. Badri, "Performance Improvement of MEMS Accelerometers in Vibration Based Diagnosis," University of Manchester, 2011.

[199] Analog-Devices, "ADXL105," *Technical Datasheet*, 1999. [Online]. Available: http://www.analog.com/static/imported-files/data_sheets/ADXL105.pdf.

[200] Brüel & Kjær, "Piezoelectric Deltashear Accelerometers," *Product Data*. [Online]. Available: http://www.titak.itu.edu.tr/Accelerometers/accel_BK_4384.pdf.

[201] Analog-Devices, "ADXL335," 2010. [Online]. Available: www.analog.com. [Accessed: 05-Dec-2011].

[202] National Instruments Corporation, "M Series User Manual," 2008. [Online]. Available: http://www.ni.com/pdf/manuals/371291h.pdf.

[203] C. Kitchin, "Understanding Accelerometer Scale Factor and Offset Adjustments," MASSACHUSETTS, 2009.

[204] MATHalino.com, "Components of a Force," *Engineering Mechanics*, 2014. [Online]. Available: http://www.mathalino.com/reviewer/engineering-mechanics/components-of-a-force.

[205] intan Technologies LLC, "RHD2000-EVAL Application Note: Accelerometer Calibration," 2013. [Online]. Available: http://www.intantech.com/files/Intan_RHD2000_accelerometer_calibration.pdf.

[206] Starlino, "A Guide To using IMU (Accelerometer and Gyroscope Devices) in Embedded Applications .," *IMU Theory and Experiments*, 2009. [Online]. Available: http://www.starlino.com/imu_guide.html.

[207] B. J. Morgan and R. G. Oesterle, "On-site Modal Analysis - A New Powerful Inspection Technique," in *Proc. 2nd International Bridge Conference*, 1994, pp. 108 – 114.

[208] A. Ruina and R. Pratap, "Center of mass and gravity," in *Introduction to Statics and Dynamics*, Oxford: Oxfors University Press, 2010, pp. 78 – 91.

[209] Massachusetts Institute of Technology (MIT), "Module 5 -- Center of Mass: definition," *PER wiki*, 2012. [Online]. Available: https://scripts.mit.edu/~srayyan/PERwiki/index.php?title=Module_5_--_Center_of_Mass:_definition. [Accessed: 29-Jun-2015].

[210] S. G. Creed, "Assessment of large engineering structures using data collected during in-service loading," in *Structural Assessment*, F. K. Garas, J. L. Clarke, and G. S. T. Armer, Eds. London: Butterworths, 1995, pp. 55 – 62.

[211] Visaton, "Basic Principles of Visaton Exciter-Technology." [Online]. Available: http://www.visaton.com/downloads/pdf/visaton_exciter_principles.pdf.

[212] FLI, "FLI Amplifier 360.2," *Instruction and Installation Manual*. [Online]. Available: http://www.fliaudio.co.uk/portfolio/fu-360-2/.

[213] J. T. Broch, "Technical Review: Vibration Exciter Characteristics," Copenhagen, Denmark, 1960.

[214] G. F. Lang, "Electrodynamic Shaker Fundamentals," *Sound and Vibration*, San Jose, California, pp. 1–8, Apr-1997.

[215] J. S. Rao and K. Gupta, "Experimental Methods in Vibration Analysis: Vibration Exciters," in *Introductory Course on Theory and Practice of Mechanical Vibrations*, New Delhi: New Age International (P) Limited Publishers, 1999, pp. 451 – 453.

[216] G. R. Tomlinson, "Determination of the Modal Properties of Complex Structures Including Non-Linear Effects," University of Salford, 1979.

[217] A. B. Chatfield, *Fundamentals Of High Accuracy Inertial Navigation*. Reston , VA: American Institute of Aeronautics and Astronautics, 1997.

[218] The Modal Shop Inc. (TMS), "Accelerometer Calibration Overview," *Dynamic Calibration Education*, 2014. [Online]. Available: http://www.modalshop.com/calibration/Accelerometer-Calibration-Overview?ID=412.

[219] Endevco, "Minimizing measurement uncertainty in calibration and use of accelerometers," *TP-299*, 20102. [Online]. Available: https://www.endevco.com/news/archivednews/2010/2010_01/TP-299.pdf.

[220] M. Pedley, "High Precision Calibration of a Three-Axis Accelerometer," *Freescale Semiconductor Application Note*, 2013. [Online]. Available: http://cache.freescale.com/files/sensors/doc/app_note/AN4399.pdf.

[221] F. du Plessis, F. Swanepoel, and A. Nel, "An Alternative Methodology for Fiber Optic Gyroscope Calibration," in *Proceedings of the AIAA Guidance, Navigation and Control Conference*, 2009, no. August, pp. 1–24.

[222] C. Fisher, "Using an Accelerometer for Inclination Sensing," Norwood, 2010.

[223] J. Yang, W. Wu, Y. Wu, and J. Lian, "Improved iterative calibration for triaxial accelerometers based on the optimal observation.," *Sensors (Basel).*, vol. 12, no. 6, pp. 8157–75, Jan. 2012.

[224] G. Panahandeh, I. Skog, and M. Jansson, "Calibration of the accelerometer triad of an inertial measurement unit, maximum likelihood estimation and Cramer-Rao bound," in *International Conference on Indoor Positioning and Indoor Navigation (IPIN)*, 2010, no. September, pp. 1–6.

[225] J. Hung, J. Thacher, and H. White, "Calibration of accelerometer triad of an IMU with drifting Z-accelerometer bias," in *Proceedings of the IEEE National Aerospace and Electronics Conference*, 1989, pp. 153–158.

[226] M. Pedley, "Tilt Sensing Using a Three-Axis Accelerometer," Arizona, USA, Rev 6, 2013.

[227] Carter Wind Energy, "Carter Wind Turbines." [Online]. Available: http://www.carterwindenergy.com/.

[228] Beacon Energy, "Professor Tony Marmont," *Welcome to Beacon Energy*, 2014. [Online]. Available: http://www.beaconenergy.co.uk/pmarmont.html. [Accessed: 19-Nov-2014].

[229] Brüel & Kjær, "Instruction Manual: Impact Hammer Type 8202," 1984. [Online]. Available: http://www.titak.itu.edu.tr/Hammers_Shakers/Hammer_BK_8202.pdf.

[230] J. C. Lötters, J. Schipper, P. H. Veltink, W. Olthuis, and P. Bergveld, "Procedure for in-use calibration of triaxial accelerometers in medical applications," *Sensors Actuators A Phys.*, vol. 68, no. 1–3, pp. 221–228, Jun. 1998.

[231] Sentera Technology Corporation, "Tri-axial Accelerometer Calibration," *MEMS IMU Calibration Example*. [Online]. Available: http://motionsense.com/services/pdf/Calibration Report Example.pdf.

[232] STMicroelectronics, "Tilt measurement using a low-g 3-axis accelerometer," AN3182, 2010.

[233] O. O. Esu, J. A. Flint, and S. J. Watson, "Static Calibration of Microelectromechanical Systems (MEMS) Accelerometers for In-Situ Wind Turbine Blade Condition Monitoring," in *Special Topics in Structural Dynamics, Volume 6: Proceedings of the 33rd IMAC, A Conference and Exposition on Structural Dynamics, 2015*, R. Allemang, Ed. Springer International Publishing, 2015, pp. 91–98.

[234] MathWorks, "Least Squares." [Online]. Available: http://www.mathworks.co.uk/moler/leastsquares.pdf.

[235] S. J. Miller, "The Method of Least Squares." [Online]. Available: http://web.williams.edu/Mathematics/sjmiller/public_html/BrownClasses/54/handouts/Method LeastSquares.pdf.

[236] S. Boyd, "Lecture 5: Least Squares," *EE263 Autumn 2007-08*, 2007. [Online]. Available: http://see.stanford.edu/materials/lsoeldsee263/05-ls.pdf.

[237] STMicroelectronics, "AN3192 Application note: Using LSM303DLH for a tilt compensated electronic compass," 2010. [Online]. Available: http://www.pololu.com/file/download/LSM303DLH-compass-app-note.pdf?file_id=0J434.

[238] A. Burgess, "TRANSIENT RESPONSE OF MECHANICAL STRUCTURES USING MODAL ANALYSIS," Imperial College, 1988.

[239] P. Frohboese and A. Anders, "Effects of Icing on Wind Turbine Fatigue Loads," *Journal of Physics: Conference Series*, vol. 75. IOP Publishing Ltd, Hamburg, pp. 1 − 14, 2007.

[240] P. Frohboese, M. Steiniger, and A. Anders, "Ice Loads on Wind Turbines," in *European Wind Energy Conference (EWEC) Conference*, 2007, pp. 1–10.

[241] H. Seifert, "Technical Requirements for Rotor Blades Operating in Cold Climate," *Proceedings of BOREAS VI Conference*, DEWI Magazin, Wilhelmshaven, Germany, pp. 1 − 13, Apr-2003.

[242] M. C. Homola, P. J. Nicklasson, and P. a. Sundsbø, "Ice sensors for wind turbines," *Cold Reg. Sci. Technol.*, vol. 46, pp. 125–131, 2006.

[243] N. Harper, "Detecting Ice on Wind Turbine Blades," *Wind Power Engineering and Development*, 2011. [Online]. Available: http://www.windpowerengineering.com/maintenance/detecting-ice-on-wind-turbine-blades/. [Accessed: 08-Oct-2013].

[244] V. Carlsson, "Measuring routines of ice accretion for Wind Turbine applications: The correlation of production losses and detection of ice," Skelleftea Kraft, 2010.

[245] O. Parent and A. Ilinca, "Anti-icing and de-icing techniques for wind turbines: Critical review," *Cold Reg. Sci. Technol.*, vol. 65, no. 1, pp. 88–96, 2011.

[246] E. Rindeskär, "Modelling of icing for wind farms in cold climate," Uppsala, Sweden, 2010.

[247] M. S. Virk, M. C. Homola, and P. J. Nicklasson, "Atmospheric Icing on Large Wind Turbine Blades," *Int. J. Energy Environ.*, vol. 3, no. 1, pp. 1–8, 2012.

[248] C. Hochart, G. Fortin, J. Perron, and A. Ilinca, "Wind turbine performance under icing conditions," *Wind Energy*, vol. 11, no. October 2007, pp. 319–333, 2008.

[249] "COST-727, Atmospheric Icing on Structures: 2006, Measurements and Data Collection on Icing: State of the Art," *Publ. MeteoSwiss*, vol. 75, p. 110 pp, 2006.

[250] Siemens, "NX for Design." 2016.

[251] P. Malhotra, "Advanced Blade Testing Methods for Wind Turbines," University of Massachusetts - Amherst, 2010.

[252] Microchip Technology, "dsPIC33F Microcontroller Data Sheet," USA, 2012.

[253] B. Ivey, "Low-Power Design Guide," DS01416, 2011.

[254] J. Borgeson, S. Schauer, and H. Diewald, "Benchmarking MCU power consumption for ultra-low-power applications." Texas Instruments, Dallas, p. 8, 2012.

[255] STMicroelectronics, "Accurate Power Consumption Estimation For STM32L1 Series of Ultra-Low-Power Microcontrollers," 018552 Rev 2, 2013.

[256] Microchip Technology, "PIC Microcontroller Low Power Tips 'n Tricks," 2009.

[257] D. Hannaford and F. Minos, "Data logging on the dsPIC For MINOS 2011 What is a dsPIC33FJ128MC804 ?," 2011.

[258] B. Ivey, "nanoWatt and nanoWatt XLP^TM Technologies: An Introduction to Microchip‟s Low-Power Devices," DS01267, 2009.

[259] Tranzeo Wireless Technologies Inc, "Wireless Link Budget Analysis: How to Calculate Link Budget for Your WIrless Network," Pitt Meadows, TR3014-01, 2010.

[260] S. P. Beeby and N. White, *Energy Harvesting for Autonomous Systems*. Norwood, Massachusetts: Artech House, 2010.

[261] F. Silva and R. Zurawski, "Energy Harvesting and Real-Time Embedded Systems," *IEEE Ind. Electron. Mag.*, vol. 6, no. 1, pp. 60–61, Mar. 2012.

[262] S. P. Beeby, M. J. Tudor, and N. M. White, "Energy harvesting vibration sources for microsystems applications," *Meas. Sci. Technol.*, vol. 17, no. 12, pp. R175–R195, Dec. 2006.

[263] T. H. Owen, S. Kestermann, R. Torah, and S. P. Beeby, "Self Powered Wireless Sensors for Condition Monitoring Applications," *Sens. Rev.*, vol. 29, no. 1, pp. 38–43, 2009.

[264] Digi-Key Corporation, "Solar Cells | Sensors, Transducers | DigiKey." [Online]. Available: http://www.digikey.co.uk/product-search/en/sensors-transducers/photovoltaic-cells/1966326?k=photovoltaic. [Accessed: 12-Aug-2013].

[265] Centre for Alternative Technology, "How long do solar electric PV panels last?," *CAT Information Service*. [Online]. Available: http://info.cat.org.uk/questions/pv/life-expectancy-solar-PV-panels. [Accessed: 18-Sep-2013].

[266] V. Raghunathan, A. Kansal, J. Hsu, J. K. Friedman, and M. B. Srivastava, "Design Considerations for Solar Energy Harvesting Wireless Embedded Systems," in *Fourth International Symposium on Information Processing in Sensor Networks, IPSN 2005, April 25 - 27, 2005, UCLA, Los Angeles, California, USA*, 2005, pp. 457 – 462.

[267] R. Vullers, R. Schaijk, H. Visser, J. Penders, and C. Hoof, "Energy Harvesting for Autonomous Wireless Sensor Networks," *IEEE Solid-State Circuits Mag.*, vol. 2, no. 2, pp. 29–38, Jan. 2010.

[268] S. A. Weddell, V. G. Merrett, R. N. Harris, and M. B. Al-Hashimi, "Energy Harvesting and Management for Wireless Autonomous Sensors," *Meas. Control*, vol. 41, no. 4, pp. 104–108, 2008.

[269] Y.-C. Shu, "Performance Evaluation of Vibration-Based Piezoelectric Energy Scavengers," in *Energy Harvesting Technologies*, S. Priya and D. J. Inman, Eds. Boston, MA: Springer US, 2009, pp. 79 – 105.

[270] R. Torah, P. Glynne-Jones, M. Tudor, T. O'Donnell, S. Roy, and S. Beeby, "Self-powered autonomous wireless sensor node using vibration energy harvesting," *Meas. Sci. Technol.*, vol. 19, no. 12, p. 125202, Dec. 2008.

[271] Powercast Corporation, "P1110 - 915 MHz RF Powerharvester Receiver," *Product Datasheet*, 2010. [Online]. Available: http://www.powercastco.com/PDF/P1110-datasheet.pdf. [Accessed: 12-Aug-2013].

[272] Powercast Corporation, "P2110 - 915 MHz RF Powerharvester Receiver," *Product Datasheet*, 2010. [Online]. Available: http://www.powercastco.com/PDF/P2110-datasheet.pdf. [Accessed: 12-Aug-2013].

[273] Committee on UK Spectrum Strategy, "United Kingdom Frequency Allocation Table 2013," Ofcom, 2013.

[274] Tyco Electronics, "Comparison of NiCd, NiMH, and Li-Ion Batteries," *ECR-5892D*. [Online]. Available: file:///C:/Users/elooe2/Downloads/ECR-5892D NiCd NiMH Li-Ion.pdf. [Accessed: 25-Sep-2013].

[275] Linear Technology, "LTC3105 40mA Step-up DC/DC Converter with Maximum Power Point Control and 250mV Start-Up," *Technical Datasheet*, 2010. [Online]. Available: http://cds.linear.com/docs/en/datasheet/3105fa.pdf. [Accessed: 22-Aug-2013].

[276] IXYS Korea Ltd., "SLMD481H10L Photovoltaic Cell," *Technical Datasheet*, 2012. [Online]. Available: http://www.digikey.co.uk/product-detail/en/SLMD481H10L/SLMD481H10L-ND/3463128. [Accessed: 12-Aug-2013].

[277] Midé Technology Corporation, "Piezoelectric Energy Harvester," *Midé Volture Datasheet*, 2013. [Online]. Available: http://www.mide.com/pdfs/Volture_Datasheet_001.pdf. [Accessed: 31-May-2013].

[278] Linear Technology, "LTC3588-1 - Piezoelectric Energy Harvesting Power Supply Datasheet." [Online]. Available: http://www.farnell.com/datasheets/1692494.pdf.

10 APPENDIX

10.1 MATLAB CODE: CALIBRATION ROUTINE – *SECTION 5.1.3*

```matlab
Z1_down=dlmread('dc0.txt','\t',7,0);% Read Acquired DC Level for
caliberation
Z1_up=dlmread('dc180.txt','\t',7,0);% Read Acquired DC Level for
caliberation
Y1_down=dlmread('dc90.txt','\t',7,0);% Read Acquired DC Level for
caliberation
Y1_up=dlmread('dc270.txt','\t',7,0);% Read Acquired DC Level for
caliberation
% Accelerometer 1
% (Y_down)
A1xy_down = mean(Y1_down (:,1));
A1yy_down = mean(Y1_down (:,5));
A1zy_down = mean(Y1_down (:,13));
% (Y_up)
A1xy_up = mean(Y1_up (:,1));
A1yy_up = mean(Y1_up (:,5));
A1zy_up = mean(Y1_up (:,13));
 % (Z_down)
A1xz_down = mean(Z1_down (:,1));
A1yz_down = mean(Z1_down (:,5));
A1zz_down = mean(Z1_down (:,13));
% (Z_up)
A1xz_up = mean(Z1_up (:,1));
A1yz_up = mean(Z1_up (:,5));
A1zz_up = mean(Z1_up (:,13));

Y11 = [0 0 1];% (Z_down)
w11 = [A1xz_down A1yz_down A1zz_down 1];
Y21 = [0 0 -1];% (Z_up)
w21 = [A1xz_up A1yz_up A1zz_up 1];
Y31 = [0 1 0];% (Y_down)
w31 = [A1xy_down A1yy_down A1zy_down 1];
Y41 = [0 -1 0];% (Y_up)
w41 = [A1xy_up A1yy_up A1zy_up 1];
Y1 = [ Y11; Y21; Y31; Y41];
w1 = [w11; w21; w31; w41];
X1 = mldivide(w1,Y1);

% Accelerometer 2
% (Y_down)
A2xy_down = mean(Y1_down (:,2));
A2yy_down = mean(Y1_down (:,6));
A2zy_down = mean(Y1_down (:,9));
% (Y_up)
A2xy_up = mean(Y1_up (:,2));
A2yy_up = mean(Y1_up (:,6));
A2zy_up = mean(Y1_up (:,9));
 % (Z_down)
A2xz_down = mean(Z1_down (:,2));
A2yz_down = mean(Z1_down (:,6));
A2zz_down = mean(Z1_down (:,9));
% (Z_up)
A2xz_up = mean(Z1_up (:,2));
A2yz_up = mean(Z1_up (:,6));
A2zz_up = mean(Z1_up (:,9));

Y12 = [0 0 1];% (Z_down)
```

```matlab
w12 = [A2xz_down A2yz_down A2zz_down 1];


Y22 = [0 0 -1];% (Z_up)
w22 = [A2xz_up A2yz_up A2zz_up 1];
Y32 = [0 1 0];% (Y_down)
w32 = [A2xy_down A2yy_down A2zy_down 1];
Y42 = [0 -1 0];% (Y_up)
w42 = [A2xy_up A2yy_up A2zy_up 1];
Y2 = [ Y12; Y22; Y32; Y42];
w2 = [w12; w22; w32; w42];
X2 = mldivide(w2,Y2);


% Accelerometer 3
% (Y_down)
A3xy_down = mean(Y1_down (:,10));
A3yy_down = mean(Y1_down (:,7));
A3zy_down = mean(Y1_down (:,14));
% (Y_up)
A3xy_up = mean(Y1_up (:,10));
A3yy_up = mean(Y1_up (:,7));
A3zy_up = mean(Y1_up (:,14));
 % (Z_down)
A3xz_down = mean(Z1_down (:,10));
A3yz_down = mean(Z1_down (:,7));
A3zz_down = mean(Z1_down (:,14));
% (Z_up)
A3xz_up = mean(Z1_up (:,10));
A3yz_up = mean(Z1_up (:,7));
A3zz_up = mean(Z1_up (:,14));


Y13 = [0 0 1];% (Z_down)
w13 = [A3xz_down A3yz_down A3zz_down 1];
Y23 = [0 0 -1];% (Z_up)
w23 = [A3xz_up A3yz_up A3zz_up 1];
Y33 = [0 1 0];% (Y_down)
w33 = [A3xy_down A3yy_down A3zy_down 1];
Y43 = [0 -1 0];% (Y_up)
w43 = [A3xy_up A3yy_up A3zy_up 1];
Y3 = [ Y13; Y23; Y33; Y43];
w3 = [w13; w23; w33; w43];
X3 = mldivide(w3,Y3);


% Accelerometer 4
% (Y_down)
A4xy_down = mean(Y1_down (:,11));
A4yy_down = mean(Y1_down (:,3));
A4zy_down = mean(Y1_down (:,15));
% (Y_up)
A4xy_up = mean(Y1_up (:,11));
A4yy_up = mean(Y1_up (:,3));
A4zy_up = mean(Y1_up (:,15));
% (Z_down)
A4xz_down = mean(Z1_down (:,11));
A4yz_down = mean(Z1_down (:,3));
A4zz_down = mean(Z1_down (:,15));
% (Z_up)
A4xz_up = mean(Z1_up (:,11));
A4yz_up = mean(Z1_up (:,3));
A4zz_up = mean(Z1_up (:,15));
```

```matlab
Y14 = [0 0 1];% (Z_down)
w14 = [A4xz_down A4yz_down A4zz_down 1];
Y24 = [0 0 -1];% (Z_up)
w24 = [A4xz_up A4yz_up A4zz_up 1];
Y34 = [0 1 0];% (Y_down)
w34 = [A4xy_down A4yy_down A4zy_down 1];
Y44 = [0 -1 0];% (Y_up)
w44 = [A4xy_up A4yy_up A4zy_up 1];
Y4 = [ Y14; Y24; Y34; Y44];
w4 = [w14; w24; w34; w44];
X4 = mldivide(w4,Y4);

% Accelerometer 5
% (Y_down)
A5xy_down = mean(Y1_down (:,8));
A5yy_down = mean(Y1_down (:,4));
A5zy_down = mean(Y1_down (:,16));
% (Y_up)
A5xy_up = mean(Y1_up (:,8));
A5yy_up = mean(Y1_up (:,4));
A5zy_up = mean(Y1_up (:,16));
% (Z_down)
A5xz_down = mean(Z1_down (:,8));
A5yz_down = mean(Z1_down (:,4));
A5zz_down = mean(Z1_down (:,16));
% (Z_up)
A5xz_up = mean(Z1_up (:,8));
A5yz_up = mean(Z1_up (:,4));
A5zz_up = mean(Z1_up (:,16));

Y15 = [0 0 1];% (Z_down)
w15 = [A5xz_down A5yz_down A5zz_down 1];
Y25 = [0 0 -1];% (Z_up)
w25 = [A5xz_up A5yz_up A5zz_up 1];
Y35 = [0 1 0];% (Y_down)
w35 = [A5xy_down A5yy_down A5zy_down 1];
Y45 = [0 -1 0];% (Y_up)
w45 = [A5xy_up A5yy_up A5zy_up 1];
Y5 = [ Y15; Y25; Y35; Y45];
w5 = [w15; w25; w35; w45];
X5 = mldivide(w5,Y5);

% Testing the algorithm
a = dlmread('dc0.txt','\t',7,0);% Read Acquired DC Level for caliberation
b = dlmread('r0.txt','\t',7,0);% Read Acquired Data
% Impact hammer
ham0=(b(:,12)-mean(a(:,12)));
% Normalising Hammer measurement (Converting from Volts to Newtons)
% Sensitivity of transducer is 3.95 pC/N and Charge Amplifier Scaling value
% is 10N/V
hamt=ham0.*10;

xo1= b(:,1);
xo2= b(:,2);
yo1= b(:,5);
zo1= b(:,13);
yo2= b(:,6);
zo2= b(:,9);
xo3= b(:,10);
yo3= b(:,7);
```

```
zo3= b(:,14);
xo4= b(:,11);
yo4= b(:,3);
zo4= b(:,15);
xo5= b(:,8);
yo5= b(:,4);
zo5= b(:,16);


n=length (a);
c=ones(n,1);
h1 = [xo1 yo1 zo1 c]*X1;
h2 = [xo2 yo2 zo2 c]*X2;
h3 = [xo3 yo3 zo3 c]*X3;
h4 = [xo4 yo4 zo4 c]*X4;
h5 = [xo5 yo5 zo5 c]*X5;


x1=h1(:,1);
y1=h1(:,2);
z1=h1(:,3);
x2=h2(:,1);
y2=h2(:,2);
z2=h2(:,3);
x3=h3(:,1);
y3=h3(:,2);
z3=h3(:,3);
x4=h4(:,1);
y4=h4(:,2);
z4=h4(:,3);
x5=h5(:,1);
y5=h5(:,2);
z5=h5(:,3);
```